

ANALYTICAL INVESTIGATION OF INERTIAL FORCE-LIMITING FLOOR
ANCHORAGE SYSTEM FOR SEISMIC RESISTANT BUILDING STRUCTURES

by

Zhi Zhang

Copyright © Zhi Zhang 2017

A Dissertation Submitted to the Faculty of the

DEPARTMENT OF CIVIL ENGINEERING AND ENGINEERING MECHANICS

In Partial Fulfillment of the Requirements

For the Degree of

DOCTOR OF PHILOSOPHY

In the Graduate College

THE UNIVERSITY OF ARIZONA

2017

THE UNIVERSITY OF ARIZONA
GRADUATE COLLEGE

As members of the Dissertation Committee, we certify that we have read the dissertation prepared by Zhi Zhang, titled Analytical Investigation of Inertial Force-limiting Floor Anchorage System for Seismic Resistant Building Structures and recommend that it be accepted as fulfilling the dissertation requirement for the Degree of Doctor of Philosophy.

Robert B. Fleischman

Date: (04/17/2017)

Tribikram Kundu

Date: (04/17/2017)

Hongki Jo

Date: (04/17/2017)

Dichuan Zhang

Date: (04/17/2017)

Final approval and acceptance of this dissertation is contingent upon the candidate's submission of the final copies of the dissertation to the Graduate College.

I hereby certify that I have read this dissertation prepared under my direction and recommend that it be accepted as fulfilling the dissertation requirement.

Dissertation Director: Robert B. Fleischman

Date: (04/17/2017)

STATEMENT BY AUTHOR

This dissertation has been submitted in partial fulfillment of the requirements for an advanced degree at the University of Arizona and is deposited in the University Library to be made available to borrowers under rules of the Library.

Brief quotations from this dissertation are allowable without special permission, provided that an accurate acknowledgement of the source is made. Requests for permission for extended quotation from or reproduction of this manuscript in whole or in part may be granted by the head of the major department or the Dean of the Graduate College when in his or her judgment the proposed use of the material is in the interests of scholarship. In all other instances, however, permission must be obtained from the author.

SIGNED: Zhi Zhang

ACKNOWLEDGEMENTS

This dissertation presented here is under the guidance of Dr. Robert B. Fleischman and supervision of the doctoral committee. This dissertation is based on research performed as part of a multi-university project supported by the National Science Foundation (NSF).

The author would like to thank Dr. Robert B. Fleischman, research advisor, for his time, mentoring and tremendous contribution for the author's academic growth. The author would like to thank Dr. Dichuan Zhang, who served as a Post-Doc at the outset of the project for his guidance, tremendous help in both academic and daily life.

The author would like to thank Dr. Tribikram Kundu and Dr. Hongki Jo, not only for serving on the committee, but also for their help, suggestions and discussions for these years.

The author would like to thank Dr. Jose Restrepo, Dr. Richard Sause, Arpit Nema, Dr. Georgios Tsampras, Ulina Shakya, Anshul Agarwal, Baha Kuzucu, Scott Kuhlman, Austin Houk, Mackenzie Lostra, Ziyi Li, Patrick Hughes, all the students from UCSD that helped perform the shake table test, and all the staff from NEES@UCSD and NHERI@Lehigh for their assistance and help in this project.

The author would like to thank Dr. Kevin Lansey, head of the Department of Civil Engineering and Engineering Mechanics (CEEM Department) at the University of Arizona, for his continuous financial supports over the years.

The author would like to thank the faculty serving as instructor for the classes which the author took or audited over these years. The author learned plenty of new material in the classes. The author would like to thank Dr. Jianqiang Cheng from Department of Systems & Industrial Engineering for his suggestions and help for the design optimization.

The author would like to thank Therese Lane, Karen Van, Brandie Righetti, and Brad Lukso for their help during his graduate work.

The author would like to thank all the graduate students from CEEM Department at the University of Arizona for their discussions, and assistance. Many good ideas and helpful solutions came out from these discussions.

The author would like to thank the HPC (High Performance Computing) team in the University of Arizona for offering this great computing resource to students.

The author would like to thank his teachers and friends for their help and encouragement. There are too many of you, including his previous advisor, Dr. Shaoping Meng, previous lab mates, previous classmates and so on. Your help and encouragement makes the author feel he is not alone and lives in a world full of love.

The author would like to thank everyone from the Chinese Student Soccer Club at the University of Arizona. Soccer is the only sport that the author still plays frequently. There are a lot of unforgettable memories with you guys.

The author would like to thank all the people from the Tucson Chinese Christian Church (TCCC) especially the people from the Student Fellowship. The TCCC provides the author a relaxed, calm and friendly place to stay during busy days.

The author would like to thank his mother, Lanying Su, for her support, encouragement and unconditional love for all these years.

DEDICATIONS

To the memory of my father.

*To my mother, who has gone far beyond the call of duty in supporting my pursuit of
education.*

TABLE OF CONTENTS

ABSTRACT	32
1. INTRODUCTION	34
1.1 IFAS Concept.....	35
1.2 Overall Research Program to Develop the IFAS	39
1.3 IFAS Prototype Development.....	40
1.4 Scope of Dissertation Research	42
1.5 Dissertation Research Unique Intellectual Contribution	44
1.6 Organization of Dissertation	44
2. BACKGROUND	47
2.1 Structure Damage and Economic Loss in Past Earthquakes	47
2.2 Development of Low-damage Structure Systems.....	48
2.3 Floor Isolation Systems.....	49
2.4 Diaphragm Design	50
3. IFAS: 2DOF SYSTEM INVESTIGATION	53
3.1 Overview	53
3.2 2DOF System.....	53
3.3 Background: TMD Modeling as a 2DOF System.....	56
3.4 IFAS: Elastic 2DOF System	58
3.5 Inelastic 2DOF System	76

3.6	Conclusions for 2DOF System	83
4.	IFAS: 2D EVALUATION STRUCTURE MODELS	85
4.1	Evaluation Structure.....	85
4.2	Parameters under Investigation.....	87
4.3	2D Model Description.....	94
4.4	Ground Motion Suites.....	96
4.5	Fundamental Response of the IFAS Structure.....	97
4.6	Effect of IFAS Strength	99
4.7	Effect of Building Height.....	102
4.8	Effect of LFRS Overstrength	103
4.9	Effect of IFAS Secondary Stiffness	106
4.10	Effect of LFRS Type.....	107
4.11	Effect of GLRS Column Properties	108
4.12	Effect of IFAS Strength Profiles.....	109
4.13	Study on Floor Interface Configuration.....	110
4.14	Effect of Using Relative Displacement Limitation Device	114
4.15	Design Space of the FD + RB Combination.....	115
4.16	Design Equation Development	118
4.17	Conclusions for 2D Evaluation Structure Models	122

5.	3D NONLINEAR MODEL DEVELOPMENT AND CALIBRATION.....	124
5.1	Shake Table Test Introduction.....	124
5.2	Analytical Modeling of the Test Specimen	134
5.3	Analytical Prediction Results.....	140
5.4	Response Comparison of the Shake Table Test.....	141
5.5	Damage Calibration of the Pristine Model	155
5.6	Comparisons between 3D Models and the Shake Table Test Specimen	157
5.7	Conclusions for 3D Nonlinear Model Development and Conclusion	166
6.	IFAS: CALIBRATED 3D MODEL ANALYSES	168
6.1	Analyses of the Updated Model.....	168
6.2	Analyses of the Calibrated Model.....	176
6.3	Conclusions for Calibrated 3D Model Analyses	178
7.	Bumper Impact Testing	180
7.1	Test Introduction.....	180
7.2	Preliminary Bumper Force-Deformation Responses	185
7.3	Conclusions for Bumper Impact Testing	188
8.	CONCLUSIONS AND SUGGESTED FUTURE WORK.....	190
8.1	Conclusions.....	190
8.2	Suggested Future Work.....	195

APPENDIX A – SUPPLEMENTAL INFORMATION FOR CHAPTER 3.....	197
A.1 Development of the Simplified 2DOF System	197
A.2 Response of the Elastic 2DOF System Using the Undamped LFRS.....	200
A.3 Modal Analysis	204
A.4 Damping Sweep Method (DSM)	208
A.5 Numerical Central Differential Method (NCDM)	208
A.6 Parameter Sweep Method (PSM).....	210
A.7 x_1 Target Curve in Region II.....	211
A.8 Explanation on PSM when x_1 is Minimized.....	212
A.9 Influence on the Elastic 2DOF System Optimization from ϕ	213
A.10 Global Total Relative Error	216
A.11 Design Space and Related Relative Errors on x_1 , x_2 , \ddot{u}_2 for the Elastic 2DOF.....	217
A.12 Sensitivity Study on Design Parameters of the Elastic 2DOF System	221
A.13 Parameter Sweep Method for Inelastic 2DOF System (PSM_Inelastic)	223
A.14 NTHA on Traditional Elastic 2DOF and Inelastic 2DOF Systems	225
A.15 Single Objective Optimization on the Inelastic 2DOF system	226
APPENDIX B – SUPPLEMENTAL INFORMATION FOR CHAPTER 4.....	232
B.1 Fundamental Response of the IFAS Structure.....	232
B.2 Effect of LFRS Overstrength	233

B.3	Effect of IFAS Secondary Stiffness	235
B.4	Effect of IFAS Initial Stiffness	237
B.5	Design Plot Considering the LFRS Type Effect.....	238
B.6	Effect of GLRS Column Properties	239
B.7	Effect of IFAS Strength Profiles.....	241
B.8	Effect of IFAS Configurations.....	242
B.9	IFAS Properties.....	243
B.10	Parametric Study of Using Ledges	243
B.11	Design Space of the FD + RB Combination.....	246
B.12	Design Space Equation Development.....	250
APPENDIX C – SUPPLEMENTAL INFORMATION FOR CHAPTER 5		255
C.1	Shake Table Test Introduction	255
C.2	Analytical Prediction Results.....	258
C.3	Structural Response Calculations	261
C.4	Accumulated Wall Base Rotation and Structure Drift Envelope in MCE.....	269
C.5	Shear and Moment Envelopes	270
C.6	Floor Acceleration Response in the Shake Table Test	272
C.7	Selected FD and BRB Force-Deformation Response.....	274
C.8	Model Verification using Sequential Analysis	276

APPENDIX D – SUPPLEMENTAL INFORMATION FOR CHAPTER 6.....	279
D.1 Energy Dissipation in Different Components.....	279
D.2 PSA and FD Force in Phase II	279
D.3 Influence from Different Transverse Wall Strength	283
APPENDIX E – SUPPLEMENTAL INFORMATION FOR CHAPTER 7	285
E.1 Advantages and Disadvantages of Each Test Protocol.....	285
E.2 Relationships between Different Test Parameters	285
9. REFERENCES	287

LIST OF FIGURES

Fig. 1-1. Structure deformation under lateral forces: (a) without slip; (b) with slip.....	36
Fig. 1-2. Early IFAS Concepts: (a) smart frame [1]; (b) shake table test specimen [2]. .	37
Fig. 1-3. Anticipated benefits and tradeoffs in response at different IFAS strength.	38
Fig. 1-4. Photos of test specimens: (a) full-scale sub-structure; (b) half-scale shake table test specimen.	40
Fig. 1-5. IFAS devices: (a) BRB; (b) FD; (c) RB; (d) bumper.	41
Fig. 1-6. IFAS Prototype System: (a) elevation view; (b) plan view.	42
Fig. 2-1. ELF design: (a) lateral seismic force; (b) base shear; (c) diaphragm design force.	51
Fig. 3-1. IFAS Models: (a) evaluation structure; (b) elastic 2DOF; (c) inelastic 2DOF. .	54
Fig. 3-2. Floor isolation schematic drawing: (a) Full floor; (b) Partial floor.....	55
Fig. 3-3. IFAS hysteresis: (a) inelastic IFAS; (b) linear elastic spring; (c) viscous damping.	56
Fig. 3-4. TMD structure: (a) schematic; (b) frequency response.....	57
Fig. 3-5. Validation of the equations: (a) x_1 ; (b) x_2 ; (c) $x_2 - x_1$; (d) \ddot{u}_1 ; (e) \ddot{u}_2	60
Fig. 3-6. Natural frequencies vs. μ : (a) full plot; (b) close-up at $\mu=\phi$	61
Fig. 3-7. Effective modal mass ratio for: (a) $\mu=1$; (b) $\mu=0.25$; (c) $\mu=10$; Modal expansion of effective modal mass ratio for: (d) $\mu=1$; (e) $\mu=0.25$; (f) $\mu=10$	62
Fig. 3-8. Optimization Procedure: (a) General Response; (b) Balanced Nodes; (c) Minimized Nodes; (d) Optimum Damping.....	63
Fig. 3-9. x_1 Target Curve for 2DOF IFAS when $\phi=0.03$	64
Fig. 3-10. Target Curve: (a) x_1 ; (b) x_2 ; (c) \ddot{u}_2	65

Fig. 3-11. Response: (a) x_1 target curve; (b) optimized x_1 in Region I.	65
Fig. 3-12. x_2 response vs. ζ when $\phi = 0.07, \mu = 1, \beta = 0.04$	66
Fig. 3-13. Responses vs. μ for x_1 minimization, Region I: (a) $ x_1 /x_{st}$; (b) $ x_2 /x_{st}$; (c) $ \ddot{u}_2 /a_g$	67
Fig. 3-14. Responses versus μ when optimizing x_1 : (a) $ x_1 /x_{st}$; (b) $ x_2 /x_{st}$; (c) $ \ddot{u}_2 /a_g$	68
Fig. 3-15. Response contour plots of the elastic 2DOF system when optimizing x_1 ($\phi = 0.03$): (a) $ x_1 /x_{st}$; (b) ζ_{opt} ; (c) $ x_2 /x_{st}$; (d) $ \ddot{u}_2 /a_g$	69
Fig. 3-16. Response of the elastic 2DOF system and related design parameters when minimizing ε_{tot} : (a) ε_{tot}^* ; (b) ε_{x1} ; (c) $\varepsilon_{\ddot{u}2}$; (d) ε_{x2} ; (e) μ ; (f) β ; (g) ζ_{opt}	71
Fig. 3-17. Contour plot of minimized x_1, x_2, \ddot{u}_2 relative error response at each (μ, β) when $\varepsilon_{tot} < 150\%$ ($\phi = 0.03$): (a) ε_{x1} ; (b) ε_{x2} ; (c) $\varepsilon_{\ddot{u}2}$; (d) design space.	72
Fig. 3-18. Elastic 2DOF system with added viscous damping to the LFRS.....	73
Fig. 3-19. Ground motions response spectrum with 5% damping and design spectrum..	74
Fig. 3-20. Time history responses of the 2DOF system: (a) acceleration; (b) displacement.	74
Fig. 3-21. Schematic drawing of an inelastic 2DOF system with force-deformation relationship of the IFAS and wall base plastic hinge.....	77
Fig. 3-22. Time history responses of an inelastic 2DOF system ($\phi = 0.03, \mu = 20, \alpha' = 0.8, k' = 1, \gamma = 0\%$, EQ4): (a) acceleration; (b) displacement.	80
Fig. 3-23. Inelastic 2DOF system ($\phi = 0.03$) responses: minimizing x_1 : (a) x_1 ; (b) x_2 ; (c) \ddot{u}_2 ; minimizing x_2 : (d) x_1 ; (e) x_2 ; (f) \ddot{u}_2	81
Fig. 3-24. Contour plot of minimized x_1, x_2, \ddot{u}_2 relative error response at each (μ, α) when $\varepsilon_{tot} < 300\%$ ($\phi = 0.03$): (a) ε_{x1} ; (b) ε_{x2} ; (c) $\varepsilon_{\ddot{u}2}$; (d) design space.	83

Fig. 4-1. Plan view of evaluation structure: (a) floor plan; (b) shear wall cross section. .	86
Fig. 4-2. Schematic drawings showing parameters: (a) IFAS force-deformation; (b) LFRS moment-rotation.....	88
Fig. 4-3. Cyclic material testing results: (a) FD; (b) BRB; (c) RB.	89
Fig. 4-4. Shear wall base moment-rotation backbone: (a) 4-story.....	91
Fig. 4-5. Rocking wall: (a) rocking wall base moment-rotation hysteretic property; wall base moment-rotation backbone: (b) 4-story; (c) 8-story; (d) 12-story.	92
Fig. 4-6. GLRS column (12-story) properties: (a) different stiffness; (b) different strength.	93
Fig. 4-7. IFAS strength profiles: (a) constant profile; (b) triangular profile.....	94
Fig. 4-8. Schematic drawing: (a). half structure; (b). Numerical model; force-deformation: (c) IFAS; (d) wall base; (e) plastic hinge moment-curvature backbones.	95
Fig. 4-9. Ground motions response spectrum with 5% damping and design spectrum....	97
Fig. 4-10. Evaluation structure ($\Omega_e=1.0$, $\alpha=0.3$) response under EQ2 at MCE level: (a) conceptual schematic drawing; (b) shear wall displacement at selected floor levels; (c) shear wall roof drift, base rotation and GLRS roof drift.....	98
Fig. 4-11. Evaluation structure ($\Omega_e=1.0$, $\alpha=0.3$) response at selected time spots in Fig. 4-10.	99
Fig. 4-12. 12-story structure ($\Omega_e = 1.0$) maximum response envelopes: (a) floor acceleration; (b) shear wall inter-story drift; (c) GLRS column inter-story drift; (d) relative displacement.	100

Fig. 4-13. Baseline structure ($\Omega_e = 1.0$) response parametric plot: (a) floor acceleration ($0 < \alpha < 2$); (b) Inter-story drift; (c) relative displacement; (d) floor acceleration ($0 < \alpha < 8$); (e) MCE energy dissipation distribution; (f) DBE energy dissipation distribution.	101
Fig. 4-14. Parametric plot of different building height ($\Omega_e = 1.0$): (a) floor acceleration ($0 < \alpha < 2$); (b) inter-story drift; (c) relative displacement; (d) floor acceleration ($0 < \alpha < 8$); energy dissipation: (e) total, GLRS; (f) IFAS, wall.....	103
Fig. 4-15. 12-story structure response comparison at different Ω_e and α under MCE ($\gamma=2\%$): (a) wall inter-story drift; (b) floor acceleration; (c) GLRS column inter-story drift; (d) relative displacement; (e) IFAS energy dissipation; (f) wall energy dissipation.....	104
Fig. 4-16. Design plot for different structure height and Ω_e : (a) α ; (b) LFRS drift reduction; (c) floor acceleration reduction; (d) GLRS drift; (e) LFRS drift; (f) floor acceleration.	106
Fig. 4-17. 4-story structures using different γ ($\Omega_e=1.0$): (a) floor acceleration ($0 < \alpha < 4$); (b) LFRS drift; (c) floor acceleration ($0 < \alpha < 2$); (d) relative displacement; (e) GLRS drift..	107
Fig. 4-18. 12-story structures using different LFRS: (a) floor acceleration ($0 < \alpha < 10$); (b) LFRS drift; (c) floor acceleration ($0 < \alpha < 2$); (d) relative displacement; (e) GLRS drift..	108
Fig. 4-19. 4-story structures using different column stiffness under MCE: (a) floor acceleration ($0 < \alpha < 8$); (b) LFRS drift; (c) floor acceleration; (d) relative displacement; (e) GLRS drift.	109
Fig. 4-20. 4-story structure response comparison using different IFAS strength pattern: (a) IFAS strength pattern; (b) shear wall drift; (c) relative displacement; (d) floor acceleration.	110
Fig. 4-21. Cantilever Slab Case: (a) plan view; (b) elevation view.....	111
Fig. 4-22. Ledge Case: (a) plan view; (b) elevation view.....	111

Fig. 4-23. 2D model: (a) IFAS device; (b) wall base; (c) elevation view of first floor. .	113
Fig. 4-24. Dynamic pounding force acts on ledge: (a) left; (b) middle; (c) right.	113
Fig. 4-25. Numerical model: (a) 2D model with bumper; (b) initial gap for the bumper.	114
Fig. 4-26. Parametric response: (a) Relative displacement; (b) floor acceleration; (c) LFRS drift.....	115
Fig. 4-27. 12-story RC wall structures using LFRS with different Ω_e : (a) LFRS drift; (b) floor acceleration; (c) GLRS drift; (d) α ; energy dissipation: (e) LFRS; (f) IFAS.....	116
Fig. 4-28. 12-story RC wall structures with different Ω_e : (a) LFRS drift; (b) α	118
Fig. 4-29. Regression analysis of Δ_{LFRS} and δ_r when Ω_e : (a) 0.7; (b) 1.0; (c) 1.3; (d) 1.6.	119
Fig. 4-30. Regression analysis of α and δ_r when Ω_e : (a) 0.7; (b) 1.0; (c) 1.3; (d) 1.6.....	119
Fig. 4-31. Regression analysis results of b_0 , b_1 vs. γ : (a) b_0 ; (b) b_1 ; vs. Ω_e : (c) b_0 ; (d) b_1	120
Fig. 4-32. Prediction equation of b_0 , b_1 vs. γ : (a) b_0 ; (b) b_1 ; vs. Ω_e : (c) b_0 ; (d) b_1	120
Fig. 4-33. Regression analysis results of c_0 , c_1 vs. γ : (a) c_0 ; (b) c_1 ; vs. Ω_e : (c) c_0 ; (d) c_1 .	121
Fig. 4-34. Prediction equations of c_0 , c_1 vs. γ : (a) c_0 ; (b) c_1 ; vs. Ω_e : (c) c_0 ; (d) c_1	121
Fig. 5-1. Shake Table Test Specimen: (a) Isometric Model View (Courtesy of Nema Arpit); (b) Photo (northeast view).	125
Fig. 5-2. Shake table test specimen: (a) plan view; (b) elevation view.	126
Fig. 5-3. North wall design capacity: (a) Relative to design strength; (b) Phase III Comparison.	127

Fig. 5-4. IFAS backbone characteristic curves (at half-scale) targeted for: (a) DBE; (b) MCE.....	129
Fig. 5-5. DBE level: (a) SE time history; (b) BE time history; (c) Response spectrum.	130
Fig. 5-6. Floor anchorages for typical floor: (a) device locations; (b) PSA; (c) roller bearing.	132
Fig. 5-7. Deformable connection: (a) annotated FD photo; (b) BRB schematic drawing.	133
Fig. 5-8. Restoring and limitation devices: (a) specimen layout; (b) RB assembly; (c) bumper.	133
Fig. 5-9. Concrete property: (a) column; (b) North PT wall; (c) NS PT wall.	135
Fig. 5-10. Shake table test model in ANSYS for Phase I.	135
Fig. 5-11. PT wall base model: (a) nonlinear link distribution and property; (b) NF.....	136
Fig. 5-12. Component behavior: (a) PT bars constitutive; (b) ED hysteresis.....	137
Fig. 5-13. Precast column model: (a) nonlinear link distribution; (b) NF; (c) steel stress-strain.....	138
Fig. 5-14. Model: (a) near North wall; (b) bumper model and force-deformation property; (c) PSA model and force-deformation property.	139
Fig. 5-15. Deformable connection force-deformation property: (a) FD; (b) BRB.	139
Fig. 5-16. Sequence prediction - North wall base rotation.	141
Fig. 5-17. Structure fundamental period change.....	142
Fig. 5-18. Structure property change: (a) fundamental period; (b) moment strength (EW).	143

Fig. 5-19. North wall base in plane rotation: (a) SE DBE; BE: (b) SVC; (c) DBE; (d) MCE.	144
Fig. 5-20. West wall base in plane rotation: (a) SE DBE; BE: (b) SVC; (c) DBE; (d) MCE.	145
Fig. 5-21. GLRS inter-story drift envelopes: (a) SE DBE; BE: (b) SVC; (c) DBE; (d) MCE.	145
Fig. 5-22. GLRS EW inter-story drift (4 th story) at Col. Line C: (a) SE DBE; (b) BE SVC.	146
Fig. 5-23. GLRS resultant acceleration envelope: (a) SE DBE; BE: (b) SVC; (c) DBE; (d) MCE.....	147
Fig. 5-24. Slab twisting, ϕ , envelope: (a) SE DBE; BE: (b) SVC; (c) DBE; (d) MCE.	148
Fig. 5-25. Roof relative displacement: (a) EW; (b) NS (West wall).	149
Fig. 5-26. IFAS Relative Displacement Profile: (a) SE DBE; BE: (b) SVC; (c) DBE; (d) MCE.....	150
Fig. 5-27. FD force-deformation responses at Test 11 and Test 17.....	151
Fig. 5-28. FD deformation in Test 17: schematic drawing: (a) before the specimen deformed; (b) after the specimen deformed; (c) FD axial deformation and wall base rotation.	152
Fig. 5-29. Overturning moment: (a) SE DBE; BE: (b) Svc; (c) DBE; (d) MCE.....	153
Fig. 5-30. Hysteretic energy dissipation: (a) BE DBE ($\alpha=0.59$ & $\alpha=0.43$); (b) SE DBE ($\alpha=0.59$); BE: (c) SVC ($\alpha=0.45$); (d) DBE ($\alpha=0.43$); (e) DBE ($\alpha=0.55$); (f) MCE ($\alpha=0.56$).	154

Fig. 5-31. Force-deformation relationship of FD, FD+RB, wall shear and floor inertial force at roof for: (a) BE SVC; (b) BE DBE; (c) BE MCE.	155
Fig. 5-32. Transverse wall cracks after Test 14: (a) East wall; (b) West wall.....	156
Fig. 5-33. Precast components damages: (a) North wall; (b) Precast columns.	156
Fig. 5-34. Comparison of moment-rotation behavior between damaged wall and test. .	157
Fig. 5-35. Responses: (a) floor displacement at column line C; (b) floor acceleration near column B1; (c) relative displacement; (d) slab twisting; (e) North wall base rotation...	158
Fig. 5-36. (a) North wall base moment-rotation; force-deformation: (b) FD; (c) BRB..	158
Fig. 5-37. Moment-roof drift behavior (a) structure overturning; (b) GLRS overturning; (c) structure overturning moment decomposition.	159
Fig. 5-38. Time history responses (Test 10): (a) floor displacement at column line B; (b) floor acceleration near column B1; (c) slab twisting; (d) north wall base rotation.	160
Fig. 5-39. Moment-rotation responses (Test 10): (a) structure overturning; (b) North wall base; (c) roof FD force-deformation; (d) roof BRB force-deformation.	160
Fig. 5-40. Bumper engagement at roof (Test 10): (a) acceleration; (b) slab twisting, GLRS roof drift and North wall base rotation; (c) bumper deformation; (d) relative displacement.	161
Fig. 5-41. Bumper engagement at roof (zoomed in at Test 10): (a) acceleration; (b) slab twisting, GLRS roof drift and North wall base rotation; (c) bumper deformation; (d) relative displacement.	162
Fig. 5-42. Schematic drawing of deformed structure when the bumper is engaged in Fig. 5-41d.	163

Fig. 5-43. Time history responses (Test 17): (a) floor displacement at column line B; (b) floor acceleration near column B1; (c) slab twisting; (d) north wall base rotation.	164
Fig. 5-44. Moment-rotation responses (Test 17): (a) structure overturning; (b) North wall base; (c) West wall base; (d) East wall base; (e) roof FD force-deformation; (f) roof BRB force-deformation.	165
Fig. 5-45. Structure response envelopes (Test 17): (a) floor resultant acceleration; (b) North wall drift; (c) GLRS resultant drift; (d) slab twisting.	166
Fig. 6-1. Response envelopes: (a) resultant acceleration; (b) LFRS drift; (c) GLRS resultant drift; (d) slab twisting; (e) relative displacement.	170
Fig. 6-2. Acceleration: (a) location of the occurrence of the maximum resultant acceleration at each floor; Fourier Transform of the floor acceleration indicated in (a) at: (b) level 4; (c) level 2.	171
Fig. 6-3. Energy dissipation among different components.	172
Fig. 6-4. Location of the occurrence of the maximum resultant acceleration at each floor.	172
Fig. 6-5. Acceleration: Fourier Transform of the floor acceleration indicated in Fig. 6-4 at: (a) level 4; (b) level 2; (c) envelopes.	173
Fig. 6-6. Structure layout: (a) eccentric; (b) concentric.	173
Fig. 6-7. Structure response envelopes between eccentric and concentric cases ($\rho=0.6$, $\alpha=0.57$): (a) floor acceleration; (b) North wall drift; (c) GLRS drift; (d) slab twisting..	175
Fig. 6-8. Bumper property and structure responses: (a) bumper force-deformation; response envelope: (b) floor acceleration; (c) North wall drift; (d) slab twisting.	176

Fig. 6-9. Structure response envelopes: (a) resultant floor acceleration; (b) North wall drift.	177
Fig. 6-10. North wall moment-rotation: (a) models using damaged GLRS; (b) models using pristine GLRS.	177
Fig. 6-11. Structure overturning moment-roof drift at column line B: (a) models using damaged GLRS; (b) models using pristine GLRS.	178
Fig. 7-1. Test set up (Courtesy of Tsampras Georgios).	181
Fig. 7-2. Photo of the test specimen and the connected actuators.	181
Fig. 7-3. Photo of the tested bumper: (a) yellow bumper; (b) black bumper.	181
Fig. 7-4. Instrumentation plan: (a) top view - zoom out; (b) bottom view; (c) GoPro camera at the wall top; (d) top view – zoom in; (e) location and zoom in of the web camera.	183
Fig. 7-5. Predefined displacement time history: (a) simplified single pulse; (b) smoothed bumper deformation from the shake table test; (c) cyclic deformation using constant loading velocity; (4) mimicking bumper deformation from the shake table test.	184
Fig. 7-6. Bumper response time history: (a) deformation; (b) force; (c) force-deformation.	186
Fig. 7-7. Bumper force-deformation behavior: (a) $V_0=5$ in/s; (b) $V_0=10$ in/s.	187
Fig. 7-8. Bumper force-deformation behavior: (a) $\delta_{\max} = 0.4$ in; (b) $\delta_{\max} = 0.5$ in.	187
Fig. 7-9. Bumper response time history: (a) revised slab displacement; (b) force; (c) force-deformation.	188
Fig. A-1. Natural Frequencies vs. μ : (a) 1 st mode; (b) 2 nd mode; (c) switch point; (d) effective modal mass ratio at $\beta = 0$; (e) S_{22} at different β .	205

Fig. A-2. Effective modal mass ratio for: (a) $\mu=1$; (b) $\mu=0.25$; (c) $\mu=10$; Modal expansion of effective modal mass ratio for: (d) $\mu=1$; (e) $\mu=0.25$; (f) $\mu=10$	207
Fig. A-3. DSM method explanation, use x_1 response as an example.	208
Fig. A-4. NCDM method explanation: (a) x_1 resp. as an example; (b) case 1; (c) case 2.	209
Fig. A-5. 2DOF system response matrix with varying: (a) ζ and ω/ω_n ; (b) β and ζ ; (c) μ and β	210
Fig. A-6. Target curve and the 2DOF system frequency response: (a) x_1 target curve; (b) P, Q, M frequency values; (c) example x_1 response in Region II.	212
Fig. A-7. Response contour plots of the elastic 2DOF system when optimizing x_1 ($\phi = 0.03$): (a) $ x_1 /x_{st}$; (b) ζ_{opt} ; (c) $ x_2 /x_{st}$; (d) $ \ddot{u}_2 /a_g$	212
Fig. A-8. Elastic 2DOF response at x_1^* : (a) $ x_1^* /x_{st}$; (b) ζ_{opt} ; (c) μ ; (d) β ; (e) $\varepsilon_{\ddot{u}2}$; (f) ε_{x2}	214
Fig. A-9. Elastic 2DOF response at \ddot{u}_2^* : (a) $ \ddot{u}_2^* /a_g$; (b) ζ_{opt} ; (c) μ ; (d) β ; (e) ε_{x1} ; (f) ε_{x2}	215
Fig. A-10. Elastic 2DOF response at x_2^* : (a) $ x_2^* /x_{st}$; (b) ζ_{opt} ; (c) μ ; (d) β ; (e) ε_{x1} ; (f) $\varepsilon_{\ddot{u}2}$	216
Fig. A-11. Response of the elastic 2DOF system and related design parameters when minimizing ε_{tot} : (a) ε_{tot}^* ; (b) ε_{x1}' ; (c) $\varepsilon_{\ddot{u}2}'$; (d) ε_{x2}'	217
Fig. A-12. Contour plot of minimized x_1, x_2, \ddot{u}_2 relative error response at each (μ, β) when $\varepsilon_{tot} < 150\%$ ($\phi = 0.03$): (a) ε_{x1} ; (b) ε_{x2} ; (c) $\varepsilon_{\ddot{u}2}$; (d) design space.	218
Fig. A-13. Contour plot of minimized x_1, x_2, \ddot{u}_2 relative error response at each (μ, β) when $\varepsilon_{tot} < 150\%$ ($\phi = 0.05$): (a) ε_{x1} ; (b) ε_{x2} ; (c) $\varepsilon_{\ddot{u}2}$; (d) design space.	218
Fig. A-14. Contour plot of minimized x_1, x_2, \ddot{u}_2 relative error response at each (μ, β) when $\varepsilon_{tot} < 150\%$ ($\phi = 0.1$): (a) ε_{x1} ; (b) ε_{x2} ; (c) $\varepsilon_{\ddot{u}2}$; (d) design space.	219

Fig. A-15. Contour plot of minimized x_1, x_2, \ddot{u}_2 relative error response at each (μ, β) when $\varepsilon_{tot} < 150\%$ ($\phi = 0.15$): (a) ε_{x1} ; (b) ε_{x2} ; (c) $\varepsilon_{\ddot{u}2}$; (d) design space.	219
Fig. A-16. Contour plot of minimized x_1, x_2, \ddot{u}_2 relative error response at each (μ, β) when $\varepsilon_{tot} < 150\%$ ($\phi = 0.19$): (a) ε_{x1} ; (b) ε_{x2} ; (c) $\varepsilon_{\ddot{u}2}$; (d) design space.	220
Fig. A-17. Contour plot of minimized x_1, x_2, \ddot{u}_2 relative error response at each (μ, β) when $\varepsilon_{tot} < 150\%$ ($\phi = 0.21$): (a) ε_{x1} ; (b) ε_{x2} ; (c) $\varepsilon_{\ddot{u}2}$; (d) design space.	220
Fig. A-18. Contour plot of minimized x_1, x_2, \ddot{u}_2 relative error response at each (μ, β) when $\varepsilon_{tot} < 150\%$ ($\phi = 0.23$): (a) ε_{x1} ; (b) ε_{x2} ; (c) $\varepsilon_{\ddot{u}2}$; (d) design space.	221
Fig. A-19. Maximum 2DOF system responses in earthquakes at different μ : acceleration: (a) zoom out; (b) zoom in; displacement: (c) zoom out; (d) zoom in.....	222
Fig. A-20. Maximum 2DOF system responses in earthquakes at different β : acceleration: (a) zoom out; (b) zoom in; displacement: (c) zoom out; (d) zoom in.....	223
Fig. A-21. Maximum 2DOF system responses in earthquakes at different ξ : acceleration: (a) zoom out; (b) zoom in; displacement: (c) zoom out; (d) zoom in.....	223
Fig. A-22. PSM_Inelastic method: (a) response matrix for (k', γ) ; (b) response matrix for (k', α') ; (c) response matrix for (μ, α') ; (d) response matrix for (μ, ϕ)	225
Fig. A-23. Response of the 2DOF_R in the elastic and inelastic 2DOF system: shear force: (a) LFRS; (b) GLRS; displacement; (c) x_1 ; (d) x_2	226
Fig. A-24. Responses of parametric study of inelastic 2DOF systems ($\phi = 0.03, \mu = 20, \alpha' = 0.8$): (a) acceleration; (b) displacement.	227
Fig. A-25. Contour plots of parametric study of inelastic 2DOF systems ($\phi = 0.03, \mu = 20, \alpha' = 0.8$): (a) x_1 ; (b) x_2 ; (c) \ddot{u}_2 ; (d) $ x_2 - x_1 $	228

Fig. A-26. Contour plots of parametric study of inelastic 2DOF systems when x_1 is minimized ($\phi=0.03, \mu=20$): (a) x_1 ; (b) x_2 ; (c) \ddot{u}_2 ; (d) $ x_2-x_1 $; (e) γ	229
Fig. A-27. Contour plots of parametric study of inelastic 2DOF systems when x_1 is minimized ($\phi=0.03$): (a) x_1 ; (b) x_2 ; (c) \ddot{u}_2 ; (d) $ x_2-x_1 $; (e) γ ; (f) k'	230
Fig. A-28. Contour plots of parametric study of inelastic 2DOF systems when x_2 is minimized ($\phi=0.03$): (a) x_1 ; (b) x_2 ; (c) \ddot{u}_2 ; (d) $ x_2-x_1 $; (e) γ ; (f) k'	231
Fig. B-1. Evaluation structure ($\Omega_e=1.0, \alpha=0.3$) response at selected time spots in Fig. 4-10.	233
Fig. B-2. 4-story structure response comparison at different Ω_e and α under MCE ($\gamma=2\%$): (a) wall inter-story drift; (b) floor acceleration; (c) GLRS column inter-story drift; (d) relative displacement; (e) IFAS energy dissipation; (f) wall energy dissipation.....	234
Fig. B-3. 8-story structure response comparison at different Ω_e and α under MCE ($\gamma=2\%$): (a) wall inter-story drift; (b) floor acceleration; (c) GLRS column inter-story drift; (d) relative displacement; (e) IFAS energy dissipation; (f) wall energy dissipation.....	234
Fig. B-4. 12-story structures using different γ ($\Omega_e=1.0$): (a) floor acceleration ($0<\alpha<8$); (b) LFRS drift; (c) floor acceleration ($0<\alpha<2$); (d) relative displacement; (e) GLRS drift..	235
Fig. B-5. 12-story structure responses in EQ3 ($\gamma = 1\%$, MCE): (a) wall drift envelopes; wall base moment decomposition: (b) $\alpha = 0.01$; (c) $\alpha = 0.1$	236
Fig. B-6. Design plot for IFAS secondary stiffness ($\Omega_e=1.0, 1.6$): (a) α ; (b) LFRS drift reduction; (c) floor acceleration reduction; (d) GLRS drift; (e) LFRS drift; (f) floor acceleration.	237
Fig. B-7. 12-story structures using different IFAS K_i : (a) floor acceleration ($0<\alpha<8$); (b) LFRS drift; (c) floor acceleration ($0<\alpha<2$); (d) relative displacement; (e) GLRS drift..	238

Fig. B-8. Design plot for different LFRS types ($\Omega_e=1.0$): (a) α ; (b) LFRS drift reduction; (c) floor acceleration reduction; (d) GLRS drift; (e) LFRS drift; (f) floor acceleration.	239
Fig. B-9. 12-story RC wall structures using different column stiffness: (a) floor acceleration ($0<\alpha<8$); (b) LFRS drift; (c) floor acceleration; (d) relative displacement; (e) GLRS drift.	239
Fig. B-10. 12-story rocking wall structures using different column stiffness: (a) floor acceleration ($0<\alpha<15$); (b) LFRS drift; (c) floor acceleration; (d) relative displacement; (e) GLRS drift.	240
Fig. B-11. 12-story RC wall structures using different column strength: (a) floor acceleration ($0<\alpha<8$); (b) LFRS drift; (c) floor acceleration; (d) relative displacement; (e) GLRS drift.	241
Fig. B-12. 12-story structure response comparison using different IFAS strength pattern: (a) IFAS strength pattern; (b) shear wall drift; (c) relative displacement; (d) floor acceleration.	241
Fig. B-13. Responses envelopes of an evaluation structure with different IFAS configurations: (a) floor acceleration; (b) inter-story drift; (c) relative displacement....	243
Fig. B-14. Wall base comparison: (a) Moment-rotation; (b) Base shear-top displacement.	244
Fig. B-15. Schematic plot on deformed IFAS: (a) energy dissipation device; (b) RB..	245
Fig. B-16. Energy dissipation device deformation between two pins: (a) Horizontal direction; (b) Vertical direction; (c) Axial direction.....	245
Fig. B-17. Slab local moment: (a) Left side of anchorage; (b) Right side of anchorage.	246

Fig. B-18. 12-story RC wall structures using IFAS with different γ in MCE: (a) LFRS drift; (b) floor acceleration; (c) GLRS drift; (d) α ; energy dissipation: (e) LFRS; (f) IFAS. ...	247
Fig. B-19. 12-story structures using different LFRS: (a) LFRS drift; (b) floor acceleration; (c) GLRS drift; (d) α ; energy dissipation: (e) LFRS; (f) IFAS.	248
Fig. B-20. 12-story structures using different GLRS stiffness: (a) LFRS drift; (b) floor acceleration; (c) GLRS drift; (d) α ; energy dissipation: (e) LFRS; (f) IFAS.	249
Fig. B-21. Evaluation structures with different building height: (a) LFRS drift; (b) floor acceleration; (c) GLRS drift; (d) α ; energy dissipation: (e) LFRS; (f) IFAS.	250
Fig. B-22. Prediction equation of b_0, b_1 vs. γ : (a) b_0 ; (b) b_1 ; vs. Ω_e : (c) b_0 ; (d) b_1	251
Fig. B-23. Prediction equation of c_0, c_1 vs. γ : (a) c_0 ; (b) c_1 ; vs. Ω_e : (c) c_0 ; (d) c_1	251
Fig. B-24. Prediction equation of b_0, b_1 vs. γ : (a) b_0 ; (b) b_1 ; vs. Ω_e : (c) b_0 ; (d) b_1	251
Fig. B-25. Prediction equation of c_0, c_1 vs. γ : (a) c_0 ; (b) c_1 ; vs. Ω_e : (c) c_0 ; (d) c_1	252
Fig. B-26. Prediction equation of b_0, b_1 vs. γ : (a) b_0 ; (b) b_1 ; vs. Ω_e : (c) b_0 ; (d) b_1	252
Fig. B-27. Prediction equation of c_0, c_1 vs. γ : (a) c_0 ; (b) c_1 ; vs. Ω_e : (c) c_0 ; (d) c_1	253
Fig. B-28. Prediction equation of b_0, b_1 vs. γ : (a) b_0 ; (b) b_1 ; vs. Ω_e : (c) b_0 ; (d) b_1	253
Fig. B-29. Prediction equation of c_0, c_1 vs. γ : (a) c_0 ; (b) c_1 ; vs. Ω_e : (c) c_0 ; (d) c_1	254
Fig. C-1. Typical instrumentation view: (a) Plan; Elevations: (b) North; (c) West.	257
Fig. C-2. IFAS Design Space: (a) Inter-story drift; Floor (b) relative displacement; (c) acceleration.	258
Fig. C-3. Maximum response: inter-story drift: (a) LFRS; (b) GLRS; (c) floor acceleration.	259
Fig. C-4. Maximum inter-story drift: (a) North wall (EW); (b) GLRS (EW); (c) GLRS (Resultant).	260

Fig. C-5. Maximum floor acceleration: (a) GLRS (EW); (b) GLRS (NS); (c) GLRS (Resultant).....	260
Fig. C-6. Maximum shear wall uplift: (a) North wall; (b) East wall; (c) West wall.....	261
Fig. C-7. Structure response kinematics: (a) wall base rotation; (b) GLRS drift; (c) slab twist.....	262
Fig. C-8. Force calculation diagrams: overturning: (a) structure; (b) at i^{th} floor; (c) wall base moment; (d) wall shear force and moment at i^{th} floor.....	264
Fig. C-9. Shear force in the EW direction at the 1 st floor of: (a) structure; (b) North wall; (c) GLRS and transverse walls.	267
Fig. C-10. Comparison on shear force of GLRS and GLRS & transverse walls from one analysis in Phase I.....	268
Fig. C-11. Verification of Eqn. C-12, C-15 from one analysis in Phase I: (a) north wall base; (b) Column B2.	269
Fig. C-12. BE MCE Phase I & II comparison: (a) cumulative base rotation: (b) inter-story drift.....	269
Fig. C-13. Force envelope comparison: (a) story shear (b) overturning moment.....	272
Fig. C-14. Location of maximum resultant acceleration: Test 11; Test 18; Test 20.	272
Fig. C-15. Fourier Transform of the floor acceleration at the indicated location in Fig. C-14: (a) EW; (b) NS; (c) structural period variation.....	273
Fig. C-16. Time history of the floor acceleration at the indicated location in Fig. C-14: (a) floor 4; (b) floor 2.	274
Fig. C-17. Force-deformation response: (a) FD; (b). BRB.....	275

Fig. C-18. Maximum BRB force under tension and compression at each BE DBE and MCE test.	276
Fig. C-19. Time history responses (Test 7): (a) floor displacement at column line B; (b) floor acceleration near column B1; (c) slab twisting; (d) north wall base rotation.	276
Fig. C-20. Moment-rotation responses (Test 7): (a) structure overturning; (b) North wall base; (c) roof FD force-deformation; (d) roof BRB force-deformation.	277
Fig. C-21. Time history responses (Test 11): (a) floor displacement at column line B; (b) floor acceleration near column B1; (c) slab twisting; (d) north wall base rotation.	277
Fig. C-22. Moment-rotation responses (Test 11): (a) structure overturning; (b) North wall base; (c) roof FD force-deformation; (d) roof BRB force-deformation.	278
Fig. D-1. Energy dissipation among different components (Eccentric case).	279
Fig. D-2. Deformation time history: (a) PSA; (b) FD; (c) North wall base rotation.	280
Fig. D-3. Response time history PSA and FD at level 4: (a) force; (b) deformation of FD and PSA; (c) GLRS displacement; (d) North wall base rotation and slab twisting.	281
Fig. D-4. Summation force time history between PII-w/FD-0.6 and PII-wo/FD-0.6: (a) level 1; (b) level 2; (c) level 3; (d) level 4.	283
Fig. D-5. Transverse wall moment-rotation behavior using different post-tensioned force.	283
Fig. D-6. Structure response envelopes ($\rho_{NS}=0.4$ and $\rho_{NS}=0.8$ for transverse walls): (a) floor acceleration; (b) North wall drift; (c) East wall drift; (d) GLRS drift; (e) slab twisting.	284
Fig. E-1. Scatter plots: (a) $V_0=1$ in/s; (b) $V_0=5$ in/s; (c) $V_0=10$ in/s; (d) $V_0=15$ in/s; (e) $V_0=20$ in/s.	286

LIST OF TABLES

Table 1-1. Dissertation work summary.....	45
Table 4-1. Seismic design for the evaluation structures, transverse direction (Full structure).	86
Table 4-2. Shear wall dimension for different building height.....	87
Table 4-3. Column design information (lower stories only).....	87
Table 4-4. IFAS devices properties for evaluation structure.	89
Table 4-5. Study Matrix: IFAS strength (FD + RB, constant profile).....	90
Table 4-6. Shear wall design for different building height and overstrength.	91
Table 4-7. Elastic GLRS stiffness ratio (ϕ).....	93
Table 4-8. Selected ground motion information.	96
Table 4-9. Structural response at design limits.	102
Table 5-1. North wall property (half-scale structure).	127
Table 5-2. IFAS design for the shake table test.	128
Table 5-3. Ground motions used in the test.	129
Table 5-4. Shake table test sequence.	131
Table 5-5. Description of model development	134
Table 6-1. Description of models with different floor anchorages	169
Table 6-2. Description of models with different LFRS eccentricity.	174
Table 6-3. Description of model with different damage source.	176
Table 7-1. Scatter plots classification using different V_0	185
Table A-1. 2DOF systems for comparison ($\phi = 0.03$, $\xi_1 = 0.02$).....	221
Table B-1. IFAS properties for parametric study.	243

Table B-2. IFAS eccentricities and concrete coefficient of friction for parametric study.	244
Table C-1. Sensor list.....	257
Table D-1. Description of models with different transverse wall strength.....	284
Table E-1. Advantages and limitations of different test protocol.....	285

ABSTRACT

This dissertation describes the analytical research as part of a comprehensive research program to develop a new floor anchorage system for seismic resistant design, termed the Inertial Force-limiting Floor Anchorage System (IFAS).

The IFAS intends to reduce damage in seismic resistant building structures by limiting the inertial force that develops in the building during earthquakes. The development of the IFAS is being conducted through a large research project involving both experimental and analytical research. This dissertation work focuses on analytical component of this research, which involves stand-alone computational simulation as well as analytical simulation in support of the experimental research (structural and shake table testing).

The analytical research covered in this dissertation includes four major parts:

(1) Examination of the fundamental dynamic behavior of structures possessing the IFAS (termed herein IFAS structures) by evaluation of simple two-degree of freedom systems (2DOF). The 2DOF system is based on a prototype structure, and simplified to represent only its fundamental mode response. Equations of motions are derived for the 2DOF system and used to find the optimum design space of the 2DOF system. The optimum design space is validated by transient analysis using earthquakes.

(2) Evaluation of the effectiveness of IFAS designs for different design parameters through earthquake simulations of two-dimensional (2D) nonlinear numerical models of an evaluation structure. The models are based on a IFAS prototype developed by a fellow researcher on the project at Lehigh University.

(3) Development and calibration of three-dimensional nonlinear numerical models of the shake table test specimen used in the experimental research. This model was used for predicting and designing the shake table testing program.

(4) Analytical parameter studies of the calibrated shake table test model. These studies include: relating the shake table test performance to the previous evaluation structure analytical response, performing extended parametric analyses, and investigating and explaining certain unexpected shake table test responses.

This dissertation describes the concept and scope of the analytical research, the analytical results, the conclusions, and suggests future work. The conclusions include analytical results that verify the IFAS effectiveness, show the potential of the IFAS in reducing building seismic demands, and provide an optimum design space of the IFAS.

1. INTRODUCTION

In current earthquake engineering, seismic-resistant structures are designed to dissipate earthquake energy through yielding of their structural elements. Thus, structures are intended to incur damage during strong earthquakes. This damage may be direct yielding, but can also be accompanied by local buckling and low cycle fatigue fracture for steel members and cracking crushing and spalling of concrete members. The design objective of seismic codes to date has been to prevent collapse of the structure, therefore ensuring its occupants survive the event. If possible, the damage can be repaired afterward (yellow tag) though in severe cases, the building will have to be demolished (red tag). Further, nonstructural components (cladding, glazing, partitions, ceilings, etc.) can also incur damage that can be more costly than structural damage. The level of damage to both the structural and nonstructural components is typically closely correlated to the level of lateral deformation (drift) in the structure. Finally, building contents and equipment can be damaged or lose functionality due to high floor accelerations.

Thus, a well-designed structure may survive the earthquake, but severe damage can make it costly to repair or even not worth it to repair. The temporary closure of building service may also cause economic loss and business downtime. In recent decades, the concept of performance-based seismic design has taken hold. In this approach, a level of desired performance is related to different earthquake intensities, with more critical structures tending toward immediate operability. One promising trend in this regard is the recent development of low-damage systems. These structural systems attempt to eliminate or minimize the damage in structures during earthquakes.

Traditional building structures consist of a gravity load resisting system (GLRS) and a lateral force resisting system (LFRS). The GLRS, which comprises most of the structure, is the portion of the structure (gravity system columns and the floor system) that carries the gravity load (dead and live loads) to the foundation. The LFRS, usually a limited number of specially placed elements (e.g. shear walls, braced frames, moment frames, etc.), is used to resist lateral forces such as wind or earthquakes. In essence, the LFRS provides the lateral stability to the GLRS. These systems are connected by the floor diaphragm anchorage (e.g. dowel bars extending from shear walls, studs extending from a braced frame beam, etc.), which is essentially a rigid connection. When earthquakes occur, the majority of the inertial force is generated within the GLRS (through the large mass of the floor system) and must be transferred to the LFRS.

The new low-damage system being developed in this research, the Inertial Force-limiting Floor Anchorage System (IFAS), has the potential to reduce both the structural and nonstructural component damage in earthquakes by partially isolating the large floor mass through a deformable diaphragm connection between the GLRS and the LFRS. This Ph.D. dissertation focuses on the analytical research related to the development of the IFAS.

1.1 IFAS Concept

The IFAS is proposed as a response-limiting system for building structures to minimize the earthquake damage. The IFAS reduces seismic response by partially uncoupling the GLRS and LFRS response, therefore partially isolating the floor mass. This objective is achieved by providing a deformable (ductile) connection between the floor system and the primary vertical plane elements of the LFRS (e.g. shear walls or braced frames). This deformable diaphragm connection possesses a predefined strength. At

diaphragm force levels below this strength, for instance daily wind events or small earthquakes, the floor anchorage is essentially rigid, and thus the building responds like a traditional structure (See Fig. 1-1a). However, when the diaphragm force reaches the IFAS strength, as will occur in a strong earthquake, the floor anchorage deforms, transforming the diaphragm seismic demands into relative horizontal displacement between the GLRS and LFRS, therefore limiting the seismic forces transferred to the LFRS (See Fig. 1-1b). This action will reduce LFRS drift demands and floor accelerations in comparison to traditional building structures, therefore mitigating both structural and nonstructural component damage. Elastic restoring elements, stabilizing elements, and if needed, re-centering elements to eliminate residual displacements in the floor system, complete the IFAS.

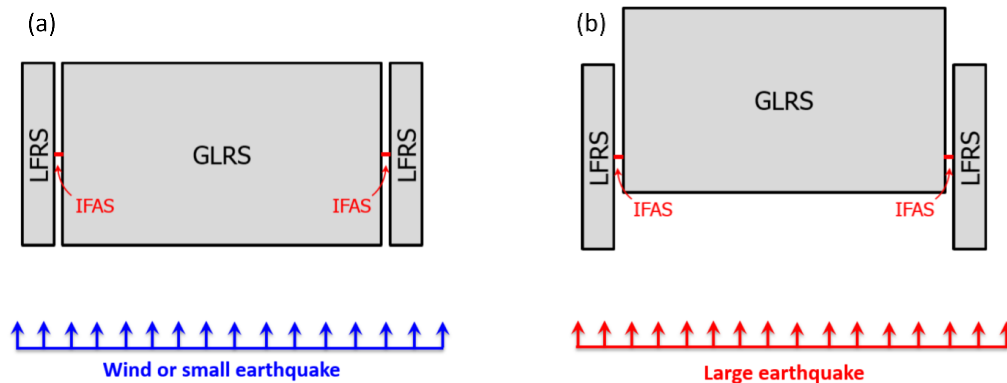


Fig. 1-1. Structure deformation under lateral forces: (a) without slip; (b) with slip.

The idea of partially uncoupling the GLRS is attractive since most of the structure's mass originates in the GLRS. Thus by limiting the force transfer, the IFAS has the potential to limit diaphragm inertial forces, therefore lowering floor accelerations and reducing LFRS seismic demands as mentioned previously. This condition will result in less damage

to the structure, non-structural elements and building contents, and prevents failure of the floor diaphragm itself.

The concept of decoupling the building mass from the LFRS was originally proposed by [1]. In this work, a smart frame was developed for uncoupling the GLRS and LFRS [1]. The smart frame involves spring and viscous damper placed between the GLRS and LFRS (See Fig. 1-2a), and isolators under each GLRS column so that the period of the structure lengthens toward lower earthquake demand.

A similar floor decoupling concept to the IFAS was pilot tested in [2]. In this work, a small scale shake table test on two six-story building specimens (See Fig. 1-2b) was conducted [2]. One specimen represented a traditional building with a rigidly connected slab; the other utilized hysteretic energy dissipation connections (triangular-plate added damping and stiffness elements or TADAS) between the slabs and the LFRS. The response comparison indicated that the use of the energy dissipation connection reduced the displacement and acceleration with respect to the specimen using the traditional rigid connection, but also had higher residual deformation.

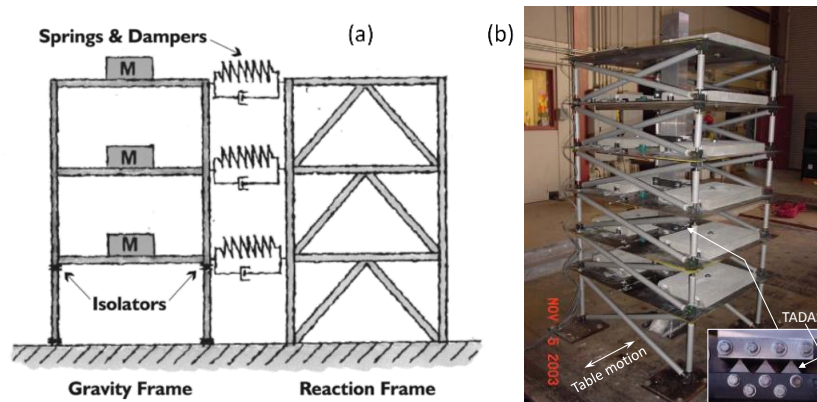


Fig. 1-2. Early IFAS Concepts: (a) smart frame [1]; (b) shake table test specimen [2].

A tradeoff exists for the IFAS in that as inertial forces and floor accelerations are lowered, the magnitude of the relative displacement between the floors and LFRS increases. Thus, an optimum IFAS strength must be identified that lowers seismic demand, yet limits the relative floor displacement within an acceptable range with respect to architectural requirements. Further, for very low IFAS strengths, the lateral drifts of the gravity system columns may also become too large. The GLRS column lateral drifts must be limited to assure a stable structure [3].

A key design parameter is the “cut-off” strength of the IFAS. A dimensionless parameter α is used to express the relative strength of the IFAS to current code diaphragm design force F_{px} [4, 5], defined as $\alpha = \Sigma F_y / F_{px}$, where the summation occurs for all LFRS connections acting in the direction of F_{px} (i.e. NS or EW direction). Note that since the diaphragm anchorage is part of the collector system, the system overstrength factor Ω_o is applied (in addition to the shear strength reduction factor ϕ) in the design [4, 5]. This leads to a current code nominal strength α value not of unity, but instead $\alpha = \Omega_o / \phi$ (typically ~ 3.33). Fig. 1-3 shows the general structure response trends at different IFAS strength.

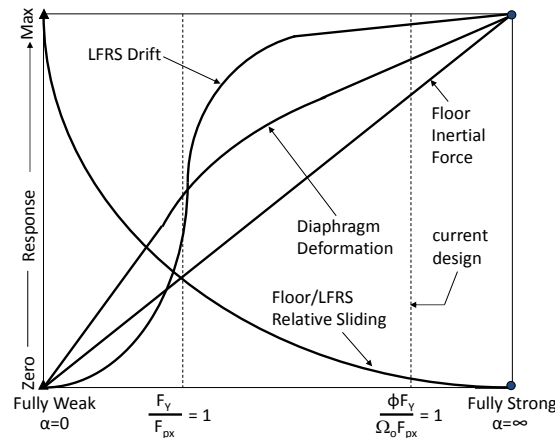


Fig. 1-3. Anticipated benefits and tradeoffs in response at different IFAS strength.

1.2 Overall Research Program to Develop the IFAS

The IFAS is being developed through a large multi-university research program with significant design consultant input [6]. The research program includes both analytical and experimental research. Pertinent details of the research program are described in Section 1.4. However, for context, the main points of the research program are summarized below:

The analytical research (this dissertation) involves five main activities: (1) developing numerical models of IFAS buildings; (2) performing parametric studies to examine the potential effectiveness and to determine a preliminary IFAS design space; (3) performing numerical predictions of the tests to support the experimental program; (4) updating and calibration of numerical models using the test data; and, (5) conducting parameter studies with the calibrated model to determine final design recommendations.

The experimental research involves two primary testing programs:

(1) Real-time dynamic tests on a full-scale specimen representing the IFAS and surrounding floor region to one wall on one floor of a reinforced concrete structure (See Fig. 1-4a). The objective of this test program was to: (a) determine the characteristics of the IFAS prototype (See Section 1.3); and, (b) examine constructability and performance aspects. The specimen was subjected to different excitation, including sinusoidal and predefined displacement histories [13].

(2) A shake table test of a half-scale four-story reinforced concrete structure (See Fig. 1-4b). The objective of this test program was to: (1) demonstrate the IFAS prototype in a structure subjected to earthquake excitations; (2) directly compare the IFAS structure to a traditional structure; and, (3) validate the numerical models of the shake table test

specimen. The test specimen, which was converted between an IFAS and traditional structure, possessed an eccentric layout in order to examine IFAS response to structure twist in plan. The test specimen was subjected to multiple strong motions.

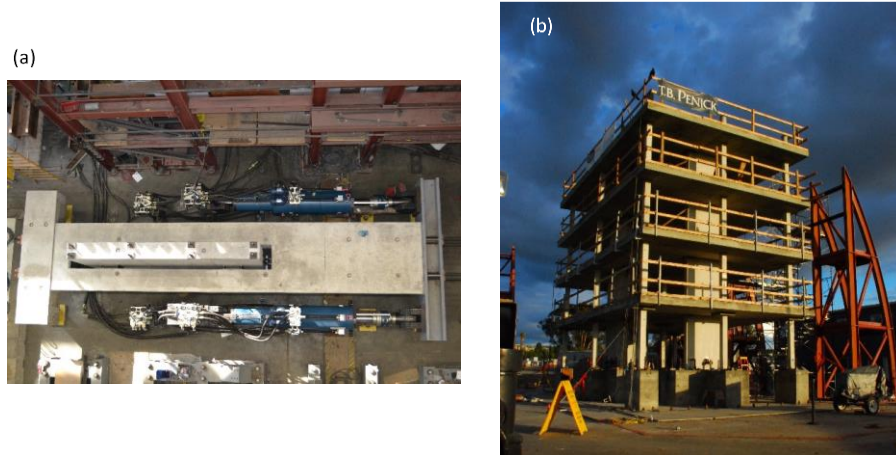


Fig. 1-4. Photos of test specimens: (a) full-scale sub-structure; (b) half-scale shake table test specimen.

Additionally, component testing was performed on a bumper element that serves as a key device in the IFAS prototype (described in Section 1.3). The bumper was originally tested under quasi-static loading rates to determine hysteretic properties for implementation into numerical models. Later, dynamic tests of the bumper were conducted to determine its force-deformation behavior under high loading rate.

1.3 IFAS Prototype Development

A key deliverable from the first phase of the research program was the development of an IFAS prototype for use in the shake table test. The IFAS prototype is composed of state-of-the-art devices to achieve the needed behavior: (1) predefined and controllable strength; (2) efficient energy dissipation; (3) elastic restoring/centering; (4) LFRS stabilization (described subsequently), and (5) relative displacement limiting.

The first step in developing the IFAS prototype was to evaluate different energy dissipation devices for suitability. Candidate devices included metallic dampers [11], viscous dampers [12], friction dampers (termed FD in this dissertation) [13], and buckling restrained braces (BRB), normally used as diagonal braces in braced frames [14, 15]. Of these, the FD and BRB were selected for the IFAS prototype due to their superior energy dissipation capabilities, large deformation capacity, high initial stiffness and well-defined and repeatable strength [16]. The device selected for elastic restoring and LFRS stabilization is a rubber bearing (RB) typically used on bridges. Each RB consists of a laminated rubber pad bonded between steel plates. The laminated rubber pad consists of rubber layers laminated to steel shim plates, which reinforce the rubber for stability [13].

In the development of the concept, more aggressive designs (lower IFAS strength) to minimize response in the design basis earthquake (DBE) were found to be possible if the resulting large relative displacement in the maximum considered earthquake (MCE) could somehow be limited [3, 7, 8]. A special bumper device was introduced for limiting relative displacement. The bumper also serves to reduce impact force between the floor and the LFRS (e.g. wall) when the floors undergo excessive relative displacement. Fig. 1-5a-d shows the individual devices that comprise the final IFAS prototype.

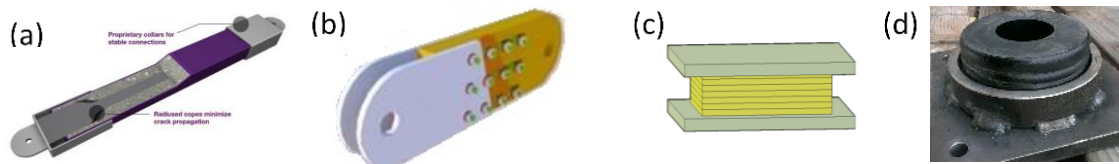


Fig. 1-5. IFAS devices: (a) BRB; (b) FD; (c) RB; (d) bumper.

Fig. 1-6a,b show an elevation and plan view of the IFAS prototype in a structure. The deformable connection (FD or BRB) connects between the vertical LFRS element (a

shear wall in this case) and the floor. The connection is installed underneath the floor slab (in the ceiling space) and connected to one end of the wall (See Fig. 1-6a). In order to accommodate the relative displacement between the LFRS and GLRS, a moat is required (See Fig. 1-6b). The moat creates an unbraced LFRS element (wall) that will not be stable out of plane. Thus, the RB is placed between the wall and slab within the moat at each floor level to ensure wall stability (See Fig. 1-6b). In addition, the RB provides an elastic restoring force to the floor system to assist in re-centering after an earthquake. Bumpers are installed on the slab within the moat at each end of the wall (See Fig. 1-6). A gap is provided between the bumper and the wall corresponding to the maximum allowable relative displacement between the wall and floor.

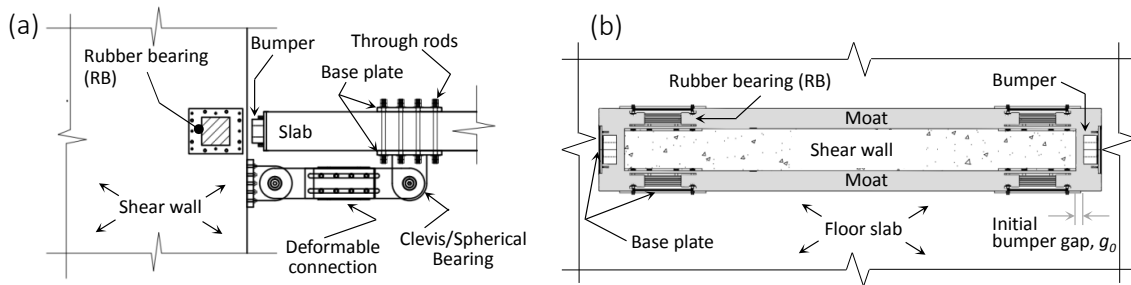


Fig. 1-6. IFAS Prototype System: (a) elevation view; (b) plan view.

1.4 Scope of Dissertation Research

The dissertation focuses on analytical research supporting the development of the IFAS concept toward an effective IFAS prototype. This analytical research includes:

- (1) An examination of the fundamental behavior of the IFAS structure through classical dynamic analysis of two-degree of freedom (2DOF) systems;
- (2) Parametric studies to determine the influence of design parameters on IFAS performance. The studies were performed as earthquake simulations of two-dimensional

(2D) nonlinear numerical models of an evaluation structure. The parameters varied included IFAS strength, stiffness, and structure properties (building height, LFRS overstrength, LFRS type, etc.). Additionally, the kinematics of the IFAS response was studied (moats vs. ledges, bumper gap magnitude, etc.).

(3) Development of three-dimensional (3D) nonlinear numerical models of the shake table test specimen tested in the project. These models were used for predicting the response of the specimen in the shake table test program. These predictions assisted in design on the specimen, both for structural elements and the IFAS, as well as selecting the appropriate ground motion records for the test program. The simulations of the shake table test also assisted in determining where to position instrumentation on the specimen and to ensure safe construction of the specimen.

(4) Calibration of the 3D model using the shake table test results. Models were first updated for actual material and device properties. Validation of the model is crucial for IFAS development by making possible extensive analytical research with high fidelity models. Such analytical research can cover a wider ranges of design parameters than is possible with physical experiments, and provide these results with a high level of confidence. The updated model was subjected to a sequential analysis that follows the test program to examine the ability of the model to capture cumulative damage during the testing. Model calibration involved adjusting strength and stiffness parameters in the analytical models to match experimental results during different stages of the shake table test sequence. A calibrated model that can successfully match a point in the test sequence will provide more effective comparisons to a pristine model rather than performing sequential runs. Once the 3D model is validated, the responses between the 3D and 2D

model can be compared. This comparison can be used to show the the level of difference between the 2D and 3D model.

Further, future analytical work can be imagined. The 2D and/or 3D models can be extended to apply to a range of IFAS building structures, including different structural systems. Thus, a parametric study investigating the IFAS design space for different types of structural systems can be performed. Other aspects of earthquake response that may influence IFAS performance can be considered, including different structure layouts and earthquake loading, different IFAS strength distributions, different mass distributions between the LFRS and GLRS, and different interface conditions.

1.5 Dissertation Research Unique Intellectual Contribution

The unique intellectual contribution of this dissertation research are related to the development of an innovative seismic response reduction system, the IFAS. These contributions include: (1) The development and analysis of simple models to provide the fundamental behavior of structures with the IFAS; (2) extensive parameter studies to determine the effect of key design parameters and to identify the optimum design space for the IFAS; (3) the development, updating, calibration and evaluation of 3D structure models to examine the response of the IFAS structure. These accomplishments will lead to design guidelines for the IFAS.

1.6 Organization of Dissertation

The dissertation is organized as follows:

Chapter 2: Background on low-damage systems and diaphragm design

Chapter 3: IFAS: 2DOF System Investigation

Chapter 4: IFAS: 2D Evaluation Structure Models

Chapter 5: IFAS: 3D Model Development and Calibration

Chapter 6: IFAS: Calibrated 3D Model Analyses

Chapter 7: Bumper Impact Testing

Chapter 8: Conclusions and Suggested Future Work

Note that results from each stage of the work described in Chapters 3-7 are shown in that section. Some of the related background information (derivation of equations, description of the methods, etc.) is provided in Appendices at the end of this dissertation. The status (progress, future work and deliverables) of each of these dissertation research topics is summarized in Table 1-1.

Table 1-1. Dissertation work summary.

Research Focus	Chapters in Dissertation	Status	Description
Fundamental Behavior of Structures with IFAS	3	Activities	<ul style="list-style-type: none">• Creation of simple 2DOF systems• Derivation of dynamic equations for the elastic 2DOF system• Harmonic analysis of the elastic 2DOF system model• Single-objective and multi-objective design optimization of the elastic 2DOF system• Align nonlinear 2DOF systems to seismic design code parameters• Nonlinear time history analyses of nonlinear 2DOF systems using earthquakes across range of design parameters: IFAS strength, GLRS mass ratio, IFAS initial stiffness, IFAS secondary stiffness
		Deliverables	<ul style="list-style-type: none">• Influences from the design parameters listed above to the 2DOF system responses• Optimum IFAS design space based on the 2DOF System response
		Suggested future work	<ul style="list-style-type: none">• Creation of relationship between the 2DOF system response and evaluation structure response
Seismic Response of Structures with IFAS	4	Activities	<ul style="list-style-type: none">• Selection and design of Evaluation Structures• Creation of 2D nonlinear models of Evaluation Structures• Parametric study of seismic performance for different IFAS strength, building height, LFRS overstrength and LFRS types

			<ul style="list-style-type: none"> • Secondary parameter studies on IFAS initial stiffness, IFAS secondary stiffness, GLRS stiffness, GLRS strength, IFAS eccentricity, IFAS strength pattern along the height • Evaluation of effectiveness of different IFAS configuration schemes (ledges, pockets, etc.)
		Deliverables	<ul style="list-style-type: none"> • Influences from the design parameters listed above to the 2D structure model responses • IFAS design space and preliminary design guidelines for multi-story structures
		Suggested future work	<ul style="list-style-type: none"> • Examination of aggressive designs using calibrated bumper model
Development and updatation of 3D IFAS Structure Models	5	Activities	<ul style="list-style-type: none"> • Development of a 3D nonlinear model of the shake table test specimen • Analyses in support of design and construction of the shake table test specimen • Prediction of shake table tests by numerical analysis • Post-processing of the shake table test data • Calibration of the 3D nonlinear model
		Deliverables	<ul style="list-style-type: none"> • Validation of a numerical modeling methodology on IFAS and precast reinforced concrete structure with generic scenario
		Suggested future work	<ul style="list-style-type: none"> • Sequential analysis of the updated 3D model
Analysis of IFAS using Updated and Calibrated Model	6	Activities	<ul style="list-style-type: none"> • Analytical studies on LFRS offset, bumper stiffness, transverse wall strength • Investigation of unexpected test specimen responses through analytical study
		Deliverables	<ul style="list-style-type: none"> • Defense of the IFAS effectiveness
		Suggested future work	<ul style="list-style-type: none"> • Bi-direction earthquake simulation of the test specimen • Summarization of the analytical work from design perspectives
Bumper test under high loading rate	7	Activities	<ul style="list-style-type: none"> • Establishment of relationship between different parameters for the bumper test from the measured relative displacement in shake table test • Investigation of bumper force-deformation property under high loading rate
		Suggested future work	<ul style="list-style-type: none"> • Development and implement of a better bumper model for the numerical analysis

2. BACKGROUND

2.1 Structure Damage and Economic Loss in Past Earthquakes

In current seismic design approaches, life safety and collapse prevention are targeted for building structures to permit occupants to survive the earthquake [9]. Reconnaissance of recent large earthquakes indicates that the amount of damage, economic loss due to downtime, and repair cost of structures were unacceptably high [26]. Building damage also makes rescue activities and critical facility operations more difficult to execute because of the loss of lifelines and cascading events [10, 18-25]. Recent earthquakes show that countries with well-developed seismic codes can still undergo significant financial loss in large earthquakes [27]. For example, the 2010 Chile Earthquake caused about US\$15-30 billion in economic losses [28], the 2011 Christchurch Earthquake caused about NZ\$8-16 billion in economic losses [29], and the 2011 East Japan Earthquake caused about US\$200-300 billion in economic losses [30].

Researchers have increased their interest in nonstructural component performance in earthquakes in recent decades [31-35] as nonstructural damage is a main source of economic loss. A nonstructural damage database was developed [34] in 1999 focusing on the nonstructural components and contents performance in previous earthquakes, and expanded in 2003 [35]. The expanded database shows examples of the cost breakdown between structural, nonstructural and contents for office buildings, hotels and hospitals [35]. This cost breakdown shows that nonstructural and contents costs dominate the overall construction costs of all these buildings (82%, 87% and 92% respectively for office buildings, hotels and hospitals) [35]. This result implies that the protection of nonstructural

components and contents of the building from earthquake demands is a key factor in avoiding excessive economic loss.

Extensive research has been conducted on economic loss from earthquakes [36-46]. Several methodologies have been developed for evaluating the potential economic loss for a community so that decision makers can assign resources according to the estimate economic risk [37-40]. The losses consist of direct losses and indirect losses. The direct losses consist of physical destruction and additional impacts following the physical destruction, such as fire after earthquakes. The indirect losses are resulted from the consequences of physical destruction, such as interruption of business or industries. Indirect loss is more difficult to measure than direct loss [41]. Research shows that the impact of indirect losses are large and can continue into a long term [42, 43, 44].

Building damage is thus unavoidable in earthquakes based on current seismic design. In order to reduce structural and nonstructural damage, reduce repair cost and economic loss in earthquakes, several low-damage structure systems have been developed. The IFAS concept treated in this dissertation is an example of such a low-damage system. Other low-damage structure systems are reviewed briefly in Section 2.2.

2.2 Development of Low-damage Structure Systems

Several low-damage systems have been proposed for reducing building response in earthquakes. These systems often attempt to reduce building seismic forces, lateral deformation (drift) and floor accelerations. Reducing these response quantities will tend to reduce the building damage, and thus economic loss in earthquakes.

New low-damage structures recently or currently under development include: self-centering rocking system [47-58]; horizontal self-centering system [59, 60]; replaceable

energy dissipation devices [61-69] that control the force transferred to the structural system and protect the structural components; base isolation technique for reducing building acceleration response [71]; active or semi-active control to improve structure performance in earthquakes [72-75]; negative stiffness devices to reduce structure base shear demand and to limit the structure deformations and accelerations in strong earthquakes [76-79].

In particular, base isolation is a design concept which decouples the horizontal motion of the superstructure from the foundation in earthquakes. Several types of base isolation devices have been developed, such as high damping rubber, lead-rubber elastomeric bearings, friction pendulum bearings. Viscous dampers can be added in parallel as a supplemental damping device for energy dissipation purposes [85].

Designing structures with isolation system shifts the structural fundamental period to a longer period and changes the fundamental mode shape. This period lengthening reduces the acceleration and inter-story drift of the superstructure, but increases the displacement demand of the superstructure at the same time. Supplemental damping can be added into the isolation system to reduce the structure displacement response [86].

Several buildings using base isolation techniques have been built in the past several decades. Some of these buildings performed well in comparison to traditional fixed base buildings in earthquakes [10,71,80,82,83].

2.3 Floor Isolation Systems

Floor isolation systems [81,84] are similar in concept to base isolation but can be more cost effective since they do not require special foundations [84,98]. Floor isolation typically introduces a secondary floor system within a traditional fixed base building [84], allowing equipment to be protected against earthquakes. Some floor isolation systems

proposed and investigated include: using roof isolation systems to reduce the building response under earthquakes [87, 88] in a manner similar to the use of tuned-mass damper [89]; applying an isolation layer in intermediate levels of high rise structures [90]; locating single-story isolations system or multiple isolation systems in a building [91]; dividing the superstructure of a base-isolated building into several segments by isolation layers [92].

Several isolation system devices have been developed for floor isolation purposes, including spring (linear and nonlinear) and damper (viscous and hysteretic) [87, 90, 97], wire rope systems [96] and friction pendulum systems [93,94,95]. Semi-active control techniques can be applied to the floor isolation to pursue lower structural response in earthquakes [98]. A negative stiffness platform has been proposed between the key non-structural equipment and the structure [99] for mitigating equipment high accelerations.

2.4 Diaphragm Design

Diaphragms are designed to transfer the seismic forces from the floor system to the vertical elements of the LFRS. Diaphragm design forces, F_{px} , are determined by an equivalent lateral force (ELF) procedure [4, 5]. These forces are used to design the diaphragm reinforcement: chords, shear reinforcement, collectors and anchorages [100].

In the ELF procedure, the expected total lateral force in the design earthquake is estimated for the structure, termed “base shear”, V_b . The lateral forces causing this base shear, F_i , are distributed at each floor level based on the fundamental mode of the building structure, thus essentially an inverted triangle, with slight modifications for cantilever structures (Fig. 2-1).

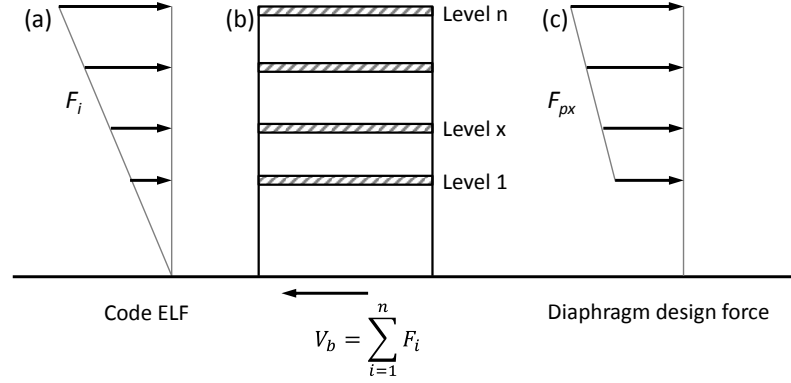


Fig. 2-1. ELF design: (a) lateral seismic force; (b) base shear; (c) diaphragm design force.

The base shear, V_b , is calculated as shown in Eqn. 2-1 [4, 5]:

$$V_b = \frac{S_{DS}}{R/I_e} W \quad (2-1)$$

where S_{DS} is the design spectral response acceleration parameter at short periods calculated from seismic maps in [4, 5], W is the total structure weight, R is a response modification coefficient and I_e is an importance factor. Note that R significantly reduces the design forces from their elastic levels (up to 8 times) based on the amount of ductility and energy dissipation possible in the building; thus, in surviving the earthquake, a typical building is expected to undergo damage.

Lateral seismic forces F_i for a given level x , F_x , is calculated based on Eqn. 2-2:

$$F_x = \frac{w_x h_x^k}{\sum_{i=1}^n w_i h_i^k} V_b \quad (2-2)$$

where w_x and w_i are the portion of the total effective seismic weight of the structure located or assigned to level x and i . h_x and h_i are the height from the base to level x and i . k is an exponent related to the structure period. The diaphragm design forces, F_{px} , are calculated based on Eqn. 2-3:

$$F_{px} = \frac{\sum_{i=x}^n F_i}{\sum_{i=x}^n w_i} w_{px} \quad (2-3)$$

where w_{px} is the weight tributary to the diaphragm at level x . Note that while the diaphragm forces and structure seismic forces refer to the same action, the diaphragm design forces F_{px} and the seismic design forces F_i follow different patterns because F_i (used for design of the vertical elements) is a profile representing the response of the structure at a given instant; while F_{px} (used for design of each floor element) is an envelope of maxima for each level occurring at different times in the earthquake. The diaphragm design force is further limited by the design code as follows:

$$F_{px} > 0.2S_{DS}I_e w_{px} \quad (2-4)$$

$$F_{px} < 0.4S_{DS}I_e w_{px} \quad (2-5)$$

Recent research indicates that current code diaphragm design forces may significantly underestimate the actual inertial forces that develop in the floor system during strong earthquakes [101, 102] because of the importance of higher modes during inelastic structural response [103]. The upcoming code version [104] will reflect these findings. Nonetheless, the IFAS strength used in concept development is referenced to F_{px} using the non-dimensional ratio α , as was introduced in Sec. 1.1 and will be further discussed in Section 4.

3. IFAS: 2DOF SYSTEM INVESTIGATION

3.1 Overview

The identification of optimum IFAS designs is being determined primarily through nonlinear time history analysis of 2D models of multi-story evaluation structures (as will be described in Section 4). These analyses provide the IFAS seismic response, but are sufficiently complicated to prevent arriving at satisfactory answers regarding fundamental behavior. For this reason, an investigation of a simplified 2DOF system of the IFAS structure is performed, as has been done in the past with other response reduction systems, for instance tuned mass dampers (TMDs).

The objectives of the study include: (1) describing the fundamental response of the IFAS structures; and (2) providing insight on selecting optimal IFAS properties. This chapter summarizes work performed on a simplified 2DOF system. The simplified 2DOF system resembles the classical representation of the TMD. Thus, the classical solutions for the TMD [113] are used to guide and interpret the results of this study.

3.2 2DOF System

The 2DOF system is a simplified version of the full 2D numerical model of the 12-story evaluation structure. In the full 2D model (described in detail in Chapter 4), the LFRS is represented as a 12-story cantilever column with lumped masses at each floor level, while the GLRS is a 12-story frame model (See Fig. 3-1a). In the simplified 2DOF system, each of these components is represented by a single DOF (See Fig. 3-1b): the LFRS is DOF 1; the GLRS is DOF 2. The IFAS is represented by a Kelvin-Voigt model: a dashpot (c_3) in parallel with an elastic spring (k_3). In the study, optimum IFAS properties (k_3 , c_3) are sought

as the relative values of the LFRS properties (k_l , m_l) and the GLRS properties are (k_2 , m_l) are varied. The total structure properties, stiffness ($k_l + k_2$) and mass ($m_l + m_2$) are determined using generalized parameters: effective modal mass (M_1^*), effective modal stiffness (K_1^*), and effective modal height (H_1^*) of the fundamental mode of the evaluation structure with a traditional (rigid) anchorage between the LFRS and GLRS (See Apdx A.1).

Two 2DOF IFAS models are examined: (a) an elastic 2DOF system See Fig. 3-1b); and (b) an inelastic 2DOF system (See Fig. 3-1c). The elastic 2DOF system provides insight on optimum IFAS stiffness, either an elastic stiffness, or more appropriately an equivalent elastic stiffness that can be assigned to the nonlinear IFAS device. The 2DOF model was extended to an inelastic system (See Fig. 3-1c) by introducing: a base plastic hinge for capturing nonlinear property of the LFRS, and an elastic-perfectly plastic IFAS.

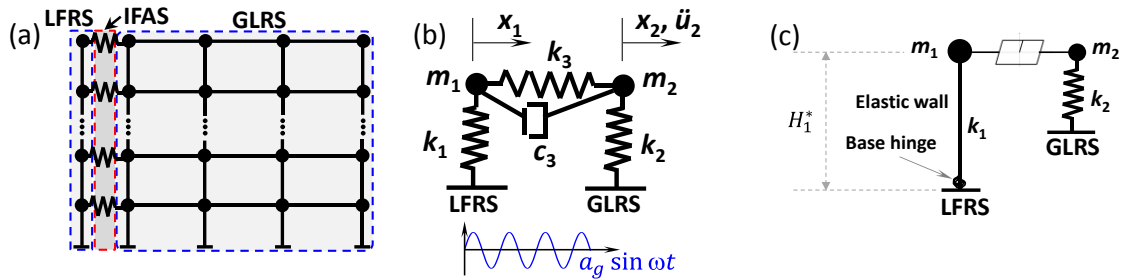


Fig. 3-1. IFAS Models: (a) evaluation structure; (b) elastic 2DOF; (c) inelastic 2DOF.

The primary design parameters evaluated using the elastic 2DOF system are: mass ratio $\mu = m_2/m_1$, IFAS stiffness ratio $\beta = k_3/k_1$, GLRS stiffness ratio $\phi = k_2/k_1$ and IFAS damping ratio $\xi = c_3/c_c$, where c_c is the critical damping of an equivalent traditional (rigidly connected) building system. The elastic 2DOF system is investigated using harmonic motions with maximum amplitude a_g and frequency ω (See Fig. 3-1b). The inelastic 2DOF system is investigated using earthquake motions.

It will be useful to provide insight on typical values of the design parameters:

GLRS Stiffness Ratio ϕ : In typical structures, the lateral stiffness of the GLRS is much lower than that of the LFRS. Thus, typical values of ϕ will be much smaller than unity. As an example, $\phi=0.03$ for the 12-story reinforced concrete evaluation structure [7, 8]. Different GLRS stiffness ratios are studied to determine the influence of GLRS stiffness.

Mass Ratio μ : As opposed to the TMD, where the TMD to structure mass ratio m_2/m_1 is small, the typical values of μ for the IFAS structure are much larger than unity. This outcome occurs because most of the mass in a building is associated with the floor. For a typical IFAS configuration, the IFAS resides between the LFRS and the floor (See Fig. 3-2a). This configuration leads to $\mu=10$ for the 12-story evaluation structure. In the study, alternate IFAS configurations are evaluated where the device acts between portions of the floor, leading to lower values of μ (See Fig. 3-2b). For instance, an IFAS device located in the middle of the floor would result in a value $\mu=1$. The IFAS could also be used between a building and an external stair tower, leading to μ smaller than unity.

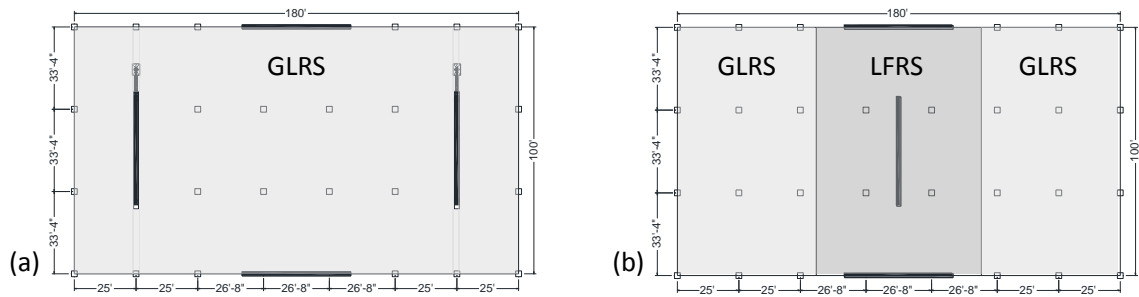


Fig. 3-2. Floor isolation schematic drawing: (a) Full floor; (b) Partial floor.

IFAS Stiffness Ratio β : The IFAS deformable connection is envisioned to be an inelastic device (See Fig. 3-3a), however it could also be a viscoelastic damper (See Fig. 3-3b, c). The inelastic IFAS device can be simplified to be an equivalent (secant) stiffness [105] (See Fig. 3-3a) and an equivalent damping based on the maximum IFAS connector

deformation. Thus, the value of β can either represent the actual (elastic) stiffness or an equivalent stiffness of an inelastic system.

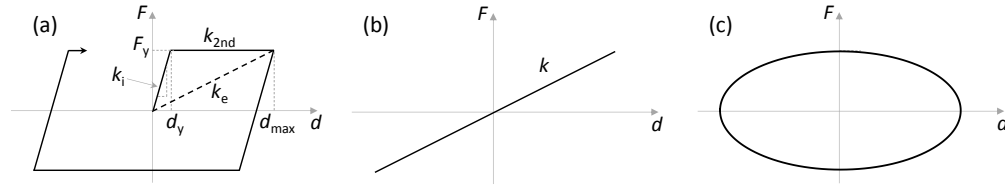


Fig. 3-3. IFAS hysteresis: (a) inelastic IFAS; (b) linear elastic spring; (c) viscous damping.

IFAS Damping Ratio ξ : The IFAS deformable connection will dissipate energy through inelastic hysteretic action (See Fig. 3-3a) or with added (e.g. viscous) dampers (See Fig. 3-3c) for a linear elastic spring. Typical values for supplemental damping from a viscous damper are in the range of $\xi = 5\% - 50\%$ [107].

3.3 Background: TMD Modeling as a 2DOF System

The TMD is a device for reducing structure vibration response, primarily in tall building response to wind. The TMD is created by placing a large mass inside the structure (though much smaller in relation to the overall mass of the structure) and connecting it to the structure using a spring-dashpot system.

The TMD is primarily designed for reducing the fundamental mode of the main structure [112]. Den Hartog [113] proposed a method to optimize the response of an undamped main structure with a damped TMD under harmonic force. This method was accomplished by controlling locations of two “fixed points” in the frequency response curve. Villaverde [89] proposed and proved that adding a small heavily-damped vibration absorber can increase the damping of a structure and thus reduces its responses in earthquakes. Miyama [114] mentioned that small TMD mass (less than 2% of the 1st mode effective mass of the building) is not effective to reduce the structure response in

earthquakes. Tsai and Lin [120] proposed a numerical searching procedure to determine the optimum parameters of the TMD for reducing damped main structures responses under harmonic motions. Sadek et al. [115] improved the method proposed in [89] and formulated new equations for calculating the optimum damping of the TMD for a given mass ratio.

The classical TMD optimization method [113] is briefly reviewed. Fig. 3-4a shows a simple representation of an undamped structure (\hat{k}_1 , \hat{m}_1) with a damped TMD (\hat{k}_2 , \hat{m}_2 , \hat{c}). A harmonic external force ($\hat{P}_0 \sin \hat{\omega} t$) acts on the structure. Fig. 3-4b shows the structure (\hat{x}_1) frequency response at different assigned damping ratios ($\hat{\xi}$) for a given TMD configuration. \hat{x}_{st} is the displacement of \hat{m}_1 under static external excitation, \hat{P}_0 . $\hat{\omega}$ is the frequency of external excitations. $\hat{\omega}_n$ is the natural frequency of the structure.

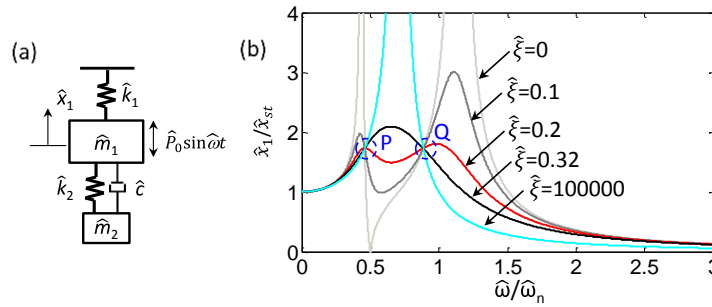


Fig. 3-4. TMD structure: (a) schematic; (b) frequency response.

As seen, the \hat{x}_1 frequency response curves always pass through two “fixed points” (P,Q) for any $\hat{\xi}$ value, implying these locations are independent from damping level. Den Hartog proposed an optimization procedure for minimizing the structure with as two steps [113]: (1) balance the two “fixed points” for a given design by adjusting the TMD frequency; (2) find a proper damping that produces the frequency response curve horizontally passes through one of the “fixed points”. Since all frequency response curves pass the “fixed points”, the damping which produces the curve horizontally passes the

“fixed points” provides the minimum response or a response close to the minimum response. This selected damping is termed optimum damping (ξ_{opt}). The structure response at the ξ_{opt} is named as optimum response. Sometimes there are two different ξ_{opt} for the two “fixed points” respectively, and the average of them is assumed as the finalized ξ_{opt} .

It is noted that there are three primary differences between the TMD structure and the 2DOF IFAS system: (1) In the 2DOF IFAS system, a spring k_2 (representing the GLRS lateral stiffness) connects m_2 to the foundation; (2) In the TMD structure, m_2 is typically much smaller than m_1 , while m_2 is typically larger than m_1 for the 2DOF system; (3) Response minimization of \hat{x}_1 is the primary concern for the TMD structure, while response minimization of x_1, x_2, \ddot{u}_2 are the objectives of the IFAS (x_1, x_2, \ddot{u}_2 were shown in Fig. 3-1b and defined in Section 3.4). Therefore, while the optimized TMD structure may not be directly applied to the 2DOF IFAS system, a similar approach to [113] is explored in the next section to determine the properties of an optimum IFAS design.

3.4 IFAS: Elastic 2DOF System

The 2DOF IFAS elastic response is derived here. The dynamic response of the system (See Fig. 3-1b) is normalized by the static (2DOF) response of a traditional structure, that is with a rigid anchorage between the LFRS and GLRS ($k_3 = \beta = \infty$), termed *rigid 2DOF system*. The static response of this rigid 2DOF system is expressed as:

$$x_{st} = \frac{F}{k} = \frac{(m_1 + m_2)a_g}{k_1 + k_2} = \frac{a_g}{\omega_n^2} \quad (3-1)$$

The circular natural frequency of the rigid 2DOF system is:

$$\omega_n = \sqrt{(k_1 + k_2)/(m_1 + m_2)} \quad (3-2a)$$

with the frequency of the individual LFRS and GLRS being:

$$\omega_L = \sqrt{k_1/m_1} \quad (3-2b)$$

$$\omega_G = \sqrt{k_2/m_2} \quad (3-2c)$$

3.4.1 Dynamic Equation Derivation

The main response parameters for the 2DOF system are (refer to Fig. 3-1b): (1) the LFRS lateral displacement, x_1 ; (2) the GLRS lateral displacement, x_2 ; (3) the relative displacement between the LFRS and the GLRS, x_2-x_1 ; (4) the LFRS absolute acceleration \ddot{u}_1 ; and, (5) the GLRS absolute acceleration \ddot{u}_2 . Dynamic amplification equations for these response parameters are derived based on classical methods [116] and expressed in terms of the dimensionless parameters (μ, β, ϕ, ξ). The derivation is shown in Apdx A.2.1. The resulting response parameter expressions ($x_1, x_2, x_2-x_1, \ddot{u}_1, \ddot{u}_2$), normalized by x_{st} or a_g , are:

$$\frac{|x_1|}{x_{st}} = \frac{1+\phi}{1+\mu} \sqrt{\frac{\left[\mu \frac{1+\phi}{1+\mu} \left(\frac{\omega}{\omega_n} \right)^2 - (\phi + \beta + \mu\beta) \right]^2 + [2\xi(1+\phi)(1+\mu) \left(\frac{\omega}{\omega_n} \right)]^2}{\left[\mu \left(\frac{1+\phi}{1+\mu} \left(\frac{\omega}{\omega_n} \right)^2 \right)^2 - (\phi + \beta + \mu + \mu\beta) \frac{1+\phi}{1+\mu} \left(\frac{\omega}{\omega_n} \right)^2 + (\phi + \beta + \phi\beta) \right]^2 + [2\xi(1+\phi)^2 (1 - \left(\frac{\omega}{\omega_n} \right)^2) \left(\frac{\omega}{\omega_n} \right)]^2}} \quad (3-3)$$

$$\frac{|x_2|}{x_{st}} = \frac{1+\phi}{1+\mu} \sqrt{\frac{\left[\mu \frac{1+\phi}{1+\mu} \left(\frac{\omega}{\omega_n} \right)^2 - (\mu + \beta + \mu\beta) \right]^2 + [2\xi(1+\phi)(1+\mu) \left(\frac{\omega}{\omega_n} \right)]^2}{\left[\mu \left(\frac{1+\phi}{1+\mu} \left(\frac{\omega}{\omega_n} \right)^2 \right)^2 - (\phi + \beta + \mu + \mu\beta) \frac{1+\phi}{1+\mu} \left(\frac{\omega}{\omega_n} \right)^2 + (\phi + \beta + \phi\beta) \right]^2 + [2\xi(1+\phi)^2 (1 - \left(\frac{\omega}{\omega_n} \right)^2) \left(\frac{\omega}{\omega_n} \right)]^2}} \quad (3-4)$$

$$\frac{|x_2-x_1|}{x_{st}} = \frac{1+\phi}{1+\mu} \sqrt{\frac{(\phi - \mu)^2}{\left[\mu \left(\frac{1+\phi}{1+\mu} \left(\frac{\omega}{\omega_n} \right)^2 \right)^2 - (\phi + \beta + \mu + \mu\beta) \frac{1+\phi}{1+\mu} \left(\frac{\omega}{\omega_n} \right)^2 + (\phi + \beta + \phi\beta) \right]^2 + [2\xi(1+\phi)^2 (1 - \left(\frac{\omega}{\omega_n} \right)^2) \left(\frac{\omega}{\omega_n} \right)]^2}} \quad (3-5)$$

$$\frac{|\ddot{u}_1|}{a_g} = \sqrt{\frac{\left[-\mu \frac{1+\phi}{1+\mu} \left(\frac{\omega}{\omega_n} \right)^2 + (\phi + \beta + \phi\beta) \right]^2 + [2\xi(1+\phi)^2 \left(\frac{\omega}{\omega_n} \right)]^2}{\left[\mu \left(\frac{1+\phi}{1+\mu} \left(\frac{\omega}{\omega_n} \right)^2 - (\phi + \beta + \mu + \mu\beta) \frac{1+\phi}{1+\mu} \left(\frac{\omega}{\omega_n} \right)^2 + (\phi + \beta + \phi\beta) \right]^2 + [2\xi(1+\phi)^2 (1 - \left(\frac{\omega}{\omega_n} \right)^2) \left(\frac{\omega}{\omega_n} \right)]^2}} \quad (3-6)$$

$$\frac{|\ddot{u}_2|}{a_g} = \sqrt{\frac{\left[-\phi \frac{1+\phi}{1+\mu} \left(\frac{\omega}{\omega_n} \right)^2 + (\phi + \beta + \phi\beta) \right]^2 + [2\xi(1+\phi)^2 \left(\frac{\omega}{\omega_n} \right)]^2}{\left[\mu \left(\frac{1+\phi}{1+\mu} \left(\frac{\omega}{\omega_n} \right)^2 - (\phi + \beta + \mu + \mu\beta) \frac{1+\phi}{1+\mu} \left(\frac{\omega}{\omega_n} \right)^2 + (\phi + \beta + \phi\beta) \right]^2 + [2\xi(1+\phi)^2 (1 - \left(\frac{\omega}{\omega_n} \right)^2) \left(\frac{\omega}{\omega_n} \right)]^2}} \quad (3-7)$$

The equations are verified by numerical analysis using OpenSees¹ of an example case (See Fig. 3-5). Note that $\xi = c_3/c_c$, where c_c is the critical damping of the rigid 2DOF system, $c_c = 2\omega_n(m_1 + m_2)$.

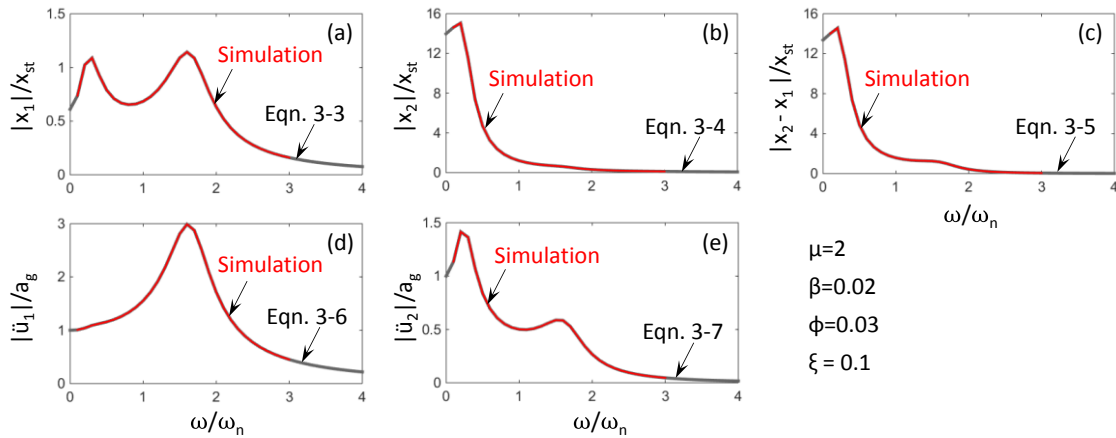


Fig. 3-5. Validation of the equations: (a) x_1 ; (b) x_2 ; (c) $x_2 - x_1$; (d) \ddot{u}_1 ; (e) \ddot{u}_2 .

3.4.2 Modal Analysis

The modal properties of the 2DOF IFAS system are first considered. The 2DOF IFAS system eigenvalues can be obtained by equating the real term of the denominator in

¹ Open System for Earthquake Engineering Simulation, <http://opensees.berkeley.edu/>.

Eqns. 3-3–3-7 to zero. The resulting general expression for the 1st and 2nd natural frequencies (ω_{n1} , ω_{n2}), normalized by ω_n , is:

$$\left(\frac{\omega_{n1,2}}{\omega_n}\right)^2 = \frac{1+\mu}{1+\phi} \frac{(\phi+\beta+\mu+\mu\beta) \mp \sqrt{(\phi+\beta+\mu+\mu\beta)^2 - 4\mu(\phi+\beta+\phi\beta)}}{2\mu} \quad (3-8)$$

Equations 3-9a–c are special cases of Eqn. 3-8 for when $\beta=0$ and $\mu=\phi$:

$$\left(\frac{\omega_{n1,2}}{\omega_n}\right)^2 = \frac{1+\mu}{1+\phi} \frac{(\phi+\mu) \mp \sqrt{(\phi-\mu)^2}}{2\mu} \quad (\beta = 0) \quad (3-9a)$$

$$\left(\frac{\omega_{n1}}{\omega_n}\right)^2 = 1 \quad \left(\frac{\omega_{n2}}{\omega_n}\right)^2 = 1 + \frac{\beta(1+\phi)}{\phi} \quad (\mu = \phi) \quad (3-9b,c)$$

Fig. 3-6a shows the natural frequencies of the 2DOF IFAS system for the typical GLRS stiffness ratio $\phi = 0.03$. Solid and dashed lines represent (ω_{n1} , ω_{n2}), respectively. Black and grey lines represent 2DOF systems with $\beta=0$ and $\beta=0.2$ respectively. The results shows that the 1st mode (solid lines) contribution is from the LFRS when $\mu < \phi$ and from the GLRS when $\mu > \phi$. This “switch point”, $\mu = \phi$ is indicated as a blue circle in Fig. 3-6b inset. When $\beta=0.02$, the switch to the 2nd mode occurs at a larger μ .

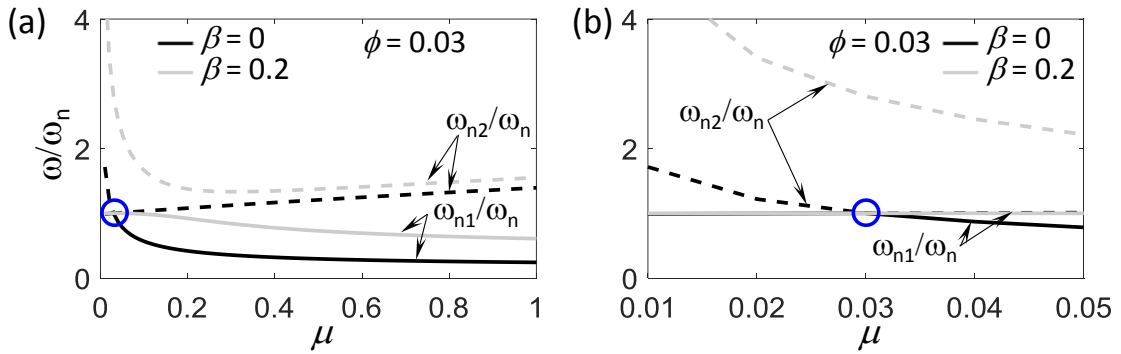


Fig. 3-6. Natural frequencies vs. μ : (a) full plot; (b) close-up at $\mu=\phi$.

Fig. 3-7 shows the 2DOF system modal properties vs. IFAS flexibility at different μ . Fig. 3-7a-c show the effective modal mass ratio, $\hat{S}_j = S_j/m_{\text{total}}$ ($S_j = \sum_{i=1}^2 S_{ji}$) vs η at

different μ , where $\eta = 1/\beta$. s_{ji} represents the effective modal mass from m_i in the j^{th} mode, $s_{ji} = \Gamma_j m_i \phi_{ji}$ [116, 118]. m_{total} represents the total mass of the 2DOF system. Fig. 3-7d-f show the expansion of \hat{S}_j in each mass of each mode, S_{ji}/m_{total} vs η , at different μ .

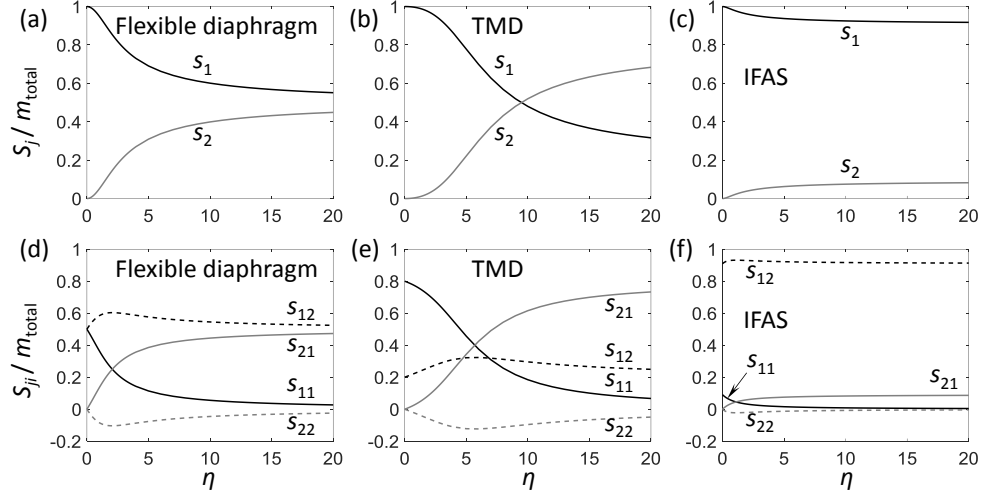


Fig. 3-7. Effective modal mass ratio for: (a) $\mu=1$; (b) $\mu=0.25$; (c) $\mu=10$; Modal expansion of effective modal mass ratio for: (d) $\mu=1$; (e) $\mu=0.25$; (f) $\mu=10$.

Fig. 3-7a-c show that \hat{S}_j decreases from unity in the 1st mode and increases from zero in the 2nd mode. This trend indicates that the 2DOF system is actually one single-degree-of-freedom (SDOF) when the IFAS is rigid ($\alpha=0$). The 2DOF system turns to two isolated SDOF systems when $\alpha=\infty$. \hat{S}_1 and \hat{S}_2 are $\mu/(1+\mu)$ and $1/(1+\mu)$ respectively when $\alpha=\infty$. More details are provided in Appdx. A.3.

3.4.3 Optimization Procedure

The optimization procedure for the elastic 2DOF IFAS system follows a similar approach to that used for the TMD [113]. Fig. 3-8a shows the x_1 frequency response (Eqn. 3-3) for a representative example case: $\mu=0.5$, $\beta=0.02$ and $\phi=0.03$. Results are shown for a range of damping ratios, including undamped ($\zeta=0$) and highly damped ($\zeta = 1000$). The

frequency response is seen to be independent of damping at three “fixed points” (P, Q, M). The derivation of the frequency values at P, Q, M, g_P g_Q g_M , is shown in Appdx. A.2, where the term ω/ω_n is replaced with g for convenience.

Several observations can be made about Fig. 3-8: (1) g_Q and g_M straddle the resonance frequency. (2) the response becomes unbounded at resonance for $\zeta = 1000$; in other words the isolating effects of a low stiffness IFAS ($\beta = 0.02$) is negated by the excessive damping force across the interface. (3) For the undamped system ($\zeta = 0$), response becomes unbounded at values outside of g_Q and g_M . Since due to the curve shape, x_{1P} is always smaller than x_{1Q} (at least when $\beta > 0$), the procedure will focus on controlling and minimizing the response at only two of the fixed points, g_Q and g_M .

The criteria of the optimization is to minimize the maximum response of the frequency response of the 2DOF IFAS system across a broad band of expected frequencies. This optimization procedure includes three steps: (1) “balance” the response at fixed points Q and M (See Fig. 3-8b); (2) minimize the response at these points (See Fig. 3-8c); and (3) find the optimum damping (ζ_{opt}) to minimize response across the broad band of expected frequencies (See Fig. 3-8d), with the response at optimum damping, ζ_{opt} , shown in red.

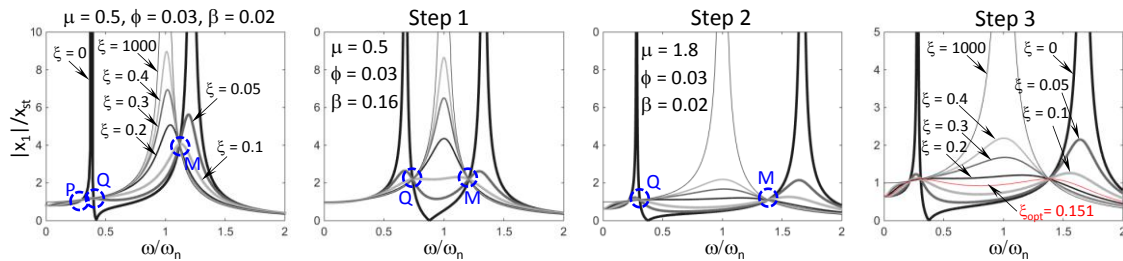


Fig. 3-8. Optimization Procedure: (a) General Response; (b) Balanced Nodes; (c) Minimized Nodes; (d) Optimum Damping.

Balancing the “fixed points” response (Step 1) can be achieved by generating a relationship among μ , β and ϕ , termed a target curve. The target curves are presented in the next section. The derivation of the target curves is provided in Appendix A.2.2.

It is important to note that the target curve optimization approach, which was used successfully to optimize the TMD [113], is not fully effective for the IFAS due to the mass ratio (μ) ranges associated with the IFAS (μ up to 10+). The target curve provides negative β (designs optimized with a negative IFAS stiffness) in certain ranges of μ ($\mu > 2.0$) (See Fig. 3-9 for example). Thus, the design range is divided into two parts for optimization: (1) Region I ($\beta \geq 0$); (2) Region II ($\beta < 0$). Region I follows the optimization procedure described in this section, as will be presented next in Section 3.4.4. Region II requires an alternative method, as will be discussed in Section 3.4.5.

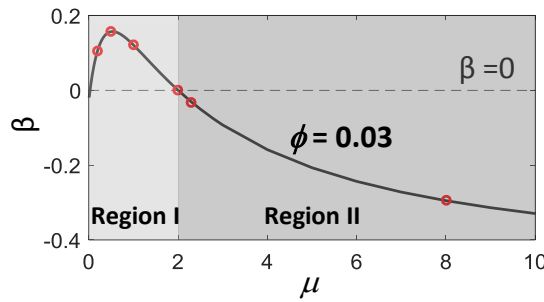


Fig. 3-9. x_1 Target Curve for 2DOF IFAS when $\phi=0.03$.

3.4.4 Region I: Target Curves

A challenge for optimizing the IFAS response is that both the LFRS and GLRS responses (x_1 , x_2 , \ddot{u}_2) need to be minimized. The Region I target curves for the LFRS displacement x_1 (analogous to lateral system drift), the GLRS displacement x_2 (analogous to gravity system drift), and the GLRS acceleration \ddot{u}_2 (analogous to floor accelerations), are given in Eqns. 3-10a,b, c and plotted in Fig. 3-10a, b, c for different ϕ values:

$$\beta = \frac{(\mu-\phi)(2-\mu)}{2(1+\mu)^2} \quad (3-10a)$$

$$\beta = \frac{(\mu-\phi)(1-2\mu)}{2(1+\mu)^2} \quad (3-10b)$$

$$\beta = \frac{(\mu-\phi)(1-\mu-2\phi\mu)}{2(1+\mu)^2(1+\phi)} \quad (3-10c)$$

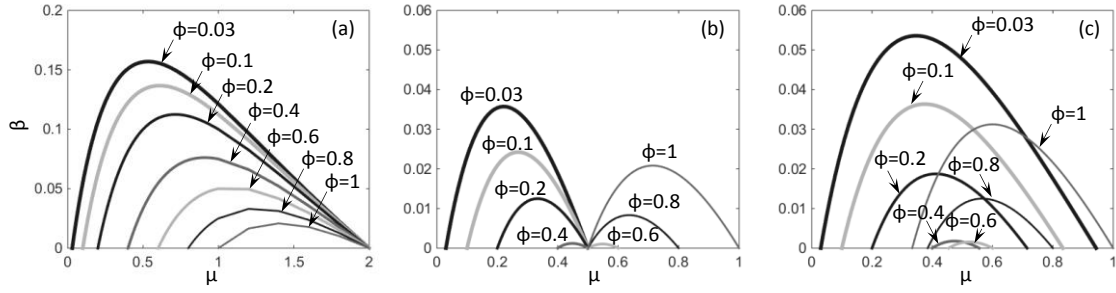


Fig. 3-10. Target Curve: (a) x_1 ; (b) x_2 ; (c) \ddot{u}_2 .

It is seen in Fig. 3-10 that the target curves (and positive β regions for that matter) for x_1 , x_2 and \ddot{u}_2 do not coincide. Regardless, the optimization of x_1 alone is first pursued:

Minimizing x_1 response at the “fixed points” (step 2) was seen to be achieved by increasing μ . An example case for x_1 , using the typical GLRS ($\phi = 0.03$), is shown in Fig. 3-11. Fig. 3-11a shows the target curve for x_1 , with a focus now on Region I. Fig. 3-11b shows the x_1 response curves from the design points on the target curve (colored lines in Fig. 3-11b correspond with colored circles in Fig. 3-11a). The results indicate that, in Region I at least, the optimized x_1 response decreases as μ increases.

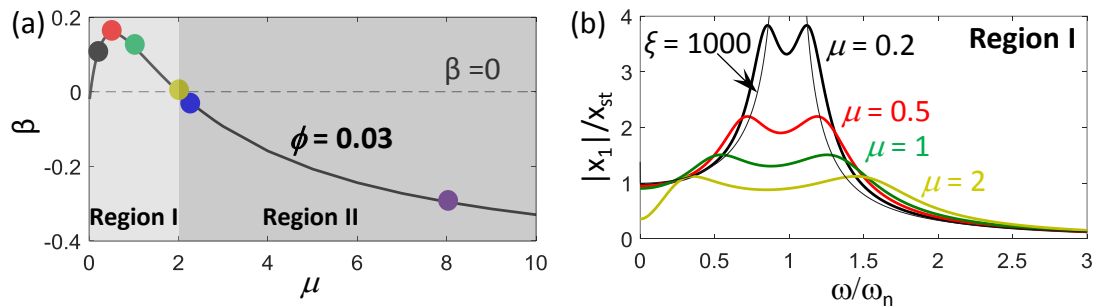


Fig. 3-11. Response: (a) x_1 target curve; (b) optimized x_1 in Region I.

Optimum damping (step 3), ζ_{opt} is obtained through numerical computation. Two numerical methods were considered: damping sweep methods (DSM) and numerical central differential method (NCDM). The DSM and NCDM methods are described in detail in Appendices. A.4 and A.5, respectively.

The methods possess the following advantages and disadvantages: (1) DSM can be used for any shape of the response curve (both convex and non-convex) and can detect the lower and upper bound of the damping values if a flat response valley (See Fig. 3-12 as an example) exists; however this method require intensive computation and the accuracy depends on the ζ interval in the calculation; (2) NCDM is more efficient and accurate, however this method only works for a convex problem and can only detect one damping value if a flat response valley exists.

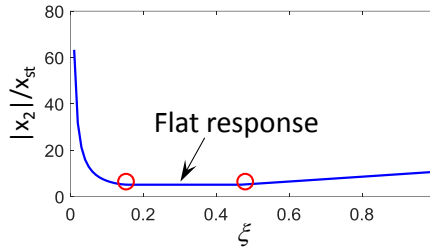


Fig. 3-12. x_2 response vs. ζ when $\phi = 0.07$, $\mu = 1$, $\beta = 0.04$.

The DSM and NCDM methods were found to produce similar ζ_{opt} results for the IFAS (x_1 , x_2 , \ddot{u}_2) responses (See Appdx. A.4, A.5 Fig. A-3, A-4). In addition, x_2 includes flat response for some design parameters (See Fig. 3-12 as an example) and it is very difficult to mathematically prove that Eqns. A-22 – A-26 are convex. Therefore, the DSM characteristics (flat, non-convex) were required. Thus for Region I, the DSM is used to find ζ_{opt} , while the NCDM is used to verify selected results. The use of UA UITS High Performance Computing (HPC) services made this approach possible.

3.4.4.1 Verification of Target Curve Effectiveness in Region I

The effectiveness of the target curve in Region I is verified in this section. A parameter sweep method (PSM) is used for generating 2DOF IFAS responses using different design parameter combinations ϕ, μ, β, ζ , (See Appdx. A.6). The PSM predefines a range of candidate values for each design parameter and then determines the optimum design by computing and comparing the 2DOF system response. Thus, the PSM sweeps ζ to provide the optimized response and associated ζ_{opt} for each (ϕ, μ, β) . The PSM is used to verify the optimum nature of the target curve responses. The following design parameter candidate ranges are used: $0.03 \leq \phi \leq 0.23$, $0.2 \leq \mu \leq 20$, $0.01 \leq \beta \leq 2$, $0.005 \leq \zeta \leq 2$)

The 2DOF IFAS response when minimizing x_1 response (for $\phi = 0.03$) is shown in Fig. 3-13: PSM results are shown in grey scale, minimized for different β ; the target curve response is shown in red. Fig. 3-13a,b,c show (x_1, x_2, \ddot{u}_2) response respectively, plotted vs. μ , *all for optimized x_1 response*. Fig. 3-13a shows that the design parameter combinations satisfying the target curve produce the minimized x_1 response at each μ . Fig. 3-13b, c show that these same design parameter combinations *do not* produce minimized response for x_2 and \ddot{u}_2 . Thus, multi-objective optimization must be considered (See Sec. 3.4.6).

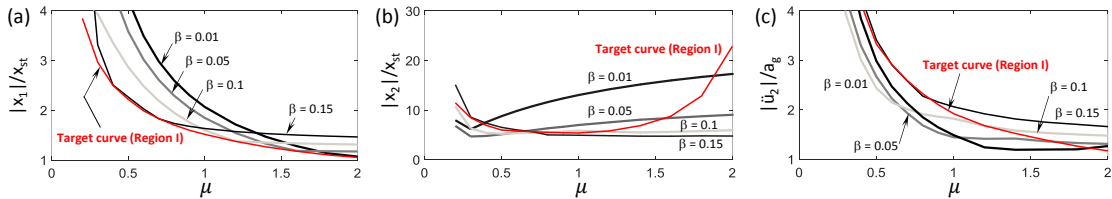


Fig. 3-13. Responses vs. μ for x_1 minimization, Region I: (a) $|x_1|/x_{st}$; (b) $|x_2|/x_{st}$; (c) $|\ddot{u}_2|/a_g$.

3.4.5 Design Optimization in Region II

In Region II ($\mu > 2$ for x_1 minimization, for example), the target curve produces negative β values (implying a negative IFAS stiffness), which cannot be easily achieved.

(Interestingly, the Region II target curve is also shown to produce non-optimum solutions, unlike Region I, as described in Appdx. A.7). Thus, the target curve design optimization procedure was abandoned in Region II in favor of direct use of the PSM.

Different from the PSM in Sec. 3.4.4.1, the PSM sweeps (μ, β, ζ) to determine the optimized response and related optimized design combination at each ϕ (See full details in Appdx. A.6).

The 2DOF IFAS response (x_1, x_2, \ddot{u}_2) when minimizing x_1 is shown in Fig. 3-14. The response, for the typical GLRS case ($\phi = 0.03$), is plotted vs. μ and extends into Region II. The PSM response is plotted in grey scale for minimized response at different β . The response satisfying the target curve is plotted in red for Region I and pink for Region II. The LFRS response x_1 (Fig. 3-14a) produces the following observations: (1) while the target curve does generate optimized x_1 in Region I as established previously, it does not produce optimum response in Region II (e.g. the hump observed near $\mu = 2.4$); (2) while x_1 decreases significantly as μ increases in Region I as previously established, only minor reduction is seen in Region II; (3) in Region II, the minimum x_1 (as determined through PSM) decreases as β decreases; (5) in Region I, when $\mu < 1$, the minimum x_1 increases as β decreases. The corresponding x_2 and \ddot{u}_2 response are shown in Fig. 3-14b, c.

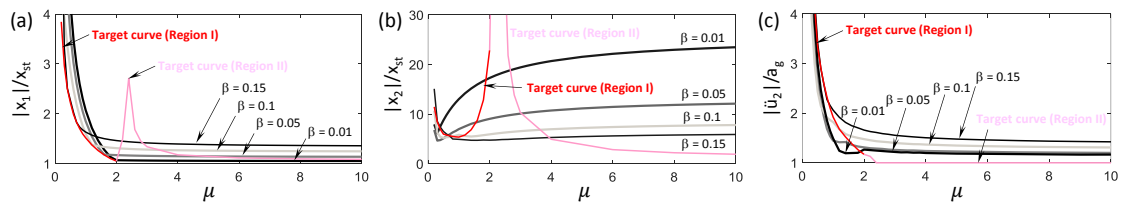


Fig. 3-14. Responses versus μ when optimizing x_1 : (a) $|x_1|/x_{st}$; (b) $|x_2|/x_{st}$; (c) $|\ddot{u}_2|/a_g$.

In totality, Fig. 3-14 shows that: (1) the optimum x_1 doesn't generate optimized response of x_2 and \ddot{u}_2 as established previously (See Fig. 3-13b, c); (2) x_1 and \ddot{u}_2 are decreased as β decreases while x_2 is increased as β decreases. Therefore, multi-objective optimization is needed and will be explained in Sec. 3.4.6.

Before discussing about the multi-objective optimization, definition of the minimized response is explained next.

x_1^* , x_2^* , \ddot{u}_2^* are used to represent the minimized response of x_1 , x_2 , \ddot{u}_2 across the candidate set at each ϕ . In order to explain this more clearly, minimization on x_1 is taken as an example and shown in contour plots in Fig. 3-15. Note that the upper limit of the contour is 10; all responses larger than 10 are in dark red. The PSM first generates optimized x_1 at each (ϕ, μ, β) and is plotted in Fig. 3-15a. The corresponding ξ_{opt} , $|x_2|/x_{\text{st}}$, $|\ddot{u}_2|/a_g$ are plotted in Fig. 3-15b,c,d. x_1^* is the minimum response of all the optimized x_1 in Fig. 3-15a. Thus, one x_1^* exists for one ϕ . x_2^* and \ddot{u}_2^* are determined using the same procedure while minimizing x_2 and \ddot{u}_2 . Further details about Fig. 3-15 is shown in Appdx. A.8.

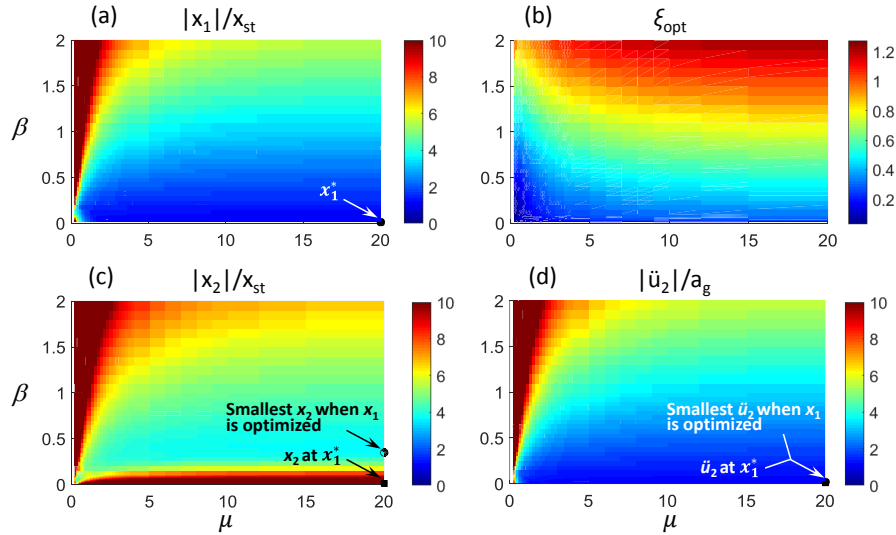


Fig. 3-15. Response contour plots of the elastic 2DOF system when optimizing x_1 ($\phi = 0.03$): (a) $|x_1|/x_{\text{st}}$; (b) ξ_{opt} ; (c) $|x_2|/x_{\text{st}}$; (d) $|\ddot{u}_2|/a_g$.

3.4.6 Multi-Objective Optimization

Multi-objective optimization is common in real world design problems. This method is widely used when several objective functions require simultaneous optimization. One widely accepted method for multi-objective optimization is the Pareto Frontier Method. In this method, every objective function is assigned a weight factor, λ_i , permitting the multi-objective optimization to be transformed into a single-objective optimization:

$$f = \lambda_1 \frac{x_1}{x_{st}} + \lambda_2 \frac{x_2}{x_{st}} + \lambda_3 \frac{\ddot{u}_2}{a_g} \quad (3-11)$$

where $\lambda_1 + \lambda_2 + \lambda_3 = 1$. The relative importance of each objective function is taken into account in Eqn. 3-11 by assigning different weighting factors. If all the possible weighting factor combinations are investigated, large computational effort is needed for obtaining the Pareto Frontier. Thus, providing no preference to any of the three response parameters creates a more efficient solution.

Since it is difficult to estimate the magnitude of how greatly x_1 , x_2 , \ddot{u}_2 deviate from optimum values, x_1^* , x_2^* , \ddot{u}_2^* , the concept of relative error is introduced, as described next.

Relative error is introduced for the purpose of quantifying the difference between each *response* parameter (x_1 , x_2 , \ddot{u}_2) with its minimized response (x_1^* , x_2^* , \ddot{u}_2^*) across all the *design* (ϕ , μ , β , ξ) parameters. The relative error for x_1 , x_2 , \ddot{u}_2 is defined as:

$$\epsilon_{x1} = \frac{(x_1 - x_1^*)}{x_1^*} \quad (3-12a)$$

$$\epsilon_{x2} = \frac{(x_2 - x_2^*)}{x_2^*} \quad (3-12b)$$

$$\epsilon_{\ddot{u}2} = \frac{(\ddot{u}_2 - \ddot{u}_2^*)}{\ddot{u}_2^*} \quad (3-12c)$$

Single objective optimization results on x_1 , x_2 , \ddot{u}_2 of the elastic 2DOF system at different ϕ are shown in Appdx. A.9 for the purpose of investigating the influence from ϕ . ε_{x1} , $\varepsilon_{\ddot{u}2}$ and ε_{x2} at the optimized design are also plotted to show the deviation from x_1^* , x_2^* , \ddot{u}_2^* .

A method of minimizing the total relative error (ε_{tot}) of the three responses [119] is used here, creating an objective function:

$$\varepsilon_{tot} = \frac{(x_1 - x_1^*)}{x_1^*} + \frac{(x_2 - x_2^*)}{x_2^*} + \frac{(\ddot{u}_2 - \ddot{u}_2^*)}{\ddot{u}_2^*} \quad (3-13)$$

Eqn. 3-13 is a single-objective optimization problem. In addition, Eqn. 3-13 can be rewritten in the following format:

$$\varepsilon_{tot} = \frac{x_1}{x_1^*} + \frac{x_2}{x_2^*} + \frac{\ddot{u}_2}{\ddot{u}_2^*} - 3 \quad (3-14)$$

This approach means Eqn. 3-14 (or Eqn. 3-13) will yield one point at the Pareto Frontier, and the weighting factors for $\frac{x_1}{x_{st}}$, $\frac{x_2}{x_{st}}$, $\frac{\ddot{u}_2}{a_g}$ are $\frac{1}{x_1^*/x_{st}}$, $\frac{1}{x_2^*/x_{st}}$, $\frac{1}{\ddot{u}_2^*/a_g}$, respectively.

The PSM (See Appdx. A.6) is used to find out the optimized response of ε_{tot} in both Regions I and II. Fig. 3-16 shows the 2DOF system response and corresponding design parameters when ε_{tot} is minimized for each ϕ .

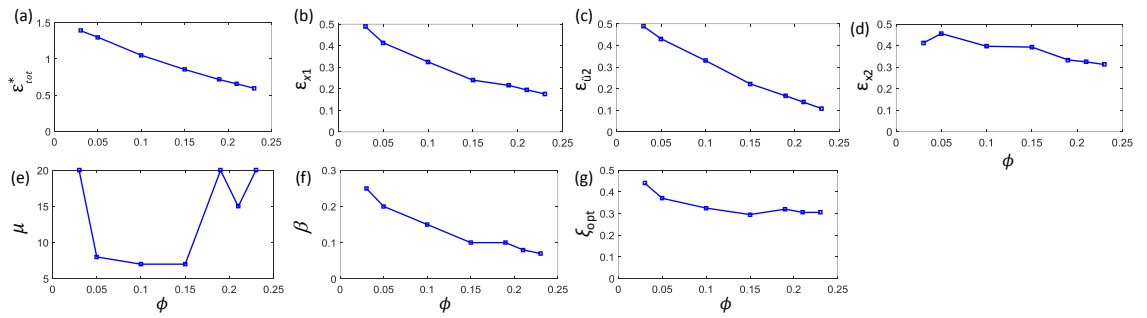


Fig. 3-16. Response of the elastic 2DOF system and related design parameters when minimizing ε_{tot} : (a) ε_{tot}^* ; (b) ε_{x1} ; (c) $\varepsilon_{\ddot{u}2}$; (d) ε_{x2} ; (e) μ ; (f) β ; (g) ζ_{opt} .

The minimized ε_{tot} (ε_{tot}^*) is about 140% when $\phi = 0.03$ and decreases as ϕ increases (See Fig. 3-16a). It can be seen that ε_{x1} , $\varepsilon_{\ddot{u}2}$ and ε_{x2} are all smaller than 50% (See Fig. 3-16b,c,d). The related design parameters are shown in Fig. 3-16e,f,g. Introduction and discussions on global relative error is explained in Appdx. A.10.

A looser requirement on ε_{tot} is used for the purpose of creating a broader design space of the 2DOF system so that a larger number of candidates of design parameters can be used. The minimized ε_{tot} is 140% when $\phi = 0.03$ (see Fig. 3-16a). 150% is assumed as the upper limit of ε_{tot} . Eqn. 3-14 turns to be:

$$\varepsilon_{tot} = \frac{x_1}{x_1^*} + \frac{x_2}{x_2^*} + \frac{\ddot{u}_2}{\ddot{u}_2^*} - 3 < 150\% \quad (3-15)$$

The design space and related relative errors at ξ_{opt} is shown in Fig. 3-17.

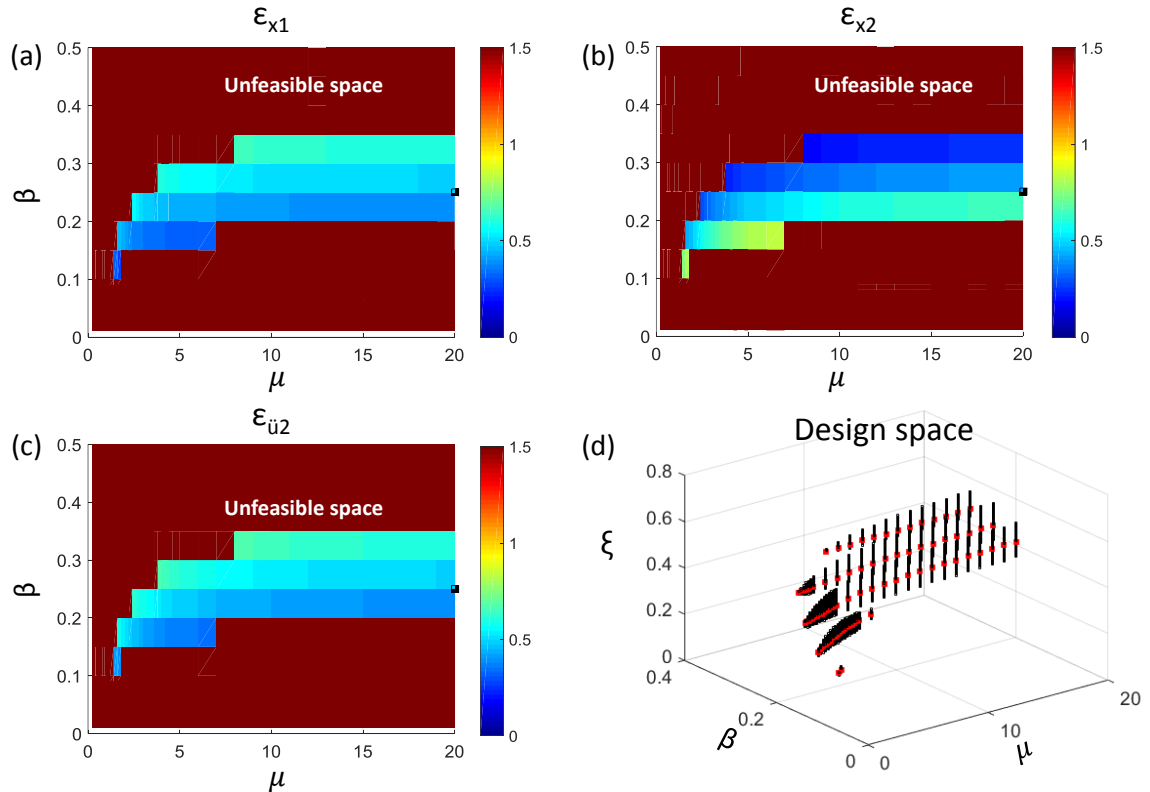


Fig. 3-17. Contour plot of minimized x_1 , x_2 , \ddot{u}_2 relative error response at each (μ, β) when $\varepsilon_{tot} < 150\%$ ($\phi = 0.03$): (a) ε_{x1} ; (b) ε_{x2} ; (c) $\varepsilon_{\ddot{u}2}$; (d) design space.

Fig. 3-17d shows the (μ, β, ζ) satisfying Eqn. 3-15. The red dot in Fig. 3-17d represent ζ_{opt} at a given (μ, β) . Fig. 3-17a, b, c show relative errors of x_1, x_2, \ddot{u}_2 at ζ_{opt} in Fig. 3-17d. Fig. 3-17d implies that a broad design parameter combinations can be used for obtaining an acceptable 2DOF system response. The design space of the 2DOF system with other ϕ are shown in Fig. A-12 – A-18 (See Appdx. A.11). The design space is enlarged as ϕ increases.

3.4.7 Responses in Earthquakes

The effectiveness of the optimization procedure is validated via earthquake simulation in this section. This validation is performed by comparing the responses of two sets of elastic 2DOF system: (1) using a rigid connection between the m_1 and m_2 to represent a 2DOF system with traditional floor anchorage (2DOF_Tra); (2) using an IFAS connection with the optimized design parameters from Fig. 3-16e,f,g (2DOF_Opt). There is no energy dissipation devices in the 2DOF_Tra (See Fig. 3-1b). Therefore, a viscous damping (c_1) is added to the LFRS of the Elastic 2DOF system for making a fair comparison between the 2DOF_Tra and 2DOF_Opt (See Fig. 3-18). The damping ratio of the LFRS is ζ_1 . Note that $\zeta_1 = c_1/c_{c1}$, where c_{c1} is the critical damping of the LFRS, $c_{c1} = 2\omega_1 m_1$. $\zeta_1 = 2\%$ is assumed for this section.

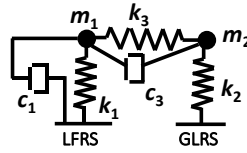


Fig. 3-18. Elastic 2DOF system with added viscous damping to the LFRS.

A suite of ten spectrum-compatible earthquakes from FEMA P695 [121] are selected for the study (See Table 4-8 for more information). The same earthquakes are used

for the nonlinear time history analysis (NTHA) of the 2D numerical model of the evaluation structure in Chapter 4. The earthquakes are scaled using the factors shown in Table 4-8 to match the 5% damped design spectrum for the generic SDC D site at the DBE level (See Fig. 3-19). The 1st period of the elastic 2DOF_Tra ($\phi=0.03$, $\mu=20$, $\beta=1000$, $\zeta=0$, $\zeta_1=0.02$) is shown with a thick solid black vertical line in Fig. 3-19. The simulations are performed at the DBE level.

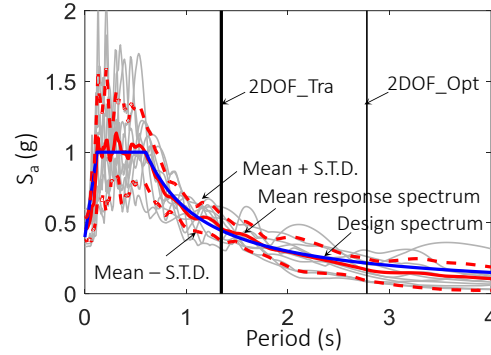


Fig. 3-19. Ground motions response spectrum with 5% damping and design spectrum.

The optimum design for the elastic 2DOF system when $\phi=0.03$ is: $\mu=20$, $\beta=0.25$, $\zeta=0.44$. The 1st period of the 2DOF_Opt is shown in Fig. 3-19 with thin solid black vertical line. The comparisons of the time history response of the 2DOF_Tra and 2DOF_Opt in EQ1 are shown as an example in Fig. 3-20.

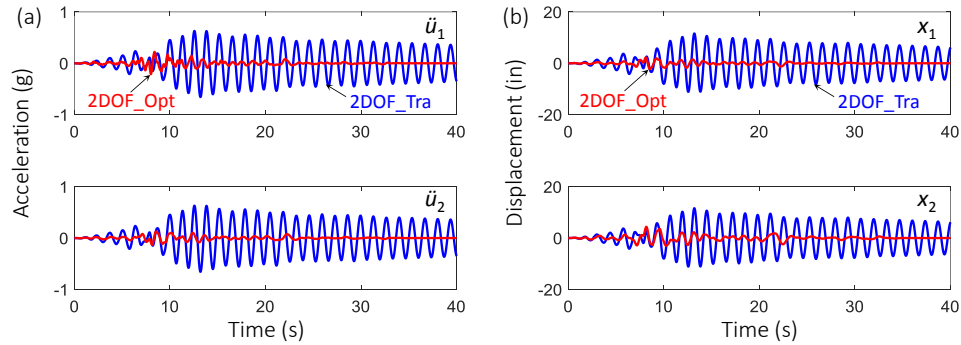


Fig. 3-20. Time history responses of the 2DOF system: (a) acceleration; (b) displacement.

The blue and red represent the responses of the 2DOF_Tra and 2DOF_Opt respectively. The figure shows that the response of the 2DOF_Opt is significantly reduced in comparison to that of the 2DOF_Tra . Therefore, the effectiveness of the optimization method is proved. A sensitivity study on the influence from variations of the design parameters is shown in Appdx. A.12.

3.4.8 Conclusions for Elastic 2DOF System

The following conclusions can be drawn out from Section 3.4:

(1) Target curve provides a relationship among (ϕ, μ, β) that can produce an optimized single-objective response when $\beta > 0$. However, the applicable design parameters range of the target curve is limited.

(2) Significant reduction in x_1, x_2, \ddot{u}_2 can be achieved as μ increases when $\mu < 2$. This reduction becomes negligible when $\mu > 2$.

(3) Small and large β produces large x_2 . x_2 is minimized in a certain range of β .

(4) The ε_{tot} is a reasonable index for performing the multi-objective optimization in the situation that no preference is applied to the objective functions.

(5) The influence from μ to the 2DOF system design optimization is not significant in comparison to the influence from β when μ is large.

(6) A broad design space is applicable for obtaining an acceptable 2DOF system response. The design space goes across from a small μ to a large μ continuously, with limitations on β and ζ . This implies that if in some situation, the mass assigned to the GLRS of the structure is determined already, there will be always a set of IFAS stiffness and damping combinations for obtaining acceptable response reduction of the 2DOF system.

(7) The 2DOF_Opt is effective for reducing the 2DOF system response in earthquakes in comparison to the 2DOF_Tra.

(8) In earthquakes, the influence to the responses from μ is negligible when μ is large, and the influence becomes significant when μ is decreased to a small value. Therefore, a full floor isolation (See Fig. 3-2a) can be used for the design since this configuration provides the largest μ in the structure.

(9) In earthquakes, the influence from β is not that significant.

(10) In earthquakes, the influence from ζ is significant if ζ is too small. However, if ζ is inside the design space shown in Fig. 3-17, the influence from ζ is negligible.

(11) The optimization method provides a design of the IFAS that significantly decreases the 2DOF system responses in comparison to a 2DOF using a rigid IFAS.

The elastic 2DOF system provides useful insight into the behavior of the IFAS. However, there are some limitations of using it for the development of the 2DOF system design space. Foremost among these is the inability to accurately determine the hysteretic energy dissipation. Another issue is related to the x_2 for highly flexible IFAS under low frequency excitation. For any appreciable m_2 , the *static* displacement of x_2 becomes too large if the IFAS doesn't provide sufficient stiffness, for instance, the design case in Fig. 3-5b where $\mu=2$, $\beta=0.02$, $\phi=0.03$. However this large static x_2 is not realistic since there is no large static lateral force acting on a multi-story structure in the real world. Therefore, an inelastic 2DOF system is introduced next.

3.5 Inelastic 2DOF System

An inelastic 2DOF system (See Fig. 3-1c) is used for the development of a design space due to the limitations of the elastic 2DOF system. The inelastic 2DOF system is

shown in Fig. 3-21 for easy reference. The LFRS is modeled with an elastic column element using a plastic hinge at the LFRS base. The elastic column of the LFRS is built using the effective modal height in the 1st mode (H_1^*) with the same cross-section property of the LFRS in the evaluation structure. The LFRS stiffness is denoted as k_{LFRS} . The LFRS base plastic hinge is modeled with a nonlinear spring, using elastic perfectly plastic material. The initial stiffness of the plastic hinge is assigned with a large value for obtaining a correct elastic LFRS response. The GLRS is modeled with an elastic spring. The IFAS is modeled with a nonlinear spring, using bilinear force-deformation property.

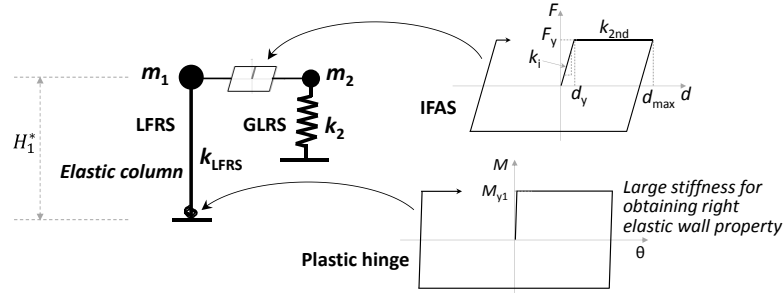


Fig. 3-21. Schematic drawing of an inelastic 2DOF system with force-deformation relationship of the IFAS and wall base plastic hinge.

The LFRS base moment (M_{b1}) and the total mass of the 2DOF system (M_1^*) is calculated from the 1st mode of the evaluation structure (See Appdx. A.1). In a practical design, the yield moment at the LFRS base is not equal to (mostly larger than) the design moment from the ELF procedure. Therefore, the amount of the LFRS base moment in the 1st mode is represented by a ratio (ρ_{Mb1}) of the total LFRS base moment in Eqn. 3-16a. ρ_{Mb1} is assumed to be the same as the ratio between the yield moment in the 1st mode (M_{y1}) and the total yield moment at the LFRS base (M_y) of the evaluation structure. M_{y1} will be applied to the LFRS base plastic hinge in the 2DOF system (See Eqn. 3-16b).

$$\rho_{Mb1} = M_{b1} / \sum_{i=1}^N M_{bi} \quad (3-16a)$$

$$M_{y1} = \rho_{Mb1} M_y \quad (3-16b)$$

Therefore the properties of the LFRS (stiffness, yield moment) and total mass of the 2DOF system are determined once the evaluation structure is designed out. The design parameters that may varies are: (1) mass ratio between the GLRS and LFRS, μ ; (2) IFAS strength, F_y (See Fig. 3-3a); (3) IFAS initial stiffness, k_i (See Fig. 3-3a); (4) IFAS secondary stiffness, k_{2nd} (See Fig. 3-3a).

In order to create relationships between the LFRS and IFAS, F_y , k_i and k_{2nd} are normalized by the M_{y1} , k_{LFRS} and k_i respectively, using the following equations:

$$\alpha' = F_y H_1^* / M_{y1} \quad (3-17a)$$

$$k' = k_i / k_{LFRS} \quad (3-17b)$$

$$\gamma = k_{2nd} / k_i \quad (3-17c)$$

where α' , k' , γ are termed as normalized IFAS strength ratio, IFAS initial stiffness ratio, IFAS strain hardening ratio.

A parametric study with varying the design parameters will be conducted for the purpose of finding an optimum design space of the inelastic 2DOF system.

If harmonic analyses are used for the parametric study, the IFAS will yield at static load ($\omega/\omega_n = 0$) when F_y satisfies the following equation:

$$F_y < m_2 a_g \quad (3-18)$$

Eqn. 3-18 seems provide a lower limit of F_y , but this is not reasonable because the energy of earthquakes is not concentrate on the long period region. Another type of lateral load, wind load, is assumed to be statically applied on the structure, but the magnitude of the wind load is much smaller than that from earthquakes for multi-story buildings.

Therefore, NTHAs using spectrum-compatible earthquakes (See Table 4-8), rather than harmonic motions, are used to conduct the parametric study for the inelastic 2DOF system.

3.5.1 Parametric Study Description

The Parametric study for obtaining the optimized design of the inelastic 2DOF system is introduced in this section. The four parameters used for the parametric study are: μ , α' , k' , and γ . Each parameter is assigned with a predefined range: $0.5 \leq \mu \leq 20$; $0.1 \leq \alpha' \leq 3$; $0.1 \leq k' \leq 500$; $0\% \leq \gamma \leq 5\%$. Only $\phi = 0.03$ is studied in this section. In addition, large k' can produce large k_i , thus, a large k_{2nd} will be generated if γ is constant. Then the IFAS connection will have large stiffness and behaves like a rigid IFAS connection, which is not realistic. Therefore, k_{2nd} at $k' = 10$ will be assigned to the IFAS with $k' > 10$ for the purpose of creating an IFAS with reasonable secondary stiffness.

A method, named PSM_Inelastic, is used to find out the IFAS design space. The steps of PSM_Inelastic are similar to the PSM. The details of the PSM_Inelastic is described in Appdx. A.13.

There are three main differences between the PSM and PSM_Inelastic: (1) harmonic analyses are used for calculating the elastic 2DOF system responses in PSM, while performing NTHAs is used in PSM_Inelastic; (2) the design parameters used in the PSM and PSM_Inelastic are different; (3) the response of the 2DOF system from the harmonic analyses is closed form solutions, while mean value of the maximum responses of the 10 NTHAs is used to present the response of the inelastic 2DOF system.

3.5.2 Parametric Study Results

The parametric study results are shown in this section. NTHA results of a 2DOF system using the IFAS (2DOF_IFAS) and a 2DOF system using traditional connection

(2DOF_Tra) between the m_1 and m_2 are first shown in Fig. 3-22. The design parameters of the 2DOF_IFAS is written in the figure caption. The mass is 27.46 kip-s²/in for both 2DOF systems. The wall height is 1187.3 in for both 2DOF systems. Cracked wall moment of inertial (35% of gross moment of inertia) is used for the LFRS of both 2DOF systems.

Fig. 3-22b shows significant reduction of x_1 in the 2DOF_IFAS in comparison to that of 2DOF_Tra. Fig. 3-22b also shows amplification in x_2 in the 2DOF_IFAS. Fig. 3-22a shows a slight reduction in \ddot{u}_2 in the 2DOF_IFAS, but not significant. This is probably because the 2DOF_Tra behaves as a single-degree-of-freedom system. Therefore no higher mode effects will be included in the 2DOF_Tra and the higher mode effect is considered as one main reason of large floor acceleration in multi-story buildings [103]. Significant reduction of the floor acceleration will be observed in the responses of multi-story evaluation structures in Chapter 4. Fig. 3-22a shows that \ddot{u}_1 is amplified significantly in the 2DOF_IFAS in comparison to that of 2DOF_Tra. Since this response is not under investigation, this response will not be presented afterwards. A comparison on NTHA of traditional elastic and inelastic 2DOF systems are shown in Appdx. A.14 for further reasons for the differences between Fig. 3-20 and Fig. 3-22a.

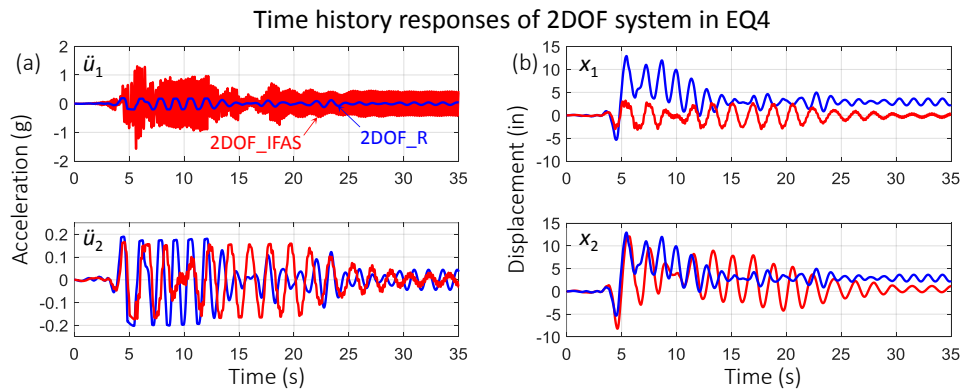


Fig. 3-22. Time history responses of an inelastic 2DOF system ($\phi = 0.03$, $\mu = 20$, $\alpha' = 0.8$, $k' = 1$, $\gamma = 0\%$, EQ4): (a) acceleration; (b) displacement.

The inelastic 2DOF system responses when minimizing x_1 and x_2 are shown in Fig. 3-23. Fig. 3-23a shows the minimized x_1 . Fig. 3-23b,c show the corresponding x_2 and \ddot{u}_2 . Note that the minimized x_2 is shown in grey in Fig. 3-23b as a reference.

Fig. 3-23a shows two phenomenons: (1) a significant reduction of x_1 is produced when $\alpha < 1$; (2) the reduction of x_1 is increased as μ increases. Fig. 3-23b shows that when x_1 is minimized, the corresponding x_2 is larger than that of minimized x_2 . A significant difference can be observed when $\alpha > 1$. The difference is decreased when $\alpha < 1$. The changes in μ has small effects on x_2 when $\mu > 2$. x_2 is reduced as α decreases ($0.5 < \alpha < 0.8$) and reversed to increase when $\alpha < 0.5$. Fig. 3-23c shows that \ddot{u}_2 undergoes significant reduction as α decreases when $\alpha < 1$. \ddot{u}_2 is decreased significantly as μ increases when $\mu < 5$ and the variation is negligible when $\mu > 5$.

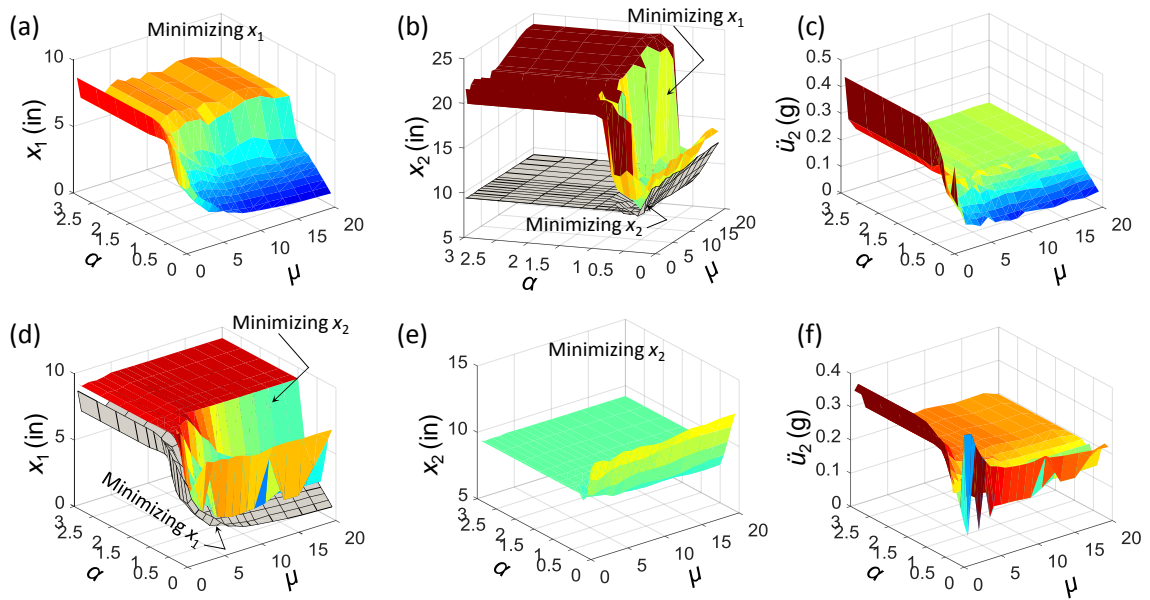


Fig. 3-23. Inelastic 2DOF system ($\phi = 0.03$) responses: minimizing x_1 : (a) x_1 ; (b) x_2 ; (c) \ddot{u}_2 ; minimizing x_2 : (d) x_1 ; (e) x_2 ; (f) \ddot{u}_2 .

Fig. 3-23e shows the minimized x_2 . Fig. 3-23d,f show the corresponding x_1 and \ddot{u}_2 . Note that the minimized x_1 is shown in grey in Fig. 3-23d as a reference. Fig. 3-23d shows that x_1 is decreased as α decreases when $\alpha < 1$. x_1 is reversed to increase when $\alpha < 0.4$ and deviates more from the minimized x_1 (in grey) as α decreases. Fig. 3-23d shows that x_2 has negligible variation as α decreases when $\alpha > 1$. x_2 is decreased first and then increased significantly as α decreases when $\alpha < 1$. Fig. 3-23f shows that \ddot{u}_2 is increased significantly as μ decreases when $\mu < 5$.

Fig. 3-23 shows that the responses of the inelastic 2DOF system are not changing in the same trend when minimizing x_1 and x_2 respectively. Thus, a multi-objective optimization is needed. More details about this section can be seen in Appdx. A.15.

3.5.3 Multi-Objective Optimization

Multi-objective optimization is applied to find a design space of the inelastic 2DOF system. A looser requirement on ε_{tot} is used for the purpose of creating a broader design space of the 2DOF system so that a larger set of candidates for the design parameters can be used. The minimized ε_{tot} is 73.5% when $\phi = 0.03$, 300% is used as the upper limit of the ε_{tot} . Eqn. 3-15 turns to be:

$$\varepsilon_{tot} = \frac{x_1}{x_1^*} + \frac{x_2}{x_2^*} + \frac{\ddot{u}_2}{\ddot{u}_2^*} - 3 < 300\% \quad (3-19)$$

Fig. 3-24d shows the (μ, α, k') that satisfies Eqn. 3-20. The red dot represents the design parameter combination that produces the minimized response at a given (μ, α) . Fig. 3-24a, b, c show the relative errors of x_1 , x_2 , \ddot{u}_2 at the red dots in Fig. 3-24d. Fig. 3-24a,b,c show that the design space is limited inside a range where $\alpha < 0.6$ and $\mu > 5$. Fig. 3-24d shows that a broad design parameter combinations can be used for obtaining an acceptable

inelastic 2DOF system response. The design space is more sensitive to μ and α rather than k' from Fig. 3-24d. Smaller k' can produce smaller 2DOF system response.

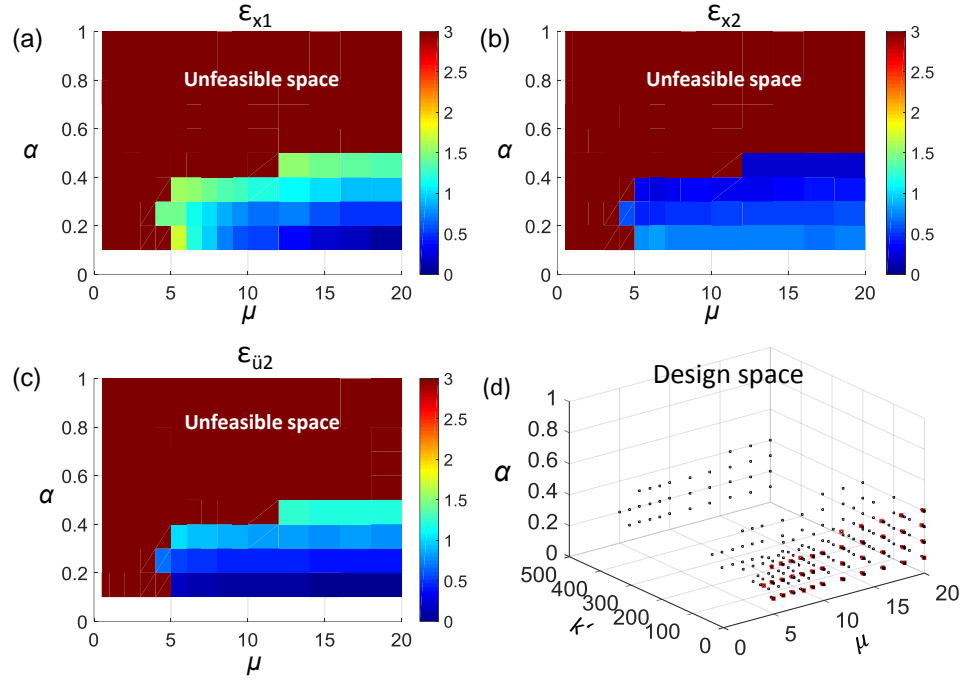


Fig. 3-24. Contour plot of minimized x_1 , x_2 , \ddot{u}_2 relative error response at each (μ, α) when $\epsilon_{tot} < 300\%$ ($\phi = 0.03$): (a) ϵ_{x1} ; (b) ϵ_{x2} ; (c) $\epsilon_{\ddot{u}2}$; (d) design space.

3.6 Conclusions for 2DOF System

2DOF systems of the evaluation IFAS structure is studied in this Chapter. The modal property of an elastic 2DOF system is first studied and harmonic analyses are used to obtain the closed form solutions of the responses of the elastic 2DOF system. Then target curve and parameter sweep method are used to obtain the design space of the elastic 2DOF system. A set of nonlinear 2DOF systems are studied using NTHAs afterwards. The following conclusions can be drawn in this chapter:

- (1) The target curve can be used to perform the design optimization of the elastic 2DOF system. However, the target curve is only applicable when β is positive.

(2) The parameter sweep method can be used to perform the design optimization of the elastic and inelastic 2DOF systems. This methodology needs large computing time, but can generate a global optimization solution.

(3) The IFAS stiffness is linear in the elastic 2DOF system, then closed form expressions can be derived out for the responses of the elastic 2DOF system in steady state using harmonic motions. This is more time efficient than performing NTHAs.

(4) The x_1 , x_2 , \ddot{u}_2 have conflicting trends when the design parameters are changed. Therefore, a multi-objective optimization is needed for performing the design optimization. Relative error can be used to find the optimized design when no preference information is considered for multiple objective functions.

(5) A combination of large mass ratio and small IFAS stiffness can produce preferable 2DOF system responses.

(6) Higher mode effect is not reflected in the inelastic 2DOF system. Therefore, no significant reduction of the floor acceleration from a 2DOF_R to a 2DOF_IFAS is observed. However, a significant reduction of the floor acceleration is observed in the elastic 2DOF system. The yield of the LFRS cause a large difference in the 2DOF system responses.

4. IFAS: 2D EVALUATION STRUCTURE MODELS

The IFAS design space is examined through analytical parameter studies of an evaluation structure under simulated earthquakes. The models use idealized IFAS Prototypes for two design approaches: (1) conservative; and (2) aggressive designs. Nonlinear time history analysis (NTHA) are used for the earthquake simulations in the study.

4.1 Evaluation Structure

The evaluation structure is a reinforced concrete (RC) flat plate residential building. The structure permits the rapid evaluation of many design parameters. Three different building heights are investigated: 4, 8 and 12 stories. Fig. 4-1a shows a typical plan of the evaluation structure. The structure has a footprint of $180' \times 100'$ with typical column spacing of $33'-4''$ in the transverse direction and approximately $26'$ in the longitudinal direction. The Lateral Force Resisting System (LFRS) is interior RC shear walls in the transverse direction and perimeter RC shear walls in the longitudinal direction. The floor slab thickness is $8''$ (normal weight concrete reinforced with #6 bars @ $5''$). Typical floor tributary mass is 135psf. The floor-to-floor height is $16'$ at the 1st story and $10.5'$ for upper stories. The IFAS is based on the Prototype FD + RB and BRB + RB configurations (Refer to Sec. 1.3). Thus, the IFAS is composed of a deformable connection: Friction Damper (FD) or Buckling Restrained Brace (BRB), in conjunction with Rubber Bearings (RB), is shown schematically in the Fig. 4-1 plan view.

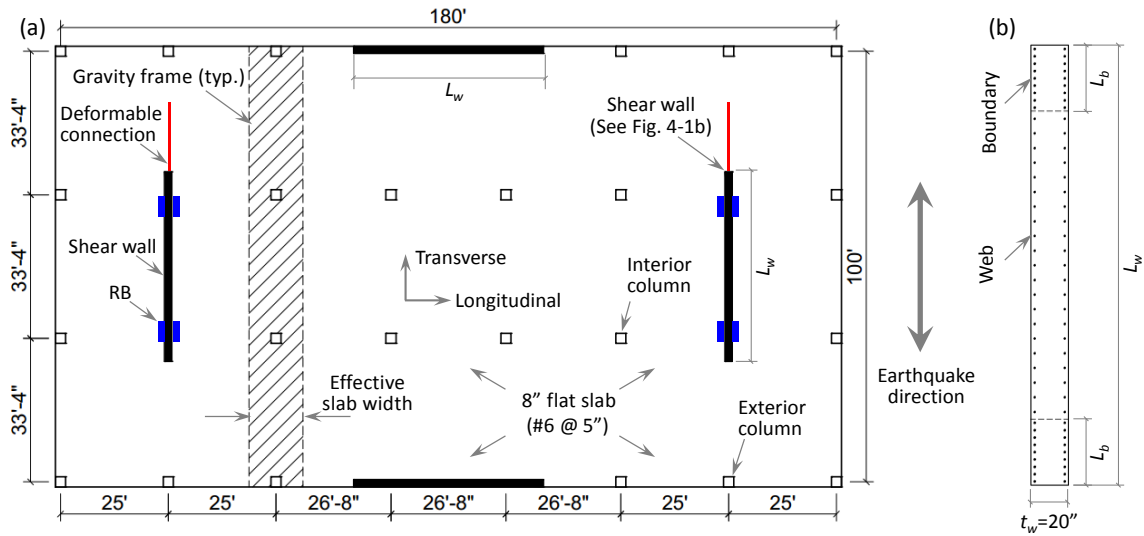


Fig. 4-1. Plan view of evaluation structure: (a) floor plan; (b) shear wall cross section.

The structure is examined for the response in the transverse direction only (indicated as “earthquake direction”) in Fig. 4-1. The seismic design of the evaluation structure is based on ASCE 7 [5]. The site is a generic Seismic Design Classification (SDC) D with soil class D ($S_s=1.5$, $S_1=0.6$). For SDC D, the seismic force resisting system is selected as special RC bearing walls ($R=5$, $\Omega_o=2.5$, $C_d=5$). The ELF design [5] for the RC walls in the transverse direction of the evaluation structure is shown in Table 4-1.

Table 4-1. Seismic design for the evaluation structures, transverse direction (Full structure).

NO. of stories	Floor weight	C_s	Roof diaphragm design force	Shear wall base design forces/per wall		
	W_x (kip)		F_{px} (kip)	V_u (kip)	M_u (kip-ft)	P_u (kip)
4	2430	0.200	765	1051	37708	796
8	2430	0.147	703	1642	106158	1808
12	2430	0.110	598	1909	181020	2903

The shear wall design follows ACI-318 [122]. The shear wall is sized and reinforced for required shear and moment strength due to the the design earthquake forces, and in the presence of design axial force due to tributary gravity loads (Refer to Table 4-1). Thus, the shear wall design is based on the required nominal strength from a P-M

interaction diagram. Table 4-2 shows the resulting wall and boundary element size for each structure.

Table 4-2. Shear wall dimension for different building height.

NO. of Stories	L_w (ft)	L_b (ft)
4	20	3.0
8	35	5.5
12	44	8.0

The GLRS columns are designed for the axial force due to tributary gravity load. The evaluation structure column design information is shown in Table 4-3. Columns are denoted as exterior and interior columns (See Fig. 4-1a). These columns carry different axial load, though possess the same dimension and reinforcing at each story for convenience.

Table 4-3. Column design information (lower stories only).

NO. of Stories	Stories	f_c'	f_y	Dimension (in)	Longitudinal Steel		Transverse Steel		
		(ksi)	(ksi)		Rebar	ρ (%)	Tie	Spacing (in)	ρ_t (%)
4	1-4	5	60	24	8#8	1.10	#4	8	0.31
8	1-2	5	60	26	12#8	1.40	#4	8	0.38
12	1-3	5	60	28	12#9	1.53	#4	8	0.36

Note: 8-story column dimension: 16", 20" for 6-8, 3-5 story;
12-story column dimension: 22", 24", 26" for 10-12, 7-9, 4-6 story.

4.2 Parameters under Investigation

The parameters under investigation will be described in this section. Primary parameters for this study are: (1) IFAS strength, α ; (2) building height (# of stories); (3) LFRS overstrength, Ω_e ; (4) IFAS secondary stiffness (γ); (5) LFRS types (RC shear wall and Precast rocking wall). Some secondary parameters under investigation include: (6) IFAS initial stiffness (K_i); (7) GLRS stiffness, ϕ ; (8) GLRS strength; (9) IFAS design strength profile (along the height of the structure).

Some of the key parameters are shown in the schematics in Fig. 4-2.

Fig. 4-2a shows the IFAS force-deformation behavior:

- The IFAS strength ratio α was introduced in Sec. 1.1 and is restated here: α is the ratio between the IFAS design strength (F_y) and current code diaphragm seismic design force F_{px} (Refer to Sec 2.4). Thus, $\alpha = \Sigma F_y / F_{px}$, where the summation occurs for all IFAS acting in the direction of F_{px} .
- The IFAS secondary stiffness ratio γ was introduced in Chap. 3 and is restated here: γ is the ratio of the IFAS secondary stiffness to the IFAS initial stiffness. Thus, $\gamma = K_2 / K_i$.
- d_y and d_u in Fig. 4-2a represent the yield (or slip) deformation and maximum deformation capacity of the IFAS. As would be typical of most devices, d_y is held constant in most studies. Thus, stiffness and strength change proportionally.

Fig. 4-2b shows the LFRS moment-rotation. Ω_e is defined as the ratio between the nominal moment of the shear wall (M_e) and the design moment of the shear wall (M_u), where M_e is defined as the nominal moment based on expected material strength.

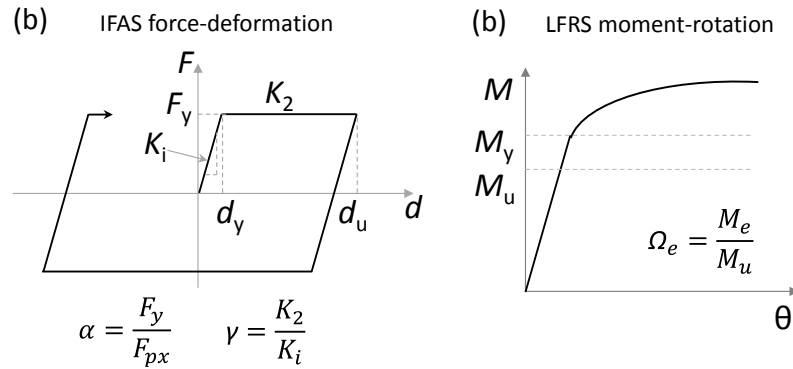


Fig. 4-2. Schematic drawings showing parameters: (a) IFAS force-deformation; (b) LFRS moment-rotation.

The IFAS properties for the parametric study are based on the IFAS devices shown in Table 4-4. The first three columns of the table list properties of the individual IFAS

devices: deformable connections (BRB, FD) and RB. The last two columns of the table list the system properties of two assembled IFAS configurations (BRB + RB, FD + RB).

Table 4-4. IFAS devices properties for evaluation structure.

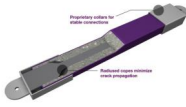
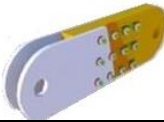
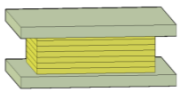
Properties	BRB	FD	RB (4 pads)	BRB + RB	FD + RB
Sketch				BRB + RB	FD + RB
F_y (kips)	224	227	-	229	231
α	0.75	0.76	-	0.77	0.77
K_i (k/in)	2033	2380	47	2080	2427
d_y (in)	0.11	0.095	-	0.11	0.095
K_{2nd} (k/in)	61	0	-	108	47
d_u (in)	2	4	4	2	4
γ	2.93%	0.00%	-	5.19%	1.94%

Fig. 4-3 shows force-deformation properties of the FD, BRB and RB. The properties for these devices are based on the IFAS Prototype [13]. The BRB and FD are seen to have controllable strength and stable energy dissipation capacity. Isotropic strain hardening is observed in the BRB force-deformation behavior (See Fig. 4-3b), meaning its strength increases during cyclic behavior; while the FD exhibits constant strength. Note that most of the parametric numerical analyses are performed using FD+RB.

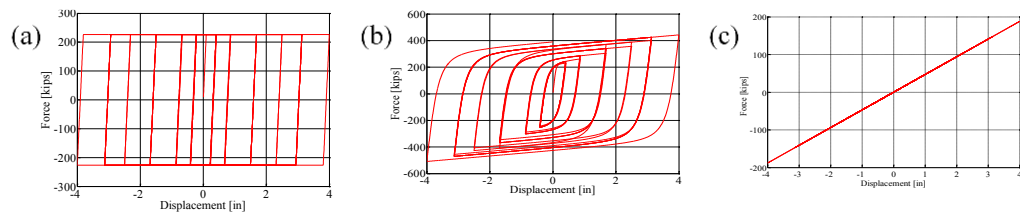


Fig. 4-3. Cyclic material testing results: (a) FD; (b) BRB; (c) RB.

Table 4-5 shows the study matrix for the *IFAS strength study* (FD + RB, constant IFAS strength profile). Three building heights are investigated in the study: 4-, 8-, 12-story structures. As seen, IFAS stiffness was kept proportional to strength for these studies.

Table 4-5. Study Matrix: IFAS strength (FD + RB, constant profile).

α	4-story		8-story		12-story	
	F_y (kips)	K_i (kips/in)	F_y (kips)	K_i (kips/in)	F_y (kips)	K_i (kips/in)
0.01	3.83	40.15	3.51	36.88	2.99	31.37
0.1	38.3	401	35.1	369	29.9	314
0.3	114.8	1204	105.4	1106	89.7	941
0.4	153.0	1606	140.6	1475	119.6	1255
0.5	191.3	2007	175.7	1844	149.5	1568
0.6	229.5	2409	210.9	2213	179.3	1882
0.7	267.8	2810	246.0	2581	209.2	2196
0.8	306.1	3212	281.1	2950	239.1	2509
1.0	382.6	4015	351.4	3688	298.9	3137
1.2	459.1	4817	421.7	4425	358.7	3764
1.5	573.8	6022	527.1	5532	448.4	4705
2.0	765.1	8029	702.9	7376	597.8	6273
2.5	956.4	10036	878.6	9219	747.3	7842
3.0	1147.7	12044	1054.3	11063	896.7	9410
Elastic	-	20844	-	20844	-	20844

The *IFAS initial stiffness study* involves three different stiffness levels: (1) the baseline K_i shown in Table 4-5; (2) a flexible IFAS, taken as half of the baseline ($0.5K_i$); (3) a stiff IFAS, taken as twice of the baseline ($2.0K_i$). The *IFAS secondary stiffness study* examines the following secondary slope ratios γ : 0%, 1%, 2%, 5%.

Wall design details for different building heights are shown in Table 4-6. The associated shear wall base moment-rotation backbones are shown in Fig. 4-4. (The plastic hinge length assumed for the walls is 120", 192", 192" for the 4, 8 and 12 story buildings.)

Note that several shear wall overstrengths are studied, as expressed with Ω_e . It should be noted that diaphragm demands have been shown to be highly affected by LFRS Overstrength [102]. Thus this parameter should also affect IFAS response. Note that the

LFRS often possesses a significant overstrength (larger moment capacity than the required strength) for an assortment of reasons (including safety factors, higher than nominal actual material strengths, design unity ratios greater than unity, stiffness controlled designs, strain hardening, plastic distributions etc.). Additionally, for alternate design methodologies (e.g. displacement-based design), the possibility exists for having a LFRS possessing lower moment capacity than the required strength. For this reason, Ω_e values less than unity are also found in Table 4-6.

Table 4-6. Shear wall design for different building height and overstrength.

NO. of Stories	Ω_e	f'_c (ksi)	f_y (ksi)	f'_{ce} (ksi)	f_{ye} (ksi)	ρ_b (%)	ρ_{web} (%)	ρ_{bt} (%)	ρ_t (%)
4	0.7	4	40	4	40	1.32	1.07	0.42	0.13
4	1.0	5	60	5	60	1.98	0.93	0.63	0.19
4	1.6	5	60	7.5	75	2.50	1.04	0.63	0.19
4	0.7	5	60	7.5	90	1.32	0.67	0.42	0.13
8	0.7	4	40	4	40	1.44	0.83	0.45	0.14
8	1.0	5	60	5	60	1.44	1.02	0.45	0.14
8	1.3	5	60	7.5	75	2.12	0.88	0.53	0.17
8	1.6	5	60	7.5	90	1.06	0.73	0.44	0.16
12	0.7	4	40	4	40	1.32	0.95	0.42	0.15
12	1.0	5	60	5	60	1.67	0.93	0.42	0.15
12	1.3	5	60	7.5	75	1.88	1.11	0.47	0.17
12	1.6	5	60	7.5	90	1.32	1.07	0.42	0.13

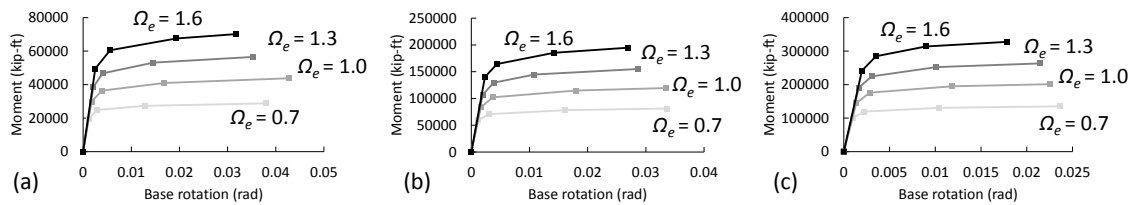


Fig. 4-4. Shear wall base moment-rotation backbone: (a) 4-story

Two LFRS types are studied: one is the RC shear wall shown in Table 4-6; the other is a rocking wall (Shown subsequently in Sec. 5.1.2). Fig. 4-5a shows rocking wall base

moment-rotation hysteretic properties. As seen, rocking walls have a different hysteretic response since they “self-center” due to unbonded post-tensioning. The different hysteresis can lead to different diaphragm demands, and hence could affect the IFAS response. The main reason the rocking wall is examined in the parameter study is that it is the LFRS used in the shake table program, for repeatability issues (See Sec. 5.1.2). For the rocking wall, M_y represents the yield strength and $a\%$ represents the ratio between the loading and unloading force in the rocking wall (Refer to Fig. 4-5). $a=0$ means no energy dissipation capacity assigned to the rocking wall. Three different values are selected for a : 0, 20%, and 40%. Fig. 4-5b, c, d show the moment-rotation backbone of the rocking wall used in the study, seen to match the RC shear wall for the 4-, 8- and 12-story structures ($\Omega_e=1.0$).

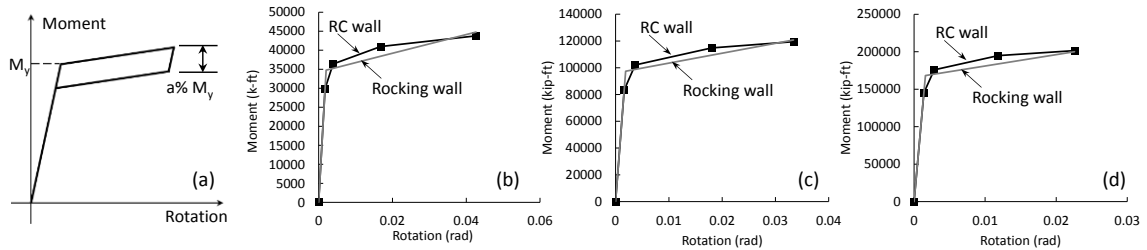


Fig. 4-5. Rocking wall: (a) rocking wall base moment-rotation hysteretic property; wall base moment-rotation backbone: (b) 4-story; (c) 8-story; (d) 12-story.

The properties (strength and stiffness) of the GLRS may vary for different construction (reinforced concrete and structural steel gravity columns and framing connections). Therefore, the influence of the GLRS on IFAS performance is also studied. This influence is studied by changing the stiffness and the strength of gravity system columns (See Fig. 4-6): (1) if the stiffness of the columns shown in Table 4-3 is denoted as K_{col} , the stiffness variation of the GLRS columns is $2K_{col}$ and $4K_{col}$, the corresponding GLRS stiffness ratio, ϕ , is shown in Table 4-7; (2) the GLRS column base plastic hinge

strength of one column is modified to $\pm 48.7\%$ (for 12-story structure) from that of the columns shown in Table 4-3 to create stronger/weaker columns.

Table 4-7. Elastic GLRS stiffness ratio (ϕ).

NO. of Stories	K_{col}	$2K_{col}$	$4K_{col}$
4	0.10	0.13	0.18
12	0.03	0.04	0.05

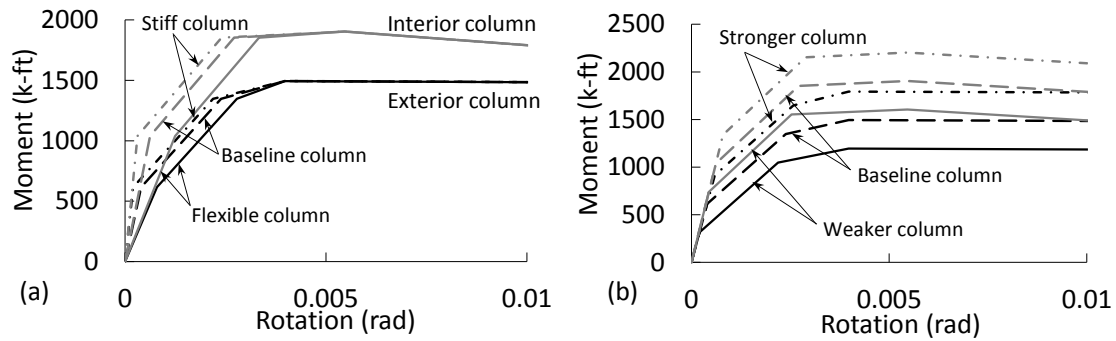


Fig. 4-6. GLRS column (12-story) properties: (a) different stiffness; (b) different strength.

Two different IFAS design strength profiles along the structure height are studied:

(a) a constant IFAS strength pattern along the structure height based on the current code diaphragm design F_{px} at roof (which is the maximum design force value along the height, refer to Fig. 4-7a, termed the “constant profile” case); (b) varying IFAS strength along the structure height based on the current code F_{px} pattern at each floor level (Fig. 4-7b), termed the “triangular profile” case. Note that for the constant profile, the strength ratio constant α is multiplied by a single value to produce the strength at each floor; for the triangular profile, each distinct F_{px} at each floor level is multiplied by the constant α to create a modified triangular profile. Note that the F_Y shown in Table 4-5 is the roof (maximum) value, so it is the strength value of all IFAS in the structure for the “constant profile” case; and is only the (maximum) roof IFAS strength value for the “triangular profile” case, with

the lower floors possessing IFAS strengths proportionally lower following the current code F_{px} pattern.

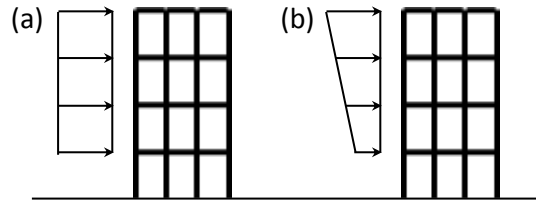


Fig. 4-7. IFAS strength profiles: (a) constant profile; (b) triangular profile.

4.3 2D Model Description

The 2D model represents half of the evaluation structure (shaded region in Fig. 4-8a). The model was created in OpenSees. The GLRS of this portion of the structure is modeled as one equivalent frame in the transverse direction (See Fig. 4-8b). The gravity load acting on the structure is 1.0DL+0.25LL which is based on [4, 5]. The P-Delta effects acting on the columns is included. The floor and gravity column mass is assigned to the GLRS degree of freedom (DOF); the shear wall mass is assigned to the LFRS DOF.

The IFAS deformable connections and RBs are modeled together as a nonlinear spring using the *steel01 material* [123] (See Fig. 4-8c). LFRS nonlinear response is assumed to concentrate at the wall base. The shear wall and rocking wall are modeled as an elastic beam-column element with inelastic action concentrated in a nonlinear rotational spring element at the base (See Fig. 4-8d). The spring hysteretic model is the *Pinching4 material* [123] for the RC wall and *SelfCentering material* [123] for the rocking wall.

Nonlinear behavior of columns is assumed to occur at the first-story column base. Columns at the first-story columns are modeled as elastic beam-column elements with plastic hinges at the base. The hysteretic model for the plastic hinge is *Pinching4 material* [123]. Columns in the upper stories are modeled as elastic beam-column elements.

Slabs are modeled as elastic beam-column elements with concentrated plastic hinges at both ends. The hysteretic model for plastic hinges is *Pinching4 material* [123]. The comparison of plastic hinge moment-curvature in the GLRS of the 12-story evaluation structure is conceptually shown in Fig. 4-8e.

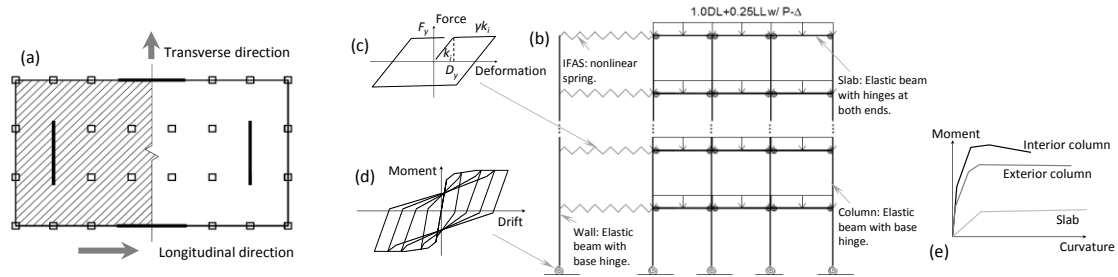


Fig. 4-8. Schematic drawing: (a). half structure; (b). Numerical model; force-deformation: (c) IFAS; (d) wall base; (e) plastic hinge moment-curvature backbones.

The earthquake simulations are performed through Nonlinear Time History Analyses (NTHA). NTHAs were performed using 2% Rayleigh damping. The damping coefficients are determined from a modal analysis anchored to the first (fundamental) and third translational mode. The cumulative mass of the first three modes is 92.8% of the total structure floor mass for the traditional 12-story structure. The dynamic and nonlinear solvers are the Newmark implicit algorithm and the Modified Newton-Raphson method, respectively. To adequately capture acceleration response, input and output time steps are 0.0025sec, while the recorded time step is 0.01sec for data storage. The acceleration responses are filtered with a low-pass filter at 24Hz. The response envelopes shown are the mean value of the maximum responses of the set of 10 NTHAs. The response shown in parametric study plots is the maximum response along the structure height.

Response reduction will be used to show the benefits of using the IFAS. Response reduction is defined as the ratio of the amount of the IFAS structure response reduction (relative to the traditional structure) to the traditional structure response.

4.4 Ground Motion Suites

A suite of ten spectrum-compatible earthquakes from FEMA P695 [121] are selected for the parametric studies. The earthquakes are scaled using the factors shown in Table 4-8 to match the 5% damped design spectrum for the generic SDC D site at the DBE level (See Fig. 4-9). The 1st and 2nd period are denoted as black solid and dashed vertical lines respectively for the traditional structures ($\Omega_e=1.3$). The NTHAs are performed at both the DBE and MCE level. The scaled DBE earthquakes are amplified by 1.5 to create MCE motions.

Table 4-8. Selected ground motion information.

NO.	ID	Earthquake	Magnitude	Year	Scaling factor	Scaled PGA (g)
1	EQ1	Kobe Japan	6.9	1995	1.66	0.35
2	EQ2	Kocaeli Turkey	7.5	1999	1.53	0.48
3	EQ3	Kocaeli Turkey	7.5	1999	0.93	0.33
4	EQ4	Loma Prieta	6.9	1989	1.40	0.51
5	EQ5	Imperial Valley	6.5	1979	1.90	0.45
6	EQ6	Imperial Valley	6.5	1979	1.28	0.45
7	EQ7	Superstition Hills	6.5	1978	1.42	0.51
8	EQ8	Superstition Hills	6.5	1978	1.97	0.59
9	EQ9	Cape Mendocino	7.0	1992	1.27	0.49
10	EQ10	Northridge	6.9	1994	0.71	0.37

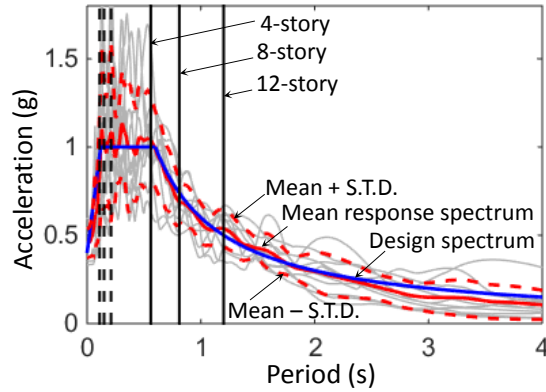


Fig. 4-9. Ground motions response spectrum with 5% damping and design spectrum.

4.5 Fundamental Response of the IFAS Structure

The fundamental response of the IFAS structure is conceptually described in this section. The 12-story RC wall evaluation structure ($\Omega_e=1.0$, $\alpha=0.3$, EQ2 MCE) is selected for the example. One cycle of the GLRS and wall response is described. The positive (rightward) and negative (leftward) displacement directions for the structure is shown on a three-story structure schematic in Fig. 4-10a. The shear wall displacement at floor level 1 and 2 is shown using dashed and solid lines respectively in Fig. 4-10b. The shear wall roof drift (blue), shear wall base rotation (red) and GLRS roof drift (black) responses are shown in Fig. 4-10c. Seven time locations are indicated in Fig. 4-10c (from A to G). The structure responses at the selected time locations are shown in Fig. 4-11.

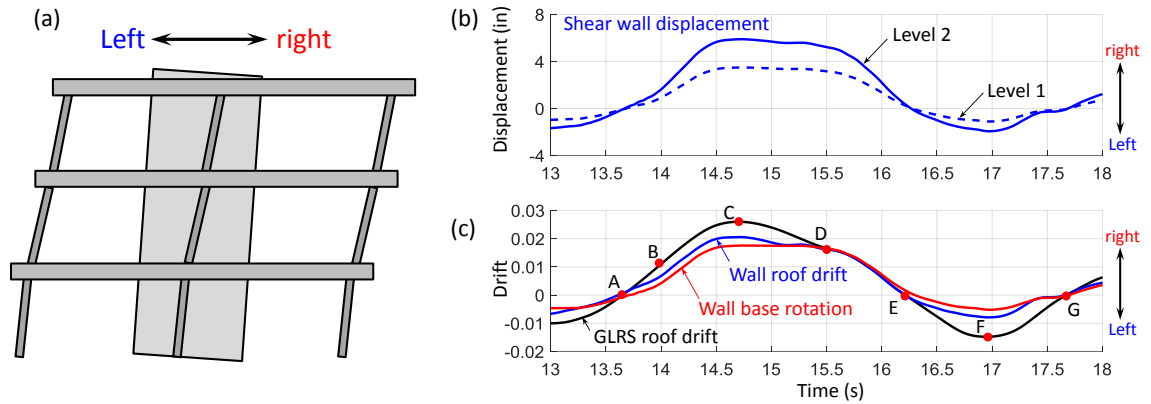


Fig. 4-10. Evaluation structure ($\Omega_e=1.0$, $\alpha=0.3$) response under EQ2 at MCE level: (a) conceptual schematic drawing; (b) shear wall displacement at selected floor levels; (c) shear wall roof drift, base rotation and GLRS roof drift.

Fig. 4-11 shows the structure responses at selected time spots in Fig. 4-10c. In each time spot, a deformation profile of the wall and GLRS is shown in blue and black respectively. Shear wall velocity, slab velocity, relative displacement and relative velocity between the GLRS and wall are shown with magnitude bars at each floor level. Note that the status the structure before the analysis is termed as the “zero location”. The GLRS deforms larger than the wall since smaller external force acts on the wall. During the process when the structure deforms from one side to the other side, the GLRS always deforms faster than the wall. The deformation shape of the wall mostly follows the 1st mode shape. While the deformation shape of the GLRS is influenced by higher mode. Details can be seen in Appdx. B.1.

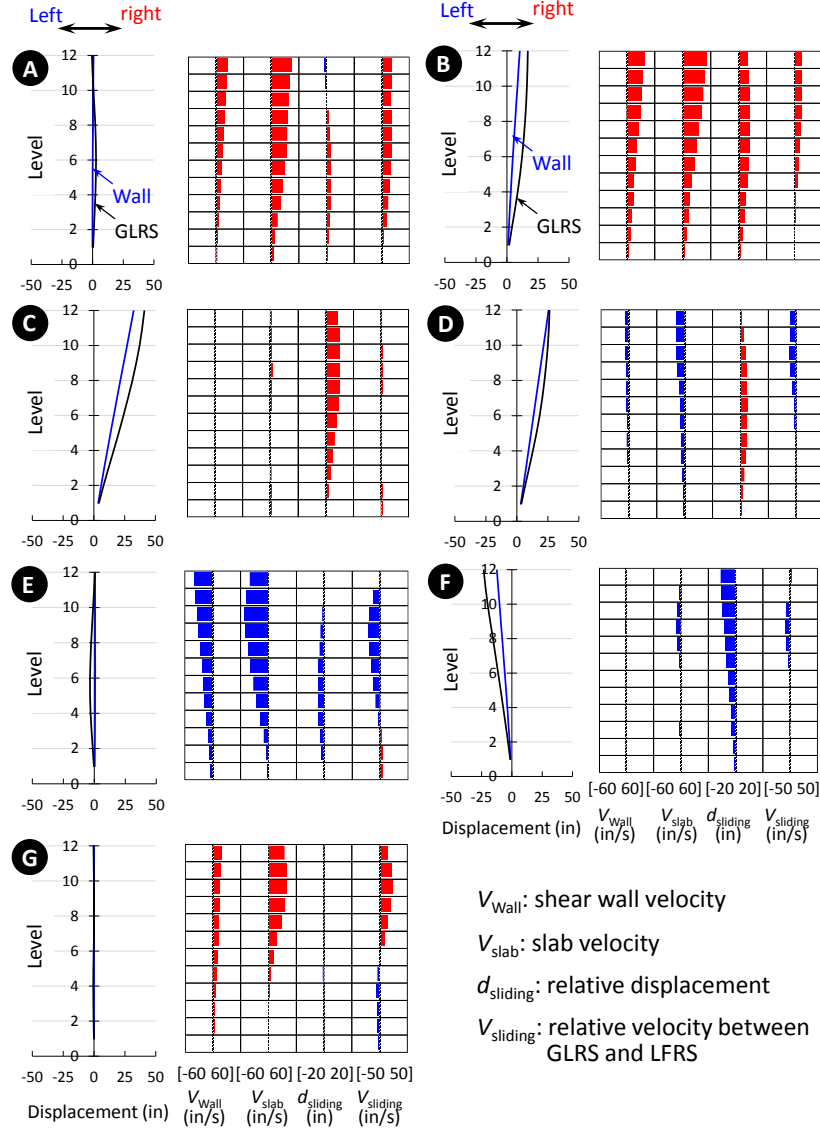


Fig. 4-11. Evaluation structure ($\Omega_e=1.0$, $\alpha=0.3$) response at selected time spots in Fig. 4-10.

4.6 Effect of IFAS Strength

A baseline structure was first used to study the effect from F_y or α . The baseline structure is a 12-story structure using the RC wall ($\Omega_e=1.0$). The IFAS is FD + RB and the IFAS strength is the same along the structure height ($\gamma = 2\%$) (See Table 4-5). Fig. 4-12 shows the response envelopes along the height of the baseline structure for different α in DBE. Fig. 4-12a shows that the floor acceleration is decreased as α decreases when $\alpha > 0.4$.

The floor acceleration at the roof is increased as α decreases when $\alpha < 0.4$. Fig. 4-12b shows that the shear wall lateral deformation demand is decreased as α increases. Fig. 4-12c shows that smaller α produces larger GLRS column drift. Fig. 4-12d shows that the relative displacement between the floor and shear wall is increased as α decreases. The first two plots imply that the IFAS has the potential to protect nonstructural elements and contents, and mitigate the structural damage in earthquakes. The last two plots indicate the tradeoffs of using the IFAS: GLRS drifts must be limited to maintain a stable structure; relative displacement must remain within practical limits from an architectural/mechanical standpoint.

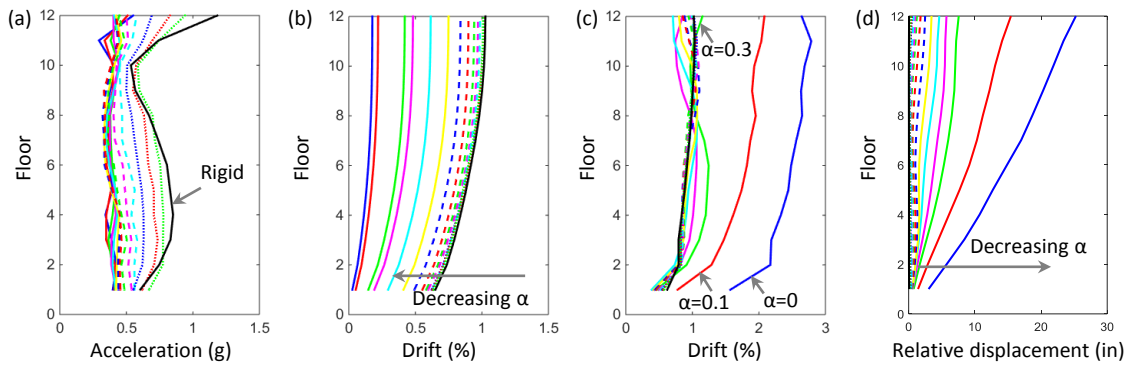


Fig. 4-12. 12-story structure ($\Omega_e = 1.0$) maximum response envelopes: (a) floor acceleration; (b) shear wall inter-story drift; (c) GLRS column inter-story drift; (d) relative displacement.

Fig. 4-13 shows responses of the baseline structure (DBE and MCE) from the parametric study. The inter-story drift, relative displacement and energy dissipation are plotted only for $\alpha \leq 2$ because the response is essentially unchanged when $\alpha > 2$. The plots show that structural response follows similar trend for both the DBE and MCE, with the latter response larger.

Fig. 4-13a, d show that the floor acceleration is decreased as α decreases when $\alpha > 0.4$. However, this trend is reversed when $\alpha < 0.4$. This reversed trend is probably due to

the dynamic behavior of the GLRS. The IFAS force transferred to the wall is small when α is small, so that the GLRS dynamic behavior relies on itself rather than the wall. However, the acceleration of the IFAS structure when $\alpha < 0.4$ also undergoes significant reduction in comparison to the traditional structure.

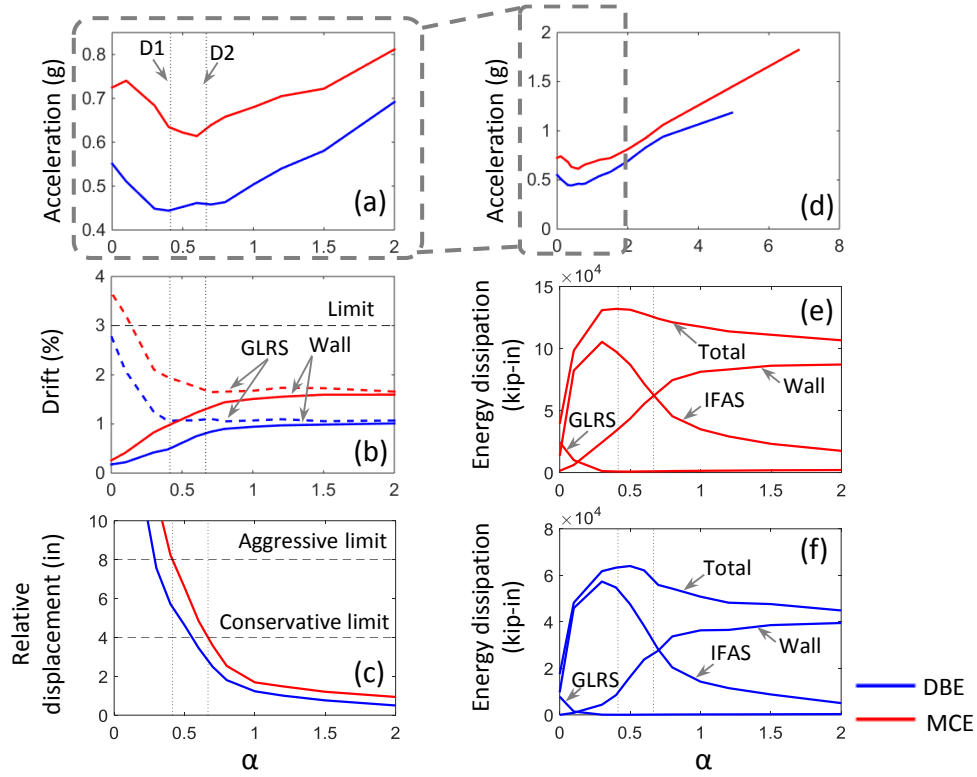


Fig. 4-13. Baseline structure ($\Omega_e = 1.0$) response parametric plot: (a) floor acceleration ($0 < \alpha < 2$); (b) Inter-story drift; (c) relative displacement; (d) floor acceleration ($0 < \alpha < 8$); (e) MCE energy dissipation distribution; (f) DBE energy dissipation distribution.

Fig. 4-13b shows that smaller α can decrease the wall lateral deformation, as well as increasing the GLRS lateral deformation. The GLRS inter-story drift limitation is 3% under MCE and was indicated by horizontal dashed line in Fig. 4-13b. The GLRS inter-story drift exceeds this limitation when $\alpha < 0.3$. Fig. 4-13c shows that smaller α produces larger relative displacement between the floor and wall. Thus, a lower boundary of α should be selected to provide an acceptable relative displacement and a stable gravity system. Fig.

4-13e, f show the energy dissipation in different components and whole structure. The gravity system dissipates most of the energy when $\alpha < 0.1$. The IFAS dissipates most of the energy (more than 50% of the total energy dissipated in the structure) when $0.1 < \alpha < 0.7$.

The two design limits (conservative and aggressive design) of the relative displacement are indicated by vertical dotted lines in Fig. 4-13c as “D2” and “D1”. Structural response under MCE at the two design limits are shown in Table 4-9. A larger reduction in the shear wall deformation can be obtained at the aggressive design. However, the GLRS deformation and relative displacement are increased at the aggressive design.

Table 4-9. Structural response at design limits.

Design limit	α	Shear wall drift (%)	Floor acceleration (g)	Floor acceleration reduction (%)	GLRS drift (%)	GLRS drift amplification
Conservative	0.67	1.30	0.63	65.38	1.68	1.02
Aggressive	0.41	0.99	0.63	65.26	1.93	1.18

4.7 Effect of Building Height

The effect from the building height is studied in this section. The structural response of the evaluation structures ($\Omega_e = 1.0$, FD + RB, $\gamma = 2\%$, MCE) with three different heights are shown in Fig. 4-14. Conservative and aggressive limits are indicated by circles and stars respectively.

The response of the three evaluation structures follows the same trend. Fig. 4-14d shows larger acceleration reduction in the 8-story and 12-story structures in comparison to that of the 4-story structure. The effective GLRS modal mass in the first mode is 76.8%, 69.6% and 67.1% of the total GLRS mass for the 4-, 8- and 12-story traditional structure

respectively. The larger floor acceleration response in the taller traditional structure is probably due to the larger contribution of higher modes. And the floor acceleration is decreased more significantly in taller structures after using the IFAS.

Fig. 4-14b shows that the wall drift is decreased while the GLRS drift is increased as α decreases. The taller IFAS structure undergoes larger wall drift when α is small, and smaller wall drift when α is large. Fig. 4-14c shows smaller relative displacement in the 4-story structure in comparison to the other two evaluation structures when α is the same.

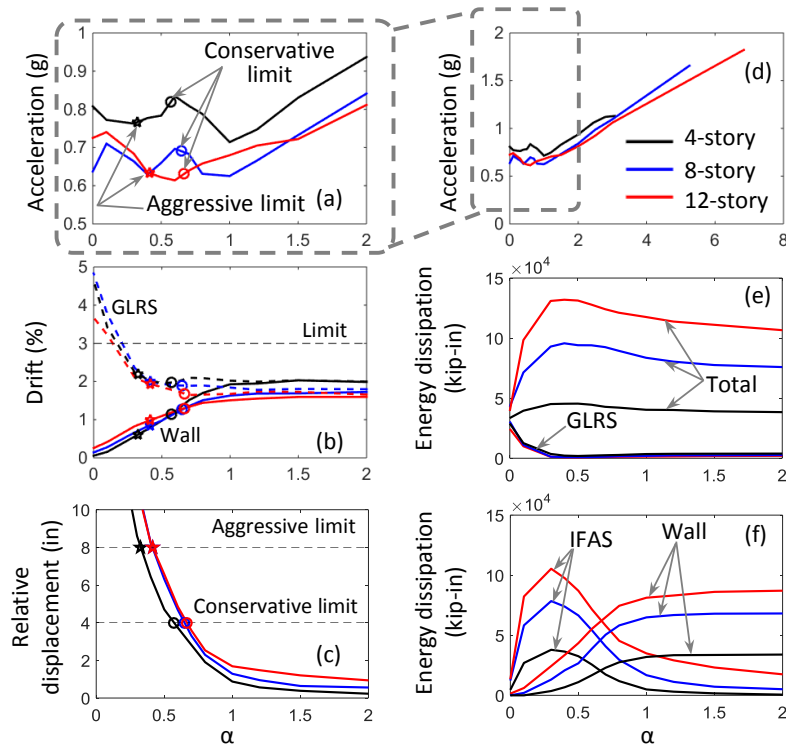


Fig. 4-14. Parametric plot of different building height ($\Omega_e = 1.0$): (a) floor acceleration ($0 < \alpha < 2$); (b) inter-story drift; (c) relative displacement; (d) floor acceleration ($0 < \alpha < 8$); energy dissipation: (e) total, GLRS; (f) IFAS, wall.

4.8 Effect of LFRS Overstrength

The effect from Ω_e (See Table 4-6) to the IFAS performance will be presented in this section. Fig. 4-15 shows parametric results (in MCE) of a 12-story evaluation structure

using the shear wall with different Ω_e (the IFAS $\gamma = 2\%$). The figure shows that each response of the structure with different Ω_e follows a similar trend.

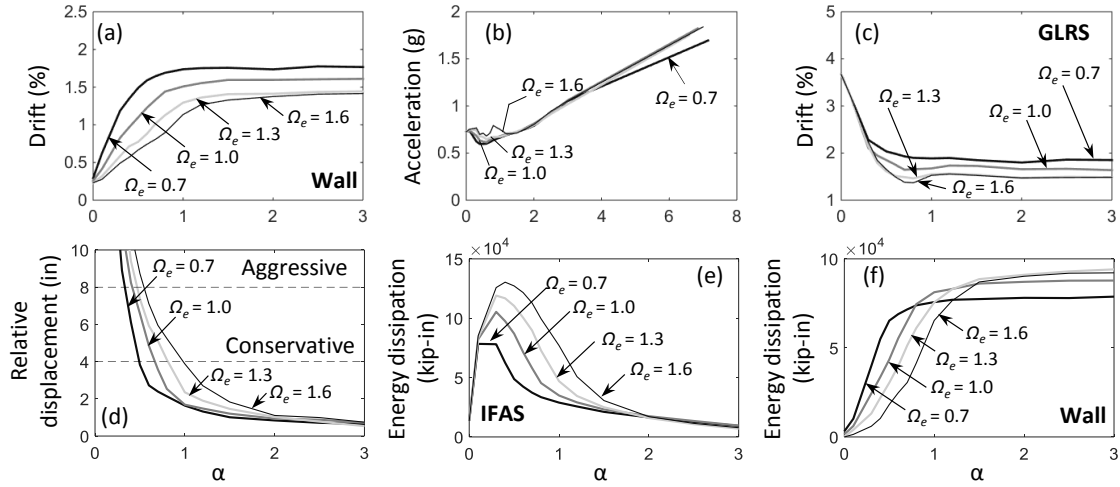


Fig. 4-15. 12-story structure response comparison at different Ω_e and α under MCE ($\gamma=2\%$): (a) wall inter-story drift; (b) floor acceleration; (c) GLRS column inter-story drift; (d) relative displacement; (e) IFAS energy dissipation; (f) wall energy dissipation.

Larger Ω_e can decrease the wall deformation demand (See Fig. 4-15a). Larger Ω_e produces larger floor acceleration (See Fig. 4-15b). The GLRS deformation demand is large and independent from Ω_e when $\alpha < 0.3$ (See Fig. 4-15c). However, the GLRS deformation demand is reduced by using a wall with larger Ω_e when $\alpha > 0.3$. Larger Ω_e produces larger relative displacement (See Fig. 4-15d). The conservative and aggressive design limits are also indicated in Fig. 4-15d with horizontal dashed lines. Fig. 4-15d indicates that the lower bound of α is increased as Ω_e increases, meaning a smaller α can be used when Ω_e is smaller. Fig. 4-15e shows that larger Ω_e generates larger energy dissipation in the IFAS, matching the larger relative displacement shown in Fig. 4-15d. Fig. 4-15f shows that larger Ω_e decrease the wall energy dissipation when α is small, matching the smaller shear wall drift shown in Fig. 4-15a.

The parametric results of the 4-, 8-story structures are similar to that of the 12-story structure. See Appdx. B.2 for more details.

The structural response at the conservative and aggressive design limits (termed design plot) for the structures with different height and Ω_e is shown in Fig. 4-16. Fig. 4-16a shows α at the conservative and aggressive limits. α at the limits becomes smaller as Ω_e decreases. This is because the relative displacement is decreased as Ω_e decreases. A shorter building and a larger Ω_e can generate a larger reduction of the shear wall drift (See Fig. 4-16b). This is probably because the contribution from the 1st mode takes a larger portion for a shorter structure. At least 20% more of the shear wall drift reduction can be achieved in an aggressive design in comparison to that of a conservative design. Fig. 4-16e indicates that a shorter building with a larger Ω_e can generate a smaller shear wall drift at the design limits. This phenomenon shows that a low-damage structure can be achieved by increasing Ω_e . Fig. 4-16c shows the floor acceleration reduction. A taller structure can achieve larger acceleration reduction: the 12-story structure achieves more than 50% reduction in the acceleration for both conservative and aggressive designs while the 4-story structure achieves 20% - 50% reduction. Fig. 4-16f shows the floor acceleration response at the design limits. Aggressive design produces smaller acceleration in comparison to that of the conservative design for 4-story and 8-story structures when Ω_e is large. Aggressive design produces larger acceleration in comparison to that of the conservative design for 4-story and 8-story structures when $\Omega_e = 0.7$. Larger Ω_e produces larger acceleration at the design limits. Fig. 4-16d shows that larger Ω_e generates smaller GLRS drift. The aggressive design produces larger GLRS drift than that of the conservative design.

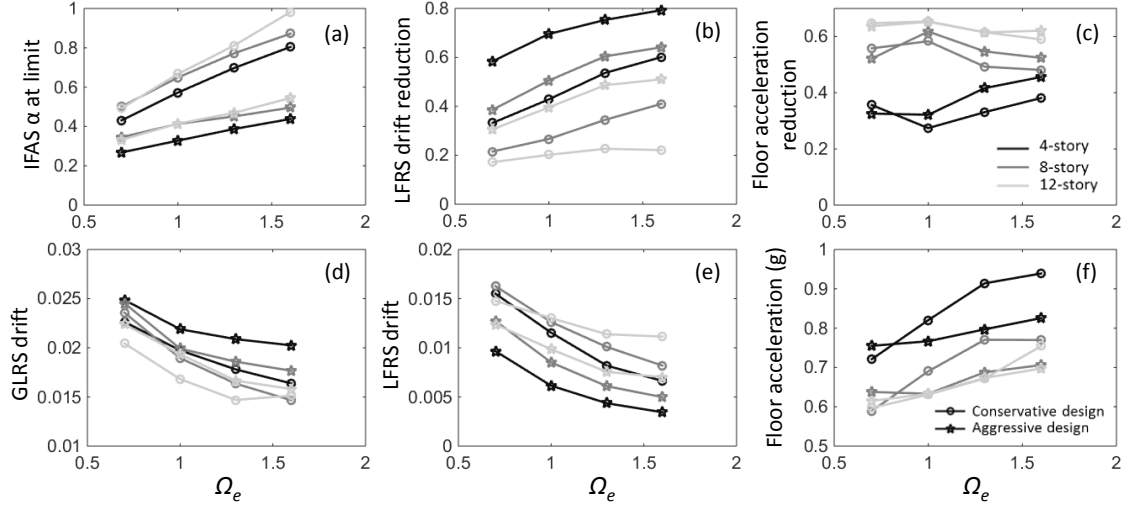


Fig. 4-16. Design plot for different structure height and Ω_e : (a) α ; (b) LFRS drift reduction; (c) floor acceleration reduction; (d) GLRS drift; (e) LFRS drift; (f) floor acceleration.

Generally speaking, the IFAS structure can achieve a good amount of reduction in the LFRS drift and floor acceleration. A smaller LFRS drift can be obtained in the aggressive design in comparison to that of the conservative design. A smaller floor acceleration can be obtained in an aggressive design when $\Omega_e \geq 1$. A larger Ω_e can generate smaller LFRS and GLRS drift.

4.9 Effect of IFAS Secondary Stiffness

This section will discuss the effect from γ to the IFAS performance. Fig. 4-17 shows the response comparison of a 4-story structure using different γ ($\Omega_e=1.0$). The figure shows that smaller γ can generate smaller acceleration and shear wall drift (See Fig. 4-17b, c). The γ has significant influence on the shear wall drift when $\alpha < 1$. The influence from the γ becomes negligible when $\alpha > 1$. Smaller γ produces larger relative displacement and GLRS drift (See Fig. 4-17d, e), however the influence on the GLRS drift is negligible. The parametric results of the 12-story structure are similar to that of the 4-story structure. See

Appdx. B.3 for more details. The influences from the IFAS initial stiffness is shown in Appdx. B.4.

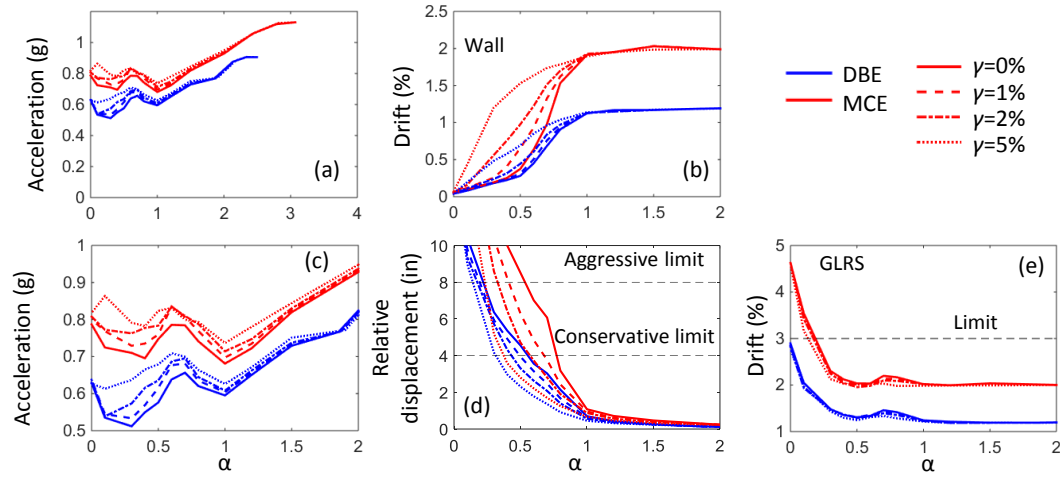


Fig. 4-17. 4-story structures using different γ ($\Omega_e=1.0$): (a) floor acceleration ($0<\alpha<4$); (b) LFRS drift; (c) floor acceleration ($0<\alpha<2$); (d) relative displacement; (e) GLRS drift.

4.10 Effect of LFRS Type

The effect of using different LFRS types will be discussed in this section. Fig. 4-18 shows the parametric results of the 12-story structure ($\Omega_e=1.0$) using different types of the LFRS. Fig. 4-18 shows that the structure using the rocking wall generates larger acceleration, LFRS drift, GLRS drift and relative displacement than that using the RC wall. The acceleration, shear wall drift, GLRS drift and relative displacement is decreased as the energy dissipation capacity of the rocking wall increases.

The design plot of the LFRS type effect is shown in Appdx. B.5.

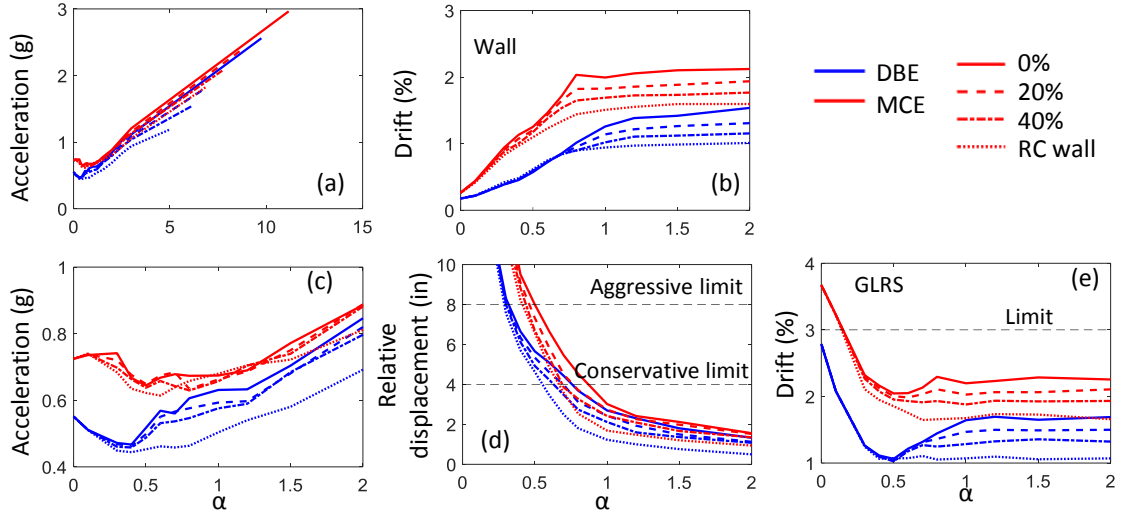


Fig. 4-18. 12-story structures using different LFRS: (a) floor acceleration ($0 < \alpha < 10$); (b) LFRS drift; (c) floor acceleration ($0 < \alpha < 2$); (d) relative displacement; (e) GLRS drift.

4.11 Effect of GLRS Column Properties

The effect of the GLRS column strength and stiffness will be discussed in this section. Fig. 4-19 shows the parametric results of the 4-story structure ($\Omega_e=1.0$) using different GLRS column stiffness. For the purpose of easy comparison, only the structure responses in MCE are presented and two LFRSs are used for the 4-story structure: RC wall and rocking wall. Fig. 4-19 shows that the structure using the rocking wall produces larger floor acceleration, GLRS drift and relative displacement. The structure using the rocking wall also produces larger wall drift when $\alpha > 0.6$. Fig. 4-19a, c indicate that larger GLRS column stiffness generates larger floor acceleration. Fig. 4-19b shows that the different column stiffness has negligible effect on the shear wall drift. Larger column stiffness generates smaller relative displacement (See Fig. 4-19d) and smaller GLRS drift (See Fig. 4-19e), however the effects is negligible. Another interesting phenomenon can be observed in Fig. 4-19e. The GLRS drift of the structure using the RC wall is decreased first and then does not change much as α increases. The GLRS drift of the structure using the rocking

wall is decreased, then reversed to increase and finally does not change much as α increases. Therefore, a valley can be observed in the GLRS drift. Similar phenomenon is observed in the 12-story structure using the rocking wall (See Fig. B-10e), however is not as clear as in Fig. 4-19e. The amplification of the GLRS drift is one of the trade-off of using the IFAS in the structure using the RC wall as the LFRS. From this result, there is a possibility of obtaining reduction in shear wall drift, floor acceleration and GLRS drift when a rocking wall structure is under investigation.

The parametric results of the 12-story structure is shown in Appdx. B.6.

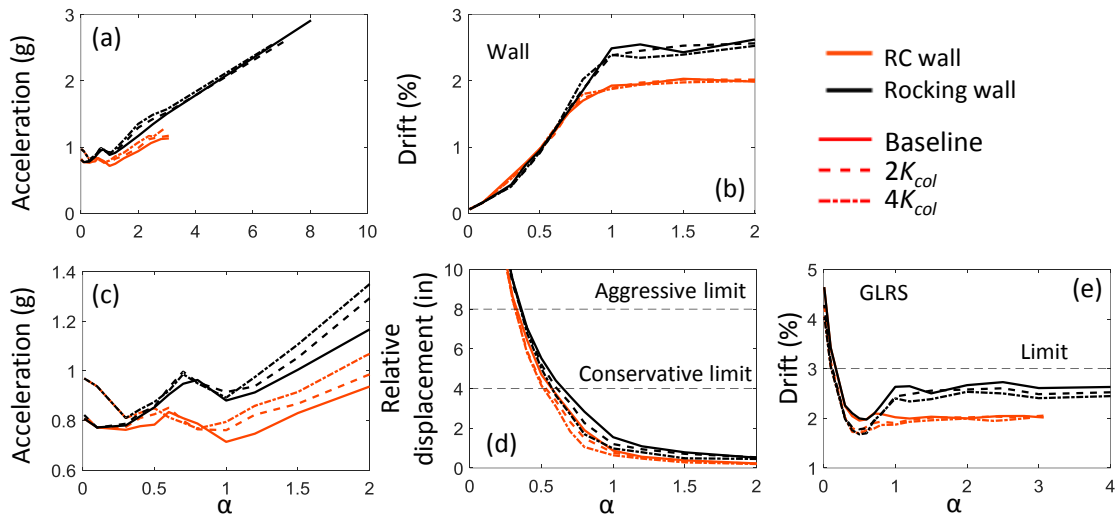


Fig. 4-19. 4-story structures using different column stiffness under MCE: (a) floor acceleration ($0 < \alpha < 8$); (b) LFRS drift; (c) floor acceleration; (d) relative displacement; (e) GLRS drift.

4.12 Effect of IFAS Strength Profiles

The results of the baseline structure using two IFAS strength patterns (constant profile vs. triangular profile) along the structure height in MCE will be discussed in this section.

Fig. 4-20a shows the profiles of the two IFAS strength patterns for a 4-story structure. Fig. 4-20b, c, d show the shear wall drift, relative displacement, floor acceleration comparison between these two sets of analyses. The figure shows that these two IFAS strength patterns produce similar structural responses. The structure using the varying IFAS strength pattern produces smaller shear wall drift and larger relative displacement because the IFAS force acting on the wall becomes smaller.

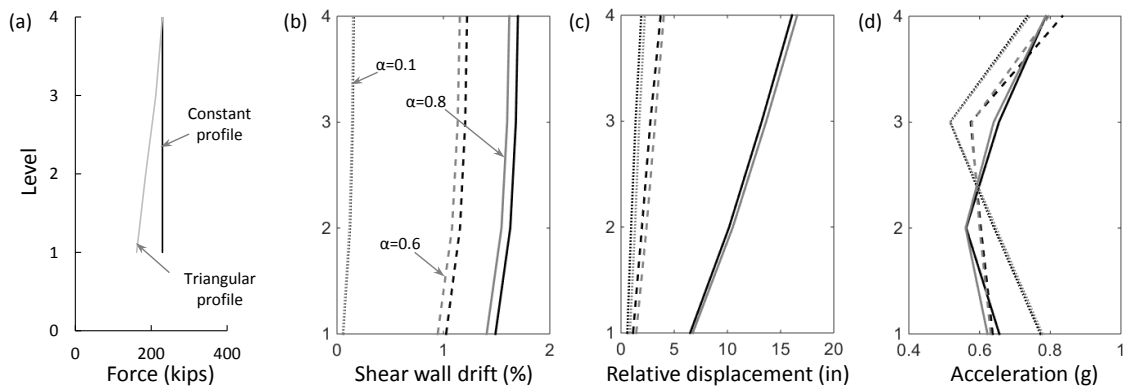


Fig. 4-20. 4-story structure response comparison using different IFAS strength pattern: (a) IFAS strength pattern; (b) shear wall drift; (c) relative displacement; (d) floor acceleration.

The results of the 12-story structure are shown in Appdx. B.7. The difference of the results generated from the constant profile and triangular profile is negligible. Therefore, using constant profile and triangular profile produce similar structure responses. The effect from using different IFAS configuration (BRB+RB, FD+RB) is also studied and shown in Appdx. B.8.

4.13 Study on Floor Interface Configuration

This section will discuss about the effect from the different floor interface configuration. To permit the partial uncoupling of the LFRS and GLRS, a moat must be designed in the floor system around the LFRS. There are two options for designing the

floor interface at this location: (1) design a cantilever slab around the LFRS (*Cantilever Slab Case*, See Fig. 4-21); (2) provide ledges on the LFRS to support the slab (*Ledge Case*, See Fig. 4-22).

The Cantilever Slab Case disconnects the slab from the LFRS in the vertical direction, with the exception of the low elastic stiffness of the rubber bearing. However, the slab span length in this case is limited because of the cantilever condition. Thus, the usage of the space near the LFRS will be limited because of the presence of nearby columns. The slab span can be increased significantly if the cantilever slab is supported on a ledge. A parametric study of using ledges on the LFRS was performed to investigate the potential issues of using ledges.

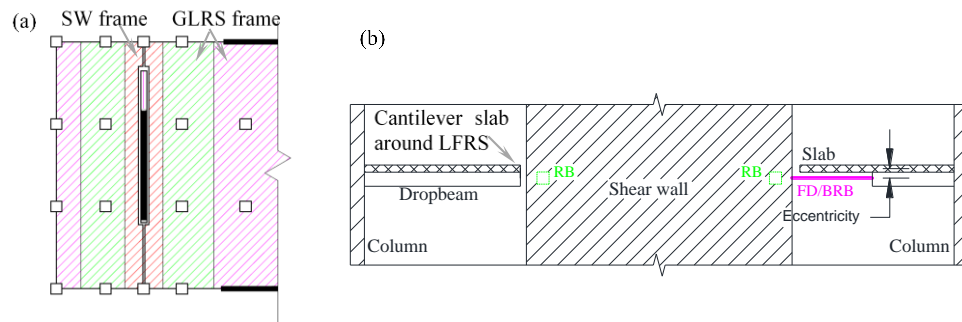


Fig. 4-21. Cantilever Slab Case: (a) plan view; (b) elevation view.

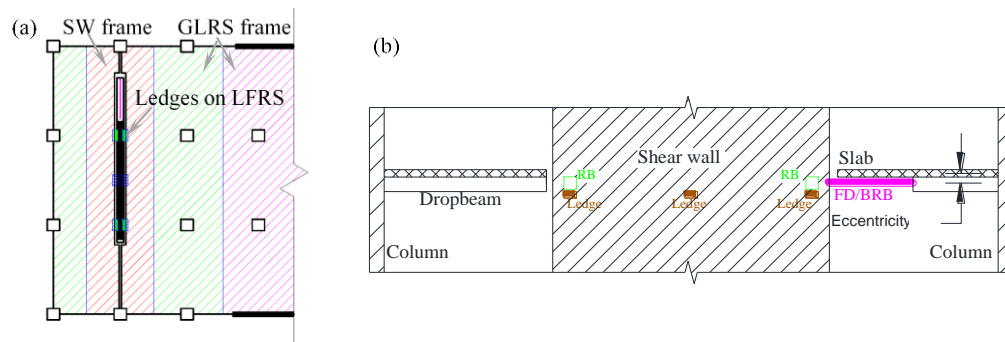


Fig. 4-22. Ledge Case: (a) plan view; (b) elevation view.

4.14.1 Description of Model

The numerical model used in this sub-section is explained. In a real building structure, the IFAS devices are installed at different locations around the LFRS (See Fig. 4-21b, 4-32b). The deformable connections (FD and BRB) will rotate in vertical plane and the RBs will undergo vertical and horizontal shear deformation in earthquakes. The 2D model introduced in Sec. 4.3 can provide response efficiently but cannot properly represent the IFAS schematic deformation in real structures. A new developed 2D model considers the rotation ability of the deformable connections in vertical plane (Fig. 4-23a) and the deformation ability of the RB in both horizontal and vertical direction. All the IFAS devices are modeled at the locations as in the structure (Fig. 4-23c). The IFAS devices properties used in this section are shown in Appdx. B.9. Fig. 4-23c represents the modeling of the Ledge Case of this new 2D model. The Cantilever Slab Case model is the same as that of the Ledge Case model except there is no contact elements (for modeling the ledges) used in the Cantilever Slab Case model.

In addition, the following three modeling techniques are used in this new 2D model: (1) the half structure is divided into several equivalent frames (See Fig. 4-21a, Fig. 4-22a); (2) the slab vertical stiffness in longitudinal direction between adjacent frames is considered; (3) rigid diaphragm assumption is applied in transverse direction of the evaluation structure.

Noted that there is a modification on the shear wall base modeling in this study. The shear wall is modeled by multi-fiber elements (fiber wall base) in order to consider the uplift of the shear wall and the wall real dimension (See Fig. 4-23b, Fig. 4-23c). The

comparison of the fiber wall base and the plastic hinge of the wall used in the previously sections is shown in Appdx. B.10.

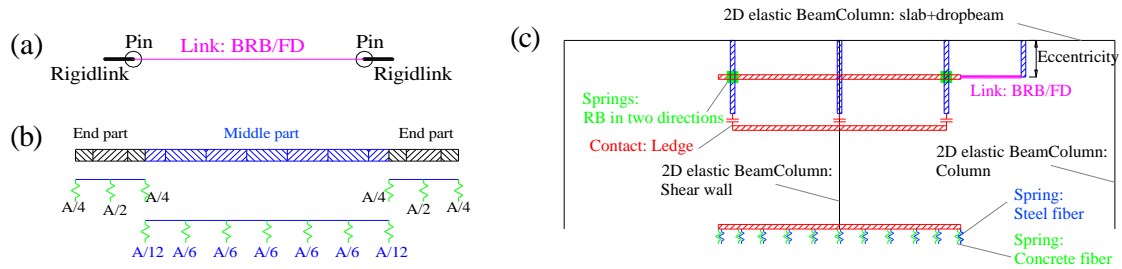


Fig. 4-23. 2D model: (a) IFAS device; (b) wall base; (c) elevation view of first floor.

4.14.2 Analysis Results

This section presents the results from the analysis. The IFAS eccentricity (See Fig. 4-23c) is set to zero in the model. Fig. 4-24a, c indicate that large local pounding force exists between the slab and left/right ledge. The pounding force is independent from the deformable connection types and coefficient of friction between the slab and ledge. Thus, it is difficult to design the slab and ledge due to the large pounding force between the slab and ledge in earthquakes. In addition, larger IFAS eccentricity generates larger moment in slab near the IFAS clevis location (See in Appdx. B.10). Therefore, Cantilever Slab Case is preferred for the controllable force acting in the slab near the LFRS.

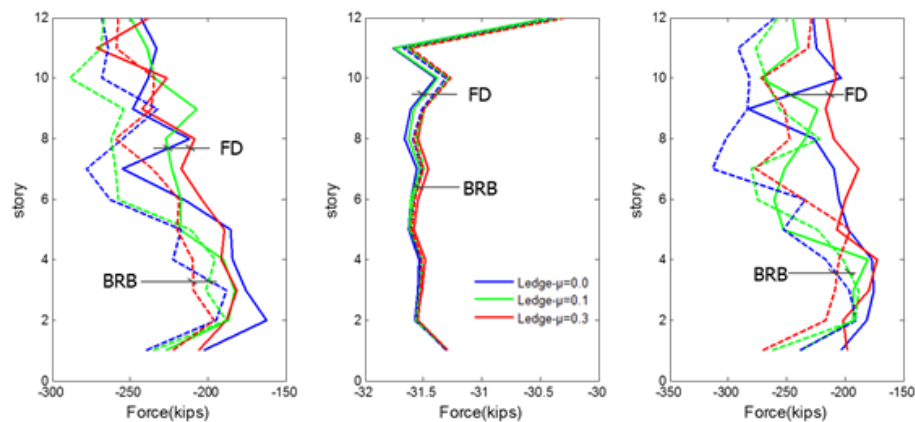


Fig. 4-24. Dynamic pounding force acts on ledge: (a) left; (b) middle; (c) right.

4.14 Effect of Using Relative Displacement Limitation Device

As implied by the results of the analytical study, a very small α cannot be used because it produces large relative displacement and GLRS drift, particularly in the MCE. In order to take advantage of the large response reduction of the usage of the IFAS with small α , an additional device, bumper, is introduced to limit the relative displacement. This device must arrest the motion of the floor without causing a large impact force. The bumper is installed with an initial gap with respect to the wall to allow free motion in the DBE. However, the bumper can engage in the MCE. Different gap sizes were studied to provide insight on the influence to the IFAS performance. The approach of using a very low α in conjunction with the inclusion of a bumper is termed an “aggressive” IFAS design.

Three different gap sizes were used to investigate the IFAS performance. The gap sizes were determined based on the relative displacement in DBE and MCE when no limitation device is used (See Fig. 4-25b). The 2D model is identical to that described in Fig. 4-8b with the exception of the introduction a nonlinear spring element representing the bumper, placed in parallel with the IFAS at each floor (See Fig. 4-25a). The parametric results for this system are shown in Fig. 4-26.

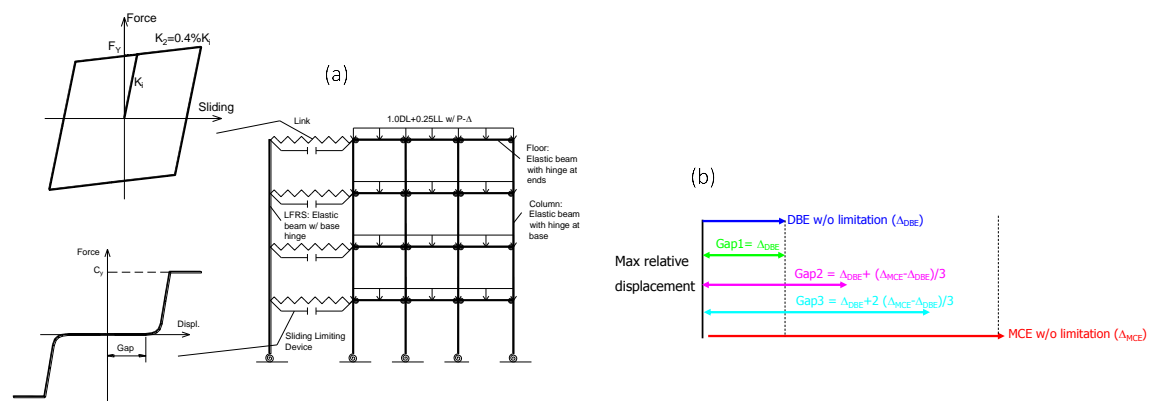


Fig. 4-25. Numerical model: (a) 2D model with bumper; (b) initial gap for the bumper.

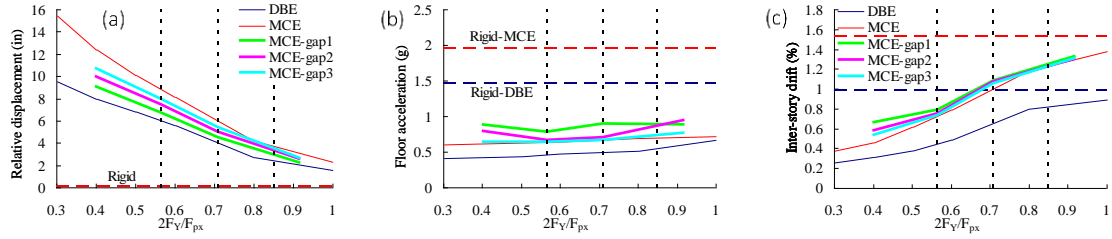


Fig. 4-26. Parametric response: (a) Relative displacement; (b) floor acceleration; (c) LFRS drift.

Fig. 4-26a shows that smaller gap size provides larger reduction in relative displacement. Fig. 4-26b shows that smaller gap size produces larger floor acceleration response, which is a tradeoff of using the bumper. This larger floor acceleration is due to the impact force occurred between the LFRS and floor. Fig. 4-26c shows a slightly increase in the LFRS drift when the bumper is used in the structure.

4.15 Design Space of the FD + RB Combination

The development of the design space is described in this section. The responses of the parametric analyses are re-plotted using the relative displacement as the horizontal axis, for the purpose of developing a preliminary method of designing the IFAS. The reason for plotting this way is to generate a direct relationship between the benefits and tradeoffs of using the IFAS. FD + RB is used in this section as an example of the IFAS for the evaluation structure. Additionally, based on the parametric study from Sec. 4.6 – 4.14, only the cases that the design parameter has large effects on the structure responses are considered in developing the design space: LFRS overstrength, IFAS secondary stiffness, LFRS type, GLRS stiffness, building height. The effect of the LFRS overstrength is shown in Sec. 4.15.1. Effects of the rest of the design parameters are shown in Appdx. B.11.

4.15.1 Effect of LFRS Overstrength

This section will described the relationship between structure responses and relative displacement at different Ω_e . Fig. 4-27 shows the 12-story structure response using LFRS (RC wall) with different Ω_e when $\gamma = 2\%$, in MCE. The conservative and aggressive design limits are denoted as vertical dashed lines.

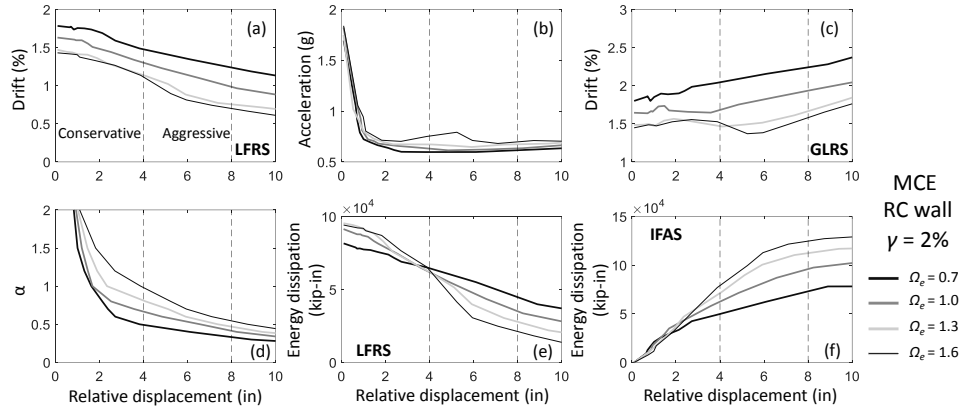


Fig. 4-27. 12-story RC wall structures using LFRS with different Ω_e : (a) LFRS drift; (b) floor acceleration; (c) GLRS drift; (d) α ; energy dissipation: (e) LFRS; (f) IFAS.

Fig. 4-27a shows a nearly linear relationship between the LFRS drift and relative displacement. Fig. 4-27b shows that the floor acceleration is increased as Ω_e increases, however the floor acceleration is reduced significantly after the relative displacement exceeds 1 in for all different Ω_e values. Fig. 4-27c shows that the GLRS drift doesn't exceed the limitation (3%) in ASCE7 [5]. When $\Omega_e = 0.7$, the GLRS drift is increased as the relative displacement increases. When $\Omega_e > 1$, the GLRS drift is increased as the relative displacement increases when the relative displacement is larger than 4 in. Fig. 4-27d shows the relationship between α and the relative displacement, which helps determining the IFAS strength based on the relative displacement. Fig. 4-27e, f show the energy dissipation in the LFRS and IFAS at different relative displacement. Increases in the relative

displacement implies smaller LFRS drift (See Fig. 4-27a) and larger IFAS deformation, therefore the energy dissipation of the LFRS and IFAS is increased and decreased respectively as the relative displacement increases.

4.15.2 Preliminary Design of the IFAS

This section will introduce the preliminary design of the IFAS. Based on the discussions in Section 4.17.1, Sections B.11.1 – B.11.4, the following conclusions can be drawn:

(1) The GLRS drift is always smaller than the 3% limit when the relative displacement is smaller than the aggressive design limit (8"). Therefore, the GLRS drift doesn't need to be considered in the preliminary IFAS design.

(2) The LFRS drift is reduced as the relative displacement increases and this relationship is nearly linear. In order to obtain a good reduction in the LFRS drift, the relative displacement should be large, however without exceeding the design limit.

(3) The floor acceleration undergoes significant reduction and doesn't vary a lot when the relative displacement exceeds 2". A good reduction in the acceleration will be obtained automatically because the relative displacement will be larger than 2" if a good reduction of the LFRS drift is obtained.

(4) The results in Sec. B.11.3 show that the floor acceleration, LFRS drift and α don't vary significantly as the GLRS stiffness changes. Therefore, the influence from the GLRS stiffness can be ignored in the development of the IFAS design space.

Only the LFRS drift and relative displacement need to be considered in the preliminary design of the IFAS. This relationship can provide benefit and tradeoff directly for decision making. And a relationship between α and relative displacement can be used

for determining the IFAS strength. Four design parameters will be considered in the development of the IFAS design space: Ω_e , γ , LFRS type and building height. Only Ω_e and γ are used in developing design space equations since building height and LFRS type is not easy to be quantified.

4.16 Design Equation Development

This section will describe the design equation development of the IFAS. A 12-story evaluation structure with using the RC wall as the LFRS ($\gamma = 2\%$) is taken as an example.

Fig. 4-27a, d are used for the development of design equations based on Sec. 4.1.2 and are replotted in Fig. 4-28. The LFRS drift (Δ_{LFRS}) and the relative displacement (δ_r) is assumed in a linear relationship: $\Delta_{\text{LFRS}} = b_0 + b_1\delta_r$. α and the relative displacement is assumed in a relationship: $\alpha = c_0\delta_r^{c_1}$.

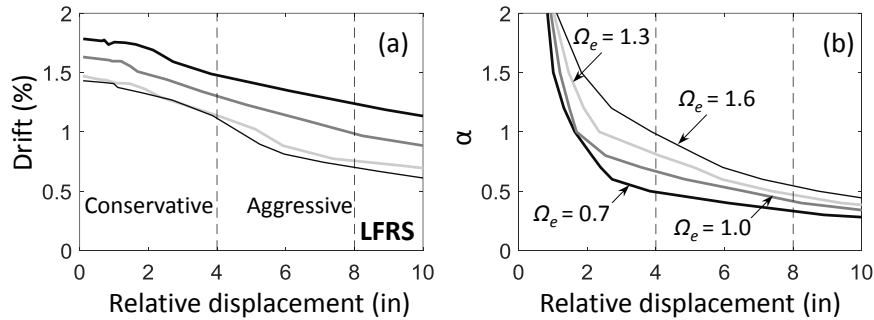


Fig. 4-28. 12-story RC wall structures with different Ω_e : (a) LFRS drift; (b) α .

The regression analysis of the results in Fig. 4-28a is shown Fig. 4-29. Blue circles represent results from numerical analysis. Red lines represent regression analysis results. The figure shows that linear relationship assumption between Δ_{LFRS} and δ_r is acceptable.

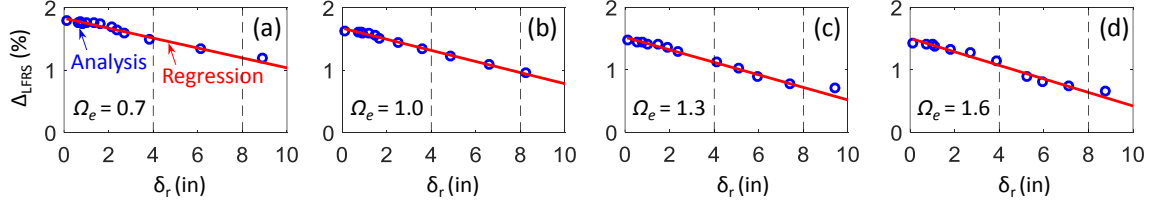


Fig. 4-29. Regression analysis of Δ_{LFRS} and δ_r when Ω_e : (a) 0.7; (b) 1.0; (c) 1.3; (d) 1.6.

The regression analysis of the results in Fig. 4-28b is shown Fig. 4-30. Blue circles represent results from numerical analysis. Red lines represent regression analysis results.

The figure shows that the assumed relationship between α and δ_r is acceptable.

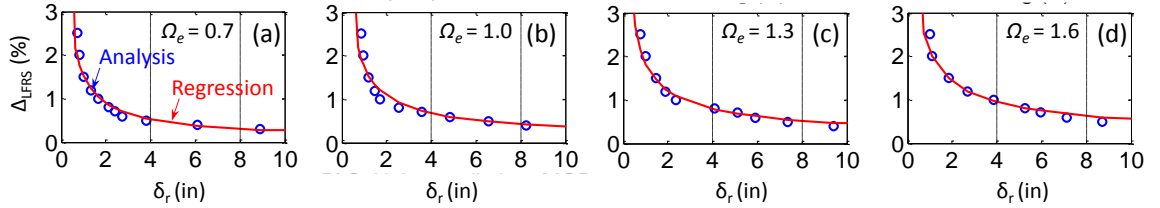


Fig. 4-30. Regression analysis of α and δ_r when Ω_e : (a) 0.7; (b) 1.0; (c) 1.3; (d) 1.6.

The parameters b_0 , b_1 for different Ω_e and γ is shown with different grey scale in Fig. 4-31. Fig. 4-31a shows that b_0 is approximately constant as γ changes for each Ω_e . Fig. 4-31c shows that the slope of b_0 vs. Ω_e changes at $\Omega_e=1.3$. Therefore, linear relationship is assumed between b_0 and Ω_e (See Eqn. 4-1). Fig. 4-31b, d don't show clear trend of b_1 as γ and Ω_e change. Therefore, relationship with cross terms is assumed between b_1 and Ω_e (See Eqn. 4-2).

$$b_0 = n_0 + n_1 \Omega_e \quad (0.7 \leq \Omega_e < 1.3) \quad (4-1a)$$

$$b_0 = n_2 + n_3 \Omega_e \quad (1.3 \leq \Omega_e < 1.6) \quad (4-1b)$$

$$b_1 = q_0 + q_1 \gamma + q_2 \Omega_e + q_3 \gamma^2 + q_4 \Omega_e^2 + q_5 \gamma \Omega_e \quad (4-2)$$

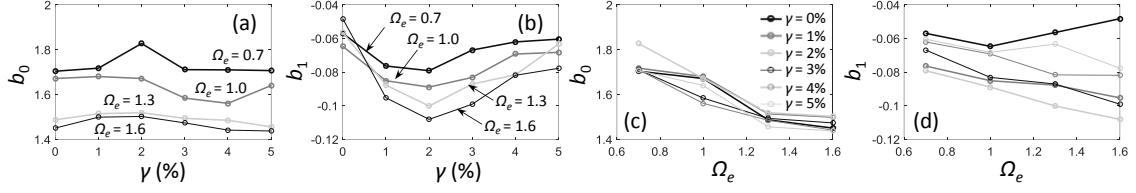


Fig. 4-31. Regression analysis results of b_0 , b_1 vs. γ : (a) b_0 ; (b) b_1 ; vs. Ω_e : (c) b_0 ; (d) b_1 .

The coefficients in Eqns. 4-1, 4-2 are calculated through regression analysis. The prediction equations for b_0 , b_1 are:

$$b_0 = 2.005 - 0.395 \Omega_e \quad (0.7 \leq \Omega_e < 1.3) \quad (4-3a)$$

$$b_0 = 1.602 - 0.084 \Omega_e \quad (1.3 \leq \Omega_e < 1.6) \quad (4-3b)$$

$$b_1 = -0.039 - 1.783\gamma - 0.034\Omega_e + 45.051\gamma^2 + 0.011\Omega_e^2 - 0.426\gamma\Omega_e \quad (4-4)$$

The predicted b_0 , b_1 are shown in different red scale in Fig. 4-32. Coefficients of determination for the b_0 , b_1 are 88.7% and 75.1% respectively.

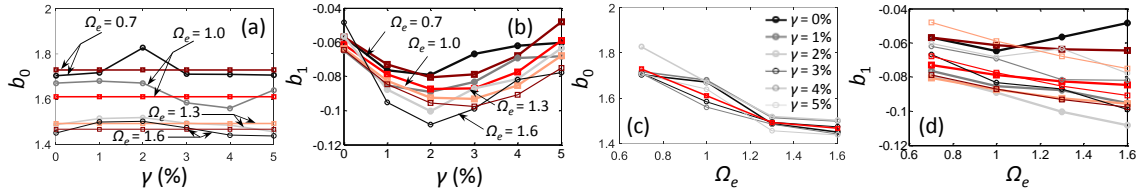


Fig. 4-32. Prediction equation of b_0 , b_1 vs. γ : (a) b_0 ; (b) b_1 ; vs. Ω_e : (c) b_0 ; (d) b_1 .

The parameters c_0 , c_1 for different Ω_e and γ is shown with different grey scale in Fig. 4-33. Fig. 4-33a,b show that c_0 , c_1 are approximately linearly decreased as γ increases for each Ω_e . Fig. 4-33c shows that c_0 is approximately linear increased as Ω_e increase. Fig. 4-33d shows that c_1 is increased quadratically as Ω_e increase. Therefore, the equation of c_0 , c_1 are assumed in the following format:

$$c_0 = n_0 + n_1 \gamma + n_2 \Omega_e \quad (4-5)$$

$$c_1 = q_0 + q_1\gamma + q_2\Omega_e + q_4\Omega_e^2 \quad (4-6)$$

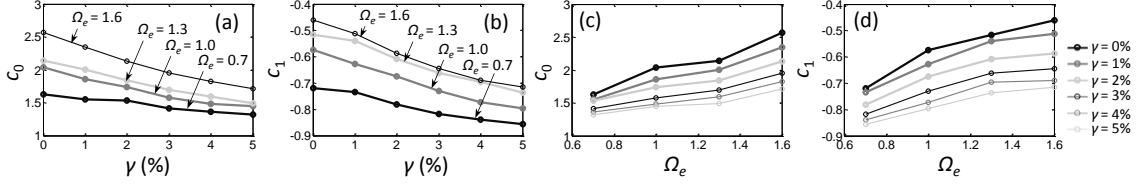


Fig. 4-33. Regression analysis results of c_0 , c_1 vs. γ : (a) c_0 ; (b) c_1 ; vs. Ω_e : (c) c_0 ; (d) c_1 .

The coefficients in Eqns. 4-5, 4-6 are calculated through regression analysis. The prediction equations for c_0 , c_1 are:

$$c_0 = 1.312 - 12.182 \gamma + 0.656 \Omega_e \quad (4-7)$$

$$c_1 = -1.052 - 4.367\gamma + 0.665\Omega_e - 0.196\Omega_e^2 \quad (4-8)$$

The predicted c_0 , c_1 are shown in different red scale in Fig. 4-34. Coefficients of determination for the c_0 , c_1 are 93.0% and 97.2% respectively.

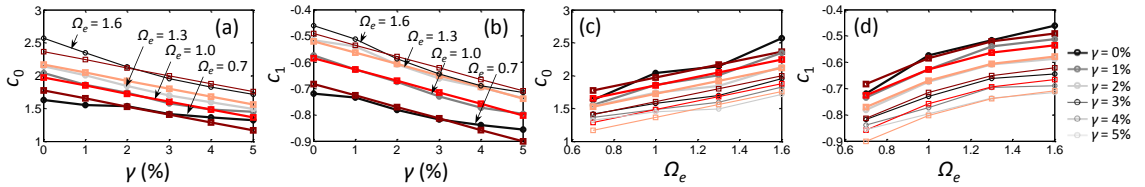


Fig. 4-34. Prediction equations of c_0 , c_1 vs. γ : (a) c_0 ; (b) c_1 ; vs. Ω_e : (c) c_0 ; (d) c_1 .

The design space equations for 12-story RC wall structure are:

$$\Delta_{\text{LFRS}} = 2.005 - 0.395\Omega_e + (-0.039 - 1.783\gamma - 0.034\Omega_e + 45.051\gamma^2 + 0.011\Omega_e^2 - 0.426\gamma\Omega_e)\delta_r \quad (0.7 \leq \Omega_e < 1.3) \quad (4-9a)$$

$$\Delta_{\text{LFRS}} = 1.602 - 0.084\Omega_e + (-0.039 - 1.783\gamma - 0.034\Omega_e + 45.051\gamma^2 + 0.011\Omega_e^2 - 0.426\gamma\Omega_e)\delta_r \quad (1.3 \leq \Omega_e < 1.6) \quad (4-9b)$$

$$\alpha = (1.312 - 12.182 \gamma + 0.656 \Omega_e) \delta_r^{-1.052 - 4.367\gamma + 0.665\Omega_e - 0.196\Omega_e^2} \quad (4-10)$$

Eqn. 4-9 can be used for determining Δ_{LFRS} at a given δ_r . Eqn. 4-10 is used for determining α at a given δ_r .

Similar equations are derived for 4-story and 8-story structure and is shown in Appdx. B.12.

4.17 Conclusions for 2D Evaluation Structure Models

A set of NTHAs are conducted for the purpose of studying the effects to the responses of IFAS structures from different design parameters. The following conclusions can be drawn from this chapter:

(1) The IFAS can effectively reduce the LFRS deformation and floor acceleration in earthquakes, meaning reduce the damage of the structural and nonstructural elements in buildings.

(2) The taller structure includes more contribution from higher modes, the floor acceleration is reduced more significantly after using the IFAS.

(3) The LFRS and GLRS drift are reduced as Ω_e increases. The floor acceleration is amplified as Ω_e increases, however, this amplification is negligible in comparison to the reduction from that of the traditional structure.

(4) The use of the IFAS can produce significant reduction on the floor acceleration and LFRS drift no matter either RC wall or rocking wall is used as the LFRS. However, the rocking wall structure has larger responses than the RC wall structure. The responses of rocking wall structures is increased as the energy dissipation capacity decreases. The variations of the structure responses is decreased as α decreases.

(5) A proper designed α produces smaller floor acceleration and LFRS drift, as well as larger GLRS drift and relative displacement in comparison to those of a traditional structure. However, when a rocking wall is used as the LFRS, floor acceleration, LFRS and GLRS drift can be reduced simultaneously when $0.3 < \alpha < 1$.

(6) The K_i doesn't have significant effect on the IFAS structure responses.

(7) A larger γ implies a larger external force acting on the LFRS, resulting a larger LFRS deformation demand and floor acceleration.

(8) The gravity system stiffness has effects on the floor acceleration and relative displacement, however the effect are not significant. The effect on the wall drift is negligible from the gravity system stiffness.

(9) The gravity system strength has negligible effects on the IFAS structure responses.

(10) A relationship between LFRS drift and relative displacement can be directly used for decision making between the benefit and tradeoff of using the IFAS. And afterwards, a relationship between α and relative displacement can be used for determining the IFAS strength.

(11) Design space equations are developed for the 4-story, 8-story and 12-story structure respectively. The formats of equations are completed and needed to be simplified.

5. 3D NONLINEAR MODEL DEVELOPMENT AND CALIBRATION

A key component of this project is the shake table test that was conducted at NEES@UCSD. A 3D nonlinear model was developed to predict the shake table test. In addition to the test prediction, this 3D model was also used to select appropriate ground motions for the test and provide instrumentation guidelines. After the shake table test, the 3D model was first **updated** using as-built properties, material test results, and improved knowledge of device response. The shake table test specimen underwent progressive damage during the test sequence. Thus, a useful analytical model must be able to capture this progression of damage accurately. If a numerical model can be calibrated to a point in the shake table test sequence using measurements and observations, this calibrated model can be used for providing comparisons with pristine structure more efficiently.

The shake table test is introduced in Section 5.1. The development of the 3D model is described in Section 5.2. The prediction results are shown in Section 5.3. The test specimen responses are shown and discussed in Section 5.4. The calibration process of the numerical model is shown in Section 5.5. The comparison between the numerical models and the test are shown in Section 5.6. Conclusions are summarized in Section 5.7.

5.1 Shake Table Test Introduction

The shake table test specimen design and the test program were accomplished by project collaborators from the University of California, San Diego.

5.1.1 Description of the Shake Table Test Specimen

The shake table test specimen was a half-scale four-story reinforced concrete building structure (See Fig. 5-1). Fig. 5-2 shows the shake table test specimen plan and elevation views. The LFRS was precast unbonded post-tensioned (PT) hybrid rocking wall

(PT wall). The PT wall in the table motion direction was intentionally offset to create an eccentric LFRS layout, to examine the system in coupled translation and twisting. More description about the test specimen is shown in Appdx. C.1.1. The table motion is in the east-west (EW) direction, the transverse direction of the specimen is simplified as NS direction.

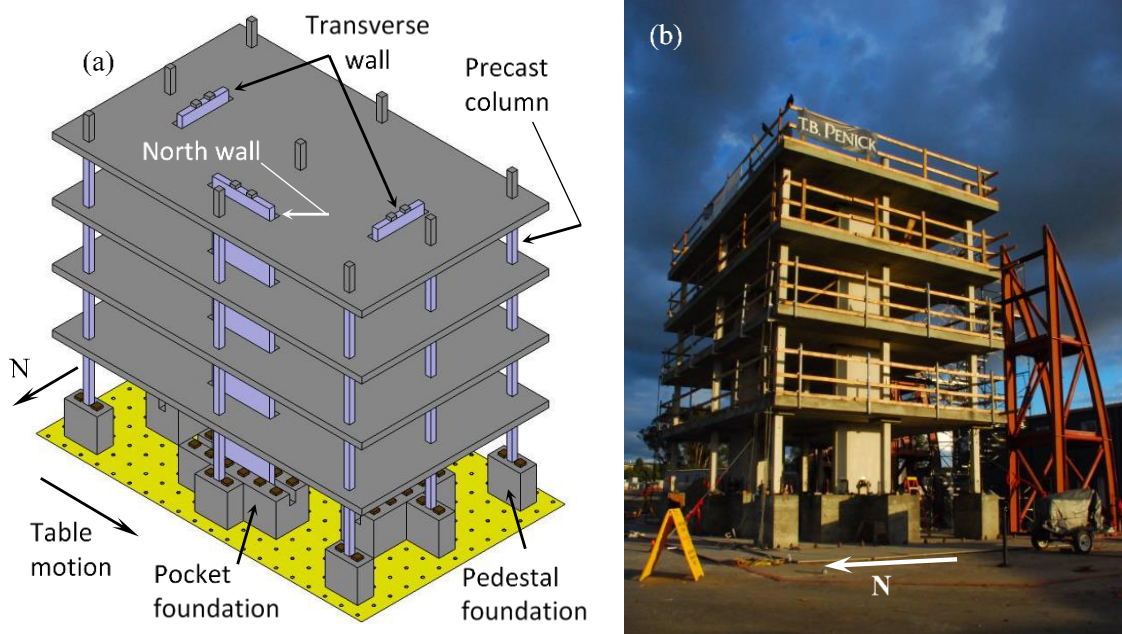


Fig. 5-1. Shake Table Test Specimen: (a) Isometric Model View (Courtesy of Nema Arpit); (b) Photo (northeast view).

The deformable connections of the IFAS were FDs [13] and BRBs [111] in EW and NS direction respectively. The instrumentation of the test specimen is shown in Appdx. C.1.2.

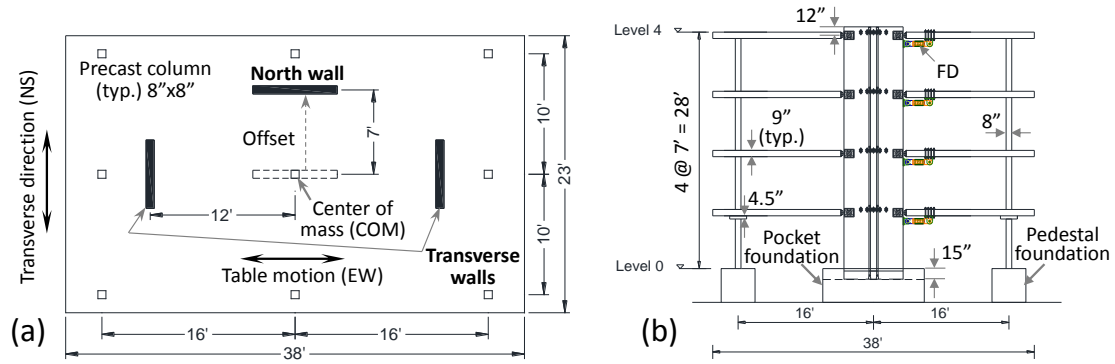


Fig. 5-2. Shake table test specimen: (a) plan view; (b) elevation view.

5.1.2 Design of Shake Table Test Specimen

The shake table test specimen is designed for a SDC E site in downtown Berkeley, California (BE Site). The PT walls used for the test specimen were designed using displacement-based design methods [51, 111]. Fig. 5-3a shows the pushover analysis result for the North wall. Indicated on the curve is the strength of the PT walls at 0.5% and 3% roof (wall tip) drift ($M_{0.005}$, $M_{0.03}$). $M_{0.005}$ is treated as the yield strength of the PT wall. Note that the transverse wall design strength (not shown) is approximately half that of the North wall since there are two transverse walls.

It will be useful to examine the structure in the context of an equivalent lateral force (ELF) design since α is based on F_{px} . A Seismic Response Modification Coefficient $R = 6$ for Special RC Shear Walls [5] is used for this comparison. Accordingly, a horizontal trend line is shown in Fig. 5-3a for the required design strength of the BE site ($M_u = 2291$ kip-ft) for the analogous ELF design. The required design strength ($M_u = 1740$ kip-ft) for a SDC D design in Seattle, WA (SE) is also indicated in the figure.

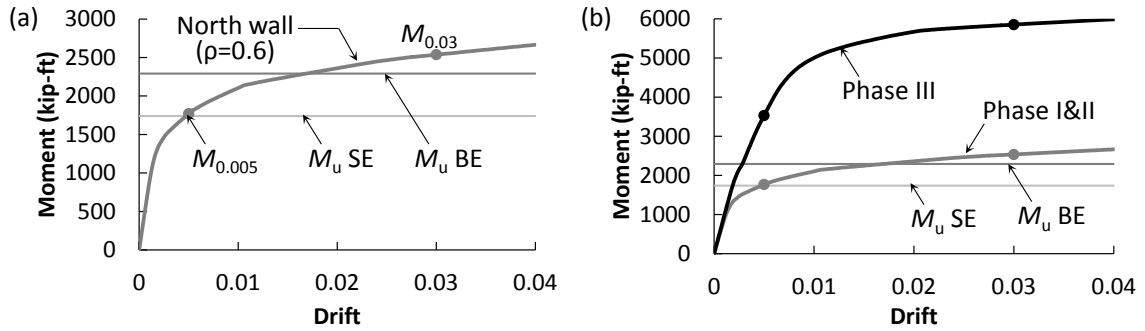


Fig. 5-3. North wall design capacity: (a) Relative to design strength; (b) Phase III Comparison.

The test structure wall and IFAS strength is adjustable. Different wall strengths are possible based on the level of initial prestress in the PT bars. Table 5-1 shows the strengths targeted in the test program, expressed in terms of overstrength relative to design ($M_{0.005}/M_u$), ($M_{0.03}/M_u$), for both the BE and SE sites. The initial prestress level is expressed as a percentage of PT bar ultimate strength (F_{ult}), i.e. $\rho=0.4$ represents $40\%F_{ult}$. The BE design is based on $\rho=0.6$. The fixed-base Phase III shear wall is also included in Table 5-1 and compared to the rocking wall in Fig. 5-3b.

Table 5-1. North wall property (half-scale structure).

Wall strength	$M_{0.005}/M_u$		$M_{0.03}/M_u$	
	BE	SE	BE	SE
$\rho = 0.4$	0.59	0.77	1.04	1.38
$\rho = 0.5$	0.68	0.90	1.09	1.43
$\rho = 0.6$	0.77	1.02	1.11	1.46
$\rho = 0.7$	0.86	1.13	1.12	1.47
Phase III	1.54	-	2.55	-

For the BE site, the diaphragm design force $F_{px}=43.6$ kips, an intermediate ($\alpha = 0.57$) and aggressive ($\alpha = 0.44$) design (See Appdx. C.1.3) result in IFAS limit strengths of 25.0 kips and 19.0 kips respectively. These values correspond to conservative ($\alpha = 0.76$) and intermediate ($\alpha = 0.57$) design for the SE site ($F_{px}=33.1$ kips). Thus 25 kips ($\alpha = 0.57$) and

19 kips ($\alpha = 0.43$) were selected for IFAS design strength. The target relative displacement between the floors and the PT wall of the half scale building is 2in based on the evaluation structure analysis. The RB stiffness is calculated based on a ratio (0.76) between the RB force and F_y at target relative displacement (1.2in). The RB is designed based on $\alpha=0.57$ for Berkeley site and its stiffness is not adjustable during the shake table test. The IFAS design is shown in Table 5-2.

Table 5-2. IFAS design for the shake table test.

Direction	Site	F_{px} (kips)	α	IFAS limit strength [†] (kips)	RB force @ 1.2in (kips)	# RB	IFAS strength @ 1.2in (kips)
EW	BE	43.6	0.57	25.0	2.9	4	36.4
			0.44	19.0	2.2		27.7
	SE	33.1	0.75	25.0	2.9	4	36.4
			0.57	19.0	2.2		27.7
NS	BE	43.6	0.44	(2@) 9.6	1.1	4	13.7
	SE	33.1	0.58	(2@) 9.6	1.1	4	13.7

[†] includes RB force at deformable connection limit strength: 0.02kip for FD; 0.14kip for BRB.

Fig. 5-4 shows the IFAS nominal strength as design backbone curves, showing the contribution of different components to the IFAS strength. Fig. 5-4a shows the EW and NS IFAS characteristic over the deformation demand range expected in the DBE. As seen, the FD is much stiffer than the BRB in the elastic range. The contribution of the RB at the IFAS design strength is fairly negligible. However, this contribution becomes important at the DBE target displacement, representing the elastic restoring of the IFAS. Fig. 5-4b shows the IFAS characteristics extended to the MCE deformation limit. Bumper gap is set to the DBE target displacement. As seen, the bumper gradually picks up force in an increasing rate, arresting the floor relative displacement by the MCE deformation limit.

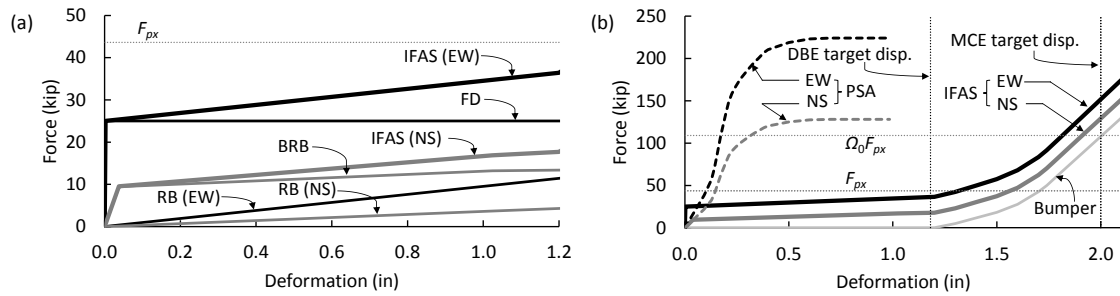


Fig. 5-4. IFAS backbone characteristic curves (at half-scale) targeted for: (a) DBE; (b) MCE.

5.1.3 Ground Motions

Two ground motions were used for this shake table test, which are listed in Table 5-3. SE and BE represent the ground motion for SE site and BE site respectively. Fig. 5-5a and Fig. 5-5b show the time history of these two ground motion records. Fig. 5-5c shows the BE and SE response spectrum in comparison to the relative design spectrum. The structural 1st and 2nd period, T1 and T2, are indicated in Fig. 5-5c.

Table 5-3. Ground motions used in the test².

EQ ID	Earthquake	Station	Component	Magnitude	Scale factor	Scaled PGA (g)
SE	1979 Imperial Valley	El Centro Array #5	140	6.5	1.14	0.59
BE	1989 Loma Prieta	LGPC	000	6.9	0.72	0.41

² <http://ngawest2.berkeley.edu/>

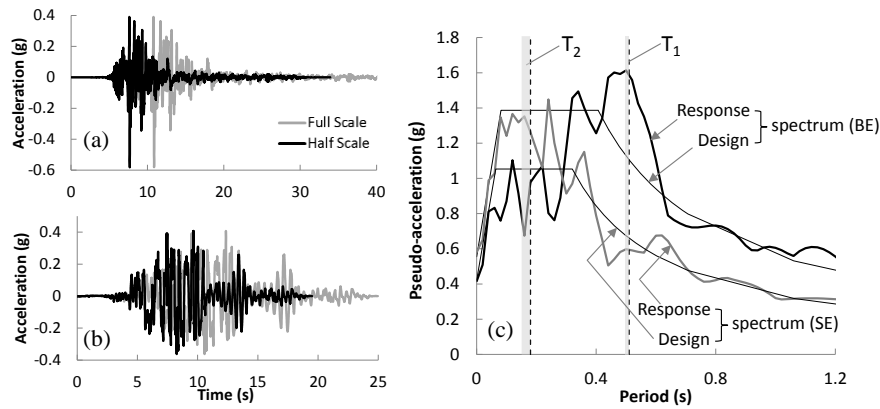


Fig. 5-5. DBE level: (a) SE time history; (b) BE time history; (c) Response spectrum.

5.1.4 Test Program

In this shake table test, three test phases were executed:

In Phase I, an IFAS structure with different PT ratio and IFAS strength was tested.

In Phase II, a special steel anchorage device (PSA³) was installed on the structure for constraining the relative horizontal displacement between the floors and the PT wall. Roller bearing was added to increase the rigidity between the floors and the PT wall (North wall) in the table motion direction.

In Phase III, the base of three PT walls was grouted, so that the wall behaves like a traditional cast in place shear wall.

A detailed test protocol for the shake table test is shown in Table 5-4. The test excitation involved: (1) Low-amplitude white noise motions and (2) strong ground motions, representing DBE and MCE for the BE and SE sites. A BE service (SVC) record was performed in the early stages to incrementally load the structure. The MCE and SVC amplitudes are obtained by scaling the DBE by 150% and 67%, respectively. The white

³ JVI Inc. 7131 North Ridgeway Ave Lincolnwood, IL 60712.

noise motions were applied to the structure typically before and after each day's test protocol. The motion name and intensity, the average measured wall PT ratio, ρ , and α are listed for each test. α value listed in the table is an average over the four floors.

Table 5-4. Shake table test sequence.

	TEST #	Motion name	Intensity	Wall PT Ratio (EW/NS)	α (EW)		TEST #	Motion name	Intensity	Wall PT Ratio (EW/NS)	α (EW)
Phase I	1-W1	WN	0.03g (RMS)	0.61/0.60 [†]	0.24	Phase II	1-W10	WN	0.03g (RMS)	0.60/0.66	0.43
	Test 1	Berkeley	SVC	0.61/0.60 [†]	0.24		Test 13	Berkeley	DBE	0.60/0.66	0.43
	1-W2	WN	0.03g (RMS)	0.61/0.43	0.45		Test 14	Berkeley	MCE	0.59/0.65	0.44
	Test 2	Berkeley	SVC	0.61/0.43	0.45		1-W11	WN	0.03g (RMS)	0.56/0.65	0.44
	Test 3	Seattle	DBE	0.61/0.43	0.59		2-W12	WN	0.03g (RMS)	0.63/0.70	PSA + damper
	Test 4	Berkeley	DBE	0.61/0.42	0.45		Test 15	Seattle	DBE	0.64/0.71	
	1-W3	WN	0.03g (RMS)	0.61/0.42	0.45		Test 16	Berkeley	SVC	0.59/0.71	
	1-W4	WN	0.03g (RMS)	0.49/0.41	0.61		Test 17	Berkeley	DBE	0.64/0.64	
	Test 5	Berkeley	SVC	0.49/0.42	0.61		2-W13	WN	0.03g (RMS)	0.64/0.63	PSA + roller bearing
	Test 6	Seattle	DBE	0.49/0.41	0.83		2-W14	WN	0.03g (RMS)	0.61/0.63	
	Test 7	Berkeley	DBE	0.49/0.41	0.61		Test 18	Berkeley	DBE	0.60/0.62	
	1-W5	WN	0.03g (RMS)	0.49/0.41	0.61		2-W15	WN	0.03g (RMS)	0.56/0.60	
	1-W6	WN	0.03g (RMS)	0.50/0.42	0.41	Test 19	Berkeley	MCE	0.46/0.70		
	Test 8	Berkeley	DBE	0.50/0.42	0.41	2-W16	WN	0.03g (RMS)	0.46/0.70		
	Test 9	Seattle	MCE	0.50/0.42	0.56	Phase III	3-W17	WN	0.03g (RMS)	0.45/0.70	Traditional wall
	Test 10	Berkeley	MCE	0.50/0.42	0.42		Test 20	Berkeley	DBE	0.45/0.70	
	1-W7	WN	0.03g (RMS)	0.42/0.42	0.42		3-W18	WN	0.03g (RMS)	0.47/0.70	
	1-W8	WN	0.03g (RMS)	0.60/0.62	0.55		Test 21	Berkeley	MCE	0.52/0.71	
	Test 11	Berkeley	DBE	0.59/0.62	0.55		Test 22	Berkeley	MCE	0.63/0.70	
	Test 12	Berkeley	MCE	0.59/0.62	0.56		3-W19	WN	0.03g (RMS)	0.64/0.71	
	1-W9	WN	0.03g (RMS)	0.53/0.62	0.56		WN = white noise. WN intensity is root mean square value. † indicates expected PT ratio, measurement not applicable.				

5.1.5 Floor Anchorage Layouts

The shake table test specimen had to be designed to allow modification of the floor diaphragm connection from the IFAS in Phase I to one simulating a traditional floor anchorage (e.g. dowel bars that provide a highly stiff and strong connection) for Phases II and III. This objective was complicated by the presence of the moat required for the IFAS.

Fig. 5-6a shows a photo of a typical floor of the test specimen for Phase I (IFAS structure). The location of the IFAS devices are indicated on the underside of the upper floor shown. Detail views of these devices (FDs, BRBs, RBs⁴, and bumpers⁵) were provided in Fig. 5-7 and Fig. 5-8. Note FDs acted on the North wall (table motion direction) and BRBs acted on the transverse walls. The bumper was installed with a predefined gap, $g_0=1.2\text{in}$. The bumper can be compressed at least 0.675in .

The location of the anchorages devices subsequently connected for Phases II, III are indicated on the lower floor visible in Fig. 5-6a. The PSA was used to connect the floors to the walls in order to simulate the traditional structure as mentioned previously. The PSA involves threaded dowels (“straps”) that are inserted into spring-loaded nuts that ride in vertical slots (“inserts”) precast into the wall elements. The diaphragm connection is completed by welding the flat end of the threaded rods to embed plates in the slab. The PSA transfers horizontal forces from the slab to the wall, however permits relative vertical movement of the wall with respect to the slab.

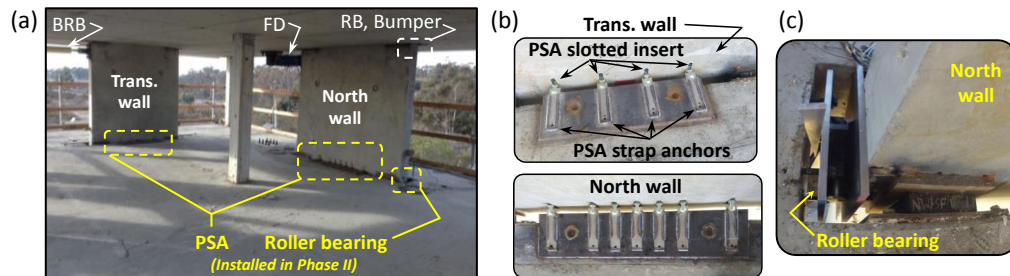


Fig. 5-6. Floor anchorages for typical floor: (a) device locations; (b) PSA; (c) roller bearing.

⁴ DYMAT™ Construction Products, Inc. PO Box 834, Solana Beach, California 92075.

⁵ Pleiger Plastics Company. P.O. Box 1271 - 498 Crile Road Washington, PA, 15301-1271.

Fig. 5-6b shows the fully-completed PSAs on the North wall (7 each face, each level) and transverse wall (4 each face, each level). Standard PSA 2in \times 3/8in straps were used with 6035 inserts⁶. The PSA strength and stiffness depends on the free span length of the strap between the wall face and the floor weld. A nominal design eccentricity of 2in was chosen resulting in a design strength of 14.2kip and a design stiffness of 49kip/in.

The PSA/moat configuration was found not to produce a completely rigid anchorage. Thus, tight-fitting roller bearings (See Fig. 5-6c) were introduced in the moat region between the North wall end and the slab for the final two Phase II tests and all the Phase III tests. These bearings provided a direct load transfer to the wall, therefore supplementing the PSA horizontal stiffness. It is also noted that the FDs and BRBs were left in place in Test 15 – Test 17 for the purpose of connecting the PT walls and slab as a secondary protecting system in case the PSA failed in the test.

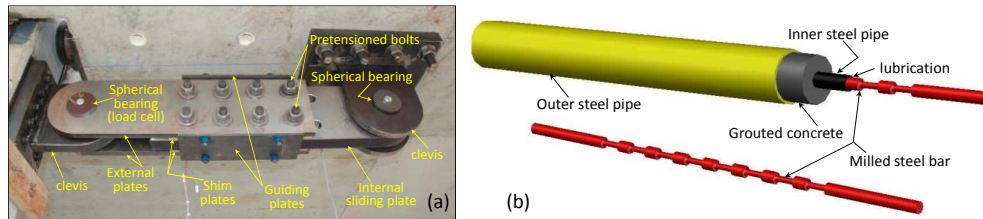


Fig. 5-7. Deformable connection: (a) annotated FD photo; (b) BRB schematic drawing.

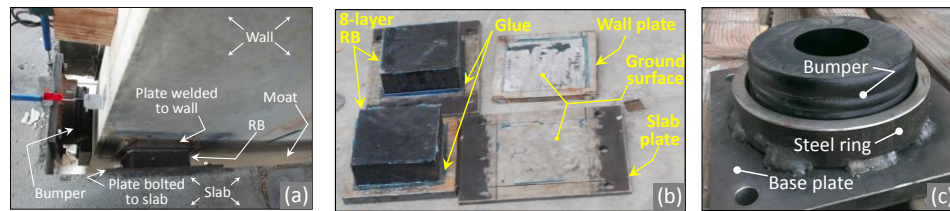


Fig. 5-8. Restoring and limitation devices: (a) specimen layout; (b) RB assembly; (c) bumper.

⁶ JVI Inc. www.jvi-inc.com.

5.2 Analytical Modeling of the Test Specimen

Three numerical models were used in the pristine model development phase. **Initial model** was the first model built for the shake table test specimen. Columns and slabs are pin connected and there is no moment resistance from the column-slab joints. **Prediction model** was the model modified from the Initial model with two main changes: (1) nonlinear fiber layers (NF) (see Fig. 5-13 later) were added to the column ends for modeling the nonlinear behavior; (2) material was updated based on the test specimen nominal strength. **Updated model** is the model updated from the Prediction model using measured device behavior in the shake table test: (1) modify the force-deformation of the devices (FD, BRB, ED) by measurements from the shake table test; (2) modify the concrete material constitutive curve property by measurements from cylinder tests; (3) modify the weight of the specimen by measurements from the shake table equipment; (4) use Mander Confined Concrete Model [126] to model the confined concrete for improving confined concrete accuracy. As opposite to the Initial model, column-slab joints in the Prediction model and Updated model provide moment resistance because of the use of the NF. Table 5-5 shows the descriptions of the three numerical models.

Table 5-5. Description of model development

Model	Column-slab joint	Concrete strength	Confined concrete	FD	BRB	ED	PT bar
Initial (IM)	Pin	5ksi ^[1]	Modified Kent-park [110]	Initial Design			Material test provided by manufacturer
Prediction (PM)	NF	7ksi ^[2]					
Updated (UM)	NF	6.5, 8.9, 9.5ksi ^[3]	Mander	Shake table test measurements			Existing test data ^[4]

[1] Based on nominal strength of prototype structure.

[2] Based on nominal strength of shake table test specimen.

[3] Based on concrete cylinder test (01-16-2014). 6.5ksi, 8.9ksi and 9.5ksi for column, North wall and transverse walls respectively.

[4] [127].

*Note: Initial model is used as **IM** later, Prediction model is used as **PM** later, Updated model is used as **UM** later.*

Fig. 5-9 shows the concrete material stress-strain assigned to the columns and the PT walls separately. The confined concrete model was initially estimated with using Modified Kent-Park Model [110], then Mander model [126] was adopted to estimate the confined concrete for improving confined concrete accuracy as mentioned previously.

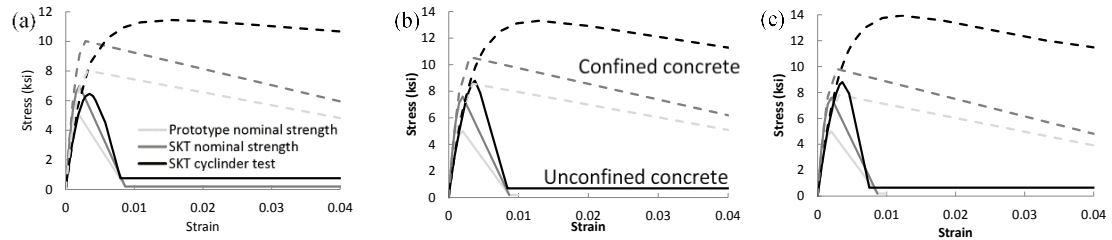


Fig. 5-9. Concrete property: (a) column; (b) North PT wall; (c) NS PT wall.

A 3D nonlinear numerical model of the shake table test specimen is created using the general purpose finite element program ANSYS (See Fig. 5-10).

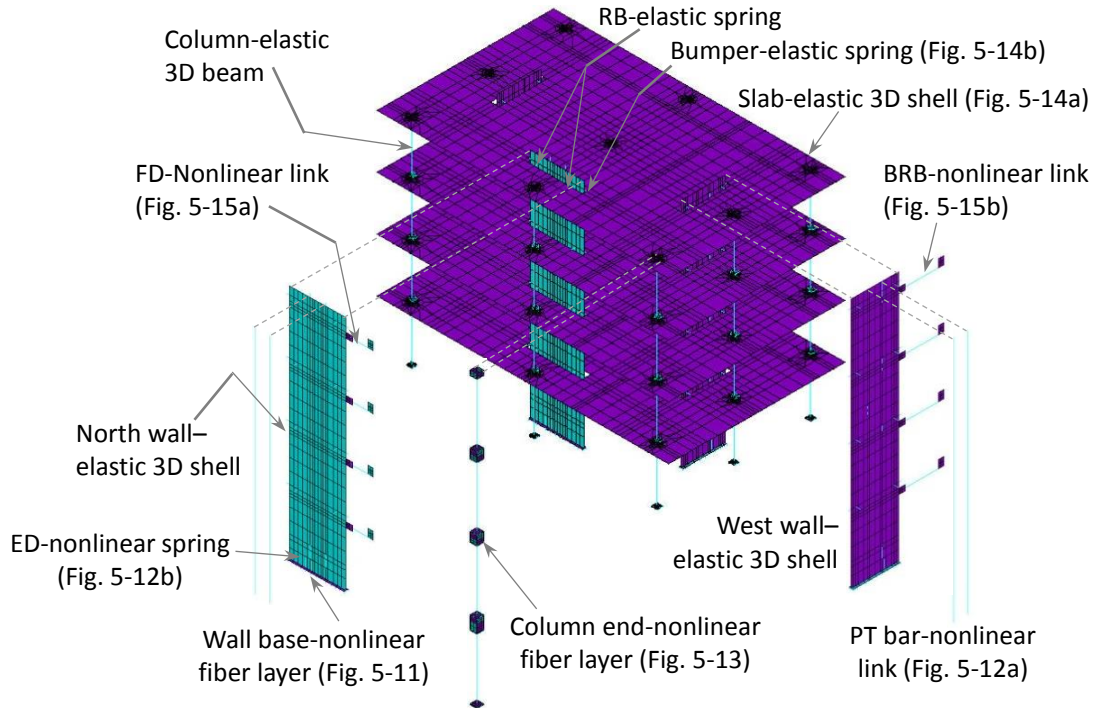


Fig. 5-10. Shake table test model in ANSYS for Phase I.

The model replicates the half-scale test specimen, thus all results are directly compared to unscaled shake table test results. The model used measured mass with reinforced concrete density in slabs, shear walls and columns. P-Delta effect is also considered. The details of the modeling of each component can be found in the following sub-sections.

5.2.1 PT Wall

PT walls are modeled with elastic 3D shell elements with assuming concentrated nonlinear behavior at the base. The shell elements possess uncracked concrete properties due to the low damage incurred in the body of the PT wall. The nonlinear behavior is modeled with a NF at the wall base. The NF is an array of nonlinear link elements (to model concrete crushing) in series with contact elements (to model uplift) at the base (Fig. 5-11b). Each combination of a nonlinear link and connected contact element is termed a concrete fiber model in this dissertation. The cross section of each nonlinear link is determined by the tributary area. In Fig. 5-11a, red and blue dots represent concrete fiber models with confined and unconfined concrete properties respectively.

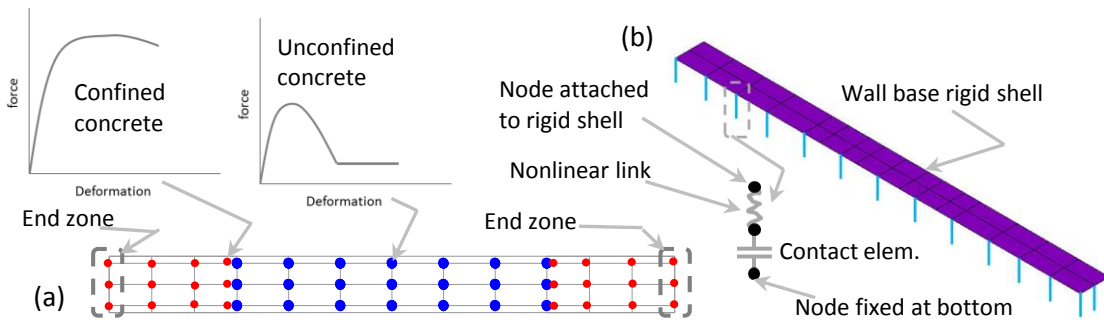


Fig. 5-11. PT wall base model: (a) nonlinear link distribution and property; (b) NF.

Fig. 5-12 shows the PT bars stress-strain constitutive and ED force-deformation behavior. The PT bar stress-strain of the North wall and transverse walls is available online

from the manufacturer. A test data for the same type of the transverse wall PT bar is applied to the numerical model [127]. PT bars are unbonded and modeled by nonlinear link element with kinematic strain hardening hysteretic rule. Initial strain is used to apply the post-tension force. The relative horizontal movement between PT bars and PT walls is constrained to zero while the relative vertical movement is released.

ED is modeled by nonlinear spring element. The initially assumed ED model was stiffer than the ED used in shake table test. Then ED property was updated with the test results.

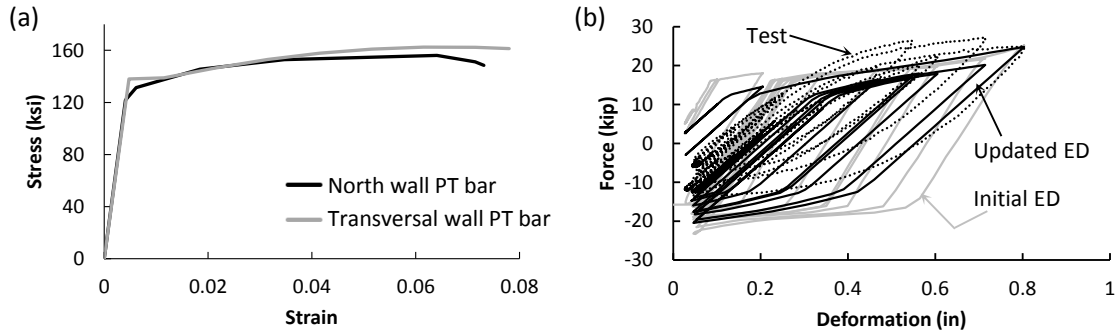


Fig. 5-12. Component behavior: (a) PT bars constitutive; (b) ED hysteresis.

5.2.2 Precast Concrete Columns

The precast concrete columns are modeled by elastic 3D beam elements with NF at both ends. The elastic beam element is assigned with cracked-reinforced concrete property, where the moment of inertial is 70% of the gross section [122].

Fig. 5-13a shows the nonlinear link element distribution at the column cross section. The black and grey dots in Fig. 5-13a represent concrete fiber models with confined and unconfined concrete properties. The concrete material stress-strain property is shown in Fig. 5-9a. Fig. 5-13b shows the NF details (only one elastic shell element is shown). Fig. 5-13c shows the reinforcing steel and the assigned stress-strain relationship. One

reinforcing steel is located in the middle of the cross section. The reinforcing steel is modeled by two parallel nonlinear link elements (for modeling reinforcing steel stress-strain behavior, termed steel fiber model) in series with one nonlinear spring element (for modeling reinforcing steel bond slip behavior) (See Fig. 5-13b). The two nonlinear link elements are different (See Fig. 5-13c): (1) one element is used to model the pseudo large stiffness of the steel that will be degraded to a low strength (2% of the tensile strength, 3.12 ksi) after yielding (stiff steel element); (2) the other is used to model the ordinary steel nonlinear behavior (ordinary steel element). The Young's modulus of the stiff steel element (when the stress is lower than the yield stress) is increased 257 times to eliminate the excessive flexibility contribution to the column from the steel model in elastic range. The steel bond slip force-deformation backbone is calculated based on a method proposed by [124].

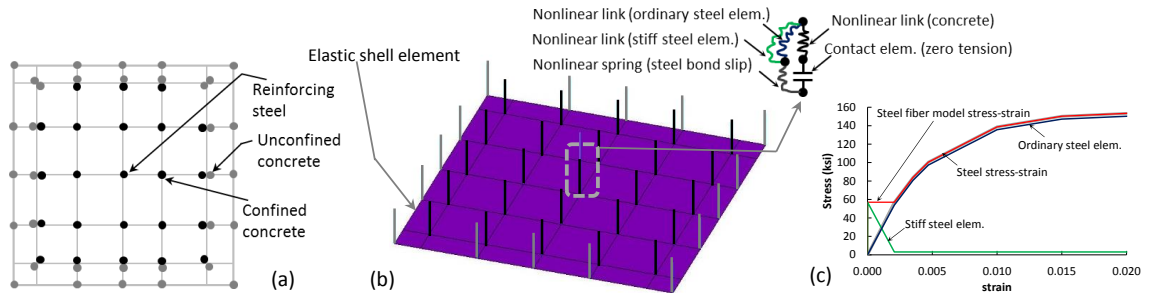


Fig. 5-13. Precast column model: (a) nonlinear link distribution; (b) NF; (c) steel stress-strain.

5.2.3 Slab

The slab is modeled by elastic 3D shell elements with cracked-reinforced concrete property, where the material elastic modulus is 25% of un-cracked concrete [122]. Rigid shells (elastic shells with high bending stiffness) are used to model the slab profile where needed to get proper interface locations (See Fig. 5-14a).

Fig. 5-14a shows the slab mesh in the region of the North wall. Slab mesh is not regular because many devices are installed in a small region (near PT wall) on the slab.

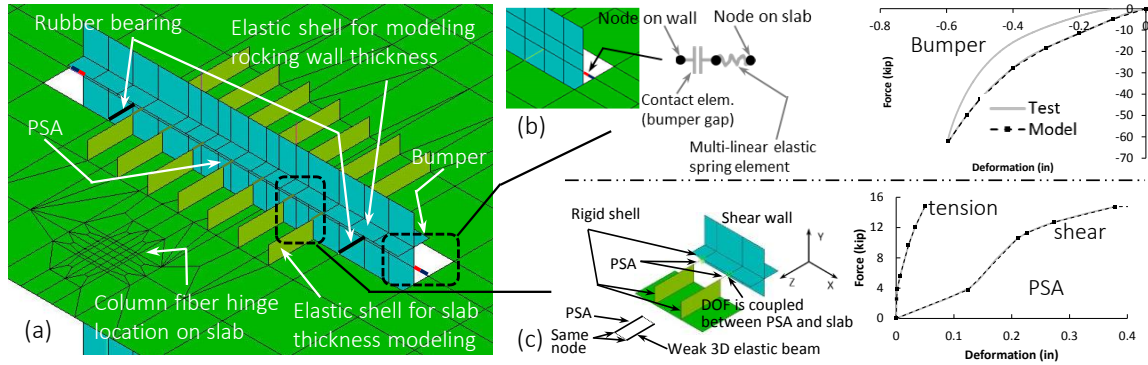


Fig. 5-14. Model: (a) near North wall; (b) bumper model and force-deformation property; (c) PSA model and force-deformation property.

5.2.4 Anchorage Device

The FDs are modeled with nonlinear link element and assigned with the FD force-deformation properties (kinematic strain hardening rule).

The BRBs are modeled with nonlinear link element and assigned with the BRB force-deformation properties (Chaboche kinematic hardening).

Fig. 5-15 shows the force-deformation properties of FD and BRB.

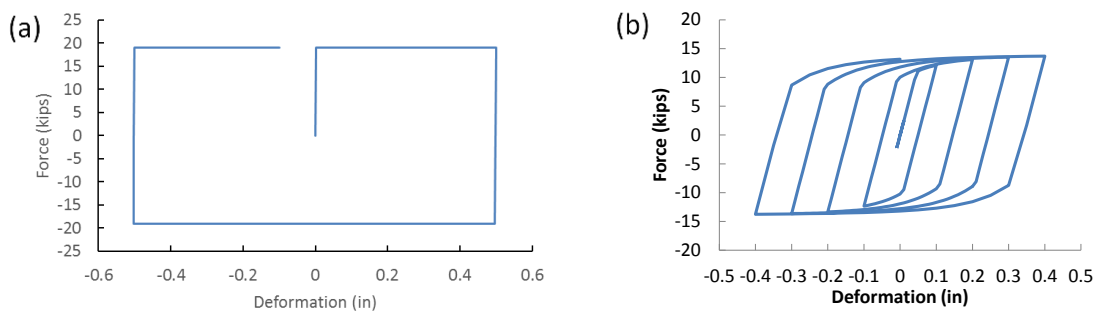


Fig. 5-15. Deformable connection force-deformation property: (a) FD; (b) BRB.

The RBs are modeled with three uncoupled elastic springs for the horizontal, vertical shear and axial properties.

The bumper is modeled by one dimensional multi-linear elastic spring in series with a contact element (for ignoring tension). The bumper model detail and bumper force-deformation property are shown in Fig. 5-14b.

The PSA is modeled with two parallel nonlinear spring elements (for modeling the PSA shear and tensile properties, [125]) in parallel with a weak elastic 3D beam element (for holding the PSA element in position in Phase I). Rigid shells are used to model the slab and wall profiles. Translational degree of freedoms (DOF) in horizontal directions (X and Z in Fig. 5-14c) are coupled between the PSA and rigid shell of the PT wall in Phase II. The PSA model detail and the PSA shear and tension force-deformation properties are shown in Fig. 5-14c.

5.3 Analytical Prediction Results

Three test phases were conducted in the shake table test. Since Phase I and Phase II were direct comparisons between using the IFAS and traditional floor anchorage, the analytical prediction was performed only for these two phases.

The analytical model used for the prediction is the Prediction model mentioned in Section 5.2. The ground motions used in the prediction was the same as planned for the test (See Table 5-3). The applied ground motion magnitudes are SVC, DBE, MCE.

Fig. 5-16 shows the north wall base rotation prediction in different ground motions and different magnitudes. This figure includes two sets of North wall PT ratio: 0.6 and 0.45. This figure shows that using IFAS is able to obtain the shear wall deformation reduction. More prediction results of SE and BE can be found in Appendix C.2.

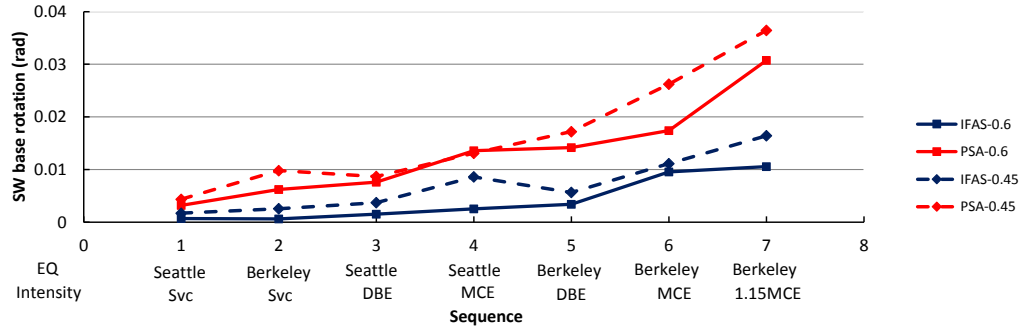


Fig. 5-16. Sequence prediction - North wall base rotation.

5.4 Response Comparison of the Shake Table Test

The shake table test results in the three phases were compared to investigate if the IFAS reduces the floor acceleration and the LFRS deformation in earthquakes. Four pairs of tests in Phase I and Phase II are selected to accomplish this comparison: Test 3 and 15 (SE DBE), Test 2 and 16 (BE SVC), Test 11 and 17 (BE DBE), Test 12 and 19 (BE MCE). In the plots, the Phase I (IFAS structure) responses are in red; the Phase II (traditional structure) responses are in blue. Note that Test 20 (BE DBE) and Test 21 (BE MCE) are used for the acceleration comparison in this section and plotted in green (representing test from Phase III).

5.4.1 Modal Property and Structure Strength

Fig. 5-17 shows a plot of test structure fundamental period over the entire shake table testing program. The period was calculated using white noise test response by applying the transfer function between the floor acceleration records and the foundation acceleration record. The period lengthening indicates softening of the structure due to cumulative structural damage. There were four major retrofits or specimen transitions that partially restored the structural stiffness: (1) replacement of damaged EDs at the PT wall base with new EDs after Test 10; (2) installation of PSAs after Test 14 to initiate Phase II;

(3) insertion of roller bearings between the North wall and floor to increase the horizontal rigidity of the Phase II diaphragm anchorage; and, (4) grouting of the PT wall base to create a fixed-base condition for Phase III. It is impossible to repeatedly test the exact same structure, but these measures permitted specimens in the period range of 0.55-0.70s for major portions of each phase.

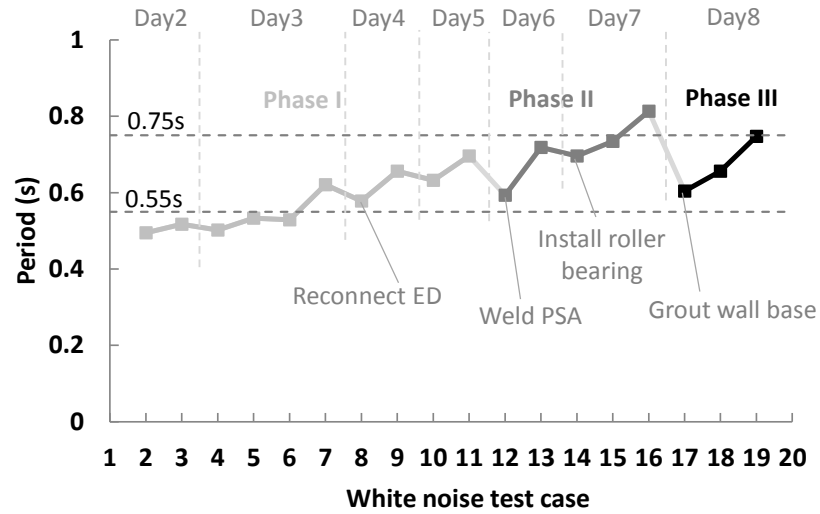


Fig. 5-17. Structure fundamental period change.

The test structure underwent unavoidable damage in earthquakes, therefore, the ρ value of the North wall was increased from 0.49 to 0.64 from Test4 to Test19 in an attempt to reduce the effects of structure softening, for the purpose of stabilizing the North wall strength (Refer to Table 5-4). Fig. 5-18a shows the change of the moment strength of the structural overturning, North wall and GLRS when the North wall base rotation is near 0.005 rad. The moment shown in Fig. 5-18a is the maximum moment when the North wall base rotation lies in the following two ranges: (0.0045, 0.0055) and (-0.0055, -0.0045). North wall base rotation from Test1 to Test4 was smaller than 0.005 rad. The moment of the structure in Test 4 is obtained by extrapolation and shown using dashed line. The North

wall base rotation from Test1 to Test3 was much smaller than 0.005 rad, therefore the moment of the structure isn't calculated by extrapolation. Note that the North wall negative moment in Test 6 is also obtained from extrapolation due to small wall base rotation. The North wall design strength ($\rho=0.6$) from a push-over analysis is shown as horizontal dashed lines. This figure shows that the North wall strength has negligible variations from Test5 and a significant strength drop can be observed from Test4 to Test5. Fig. 5-18a also indicates strength degradation of the GLRS along the test sequence.

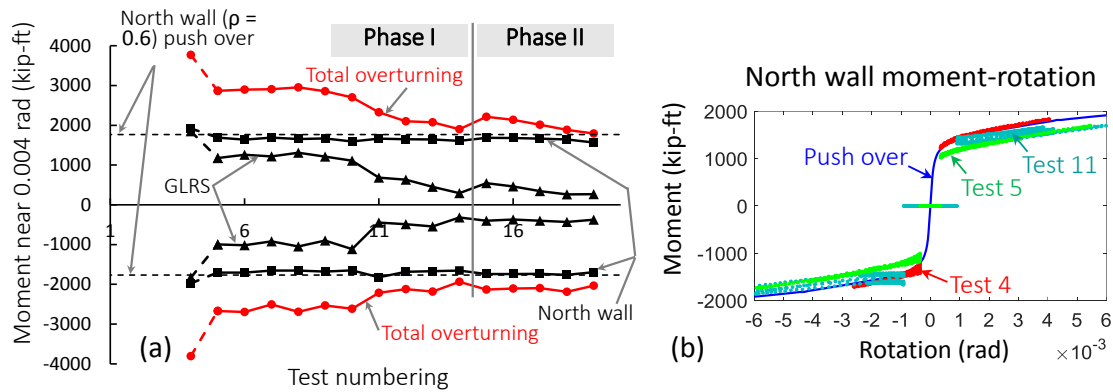


Fig. 5-18. Structure property change: (a) fundamental period; (b) moment strength (EW).

Fig. 5-18b shows a comparison between the North wall moment-rotation between the pushover analysis and selected test responses. It shows that the pushover response matches the Test 4 well. The wall strength at Test 5 and Test 11 was similar to each other, and was smaller than that of the pushover analysis.

5.4.2 Structural Responses

The test structure responses in the shake table test will be compared and summarized in this section. The notations that will be used in this section are introduced in Appdx. C.3. The methodologies on calculating the structure response and the related verification are also provided in Appdx. C.3

First, consider the LFRS response, as expressed by wall base in-plane rotation. Fig. 5-19 compares the North wall base rotation time histories for Phases I and II. The results indicate significant LFRS response reduction in the table motion direction for the IFAS structure relative to the traditional structure for the first three demand levels. Note that the North wall response reduction was not as significant in the BE MCE (See Fig. 5-19d), as will be explained.

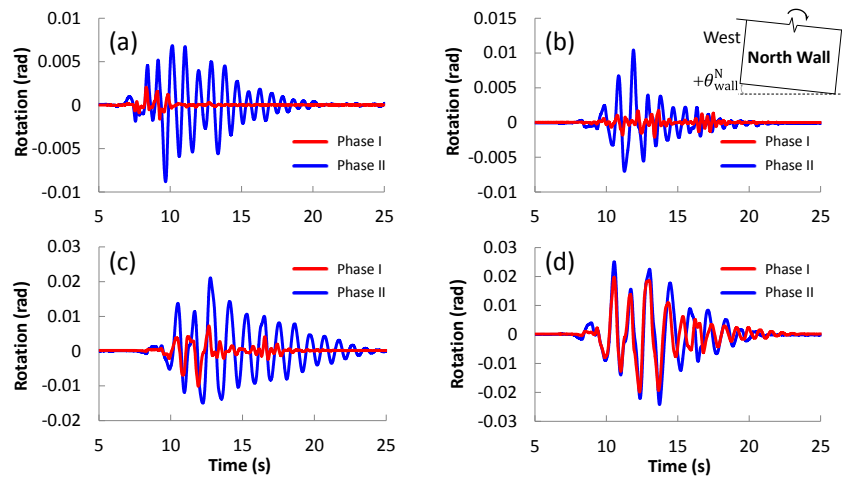


Fig. 5-19. North wall base in plane rotation: (a) SE DBE; BE: (b) SVC; (c) DBE; (d) MCE.

Fig. 5-20 shows the base rotation comparison for Phase I and II, this time for the (west) transverse wall. The plot indicates similar transverse wall response for IFAS and traditional structures at lower demand, but a significant response reduction in the IFAS structure for the two strongest motions (See Fig. 5-20c,d). These results imply the dominance of a torsional mode in stronger earthquakes, with the torsional response of the traditional structure much greater.

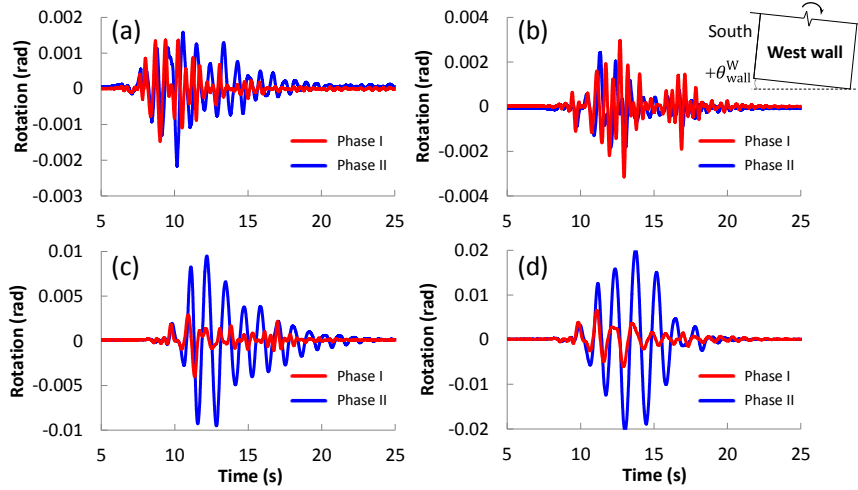


Fig. 5-20. West wall base in plane rotation: (a) SE DBE; BE: (b) SVC; (c) DBE; (d) MCE.

PT wall cumulative base rotation and structure drift envelopes in MCE are compared and shown in Appdx. C.4. Shear force and moment envelopes comparison between Phase I and Phase II are shown in Appdx. C.5.

Fig. 5-21 shows the GLRS inter-story drift envelope at the maximum drift location (column line C) for the different seismic demand levels. As seen, the maximum GLRS drifts, both EW and resultant, are consistently lower for the IFAS structure than for the traditional structure. This positive result was not always anticipated in the analytical research used to develop the IFAS, where limiting larger GLRS drift was a major design constraint [7].

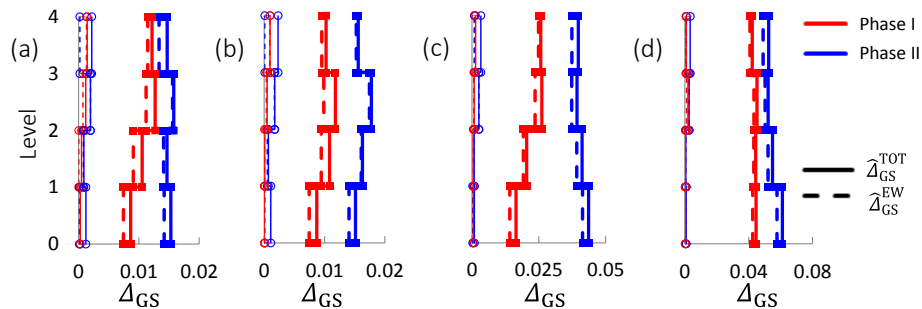


Fig. 5-21. GLRS inter-story drift envelopes: (a) SE DBE; BE: (b) SVC; (c) DBE; (d) MCE.

The reason for this positive outcome may be due to two factors: (1) a slightly stiffer and stronger GLRS in the shake table relative to the evaluation structure; and (2) the nature of the rocking wall response. The latter is probably the reason. From the parametric analysis results in Chapter 4, the changes in the GLRS stiffness and GLRS base plastic hinge strength have negligible influences on the GLRS drift (See Fig. B-9-27, 29). The use of the rocking wall produces a valley in the GLRS drift parametric plot when $0.3 < \alpha < 1$, this effect is even more significant in the 4-story structure (See Fig. B-10, 29).

Fig. 5-22 shows time histories of the 4th story GLRS drift at column line C for the lower demand earthquakes, indicating that comparing maxima, which are similar, does not always tell the complete story in response reduction in terms of cumulative demands, which are seen to be significantly lower in the IFAS structure.

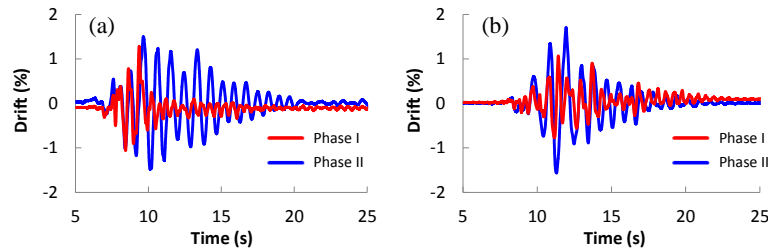


Fig. 5-22. GLRS EW inter-story drift (4th story) at Col. Line C: (a) SE DBE: (b) BE SVC.

Fig. 5-23 shows \hat{a}_{TOT} and \hat{a}_{EW} (maximum resultant acceleration and EW direction acceleration, See Fig. C-7c) for different earthquake demand levels using solid and dashed lines. The acceleration comparison also includes the Phase III structure (Fig. 5-23c,d since only BE DBE and BE MCE motions were performed in this phase). The results indicate similar maximum floor acceleration values in Phases I and II. The similar floor accelerations were not anticipated in the analytical research developing the IFAS, where significant floor acceleration reduction was observed [7]. The reason for this outcome may

be due to five factors: (1) the low overstrength of the displacement-based designed wall (Refer to Table 5-1); (2) the damage incurred in the structure between Phase I and Phase II; (3) the energy dissipation by leaving the deformable connections in Test 15 - Test 17; (4) the slab twisting due to the asymmetric plan; (5) the use of the roller bearing in Test 18+. This first conclusion is seemed correct by the significantly higher accelerations observed in Phase III where a larger wall strength existed (See Fig. 5-3b). However, the parametric results in Fig. B-2 shows that the acceleration reduction is obtained for a 4-story structure when Ω_e is small, therefore, low LFRS overstrength is not the reason and this will be proved later in Section 6.1. The 2nd reason will be discussed in Section 5.6. The 4th reason will not be true since acceleration reduction was observed in the test prediction phase. The 3rd to the 5th reason will be discussed in Section 6.1.

The frequency domain information of the acceleration is shown in Appdx. C.6.

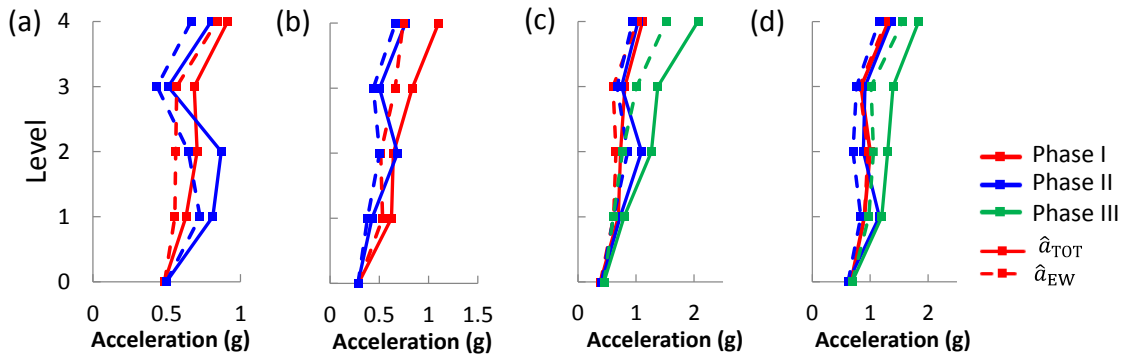


Fig. 5-23. GLRS resultant acceleration envelope: (a) SE DBE; BE: (b) SVC; (c) DBE; (d) MCE.

Fig. 5-24 shows slab twisting envelope comparison for Phases I and II. Fig. 5-24b shows a slightly slab twisting increase in Phase I in BE SVC, but not so significant. The rest of the comparisons show reduction in the slab twisting by using the IFAS in the structure. This reduction is more significant for the tests using larger earthquakes. This

result implies that the usage of the IFAS can reduce the structural twisting response in earthquakes if unsymmetrical layout is used in the structure.

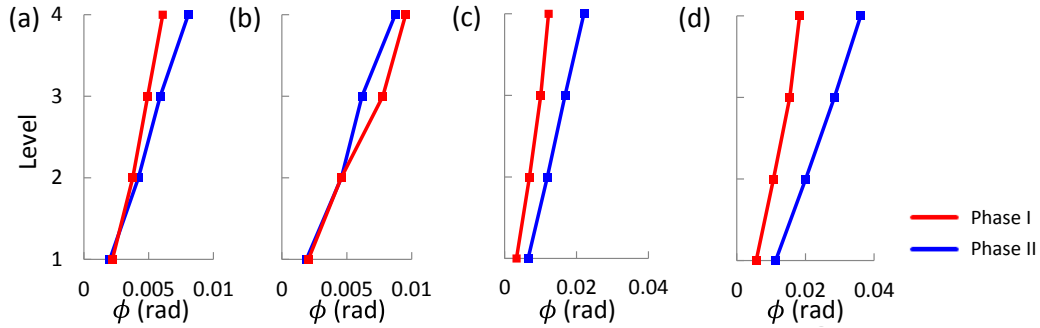


Fig. 5-24. Slab twisting, ϕ , envelope: (a) SE DBE; BE: (b) SVC; (c) DBE; (d) MCE.

Fig. 5-25a shows time histories of 4th floor relative displacement at different earthquake levels for: (a) the North wall (EW direction) $\delta_{r,4}^N$; and, (b) the West wall (NS direction) $\delta_{r,4}^W$. The bumper initial gap g_0 is indicated as horizontal trend lines in Fig. 5-25a for the stronger earthquakes (BE DBE, MCE). The results indicate EW bumper contact in these motions. Consistent with the IFAS design intent, the bumper was infrequently engaged and under only modest deformation in the DBE; while the bumper “bottoms-out” several times during the MCE event, therefore arresting the floor relative displacement.

Examining the Phase II response, e.g Fig. 5-25a SE DBE, it is important to note that the PSA diaphragm connection (Refer to Fig. 5-6b) did deform, as expected (Refer to Fig. 5-4b), and thus not as “rigid” anchorages as might be anticipated for dowel bars in a cast-in-place floor. The roller bearing introduced from Test18 is seen to increase the anchorage rigidity and reduce the relative deformation as expected (See Fig. 5-25a under BE DBE, comparing Phase II Tests 17 & 18). Note that the floor did not return exactly to zero position after each test, as indicated by the initial offsets.

Fig. 5-25b shows the 4th story NS relative displacement (with respect to the West transverse wall). The force at the transverse wall generated through twisting is less than the inertial force in the table motion direction, and thus relative displacement in the NS direction is smaller than that of the EW direction. Note that the use of the roller bearing at the North wall increased the structure twisting responses, therefore larger relative displacement is observed at transverse walls, as shown in Fig. 5-25b under BE DBE.

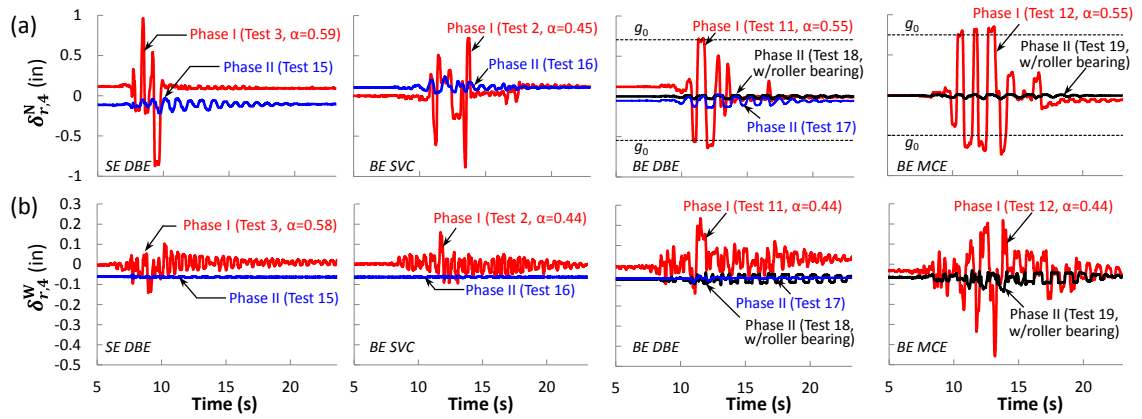


Fig. 5-25. Roof relative displacement: (a) EW; (b) NS (West wall).

Fig. 5-26 shows the maximum and residual relative displacement at each floor level for both the EW and NS directions. The bumper gap and allowable relative displacement ($g_0 + \delta_b$) at each level for Phase I test are indicated by a thin dashed and solid line (if the bumper was involved) respectively. Therefore how much the bumper compressed relative to its maximum deformation capacity at each level is shown quantitatively. Note that the maximum relative displacement in the EW direction increases with height and is maximum at the roof; it takes a first mode shape for the lower level earthquakes, but has a more uniform distribution in the BE MCE. This result implies that varying the IFAS design strength with height may lead to more optimum results, as studied by collaborators [128]. The residual floor displacement is seen to be negligible, implying that the elastic restoring

of the RBs (Refer to Fig. 5-4a) was effective and sufficient. It is noted that a portion of the RBs suffered partial or full tearing separation at the resin glue joint with the base plate (Refer to Fig. 5-8a,b). This damage was probably due to three reasons: (1) membrane stresses due to relative displacements; (2) the built in pre-compression was not large enough; (3) the assembly of the RBs was not good enough since it was done by students on site. The damaged RBs were observed at every floors. The damage did not impact the effectiveness of the RB in providing out-of-plane bracing to the shear walls, which performed as intended to drifts anticipated at MCE-level events. However, this damage could affect the efficiency of the elastic restoring, and thus it is recommended to sufficiently precompress the RBs in IFAS applications, as occurs in bridge applications due to superstructure self-weight.

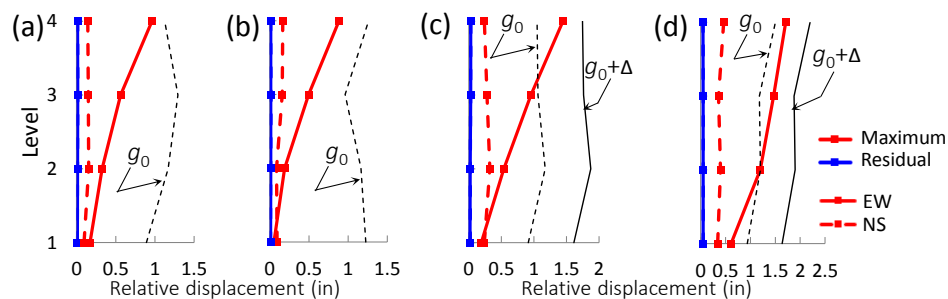


Fig. 5-26. IFAS Relative Displacement Profile: (a) SE DBE; BE: (b) SVC; (c) DBE; (d) MCE.

The FDs and BRBs were left in place in Test 15 – Test 17 as mentioned previously. A comparison on the FD force-deformation response at Test 11 and Test 17 is shown in Fig. 5-27. A good amount energy dissipation in the FDs can be observed in Test 17. The deformation of the FDs was expected to be very small (about 0.014” when the PT wall base rotation reached 0.03 rad) since the slab and PT walls were constrained in the horizontal

direction. The axial deformation of the FDs in Fig. 5-27 was much larger than the expectation. The explanation of the large FD axial deformation in Phase II is shown in Fig. 5-28. Fig. 5-28a shows a schematic drawing of the specimen before undergoing deformation. Fig. 5-28b shows a schematic drawing of the specimen undergoing deformation at 12.15s. Fig. 5-28c shows the FD axial deformation level 4 and the North wall base rotation time history. Because the slab and PT wall were constrained by the PSAs and the PSAs were welded at the top surface of the slab, the PT wall rotated around the slab top surface at each floor level when the structure deformed (See Fig. 5-28b). Therefore, a small wall base rotation will cause relative horizontal displacement between the wall and slab at the FD level. Thus, the FD underwent larger horizontal deformation than expectation. The FD and BRB force-deformation behavior in Phase I is shown in Appdx. C.7.

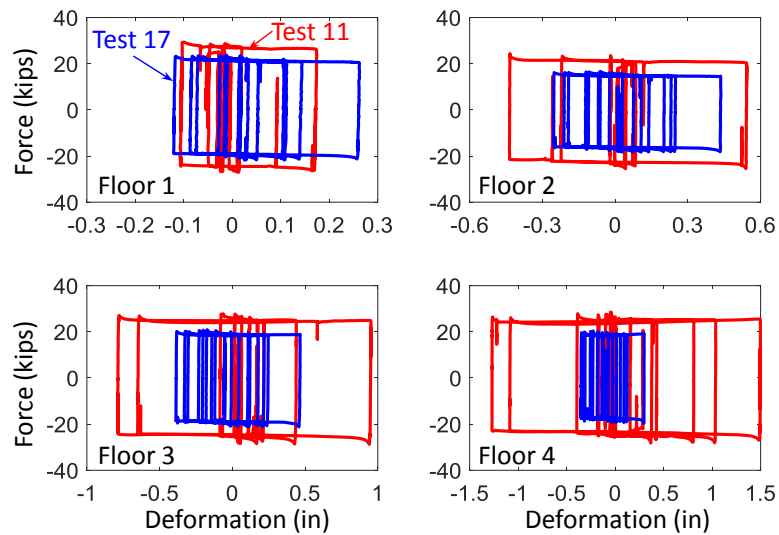


Fig. 5-27. FD force-deformation responses at Test 11 and Test 17.

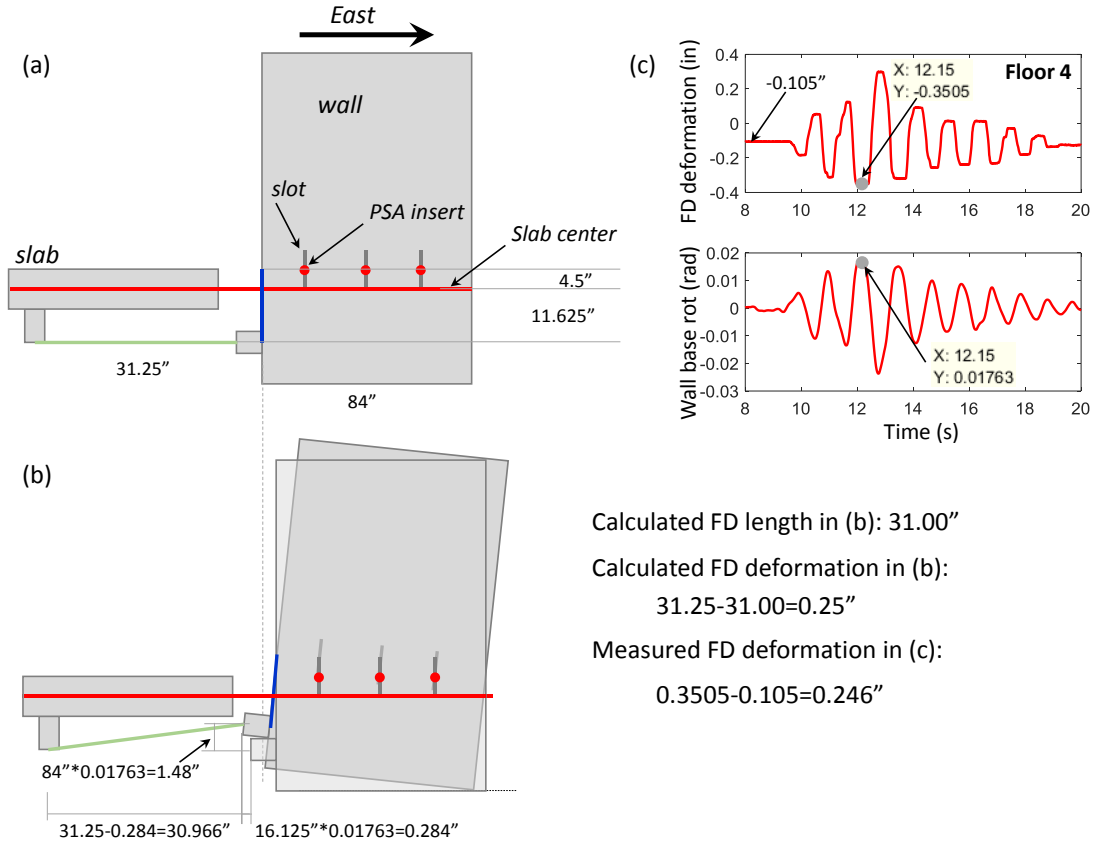


Fig. 5-28. FD deformation in Test 17: schematic drawing: (a) before the specimen deformed; (b) after the specimen deformed; (c) FD axial deformation and wall base rotation.

Fig. 5-29 shows comparison of the structural overturning moment-roof drift at Column line B between Phase I and Phase II. The overturning moment (M_o^{EW}) and roof drift ($\bar{\Delta}_{GS,roof}^{EW}$) are obtained by using Eqn. C-8 and Eqn. C-4b respectively. The structure stiffness comparison between Phase I and related Phase II test can be seen from this figure. Fig. 5-29a, b indicate structure stiffness degradation between Phase I and phase II. Fig. 5-29c, d indicates that the structure stiffness in Phase I was close to Phase II after Test 11.

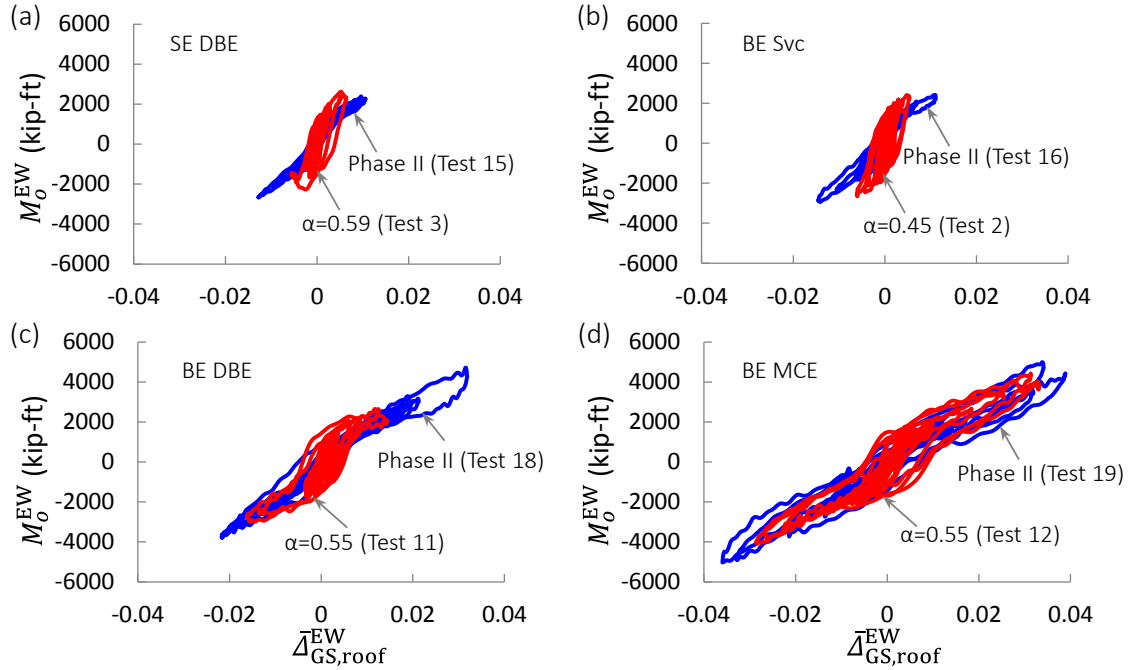


Fig. 5-29. Overturning moment: (a) SE DBE; BE: (b) Svc; (c) DBE; (d) MCE.

Fig. 5-30a shows the total energy dissipation comparison between Test 11 ($\alpha=0.59$) and 13 ($\alpha=0.43$) in Phase I. Fig. 5-30b-f show the energy dissipation comparison of the structure between Phase I and Phase II under SE DBE (Tests 3 & 15), BE SVC (Tests 2 & 16), BE DBE (Tests 13 & 17; Tests 11 & 18) and BE MCE (Tests 12 & 19). The energy dissipation of the BRBs on the west wall is calculated from the measured force and deformation in the shake table test. The energy dissipation of the BRBs on the east wall were estimated by the ratio between the east wall accumulated relative displacement and the west wall accumulated BRB deformation. Fig. 5-30a indicates that more total energy is dissipated when α is smaller. The BRBs in the transverse direction dissipated similar energy, however, more energy was dissipated in the FDs and less energy was dissipated in the North wall. This implies the potential of protecting the wall using lower FD strength. Fig. 5-30b-f indicate that more energy is dissipated in Phase I in comparison to Phase II

through using the deformable connections. Fig. 5-30b shows similar total energy dissipation in Phase I and Phase II. Fig. 5-30b indicates that the IFAS can reduce the structural response (refer to Fig. 5-19a) when the total energy dissipation is similar. Fig. 5-30d, e show that the total energy dissipated in Phase II was reduced significantly when the FDs and BRBs were removed, implying that the use of the deformable connections can help dissipating energy in earthquakes in traditional structures.

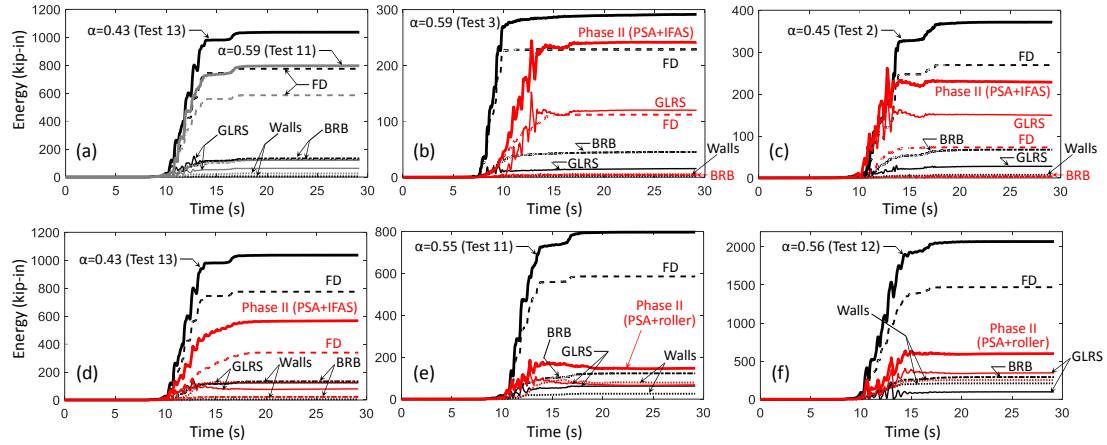


Fig. 5-30. Hysteretic energy dissipation: (a) BE DBE ($\alpha=0.59$ & $\alpha=0.43$); (b) SE DBE ($\alpha=0.59$); BE: (c) SVC ($\alpha=0.45$); (d) DBE ($\alpha=0.43$); (e) DBE ($\alpha=0.55$); (f) MCE ($\alpha=0.56$).

Fig. 5-31 shows comparisons of the force-deformation relationship of FD, combination of FD and RB (FD+RB), combination of FD, RB and bumper (wall shear force) and floor inertial force at roof for BE SVC, BE DBE and BE MCE tests in Phase I. Red represents the response of the FD. Green represents the response of FD+RB. Black represents the response of the wall shear force. Blue represents the response of the floor inertial force. Fig. 5-31a shows that the floor inertial force is increased nearly linear as the FD deformation is increased. A small stiffened tip (in grey circle) is observed in Fig. 5-31b when the FD deforms to the maximum deformation. Significant stiffened tips (in grey

circle) are observed in Fig. 5-31c when the FD reaches large deformation. These stiffened tips were probably caused by the engagement of the bumper. The bumper was used for the purpose of limiting the relative displacement and reducing the potential impact force between the slab and wall in earthquakes. However, a larger force can be transferred from the floor to the wall when the bumper was engaged and deformed. Therefore, a larger floor inertial force was generated.

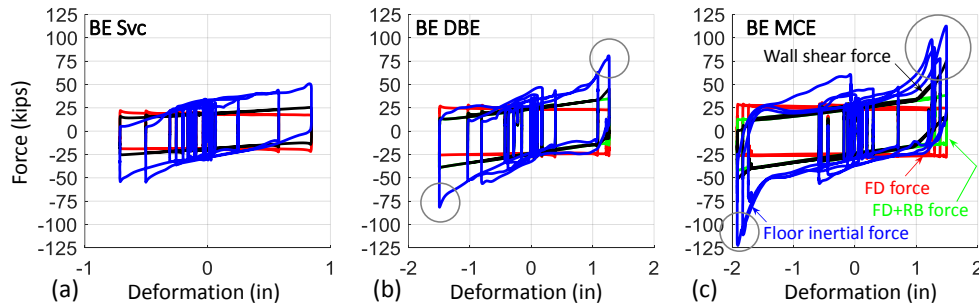


Fig. 5-31. Force-deformation relationship of FD, FD+RB, wall shear and floor inertial force at roof for: (a) BE SVC; (b) BE DBE; (c) BE MCE.

5.5 Damage Calibration of the Pristine Model

The test specimen underwent unavoidable damage in the shake table test process. The sequential analysis can be used to model the process of the cumulative damage. However, if an updated model is calibrated to a point of the damaged status using measurements and observations, the damaged structure can be used to explain the test specimen efficiently. The updated model is calibrated to Test 17 in this Section and is termed as the Calibrated model (CM).

Fig. 5-32 shows the West and East wall inspection photo after Test 15. The west faces of the West and East wall at the 1st floor are shown in Fig. 5-32a while the east faces are shown in Fig. 5-32b. Plenty of cracks can be observed in the transverse walls.

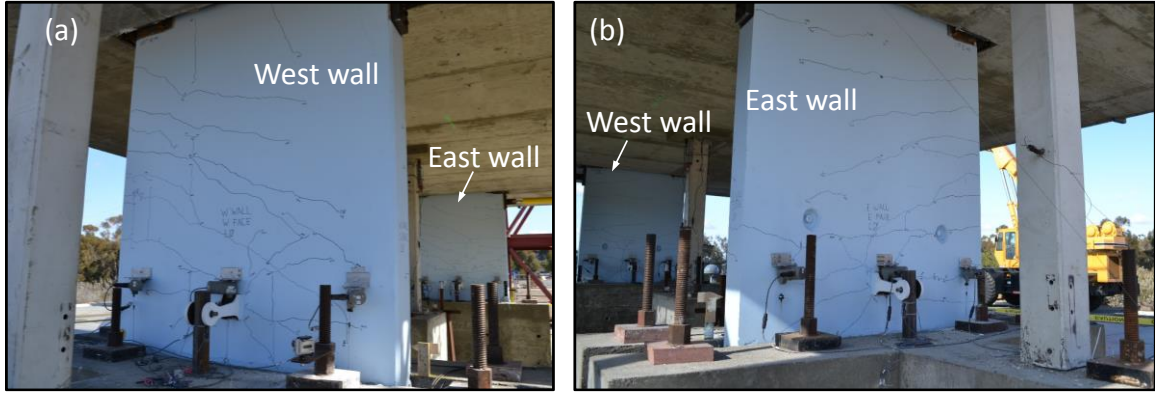


Fig. 5-32. Transverse wall cracks after Test 14: (a) East wall; (b) West wall.

Fig. 5-33a, b show the crush of concrete near the toe of the North wall and precast columns after Test 17 respectively. The confined concrete strength in the End Zone (See Fig. 5-11) of the North wall is reduced by 90%. The confined concrete strength in the End Zone of the West wall and East wall is reduced by 50% and 20% respectively. The Young's modulus of the 3D elastic shell of the transverse walls is reduced by 10%. The precast columns and slabs are assumed pin connected for the purpose of considering the damage at column ends.

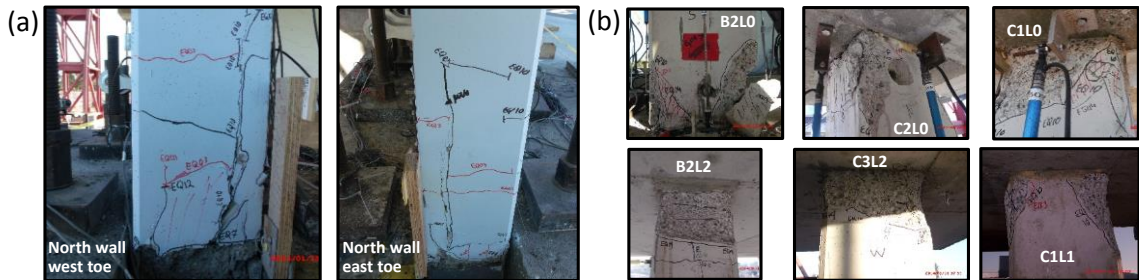


Fig. 5-33. Precast components damages: (a) North wall; (b) Precast columns.

The structure fundamental period is 0.57s. The fundamental period of the test specimen was 0.59s before Test 15. Additionally, Test 15 and Test 16 were tests using small magnitude earthquakes, so the fundamental period of the damaged model for Test 17

is reasonable. The moment-rotation behavior of the damaged walls (pushover analysis) and the wall in Test 17 is compared in Fig. 5-34.

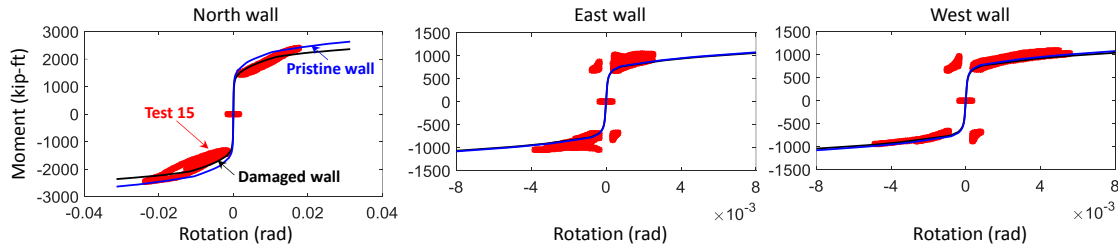


Fig. 5-34. Comparison of moment-rotation behavior between damaged wall and test.

5.6 Comparisons between 3D Models and the Shake Table Test Specimen

Three 3D models were developed in Section 5.2. Response comparisons between the 3D models and the test specimen were performed to validate the reliability of the modeling methodology. This validated model can be applied to different purposes. For example, the missed measurements that were not easy to be measured in the test can be represented from the model. Also, the unexpected test specimen behavior can also be investigated and explained by the model. In addition, the modeling methodology can be applied to other types of structures or full scale structures to study the IFAS performance.

5.6.1 Verification of the Pristine Models

Test 4 was the first BE DBE level earthquake in the shake table test. Test 4 is used for verifying the response of the pristine model validation because the specimen only underwent three small intensity earthquakes before Test 4, it can be assumed that there was little damage occurred in the specimen.

Floor displacement at column line C (See Fig. C-1), floor acceleration near column B1 (See Fig. C-1), relative displacement between the slab and North wall, slab twisting time histories and north wall base rotation between the numerical models and Test 4 are

compared in Fig. 5-35. Note that all the responses used for the comparison are from the roof level except the North wall base rotation. Fig. 5-35 shows that the response of the UM matching the test best in comparison to other two models.

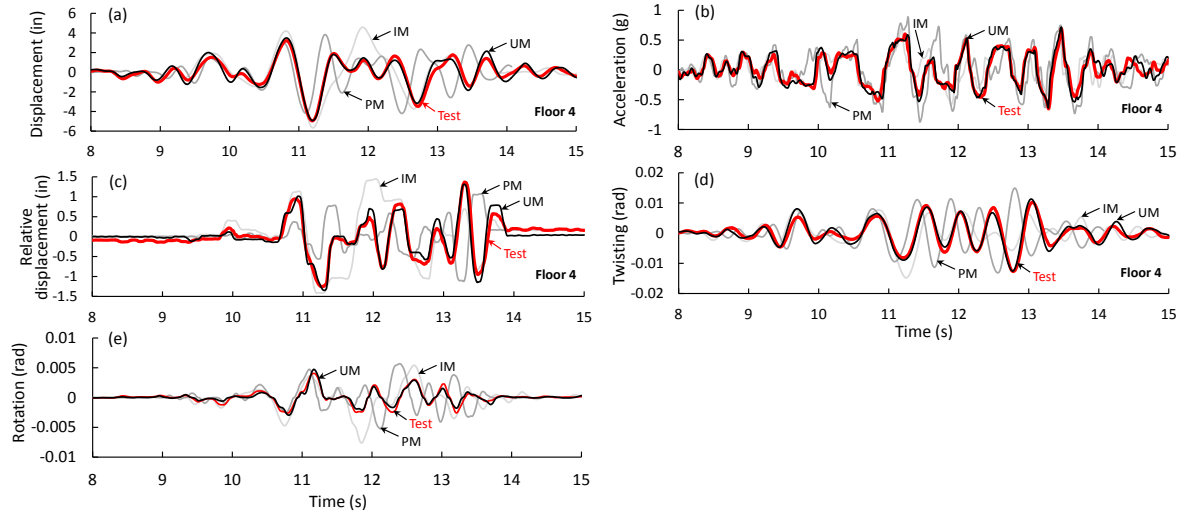


Fig. 5-35. Responses: (a) floor displacement at column line C; (b) floor acceleration near column B1; (c) relative displacement; (d) slab twisting; (e) North wall base rotation.

North wall base moment-rotation, FD and BRB force-deformation between the numerical models and test are compared in Fig. 5-36. Note that the responses of the FD and BRB used in the figure are from the roof level. Fig. 5-36 shows that the responses from the UM matches best to the test results.

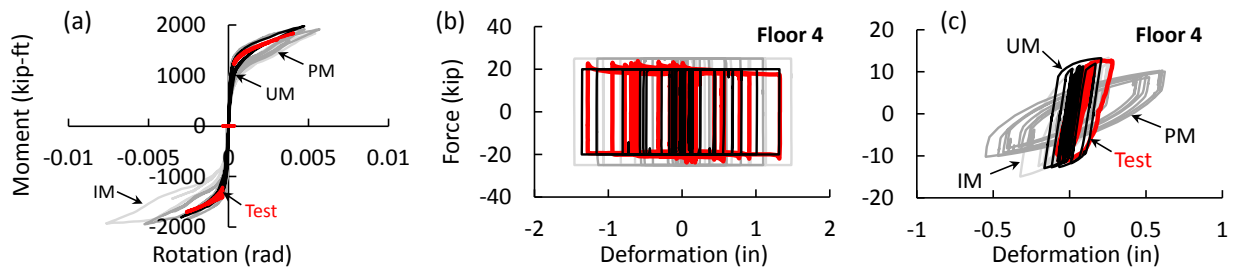


Fig. 5-36. (a) North wall base moment-rotation; force-deformation: (b) FD; (c) BRB.

Fig. 5-35, 5-36 indicate that the response of the UM matches the Test 4 well and can be used to represent the test specimen. Fig. 5-37a,b show that structure and GLRS overturning moment – roof drift at column line B of the UM matches that of Test 4. Fig. 5-37c shows the comparison on the four different components of the structure overturning moment (Eqn. C-8) between the UM and Test 4. The comparison shows that: (1) the different moment from the UM matches that of the Test 4; (2) the structure overturning moment is mainly contributed by the GLRS inertial force, and secondly contributed by the LFRS inertial force. The contribution from the P-Delta effect from the GLRS and LFRS is negligible in comparison to that from the inertial force.

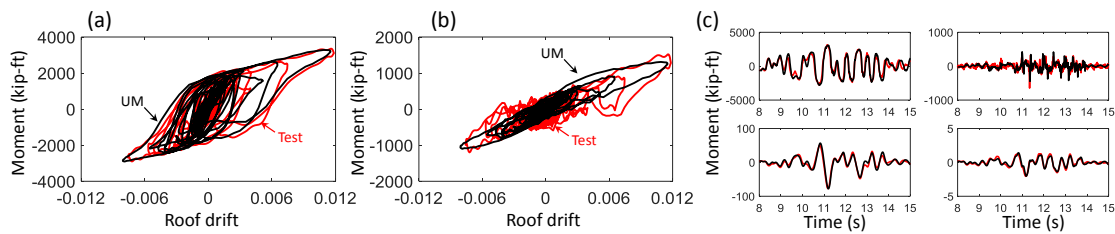


Fig. 5-37. Moment-roof drift behavior (a) structure overturning; (b) GLRS overturning; (c) structure overturning moment decomposition.

The specimen comparison in this section indicates that the UM is good enough for predicting the pristine test specimen response. The next step is to check if the model can track the cumulative damage occurred in the shake table test. Test 7 and Test 10 (See Table 5-4) are used for this comparison as mentioned previously. Note that the numerical model in the following part of the paper implies the UM unless otherwise stated.

5.6.2 Verification of the Sequential Run

This section shows the verification of the numerical model responses with subjecting to the sequential analysis. The comparison of Test 7, Test 10 and Test 11 with corresponding sequential numerical analysis responses are used to verify the updated

model. Test 10 is a test using BE MCE and will be shown in this section. Test 7 and Test 11 are shown in Appdx. C.8.

Test 10 is the 5th analysis in the sequential analysis of the UM and is the first BE MCE level earthquake that the test specimen. Fig. 5-38 shows the time history responses of the floor displacement at column line B, floor acceleration near column B1, slab twisting and North wall base rotation. Note that all the responses are from the roof level except the wall base rotation. The comparison shows that the UM underestimate the GLRS roof displacement and North wall base rotation at the peaks. However, the UM matches the test well.

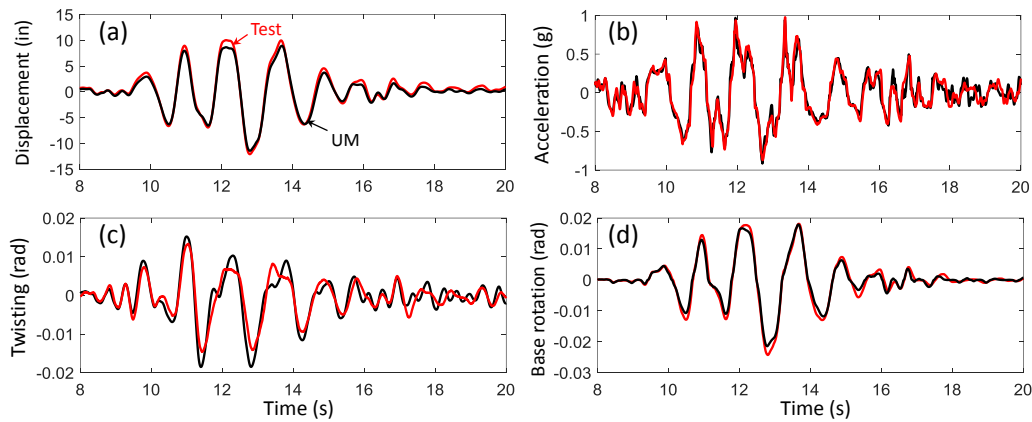


Fig. 5-38. Time history responses (Test 10): (a) floor displacement at column line B; (b) floor acceleration near column B1; (c) slab twisting; (d) north wall base rotation.

Fig. 5-39 shows the structure overturning moment-roof drift at column line B, North wall base moment-rotation, the roof FD and BRB force-deformation for Test 10.

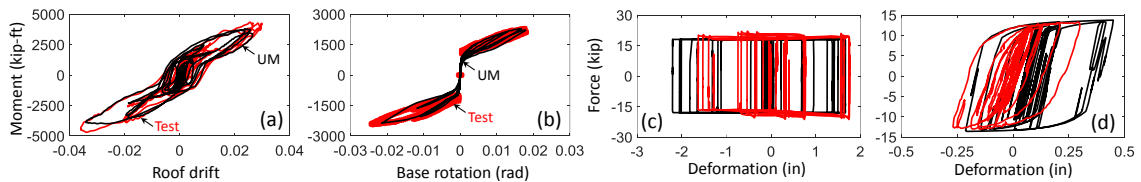


Fig. 5-39. Moment-rotation responses (Test 10): (a) structure overturning; (b) North wall base; (c) roof FD force-deformation; (d) roof BRB force-deformation.

Fig. 5-40 shows the engagement of the bumper in Test 10. Black and grey represent the responses of the numerical analysis while red and pink represent the responses of the test.

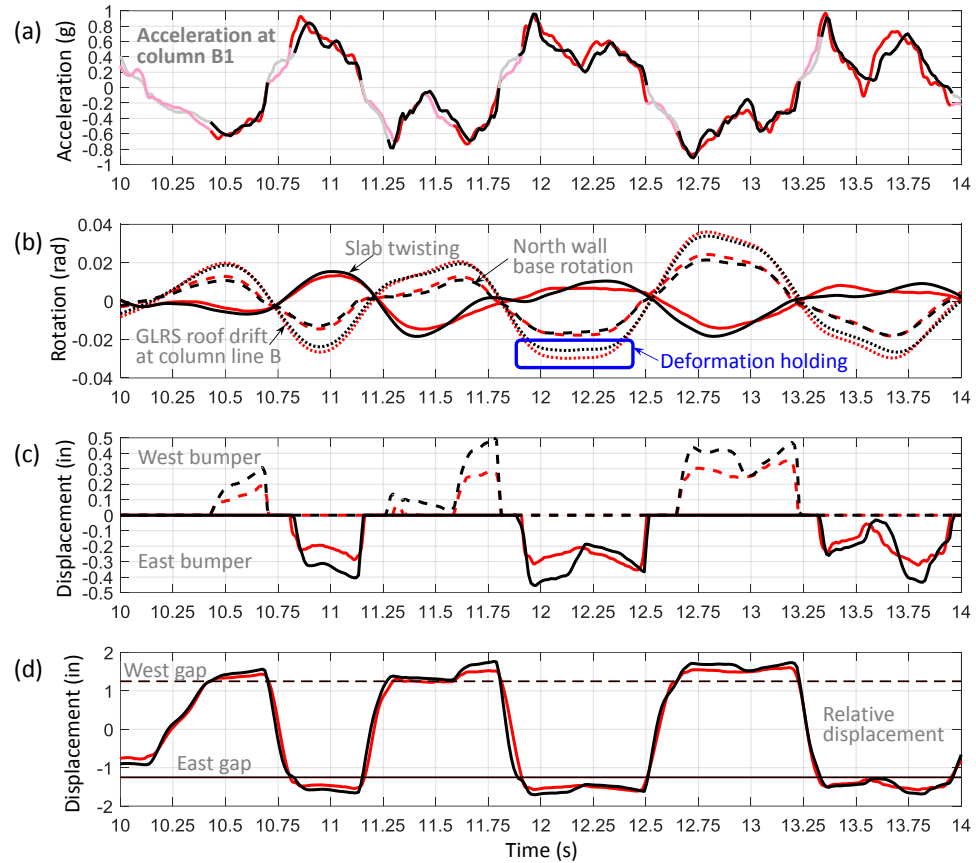


Fig. 5-40. Bumper engagement at roof (Test 10): (a) acceleration; (b) slab twisting, GLRS roof drift and North wall base rotation; (c) bumper deformation; (d) relative displacement.

Fig. 5-40a shows the acceleration in the EW direction at column B1. Red and black indicate the acceleration when the bumpers were engaged while pink and grey indicate the acceleration when the bumpers were not engaged. Fig. 5-40b shows the slab twisting (solid lines), GLRS roof drift at column line B (dotted lines) and North wall base rotation (dashed lines). A temporary holding of the roof at its extreme deformation is observed from 12s to 12.3s (in blue box). Fig. 5-40c shows the deformation of the west and east bumper.

Differences in the magnitude of the bumper deformation is observed between the test and analysis, while the sequences and duration of the engagement of the bumpers matches well.

Fig. 5-40d shows the relative displacement between the roof slab and the North wall.

Fig. 5-40 show that the numerical model responses matches the test results well, except a larger GLRS roof displacement and North wall base rotation are observed in the test. However, the comparisons in these figures show that the UM can match the response of the test during the sequential analysis, indicating that the numerical model is good for the modeling of the test specimen.

Additionally, one cycle of the structure deformation from Fig. 5-40 is selected to show the process of the engagement of the bumper (See Fig. 5-41).

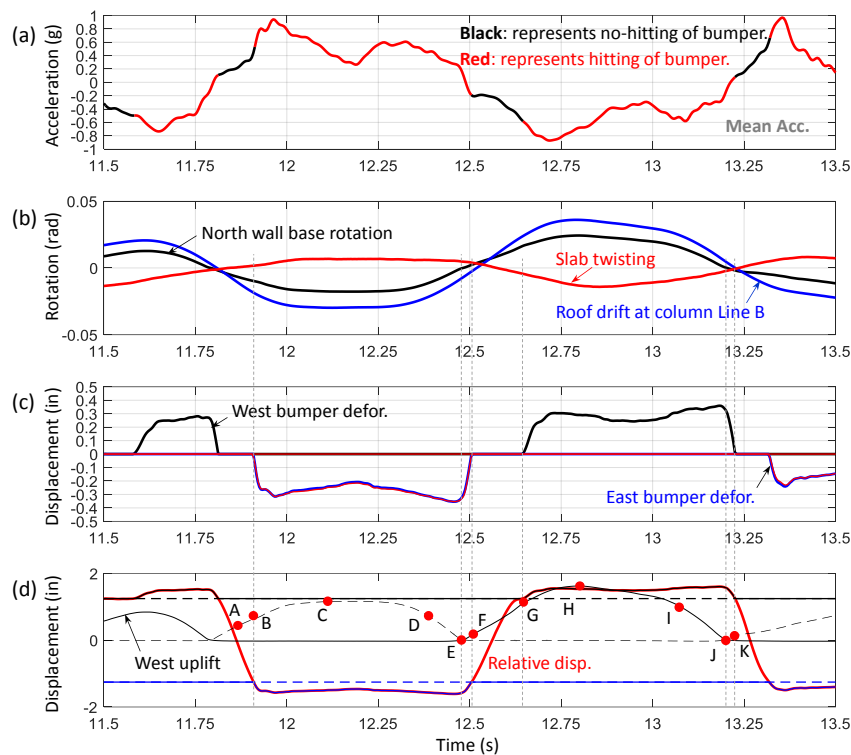


Fig. 5-41. Bumper engagement at roof (zoomed in at Test 10): (a) acceleration; (b) slab twisting, GLRS roof drift and North wall base rotation; (c) bumper deformation; (d) relative displacement.

Eleven time spots (A to K) are indicated in Fig. 5-41d. A sequence of schematic drawings are shown in to represent the algorithm of the test specimen when the bumper underwent compression (See Fig. 5-42).

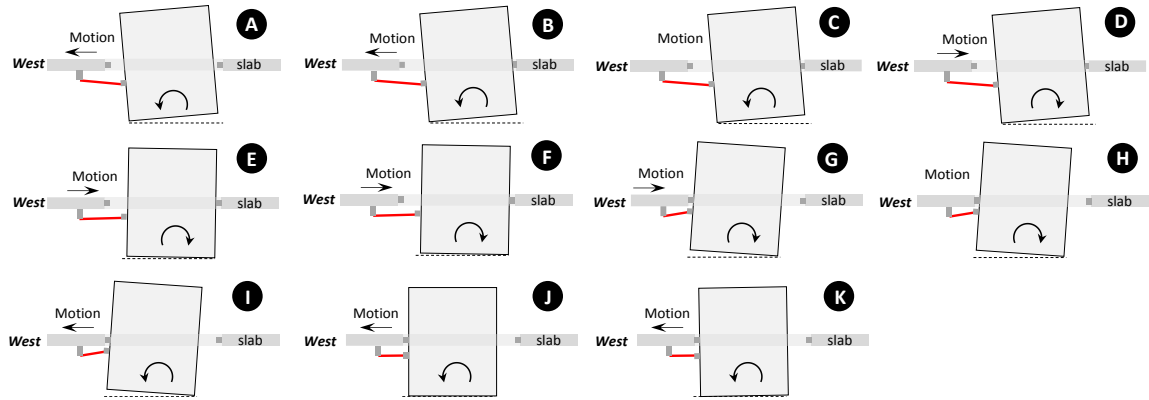


Fig. 5-42. Schematic drawing of deformed structure when the bumper is engaged in Fig. 5-41d.

At spot A, the North wall and GLRS deformed westward. The GLRS deformed more than the North wall. At spot B, the east bumper was engaged. The GLRS and North wall deformed westward still. At spot C, the GLRS and North wall reached the maximum deformation in the westward direction of this cycle and stayed there for about 0.3 second. Then, the GLRS and North wall deformed eastward. At spot D, the GLRS and North wall deformed eastward and the east bumper was still under engagement. At spot E, the North wall base gap was closed and the east bumper was still under engagement. At spot F, the North wall rocked eastward a little and the east bumper was released. At spot G, the GLRS and North wall deformed eastward and the west bumper was engaged. At spot H, the GLRS and North wall reached the maximum deformation in the eastward direction of this cycle and then deformed back to westward. At spot I, the GLRS and North wall deformed westward and the bumper was still under engagement. At spot J, the North wall base gap

was closed and the west bumper was still engaged. At spot K, the North wall rocked west ward a little and the west bumper released.

This cycle represents a typical process when the bumper was engaged in the test. The bumper was engaged when the North wall deformed to one direction. The bumper was in contact till the North wall deformed back and passed the zero location.

5.6.3 Verification of the Calibrated Model

The response of the Calibrated model is shown and compared to the structure responses in Test 17 in this section.

Fig. 5-43 shows the time history responses of the floor displacement at column line B, floor acceleration near column B1, slab twisting and North wall base rotation. Note that all the responses are from the roof level except the wall base rotation. The figure shows that the CM can capture the peak responses well. However, the CM responses doesn't match the test well after the structure reaches its peak response.

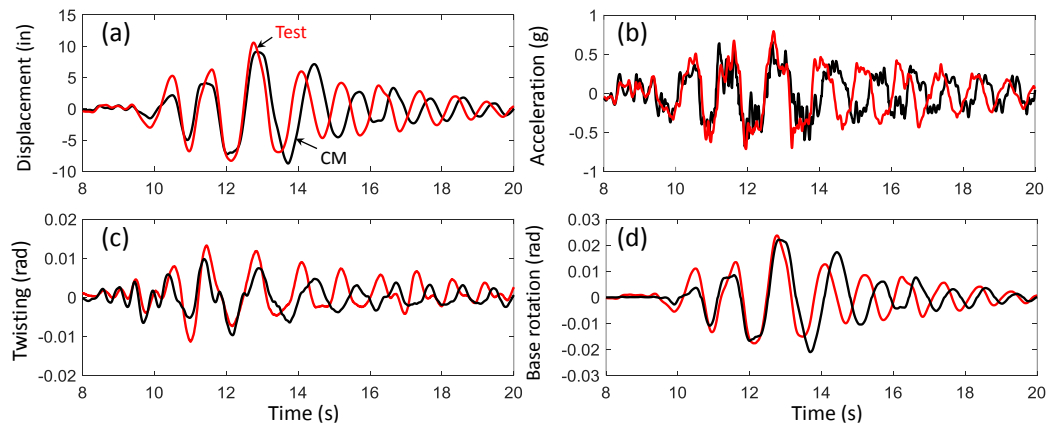


Fig. 5-43. Time history responses (Test 17): (a) floor displacement at column line B; (b) floor acceleration near column B1; (c) slab twisting; (d) north wall base rotation.

Fig. 5-44 shows the structure overturning moment-roof drift at column line B, moment-rotation of the North wall and transverse walls, roof FD and BRB force-

deformation responses. The CM underestimate the structure overturning moment when the structure drift is large and provide a stiffer initial stiffness of the structure (See Fig. 5-44a). The CM provides acceptable North wall moment-rotation and FD force-deformation responses (See Fig. 5-44b, e). The CM provides the right transverse wall strength and a smaller deformation demand of the transverse walls in comparison that of the test (See Fig. 5-44c, d). The CM doesn't provide a good match of the BRB force-deformation because the BRB force-deformation in the test was shifted (See Fig. 5-44f).

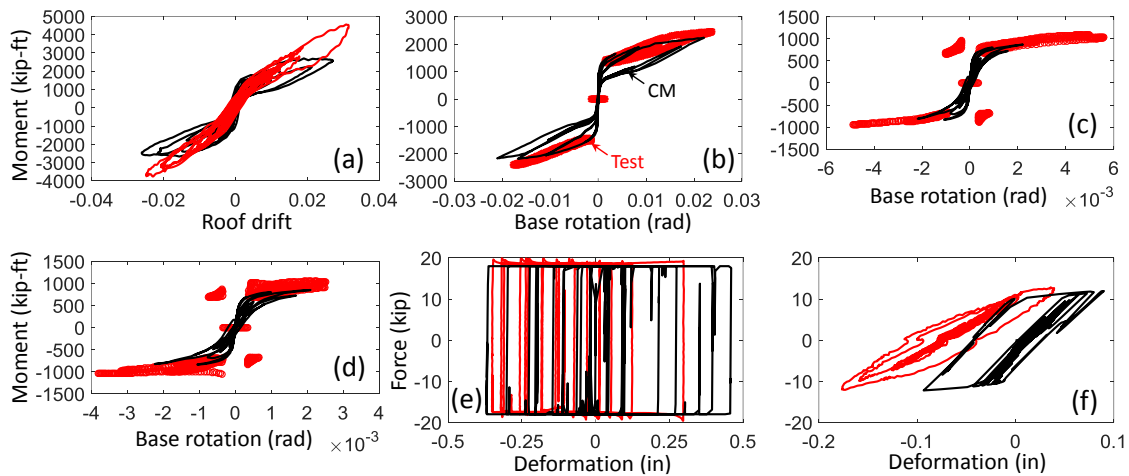


Fig. 5-44. Moment-rotation responses (Test 17): (a) structure overturning; (b) North wall base; (c) West wall base; (d) East wall base; (e) roof FD force-deformation; (f) roof BRB force-deformation.

Fig. 5-45 shows the structure response envelopes of floor resultant acceleration, North wall drift, GLRS resultant drift and slab twisting. Response of two CMs in Phase II is shown here: (1) with deformable connections (CM-w/FD); (2) without deformable connections (CM-wo/FD). The CM-w/FD predicts acceptable maximum floor acceleration and North wall deformation responses (See Fig. 5-45a, b). The CM doesn't produce good match on the GLRS drift and slab twisting (See Fig. 5-45c, d). Additionally, a significant reduction in the floor acceleration can be observed due to structure damage (solid blue to

dashed green in Fig. 5-45a). Therefore, structure damage is another reason for not observing floor acceleration reduction in the test.

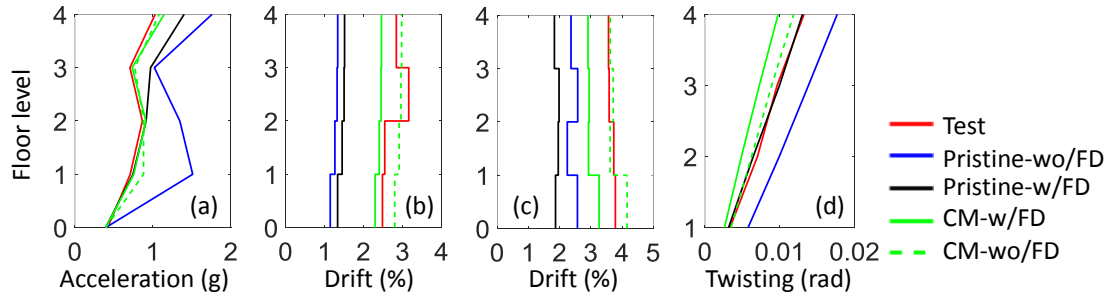


Fig. 5-45. Structure response envelopes (Test 17): (a) floor resultant acceleration; (b) North wall drift; (c) GLRS resultant drift; (d) slab twisting.

The CM doesn't produce good match to all the test specimen response. However, the CM can still be used for the purpose of studying the influence from the structure damage to the IFAS performance.

5.7 Conclusions for 3D Nonlinear Model Development and Conclusion

The test specimen and test program is introduced in this chapter. Then the details of the development of the 3D nonlinear model is described. The comparisons of the structure responses in the shake table test is presented. And afterwards, the comparison between the numerical analysis and test results is also presented. The following conclusions can be drawn from this chapter:

(1) The deformation demand reduction in the PT walls through the use of the IFAS was observed in the shake table test.

(2) The floor acceleration reduction was observed in Phase I when compared to Phase III. However, the floor acceleration reduction was not observed in Phase I when compared to Phase II in the shake table test.

(3) The pristine 3D numerical model response matches the test well and properly capture the damage accumulation occurred in the shake table test. Therefore, the numerical model can be used for the further investigation of the IFAS performance.

(4) Structure damage can cause a significant reduction in the floor acceleration in the traditional structure. Therefore, unavoidable structure damage is one reason for not observing the acceleration reduction in Phase I of the test. The Calibrated model doesn't match the test specimen response well, however it can still be used for investigating the influence from the structure damage to the IFAS performance.

6. IFAS: CALIBRATED 3D MODEL ANALYSES

In the shake table test, the LFRS deformation reduction was observed. But the floor acceleration reduction wasn't observed (See Fig. 5-23). Five reasons were assumed for not obtaining floor acceleration reduction in Section 5.4: (1) low Ω_e ; (2) cumulative damage of the test specimen; (3) energy dissipation provided from the FDs and BRBs in Phase II; (4) slab twisting; (5) use of roller bearing in Phase II. (1) and (2) were already discussed in the previous sections (Sec. 4.8 and Sec.5.6.3). Therefore, the rest of three reasons will be analytically studied using the 3D shake table test model. Moreover, the influence from the bumper stiffness to the floor acceleration in Phase I will be discussed in Sec. 6.1.4. The influence from different damage source (GLRS or PT wall) to the structure performance will be discussed in Sec. 6.2. The effectiveness of using the IFAS in different design situations (different transverse wall strength) will be shown in Sec. D.3.

6.1 Analyses of the Updated Model

6.1.1 Responses of the Pristine Phase I and Phase II Model Related to Test

For the purpose of comparing the effectiveness of the IFAS in a pristine structure, pristine models of the test specimen in Phase I and Phase II are analyzed. Four pristine numerical models are analyzed: (1) pristine model of the specimen in Test 4 (PI); (2) pristine model of the specimen in Test 17 (PII-w/FD); (3) pristine model of the specimen in Test 17 without deformable connections (PII-wo/FD); (4) pristine model of the specimen in Test 17 without deformable connections and with very stiff PSAs (PII-stiffPSA). The models are listed in Table 6-1.

Table 6-1. Description of models with different floor anchorages

Model name	Phase	Floor anchorage
PI	Phase I	IFAS
PII-w/FD	Phase II	PSA+IFAS
PII-wo/FD	Phase II	PSA+RB
PII-stiffPSA	Phase II	Stiff PSA+RB

The deformable connections were left in place in Test 15 – Test 17. That’s why *PII-w/FD* is used in this section. The horizontal stiffness of each PSA is 30.4kip/in, resulting in a stiffness of 425.6kip/in at the North wall (14 PSA at each level) and 243.2kip/in at the transverse wall (8 PSA at each level) respectively. This anchorage stiffness is much smaller than a traditional cast-in-place floor anchorage, therefore, a large stiffness (1000kip/in) is assigned to each PSA in the horizontal direction for the purpose of modeling a more realistic traditional floor anchorage. That’s why *PII-stiffPSA* is used in this section. All the models are analyzed with a BE DBE level earthquake.

The envelopes of the structure responses are shown in Fig. 6-1. The legend is shown at the right side of the figure. Fig. 6-1a shows that a significant acceleration reduction from Phase II to Phase I (blue to red). A structure with stiffer PSA can produce larger floor acceleration (blue to green). A significant reduction in the acceleration is observed by adding the deformable connections in the Phase II structure (blue to black). Fig. 6-1b shows the North wall drift envelopes in the EW direction. A significant North wall drift reduction is observed from Phase II to Phase I. The increase of the PSA stiffness produces larger North wall drift. The GLRS resultant drift envelopes are shown in Fig. 6-1c. *PII-wo/FD* produces the maximum GLRS drift. Additionally, the GLRS drift is supposed to be one trade off of the IFAS usage, however, in this figure the GLRS drift in Phase I is also smaller

than that of Phase II. Fig. 6-1d shows that the *PII-wo/FD* produces the maximum slab twisting. Fig. 6-1e shows that the relative displacement in Phase II is much smaller than that of Phase I. *PII-stiffPSA* produces a smaller relative displacement than other two Phase II models. These analytical studies prove the efficacy of using the IFAS in reducing floor acceleration and LFRS drift in comparison to a traditional floor anchorage. Since the numerical models are the pristine model of the test specimen in Test 4 and Test 17, the North wall overstrength of the numerical model is the same as that of the test and the model is asymmetric. Therefore, low LFRS overstrength and slab twisting are not the reason for not observing the floor acceleration reduction in the test.

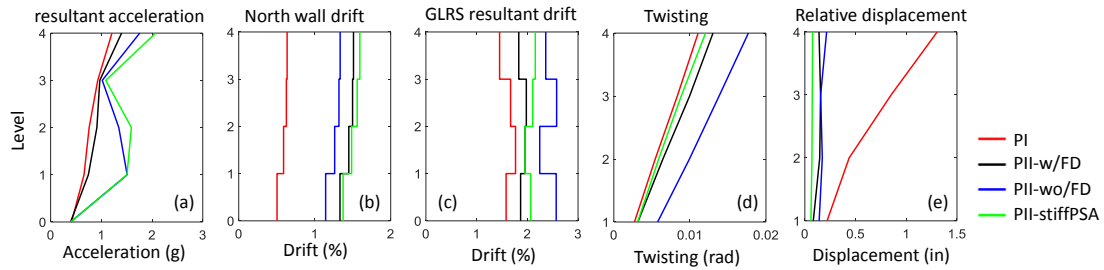


Fig. 6-1. Response envelopes: (a) resultant acceleration; (b) LFRS drift; (c) GLRS resultant drift; (d) slab twisting; (e) relative displacement.

The location of the occurrence of the maximum resultant acceleration in Fig. 6-1a is shown in Fig. 6-2a. The Fourier Transform of the accelerations indicated in Fig. 6-2a is shown in Fig. 6-2b, c. Fig. 6-2b, c show that the higher modes contribution is reduced significantly after adding deformable connections to the structure (blue to black). A significant reduction in the acceleration can be obtained by using the IFAS in comparison to a traditional structure (blue to red). The use of stiff PSA can increase the contribution of the higher modes (blue to green). Generally, the use of the IFAS decrease the contribution from higher modes and therefore decrease the floor acceleration response in earthquakes.

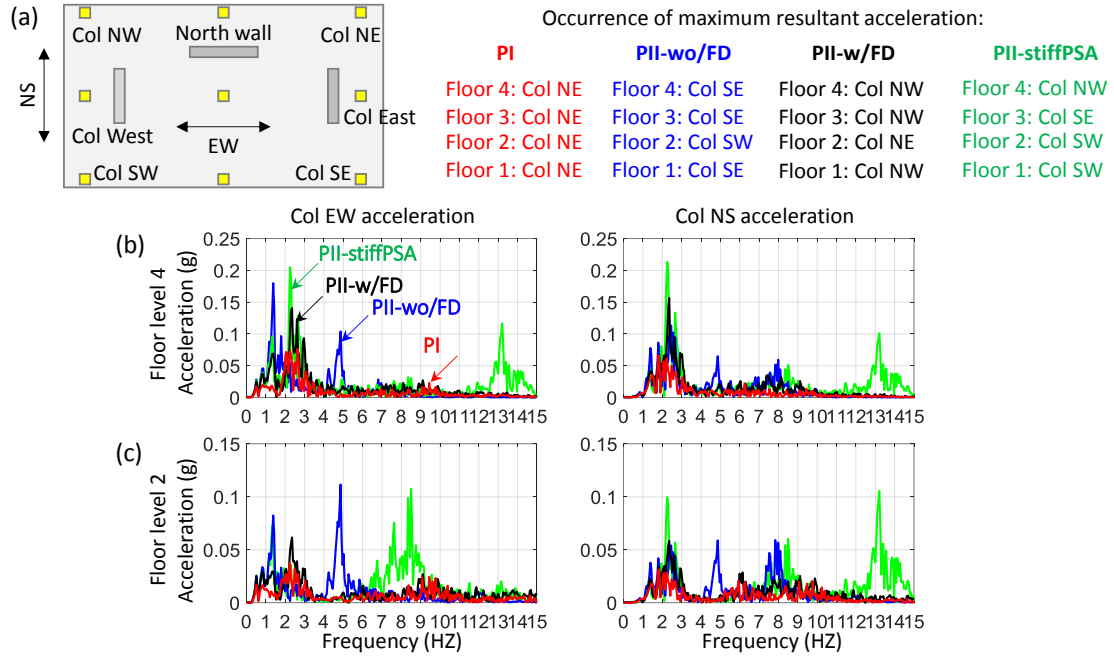


Fig. 6-2. Acceleration: (a) location of the occurrence of the maximum resultant acceleration at each floor; Fourier Transform of the floor acceleration indicated in (a) at: (b) level 4; (c) level 2.

An energy dissipation comparison among different components in the structure is compared and shown in Fig. 6-3. Fig. 6-3 shows that the deformable connections (BRBs and FDs) dissipate a significant portion of energy in *PI* and *PII-w/FD*. The energy dissipated by the PT walls is negligible in *PI*. The energy dissipated by the columns only contributes a small portion in *PI*. The energy dissipated by the columns and PT walls is increased in *PII-w/FD*. The energy dissipated by the deformable connections is decreased significantly in comparison to that in *PI*, however, still larger than the energy dissipated by the PT walls and columns. The total energy dissipated in *PII-w/FD* is about half of that is dissipated in *PI*. The total energy dissipated in *PII-wo/FD* is about 10% of that is dissipated in *PI*. The energy dissipated in columns is increased significantly and the energy dissipated in the PT walls is also increased in comparison to that in *PI*. Therefore, the IFAS can

dissipate plenty of energy in earthquakes and protect the structural components from damage.

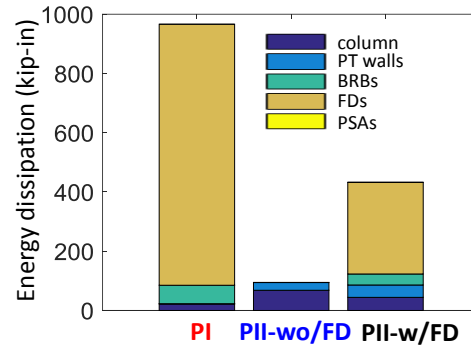


Fig. 6-3. Energy dissipation among different components.

6.1.2 Responses of Phase II Structure with and without using Roller Bearing

The effect of adding the roller bearing in Phase II is studied in this section.

Three pristine models are used for the analyses: (1) pristine model of the specimen in Test 17 (PII-w/FD); (2) pristine model of the specimen in Test 17 without deformable connections (PII-wo/FD); (3) pristine model of the specimen in Test 17 with roller bearing (PII-roller). The first two models are already investigated in the previous section. The location of the occurrence of the maximum resultant acceleration is shown in Fig. 6-4.

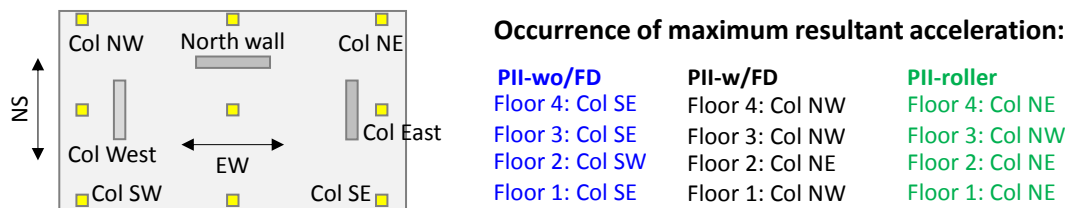


Fig. 6-4. Location of the occurrence of the maximum resultant acceleration at each floor.

The Fourier Transform of the accelerations indicated in Fig. 6-4 is shown in Fig. 6-5a, b. The floor acceleration envelopes is shown in Fig. 6-5c. Fig. 6-5a, b show that higher mode contribution can be observed in *PII-roller*. Fig. 6-5c shows that a significant

acceleration reduction can be observed in *PI* in comparison to that in *PII-roller*. The maximum resultant acceleration in *PII-roller* is larger than that of *PII-wo/FD*. This analysis implies that the use of roller bearing in Phase II doesn't reduce the maximum acceleration responses of the structures in earthquakes.

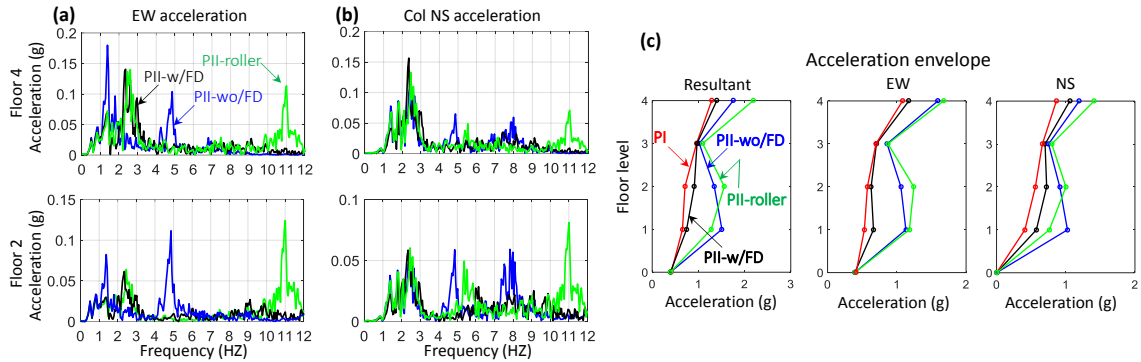


Fig. 6-5. Acceleration: Fourier Transform of the floor acceleration indicated in Fig. 6-4 at: (a) level 4; (b) level 2; (c) envelopes.

6.1.3 Influence from Eccentric Wall and Concentric Wall

The influence from the North wall eccentricity is studied in this section (See Fig. 6-6). In addition, the applied post-tensioned force were not exactly the same between different tests. In this section, the same post-tensioned force ($\rho=0.6$) is applied to the PT walls of the IFAS and traditional structures so that the influence from the different wall strength is eliminated.

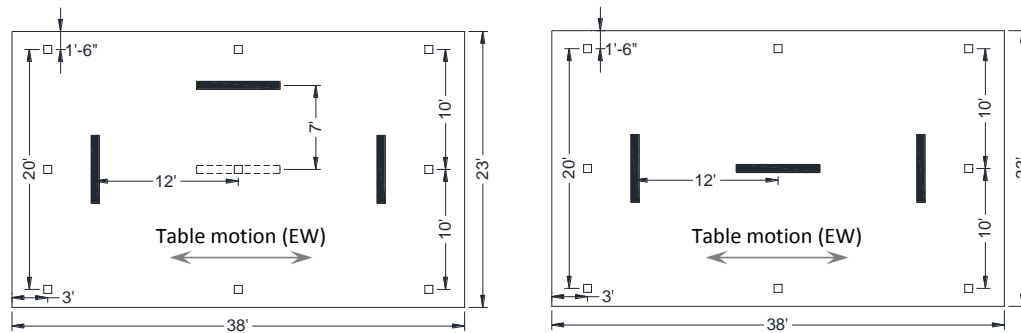


Fig. 6-6. Structure layout: (a) eccentric; (b) concentric.

A list of models used in this section is shown in Table 6-2. The earthquake used for the analysis is BE DBE.

Table 6-2. Description of models with different LFRS eccentricity.

Model	PT ratio at North wall (ρ_{EW})	PT ratio at transverse walls (ρ_{NS})	Eccentric or Concentric North wall	Note
PI-0.6	0.6	0.6	Eccentric	IFAS structure, $\alpha=0.57$
PII-wo/FD-0.6	0.6	0.6	Eccentric	Traditional structure wo/FD
PII-w/FD-0.6	0.6	0.6	Eccentric	Traditional structure w/FD
PI-0.6-Con	0.6	0.6	Concentric	IFAS structure, $\alpha=0.57$
PII-wo/FD-0.6-Con	0.6	0.6	Concentric	Traditional structure wo/FD
PII-w/FD-0.6-Con	0.6	0.6	Concentric	Traditional structure w/FD

The structure responses of the structures using the wall with $\rho=0.6$ is shown in Fig. 6-7. The slab twisting of the concentric case was not plotted because the twisting is close to zero. The following conclusions can be drawn from the figure: (1) the floor acceleration is significantly decreased by using the IFAS for concentric and eccentric cases (See Fig. 6-7a); (2) the North wall deformation is significantly decreased by using the IFAS for concentric and eccentric cases (See Fig. 6-7b); (3) the slab twisting is decreased by using the IFAS (See Fig. 6-7d); (4) the GLRS drift of the traditional structure using the eccentric wall was amplified due to the twisting (See Fig. 6-7c); (5) the maximum floor acceleration of the structures using the eccentric wall is amplified due to the twisting (See Fig. 6-7a); (6) the North wall drift of the structures using the eccentric wall is decreased (See Fig. 6-7b). The figure shows that structures using the eccentric wall can produce larger floor acceleration and smaller North wall deformation in earthquakes in comparison to those using the concentric wall. The use of the IFAS can effectively reduce the floor acceleration and North wall drift. This set of analyses proves that the slab twisting will not influence the efficacy of the IFAS.

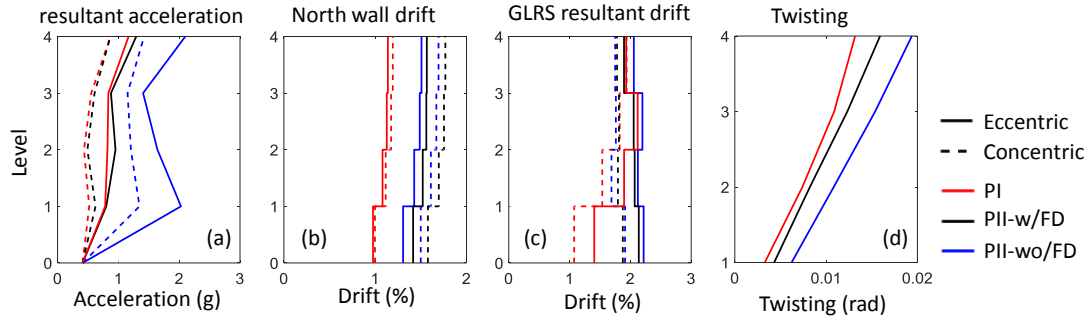


Fig. 6-7. Structure response envelopes between eccentric and concentric cases ($\rho=0.6$, $\alpha=0.57$): (a) floor acceleration; (b) North wall drift; (c) GLRS drift; (d) slab twisting.

The energy dissipation in each component from the three models are shown in Appdx. D.1. The PSA and FD force is shown in Appdx. D.2.

The effectiveness of the IFAS is studied for a structure using transverse walls with different yield strength (See Appdx. D.3).

6.1.4 Influence from Bumper Stiffness

An influence from the bumper stiffness to the IFAS performance is studied in this section. The floor acceleration will be increased when the bumper is engaged because larger force can be transferred from the slab to the wall.

The bumper force-deformation property is shown in Fig. 6-8a. Black represents the bumper used in the shake table test (Ordinary bumper). Red represents a bumper which is stiffer than the Ordinary bumper (Stiffer bumper). The floor acceleration, North wall drift and slab twisting envelopes are shown in Fig. 6-8b, c, d respectively. The floor acceleration is increased as the bumper stiffness increases (See Fig. 6-8b). However, the North wall drift and slab twisting undergo negligible influences.

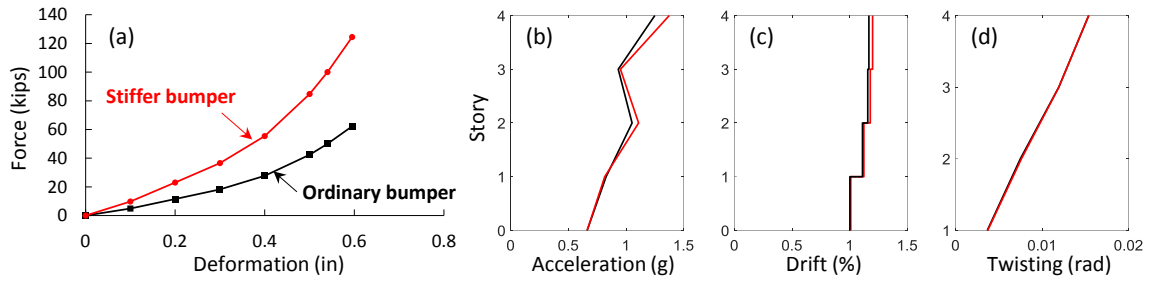


Fig. 6-8. Bumper property and structure responses: (a) bumper force-deformation; response envelope: (b) floor acceleration; (c) North wall drift; (d) slab twisting.

6.2 Analyses of the Calibrated Model

The structure responses of the CM doesn't match the Test 17 well, but it can still be used to study the influence from the structure damage to the IFAS performance as mentioned in Sec. 5.6.3. Structure damage is proved as one of the reason for not obtaining acceleration reduction in Phase I of the shake table test in comparison to Phase II, however, how is this influence distributed between the GLRS damage and LFRS damage is interesting. This section provides a preliminary study on the influence from the different softening components in the structure to the floor acceleration. The damage is identified as GLRS damage and LFRS damage. Therefore, four models are used for the investigation. The models are shown in Table 6-3. Note that all the four models are used for modeling Test 17, meaning the FDs and BRBs are used in the model.

Table 6-3. Description of model with different damage source.

Model	Note
PSWPCol	Pristine LFRS, pristine GLRS
PSWDCol	Pristine LFRS, damaged GLRS
DSWPCol	Damaged LFRS, pristine GLRS
DSWDCol	Damaged LFRS, damaged GLRS

The resultant floor acceleration and North wall drift are shown in Fig. 6-9. Red represents the responses of Test 17. The black and green represent the model using pristine and damaged LFRS respectively. The solid and dashed lines represent the model using damaged and pristine GLRS respectively. Fig. 6-9a shows that the model using the pristine columns produces larger acceleration at upper floors. The model using the pristine LFRS and damaged GLRS matches better to the test. Fig. 6-9b shows that the model using the pristine GLRS produces the smallest North wall deformation, no matter a pristine North wall or a damaged North wall is used.

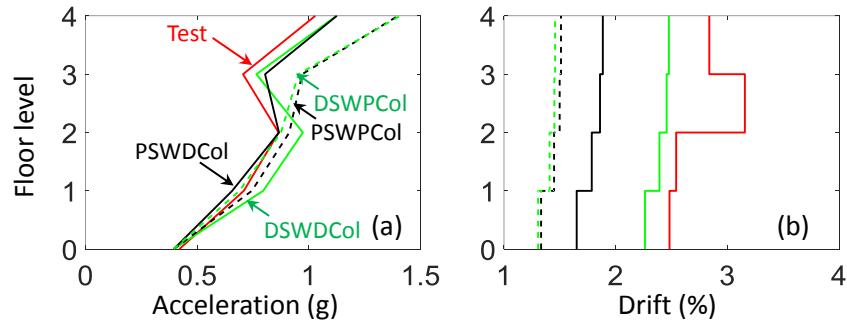


Fig. 6-9. Structure response envelopes: (a) resultant floor acceleration; (b) North wall drift.

The North wall moment-rotation is shown in Fig. 6-10. The figure shows that when the pristine GLRS is used in the model, the deformation demand of the North wall is decreased.

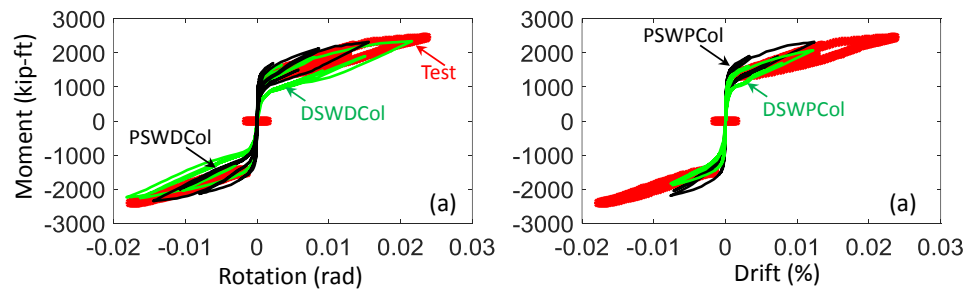


Fig. 6-10. North wall moment-rotation: (a) models using damaged GLRS; (b) models using pristine GLRS.

The structure overturning moment-roof drift at column line B is shown in Fig. 6-11. The figure shows that when the pin connection is used between the columns and slabs, the numerical model underestimates the structure overturning moment. If the pristine GLRS is used in the numerical models, the overturning moment can be predicted.

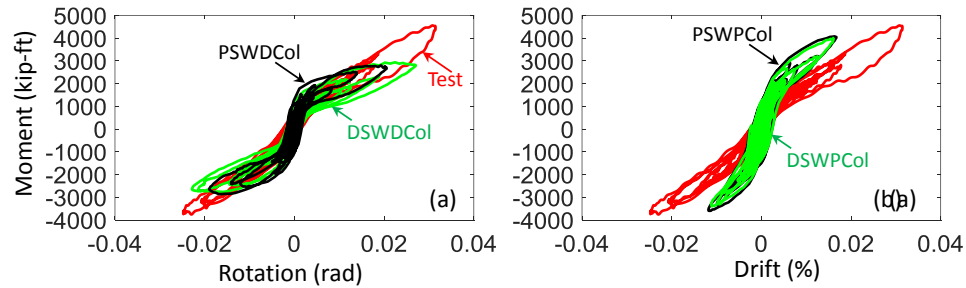


Fig. 6-11. Structure overturning moment-roof drift at column line B: (a) models using damaged GLRS; (b) models using pristine GLRS.

6.3 Conclusions for Calibrated 3D Model Analyses

The Updated and Calibrated models are analyzed extensively in this chapter for the purpose of validating the IFAS effectiveness in the following conditions: (1) the influence from different transverse wall strength; (2) the influence from the structure asymmetry; (3) the influence from the different type of floor anchorage in the traditional structure; (4) the influence from the bumper stiffness; (5) the influence from the structure damage. The following conclusions can be drawn from the study:

- (1) The floor acceleration and LFRS deformation can be effectively reduced by using the IFAS in the structure, for either a symmetric or an asymmetric floor plan;
- (2) A great amount of energy is dissipated by the deformable connections of the IFAS in earthquakes, therefore the structural components are protected due to less energy dissipation in comparison to that in the traditional structure;

(3) The floor acceleration can be effectively reduced by adding dampers with energy dissipation capacity to the traditional structure;

(4) A stiffer bumper can produce larger floor acceleration of an IFAS structure.

(4) The structure using the damaged GLRS produces smaller acceleration in comparison to that using the pristine GLRS. Therefore, the damage of the GLRS has larger influence to the floor acceleration than the damage of the LFRS. However this conclusion needs to be validated through a parametric study using different level of damage for LFRS and GLRS.

7. Bumper Impact Testing

7.1 Test Introduction

The bumper is a key device for limiting the relative displacement between the floor and LFRS. In addition, the bumper is used for decreasing the impact force between the floor and LFRS.

7.1.1 Test Objective

This test was conducted for the purpose of investigating the force-deformation property of the bumper under high loading rate and different types of loading displacement time histories. The bumper force-deformation behavior was determined by a quasi-static test and used in the shake table test specimen model. In the shake table test, the deformation history of the bumper was estimated based on measurements, but the bumper force wasn't measured. Additionally, the bumper may be underwent heating up and change its force-deformation property due to repeated compression. This behavior is very difficult or impossible to track in a structure level test. Thus, the experimental study of bumper is very necessary.

7.1.2 Test Set Up and Tested Bumper

The bumper test was conducted in the full-scale sub-structure component mentioned in Chapter 1. There were two major components for this set-up: one was the wall that was fixed in the middle, the other was the post-tensioned reinforced concrete slab which was put around the wall and connected to two actuators. The bumper was installed on the slab (red circle in Fig. 7-1). The test specimen and the related actuators are shown in Fig. 7-2.

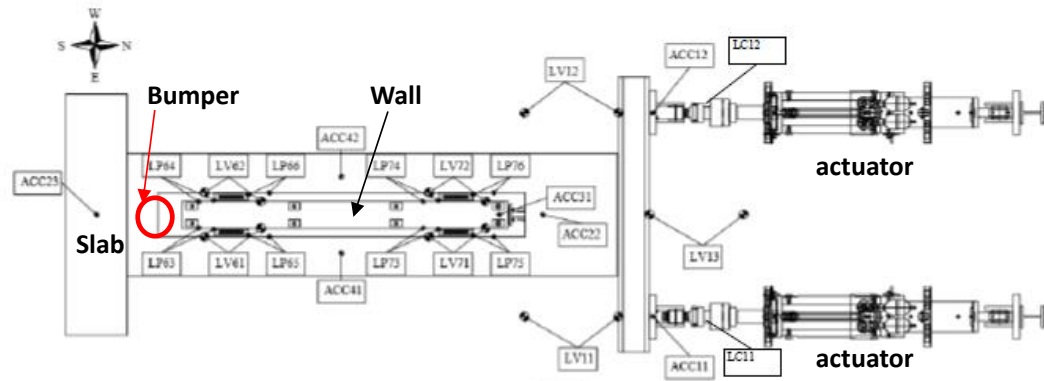


Fig. 7-1. Test set up (Courtesy of Tsampras Georgios).

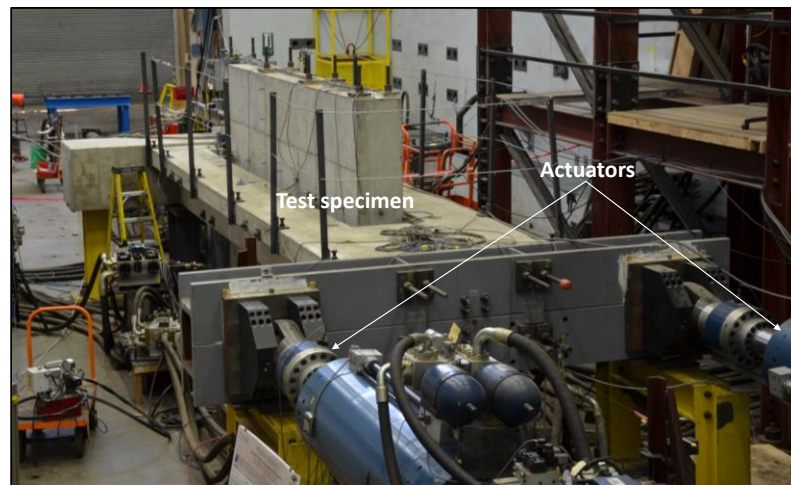


Fig. 7-2. Photo of the test specimen and the connected actuators.

Two types of bumpers were tested in this experimental program: (1) yellow bumper; (2) black bumper (See Fig. 7-3). Both bumpers were used in the shake table test program.

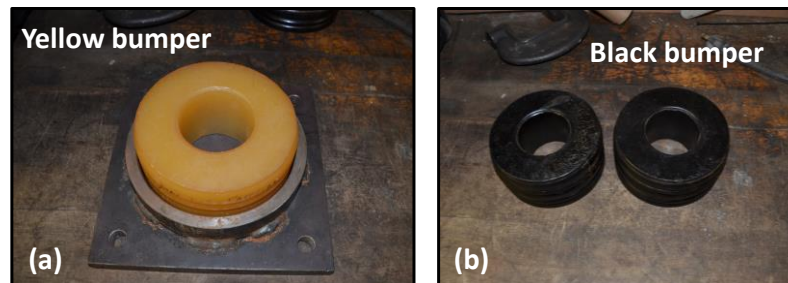


Fig. 7-3. Photo of the tested bumper: (a) yellow bumper; (b) black bumper.

7.1.3 Instrumentation Plan

The instrumentation plan of the test is shown in Fig. 7-4. Fig. 7-4a shows the instrumentation around the bumper from top view. One load cell was put on a steel plate bolted on the wall for recording the impact force. One accelerometer was installed near the bumper on the slab, the 2nd accelerometer was installed on the wall above the load cell. Both accelerometers were used for recording impact acceleration. One high speed camera was installed right above the load cell for recording the impacting process. Fig. 7-4b shows the LVDTs used at the bottom of the bumper. The LVDT directly underneath the bumper is termed “control LVDT”. The control LVDT was connected between the wall and slab. The measurement from the control LVDT is used to represent the slab displacement during the test. Two spring loaded LVDTs are shown in the photo. Fig. 7-4d shows the zoom in of the top view, four spring loaded LVDTs are indicated, as well as the control LVDT. A flat steel plate with two angles was put in front of the load cell. This steel plate was used to take and transfer the impact force from the bumper to the load cell. Fig. 7-4c, e shows the locations of two cameras used in the test.

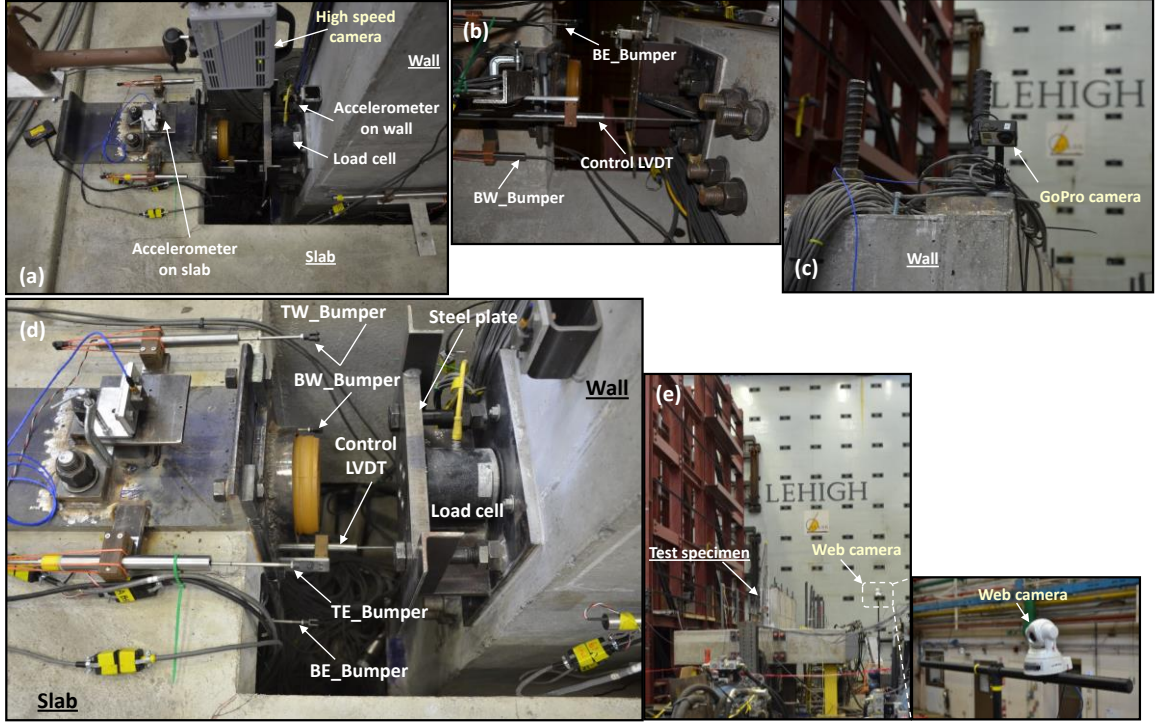


Fig. 7-4. Instrumentation plan: (a) top view - zoom out; (b) bottom view; (c) GoPro camera at the wall top; (d) top view – zoom in; (e) location and zoom in of the web camera.

7.1.4 Test Process and Test Parameters

During the test, predefined displacement time histories (will be explained later) was given to the actuators and the slab was driven by the actuators following the predefined displacement time histories. The bumper moved with the slab and hit the steel plate shown in Fig. 7-4d. The bumper deformation and force were measured during the whole test process so that the bumper force-deformation property can be achieved.

Four parameters were assumed to have influence on the bumper force-deformation behavior. These four parameters are termed as test parameters: initial velocity (V_0); maximum deformation (δ_{max}); bumper engagement duration (δT); releasing velocity (V_r).

7.1.5 Test Protocol

Four different types of predefined displacement time histories were used in this test: (1) simplified single pulse displacement protocol (See Fig. 7-5a); (2) smoothed bumper deformation (one pulse) time history from the shake table test (See Fig. 7-5b); (3) cyclic deformation using constant loading velocities (See Fig. 7-5c); (4) mimicking bumper deformation time history (cyclic test with time gap) from the shake table test (See Fig. 7-5d). The advantages and disadvantages of each protocol are shown in Appdx. E.1.

Each predefined displacement time history includes four parts: (1) the left green curve represents the ramp up part that accelerate the slab from static to V_0 ; (2) the blue line represents the loading part before hitting the bumper with constant velocity, V_0 ; (3) the red curve represents the range between the beginning and end of the engagement of the bumper; (4) the right green curve represents the releasing part that moves the slab back to its original location.

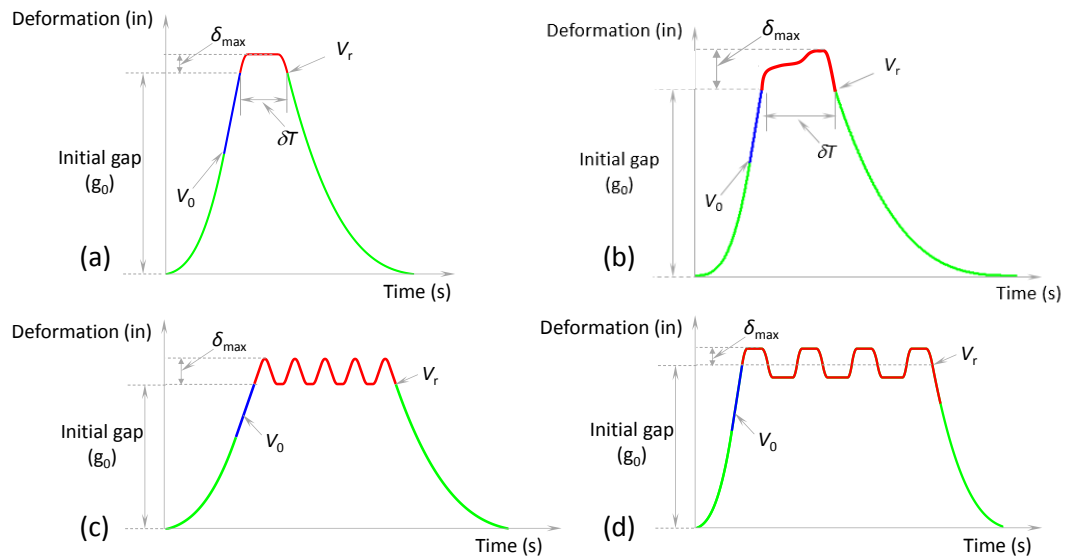


Fig. 7-5. Predefined displacement time history: (a) simplified single pulse; (b) smoothed bumper deformation from the shake table test; (c) cyclic deformation using constant loading velocity; (4) mimicking bumper deformation from the shake table test.

7.1.6 Determination of the Test Parameters

The four test parameters can be obtained from each bumper deformation time history from the shake table test. Therefore, plenty of combinations of the four test parameters are obtained. The test parameters were classified by V_0 and linear regression analysis was applied to obtain the relationship between every two parameters. V_0 used for classifying the test parameters are: 1 in/s, 5 in/s, 10 in/s, 15 in/s and 20 in/s. The details of this classification is shown in Table 7-1 and the related scatter plots are shown in Fig. E-1 (Appdx. E.2).

Table 7-1. Scatter plots classification using different V_0 .

V_0 (in/s)	V_0 range	V_0 / V_r	$\delta T / \delta_{\max}$
1	$0.5 \text{ in/s} < V_0 < 1.5 \text{ in/s}$	4.74	2.4
5	$4 \text{ in/s} < V_0 < 6 \text{ in/s}$	1.90	1.64
10	$9 \text{ in/s} < V_0 < 11 \text{ in/s}$	0.79	1.28
15	$14 \text{ in/s} < V_0 < 16 \text{ in/s}$	0.54	1.26
20	$V_0 > 16 \text{ in/s}$	0.44	1.33

7.2 Preliminary Bumper Force-Deformation Responses

A set of tests were conducted on the bumpers. The test results will be systematically studied in another Ph. D. Dissertation. A few preliminary comparisons will be shown in this section for obtaining a general idea of the bumper force-deformation behavior using different test parameters.

7.2.1 Bumper Response Time History

A test is selected for the purpose of showing the bumper response under impacting load (See Fig. 7-6). The test parameters used for this test are indicated at the right bottom of the figure.

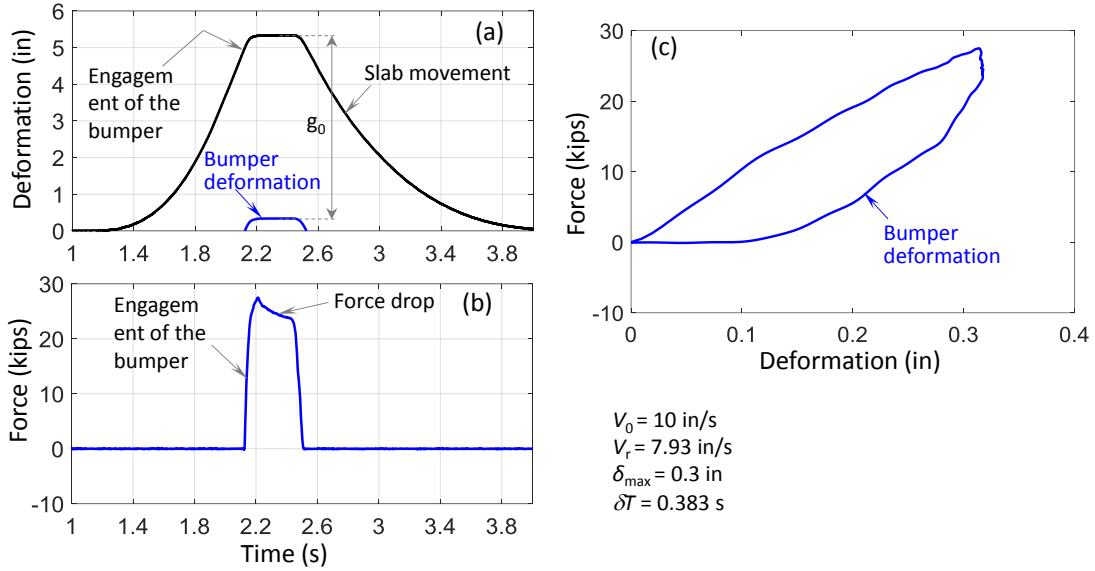


Fig. 7-6. Bumper response time history: (a) deformation; (b) force; (c) force-deformation.

Fig. 7-6a shows the slab displacement time history (solid black). The bumper deformation time history (solid blue) is obtained by subtracting the initial gap between the bumper and steel plate. The bumper is held at the maximum deformation for some time (holding time) and then underwent releasing from the engagement. Fig. 7-6b shows the measured bumper force time history. A peak is observed when the bumper reaches its maximum deformation. The bumper force dropped as the holding time increases, meaning the bumper force will be released as the engagement duration increases at a constant deformation. Fig. 7-6c shows the bumper force-deformation behavior.

7.2.2 Effect of the Maximum Deformation

The yellow bumper force-deformation under different δ_{\max} at $V_0=5$ in/s and $V_0=10$ in/s are shown in Fig. 7-7a, b respectively. The figure shows that the stiffness of the bumper is increased as the deformation increases.

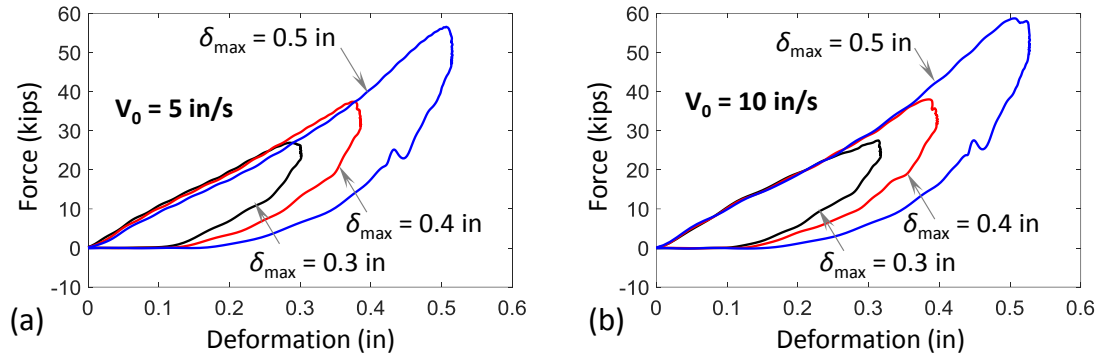


Fig. 7-7. Bumper force-deformation behavior: (a) $V_0 = 5 \text{ in/s}$; (b) $V_0 = 10 \text{ in/s}$.

7.2.3 Effect of the Initial Velocity

The yellow bumper force-deformation under different V_0 at $\delta_{\max} = 0.4 \text{ in}$ and $\delta_{\max} = 0.5 \text{ in}$ are shown in Fig. 7-8a, b respectively. The figure shows that the bumper initial loading stiffness doesn't change for different V_0 .

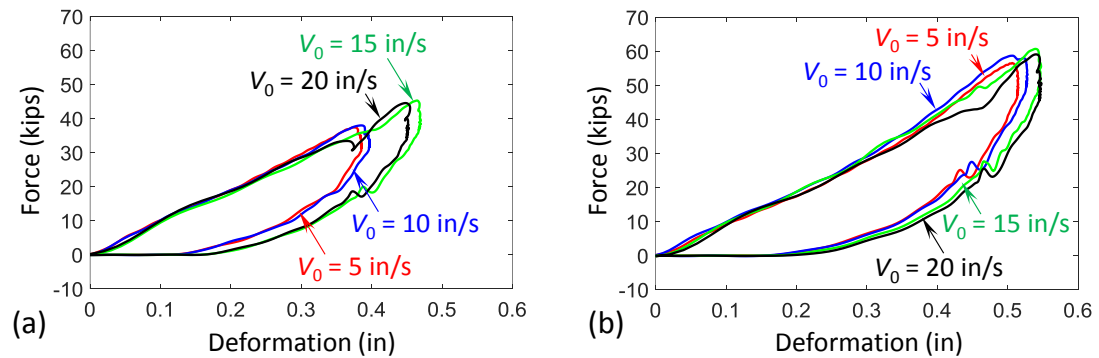


Fig. 7-8. Bumper force-deformation behavior: (a) $\delta_{\max} = 0.4 \text{ in}$; (b) $\delta_{\max} = 0.5 \text{ in}$.

7.2.4 Cyclic Loading

The yellow bumper force-deformation under cyclic loading is shown in Fig. 7-9. Four cycles were tested on the bumper.

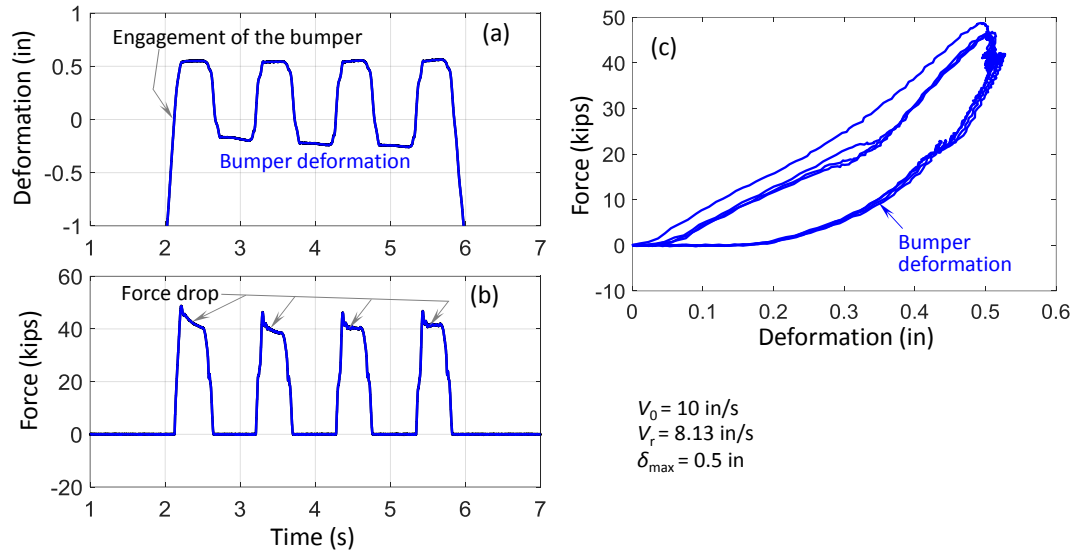


Fig. 7-9. Bumper response time history: (a) revised slab displacement; (b) force; (c) force-deformation.

Fig. 7-9a shows the revised slab displacement, the bumper deformation is the part when the deformation is larger than 0. A time gap was used between each loading cycle. Fig. 7-9b shows the measured bumper force. Force drop is observed for each cycle while the bumper is holding at a constant deformation. Additionally, the peak bumper force in the last three cycles was smaller than the peak bumper force in the first cycle. Fig. 7-9c shows the Bumper force-deformation behavior. A delay in taking the force is observed in the last three cycles.

7.3 Conclusions for Bumper Impact Testing

This chapter provides a simple introduction of the test program on investigating the bumper force-deformation under high loading rate at NEHRI@Lehigh. Four test parameters were introduced and regression analysis was applied to obtain the relationship between every two test parameters. Four different test protocols were used in the test.

Preliminary test results are presented. The following conclusions can be drawn in this chapter:

- (1) The bumper initial loading stiffness is independent from V_0 ;
- (2) The bumper force drops as the bumper compressive deformation is under holding;
- (3) The first cycle reaches a larger peak bumper force if the bumper undergoes cyclic loading.

8. CONCLUSIONS AND SUGGESTED FUTURE WORK

This dissertation focuses on the analytical investigation of the development and performance of structures using an innovative floor anchorage system, the IFAS. The IFAS is developed for reducing the floor acceleration and LFRS drift demands in earthquakes, thereby mitigating the structural and non-structural component damage.

To this end, a suite of analytical studies were performed for determining the characteristics of the IFAS, the influence of different design parameters, and validating the effectiveness of use the IFAS. Classical solutions of simplified 2DOF IFAS models under harmonic motions were derived and a design optimization for this system was performed. Extensive 2D parameter studies were performed to determine the IFAS design space, A half-scale shake table test was used for proving the IFAS effectiveness experimentally and validating 3D nonlinear numerical models. The 3D numerical model is used for extensive analyses after updating and calibration.

8.1 Conclusions

The conclusions for 2DOF system investigation are:

- Target curve provides a relationship among (ϕ, μ, β) that can be used for a single-objective optimization of the elastic 2DOF IFAS system. The target curve works with two limitations: $\beta > 0$ and $\xi = \xi_{\text{opt}}$. Thus, the applicable range of the design parameters is limited.
- The PSM can be used for determining the optimum design in Regions I and II through multi-objective optimization. The optimum design is proved to produce significant response reduction via earthquake simulations.

- The design space of the elastic 2DOF system exists for a specific range when $\phi=0.03$: $1.4 \leq \mu \leq 20$; $0.2 \leq \beta \leq 0.3$ ($\mu \geq 7$) or $0.1 \leq \beta \leq 0.25$ ($\mu \leq 6$). A range of ζ can produce acceptable response for each (μ, β) . These results show that the optimization design is not sensitive to μ , but is sensitive to β . Only a band of β can provide accepted 2DOF system responses.
- The design space of the inelastic 2DOF system exists for a specific range when $\phi=0.03$: $\mu \geq 7$ and $\alpha' \leq 0.5$.
- Higher mode effect is not reflected in the traditional inelastic 2DOF system. Therefore, no significant reduction of the floor acceleration is observed from a traditional 2DOF system to a 2DOF IFAS system.

The conclusions for the 2D evaluation structure models are:

- The use of the IFAS can effectively reduce the floor acceleration and LFRS drift. Larger reduction of the acceleration can be observed in 8-, 12-story structures in comparison to 4-story structures. The GLRS drift and relative displacement are increased as α decreases.
- The LFRS drift is reduced as α decreases. Larger Ω_e and smaller γ produce lower LFRS drift. The reduction in the LFRS drift of the structure ($\Omega_e=1.3$) occurs mostly when $\alpha < 1$. α needs to be reduced to obtain a LFRS drift reduction as Ω_e decreases. The use of rocking wall doesn't have influence on the LFRS drift for an IFAS structure (when $\alpha < 0.5$), but the use of rocking wall does increase the LFRS drift for a traditional structure. The LFRS drift decreases as the relative displacement increases. The LFRS drift and the relative displacement is almost linear.

- The floor acceleration is increased as Ω_e and γ increase. The use of rocking wall also increases the floor acceleration. However, acceleration is reduced as α decreases (for $\alpha < 1.5$). In addition, the acceleration is reduced significantly when the relative displacement exceeds 2".
- The GLRS drift and relative displacement are increased as α decreases. 3% is the GLRS drift limitation in MCE, and none of the GLRS drift exceeds this limitation while the relative displacement satisfy the aggressive design limit (8"). The relative displacement is increased as Ω_e increases. The relative displacement is increased as γ decreases. 4-story structures produces less relative displacement than 8-, 12-story structures.
- A valley can be observed in the GLRS drift of a 4-story IFAS structure when the rocking wall is used as the LFRS ($0.3 < \alpha < 1$). This phenomenon implies that there is a possibility to obtain reduction in floor acceleration, LFRS drift and GLRS drift simultaneously in a rocking wall structure through using the IFAS.
- A relationship between the LFRS drift and relative displacement directly provide the relation between the benefit and tradeoff of using the IFAS. This relationship can be directly used for decision making because floor acceleration will be automatically reduced once the relative displacement exceeds 2".
- The use of bumper provides a possibility of obtaining larger LFRS drift reduction while keeping the relative displacement below the aggressive limit.

Conclusions for the shake table tests are:

- Different α were tested in the shake table test ($\alpha=0.57, 0.44$ for the BE site; $\alpha=0.75, 0.57$ for the SE site). The effectiveness in reducing the LFRS drift through using the IFAS was proved from the shake table test.
- The effectiveness in reducing the floor acceleration through using the IFAS was not observed in the shake table test. The possible reasons are: (1) unavoidable structure damage; (2) the FDs and BRBs were left in place in Test 15 – Test 17. These two reasons are proved by analytical studies.
- Slab twisting can be reduced through using the IFAS.
- The IFAS used in the shake table test worked as expected. The ideas of the IFAS configuration was validated.
- The bumper engaged several times in the MCE tests and arrested the relative displacement as expected.

Conclusions for 3D nonlinear model development and calibration are:

- The updated 3D nonlinear model matches the test structure responses well and can properly capture the cumulative damage during a sequential analysis. This indicates that the modeling methodology is accurate and can be applied to further studies.
- The calibrated 3D nonlinear model doesn't match the test specimen well, but can be used to evaluate the influence from the structure damage. The calibrated 3D nonlinear model proves that the structure damage decreases the floor acceleration via NTHA.

- The use of eccentric LFRS does not have influence on the efficacy of using the IFAS. The floor acceleration is amplified in a structure using the eccentric LFRS in comparison to that using the concentric LFRS.
- The IFAS is effective in reducing the floor acceleration and LFRS drift.

In summary, the following main conclusions are drawn from this dissertation:

(1) Target curve can be used for a single-objective optimization of the elastic 2DOF IFAS system. However, the applicable range of the target curve is limited.

(2) The PSM can be used for determining the optimum design of the 2DOF system in Regions I and II through multi-objective optimization. The optimum design produces significant response reduction via earthquake simulations. The design space across large μ span ($1.4 \leq \mu \leq 20$).

(3) Several design parameters were analytically investigated in the parametric study of 2D evaluation structure models. The floor acceleration and LFRS drift are more dependent on the following design parameters: structure height, IFAS strength, LFRS overstrength, IFAS secondary stiffness. The floor acceleration and LFRS drift are decreased as α decreases. The LFRS and GLRS drift are decreased as Ω_e increases. The floor acceleration and relative displacement are increased as Ω_e increases. The LFRS drift, floor acceleration are increased as γ increases. The relative displacement is decreased as γ increases. The GLRS drift is not sensitive to γ .

(4) The LFRS drift is decreased as the relative displacement increases. The floor acceleration is decreased significantly when the relative displacement is larger than 2". Therefore, the relation between the LFRS drift and relative displacement can be used for determining the preliminary design of the IFAS. LFRS drift provides the benefit of the

IFAS, the relative displacement provides the IFAS deformation limitation. The relation between the IFAS strength and relative displacement can be used to determining the IFAS strength afterwards.

(5) The shake table test validated the efficacy of the IFAS in reducing the LFRS drift, slab twisting in earthquakes. The test also showed that the devices of the IFAS performed as expected.

(6) The modeling methodology is accurate to model the test structure and can be applied to other analytical studies. The analytical studies indicate that:

- The IFAS is effective in reducing the floor acceleration, LFRS drift, slab twisting.
- Structure damage and using energy dissipation devices in the structure cause reduction of the floor acceleration.

8.2 Suggested Future Work

The following work is proposed for future research on this topic:

(1) Develop the design space of the IFAS structure. As mentioned in Chapter 4, several key design parameters were investigated analytically for the IFAS structure and a preliminary design method is provided. However, to develop a feasible and robust IFAS design methodology for a given structure, further studies are required.

(2) Better calibration of the damage model to the test specimen is required. As mentioned in Chapter 5, the Calibrated model can be used to represent a damaged structure, and study the damage influence on the structure response. However, the model is not good enough for modeling the damaged test specimen in Phase II. A better Calibrated model for

the Phase II test specimen will provide more accurate result about the influence from the structure damage to the structure responses.

(3) Update the bumper model to match the bumper force-deformation from the bumper test. The current bumper model is a simplified multi-linear elastic spring that matches the loading stiffness of the bumper and doesn't consider the energy dissipation capacity. Once an updated bumper model matches the test force-deformation, the influence from the bumper to the structure response can be investigated.

(4) Apply the modeling methodology to full scale structure and investigate the design space and efficacy of the IFAS.

APPENDIX A – SUPPLEMENTAL INFORMATION FOR CHAPTER 3

A.1 Development of the Simplified 2DOF System

The development of the 2DOF system from the 12-story evaluation structure will be presented in this section. The methods used for this development is based on the procedure that was explained in [116]. The LFRS and GLRS are assumed rigid connected in the evaluation structure.

A.1.1 Modal Property of the 12-story Evaluation Structure

The stiffness matrix of the LFRS, \mathbf{k}_{LFRS} , is obtained by taking an inverse of the flexibility matrix [116]. The LFRS shear deformation is considered in the flexibility matrix. The stiffness matrix of the GLRS, \mathbf{k}_{GLRS} , is obtained by assuming GLRS as a shear building. The GLRS stiffness in each floor is calculated using the portal method [117], assuming the inflection points are at the middle of the columns and beams in the GLRS.

The mass matrix and stiffness matrix of the structure are written in the form:

$$\mathbf{m} = \mathbf{m}_{\text{GLRS}} + \mathbf{m}_{\text{LFRS}} \quad (\text{A-1})$$

$$\mathbf{k} = \mathbf{k}_{\text{GLRS}} + \mathbf{k}_{\text{LFRS}} \quad (\text{A-2})$$

where \mathbf{m} , \mathbf{k} represent the mass and stiffness matrix of the evaluation structure. \mathbf{m}_{LFRS} , \mathbf{m}_{GLRS} represent the mass matrix of the LFRS and GLRS of the evaluation structure.

The modal mass matrix is:

$$\mathbf{M} = \mathbf{\Phi}^T \mathbf{m} \mathbf{\Phi} \quad (\text{A-3})$$

where $\mathbf{\Phi}$ represents the modal matrix.

The effective modal mass, M_n^* , in the n th mode can be calculated using:

$$M_n^* = L_n^h \Gamma_n = (L_n^h)^2 / M_n \quad (\text{A-4})$$

where $\Gamma_n = L_n^h/M_n$, $L_n^h = \Phi_n^T \mathbf{m} \mathbf{u}$, $M_n = \Phi_n^T \mathbf{m} \Phi_n$, $\mathbf{u} = [1]_{12 \times 1}$.

The effective stiffness, K_n^* , in the n th mode can be calculated using:

$$K_n^* = M_n^*/(T_n/(2\pi))^2 \quad (\text{A-5})$$

where T_n represents the evaluation structure period in the n th mode.

The effective modal height, H_n^* , in the n th mode can be calculated using:

$$H_n^* = L_n^\theta/L_n^h \quad (\text{A-6})$$

where $L_n^\theta = \Phi_n^T \mathbf{m} \mathbf{H} = \sum_{i=1}^N m_i \phi_{in} H_i$, \mathbf{H} is a vector of the floor height, N is the number of stories.

The M_n^* , K_n^* , H_n^* only depends on the total mass and total stiffness of the structure.

The mass and stiffness distribution between the LFRS and GLRS doesn't influence these three modal responses.

A.1.2 Modal Expansion of the Equivalent Lateral Force

The portion of the seismic base shear induced at each floor is denoted with \mathbf{F} , from the equivalent lateral force procedure [5]. The n th mode contribution to \mathbf{F} is s_n , calculating using:

$$s_n = \Gamma_n^F \mathbf{m} \Phi_n \quad (\text{A-7})$$

where $\Gamma_n^F = \Phi_n^T \mathbf{F}/M_n$.

Then, the lateral force at the j th floor in the n th mode, s_{jn} , can be expressed as:

$$s_{jn} = \Gamma_n^F m_j \phi_{jn} \quad (\text{A-8})$$

The shear force at the j th floor in the n th mode, V_{jn} , can be calculated using:

$$V_{jn} = \sum_{i=j}^N s_{in} = \sum_{i=j}^N \Gamma_n^F m_i \phi_{in} \quad (\text{A-9})$$

The moment at the j th floor in the n th mode, M_{jn} , can be calculated using:

$$M_{jn} = \sum_{i=1}^N V_{in} h_i \quad (\text{A-10})$$

The base shear force in the n th mode, V_{bn} , can be calculated using:

$$V_{bn} = \sum_{i=1}^N s_{in} = \Gamma_n^F \sum_{i=1}^N m_i \phi_{in} = \Gamma_n^F L_n^h \quad (\text{A-11})$$

The base moment in the n th mode, M_{bn} , can be calculated using:

$$M_{bn} = \sum_{i=1}^N s_{in} H_i = \Gamma_n^F \sum_{i=1}^N m_i \phi_{in} H_i = \Gamma_n^F L_n^\theta \quad (\text{A-12})$$

A.1.3 Modal Expansion of the IFAS Strength

The IFAS in the evaluation structure should be converted to a single IFAS in the 2DOF system. If the IFAS is assumed as elastic, the only IFAS parameter (stiffness), k_3 , is represented by β and under studied for the purpose of finding the optimized structural response. If the IFAS is assumed as elastic-perfectly plastic, the IFAS strength in the 2DOF system should be determined properly. If the IFAS strength in the evaluation structure is represented as F_y , then the n th mode contribution to the F_y can be calculated using:

$$\mathbf{s}_n^{Fy} = \Gamma_n^{Fy} \mathbf{m} \boldsymbol{\phi}_n \quad (\text{A-13})$$

where $\Gamma_n^{Fy} = \boldsymbol{\phi}_n^T \mathbf{F}_y / M_n$.

The summation of the IFAS strength along the evaluation structure height in the n th mode is assumed as the IFAS strength in the n th mode:

$$F_{y,n} = \sum_{i=1}^N s_{ni}^{Fy} \quad (\text{A-14})$$

A.1.4 Modal Properties of the 2DOF System

$M_1^*, K_1^*, h_1^*, V_{b1}, M_{b1}, F_{y,1}$ are assigned to the mass, stiffness, height, designed base shear, designed base moment and IFAS strength of the 2DOF system. M_1^*, K_1^* are the summation of the mass and stiffness of the LFERS and GLRS in the 2DOF system respectively:

$$M_1^* = m_1 + m_2 \quad (\text{A-15})$$

$$K_1^* = k_1 + k_2 \quad (\text{A-16})$$

A.2 Response of the Elastic 2DOF System Using the Undamped LFRS

A.2.1 Dynamic Equation Derivation

$$\frac{x_1}{x_{st}} = \frac{1+\phi}{1+\mu} \frac{\left[\mu \frac{1+\phi}{1+\mu} \left(\frac{\omega}{\omega_n} \right)^2 - (\phi + \beta + \mu\beta) \right] - i[2\xi(1+\phi)(1+\mu) \left(\frac{\omega}{\omega_n} \right)]}{\left[\mu \left(\frac{1+\phi}{1+\mu} \left(\frac{\omega}{\omega_n} \right)^2 \right)^2 - (\phi + \beta + \mu + \mu\beta) \frac{1+\phi}{1+\mu} \left(\frac{\omega}{\omega_n} \right)^2 + (\phi + \beta + \phi\beta) \right] + i[2\xi(1+\phi)^2 \left(1 - \left(\frac{\omega}{\omega_n} \right)^2 \right) \left(\frac{\omega}{\omega_n} \right)]} \quad (\text{A-17})$$

$$\frac{x_2}{x_{st}} = \frac{1+\phi}{1+\mu} \frac{\left[\mu \frac{1+\phi}{1+\mu} \left(\frac{\omega}{\omega_n} \right)^2 - (\mu + \beta + \mu\beta) \right] - i[2\xi(1+\phi)(1+\mu) \left(\frac{\omega}{\omega_n} \right)]}{\left[\mu \left(\frac{1+\phi}{1+\mu} \left(\frac{\omega}{\omega_n} \right)^2 \right)^2 - (\phi + \beta + \mu + \mu\beta) \frac{1+\phi}{1+\mu} \left(\frac{\omega}{\omega_n} \right)^2 + (\phi + \beta + \phi\beta) \right] + i[2\xi(1+\phi)^2 \left(1 - \left(\frac{\omega}{\omega_n} \right)^2 \right) \left(\frac{\omega}{\omega_n} \right)]} \quad (\text{A-18})$$

$$\frac{x_2 - x_1}{x_{st}} = \frac{1+\phi}{1+\mu} \frac{\phi - \mu}{\left[\mu \left(\frac{1+\phi}{1+\mu} \left(\frac{\omega}{\omega_n} \right)^2 \right)^2 - (\phi + \beta + \mu + \mu\beta) \frac{1+\phi}{1+\mu} \left(\frac{\omega}{\omega_n} \right)^2 + (\phi + \beta + \phi\beta) \right] + i[2\xi(1+\phi)^2 \left(1 - \left(\frac{\omega}{\omega_n} \right)^2 \right) \left(\frac{\omega}{\omega_n} \right)]} \quad (\text{A-19})$$

$$\frac{\ddot{u}_1}{a_g} = \frac{\left[-\mu \frac{1+\phi}{1+\mu} \left(\frac{\omega}{\omega_n} \right)^2 + (\phi + \beta + \phi\beta) \right] + i[2\xi(1+\phi)^2 \left(\frac{\omega}{\omega_n} \right)]}{\left[\mu \left(\frac{1+\phi}{1+\mu} \left(\frac{\omega}{\omega_n} \right)^2 \right)^2 - (\phi + \beta + \mu + \mu\beta) \frac{1+\phi}{1+\mu} \left(\frac{\omega}{\omega_n} \right)^2 + (\phi + \beta + \phi\beta) \right] + i[2\xi(1+\phi)^2 \left(1 - \left(\frac{\omega}{\omega_n} \right)^2 \right) \left(\frac{\omega}{\omega_n} \right)]} \quad (\text{A-20})$$

$$\frac{\ddot{u}_2}{a_g} = \frac{\left[-\phi \frac{1+\phi}{1+\mu} \left(\frac{\omega}{\omega_n} \right)^2 + (\phi + \beta + \phi\beta) \right] + i[2\xi(1+\phi)^2 \left(\frac{\omega}{\omega_n} \right)]}{\left[\mu \left(\frac{1+\phi}{1+\mu} \left(\frac{\omega}{\omega_n} \right)^2 \right)^2 - (\phi + \beta + \mu + \mu\beta) \frac{1+\phi}{1+\mu} \left(\frac{\omega}{\omega_n} \right)^2 + (\phi + \beta + \phi\beta) \right] + i[2\xi(1+\phi)^2 \left(1 - \left(\frac{\omega}{\omega_n} \right)^2 \right) \left(\frac{\omega}{\omega_n} \right)]} \quad (\text{A-21})$$

Eqn. A-17 – Eqn. A-21 are in the form $x = \frac{A+iB}{C+iD}$ and thus the magnitude can be

expressed as $|x| = \sqrt{\frac{A^2+B^2}{C^2+D^2}}$.

$$\frac{|x_1|}{x_{st}} = \frac{1+\phi}{1+\mu} \sqrt{\frac{\left[\mu \frac{1+\phi}{1+\mu} \left(\frac{\omega}{\omega_n} \right)^2 - (\phi + \beta + \mu\beta) \right]^2 + [2\xi(1+\phi)(1+\mu) \left(\frac{\omega}{\omega_n} \right)]^2}{\left[\mu \left(\frac{1+\phi}{1+\mu} \left(\frac{\omega}{\omega_n} \right)^2 \right)^2 - (\phi + \beta + \mu + \mu\beta) \frac{1+\phi}{1+\mu} \left(\frac{\omega}{\omega_n} \right)^2 + (\phi + \beta + \phi\beta) \right]^2 + [2\xi(1+\phi)^2 \left(1 - \left(\frac{\omega}{\omega_n} \right)^2 \right) \left(\frac{\omega}{\omega_n} \right)]^2}} \quad (\text{A-22})$$

$$\frac{|x_2|}{x_{st}} = \frac{1+\phi}{1+\mu} \sqrt{\frac{\left[\mu \frac{1+\phi}{1+\mu} \left(\frac{\omega}{\omega_n}\right)^2 - (\mu + \beta + \mu\beta)\right]^2 + [2\xi(1+\phi)(1+\mu)\left(\frac{\omega}{\omega_n}\right)]^2}{\left[\mu \left(\frac{1+\phi}{1+\mu} \left(\frac{\omega}{\omega_n}\right)^2\right)^2 - (\phi + \beta + \mu + \mu\beta) \frac{1+\phi}{1+\mu} \left(\frac{\omega}{\omega_n}\right)^2 + (\phi + \beta + \phi\beta)\right]^2 + [2\xi(1+\phi)^2(1 - \left(\frac{\omega}{\omega_n}\right)^2)\left(\frac{\omega}{\omega_n}\right)]^2}}$$

(A-23)

$$\frac{|x_2 - x_1|}{x_{st}} = \frac{1+\phi}{1+\mu} \sqrt{\frac{(\phi - \mu)^2}{\left[\mu \left(\frac{1+\phi}{1+\mu} \left(\frac{\omega}{\omega_n}\right)^2\right)^2 - (\phi + \beta + \mu + \mu\beta) \frac{1+\phi}{1+\mu} \left(\frac{\omega}{\omega_n}\right)^2 + (\phi + \beta + \phi\beta)\right]^2 + [2\xi(1+\phi)^2(1 - \left(\frac{\omega}{\omega_n}\right)^2)\left(\frac{\omega}{\omega_n}\right)]^2}}$$

(A-24)

$$\frac{|\ddot{u}_1|}{a_g} = \sqrt{\frac{\left[-\mu \frac{1+\phi}{1+\mu} \left(\frac{\omega}{\omega_n}\right)^2 + (\phi + \beta + \phi\beta)\right]^2 + [2\xi(1+\phi)^2\left(\frac{\omega}{\omega_n}\right)]^2}{\left[\mu \left(\frac{1+\phi}{1+\mu} \left(\frac{\omega}{\omega_n}\right)^2\right)^2 - (\phi + \beta + \mu + \mu\beta) \frac{1+\phi}{1+\mu} \left(\frac{\omega}{\omega_n}\right)^2 + (\phi + \beta + \phi\beta)\right]^2 + [2\xi(1+\phi)^2(1 - \left(\frac{\omega}{\omega_n}\right)^2)\left(\frac{\omega}{\omega_n}\right)]^2}}$$

(A-25)

$$\frac{|\ddot{u}_2|}{a_g} = \sqrt{\frac{\left[-\phi \frac{1+\phi}{1+\mu} \left(\frac{\omega}{\omega_n}\right)^2 + (\phi + \beta + \phi\beta)\right]^2 + [2\xi(1+\phi)^2\left(\frac{\omega}{\omega_n}\right)]^2}{\left[\mu \left(\frac{1+\phi}{1+\mu} \left(\frac{\omega}{\omega_n}\right)^2\right)^2 - (\phi + \beta + \mu + \mu\beta) \frac{1+\phi}{1+\mu} \left(\frac{\omega}{\omega_n}\right)^2 + (\phi + \beta + \phi\beta)\right]^2 + [2\xi(1+\phi)^2(1 - \left(\frac{\omega}{\omega_n}\right)^2)\left(\frac{\omega}{\omega_n}\right)]^2}}$$

(A-26)

A.2.2 Derivation of Target Curve

In the frequency response curves, replace ω/ω_n to g for simplification purpose in equation expression. Target curve is a mathematical relationship among μ , β and ϕ . This curve is able to locate the fixed points of the 2DOF system at the same level in the response, which is step 1 of the optimization procedure of the 2DOF system. The parameters to

balance the fixed points response are first derived for LFRS displacement x_1 . Eqn. A-22 takes the form of:

$$\frac{|x_1|}{x_{st}} = \sqrt{\frac{A\xi^2+B}{C\xi^2+D}} \quad (\text{A-27})$$

In order to be independent of damping as is the case at the fixed points requires: $A/C = B/D$ [113], which produces the following expression:

$$\frac{(1+\mu)}{(1+\phi)(1-g^2)} = \pm \frac{\mu \frac{1+\phi}{1+\mu} g^2 - (\phi + \beta + \mu\beta)}{\mu (\frac{1+\phi}{1+\mu} g^2)^2 - (\phi + \beta + \mu + \mu\beta) \frac{1+\phi}{1+\mu} g^2 + (\phi + \beta + \phi\beta)} \quad (\text{A-28})$$

Evaluating Eqn. A-28 for a negative sign produces point P:

$$g_P^2 = [\phi(1 + \mu)] / [\mu(1 + \phi)] \quad (\text{A-29})$$

Evaluating Eqn. A-28 for a positive sign produces the following expression:

$$2\mu \frac{(1+\phi)^2}{1+\mu} g^4 - \left[\mu \frac{(1+\phi)^2}{1+\mu} + (1 + \phi)(2\phi + 2\beta + \mu + 2\mu\beta) \right] g^2 + (2\phi + 2\beta + 2\phi\beta + 2\mu\beta + 2\mu\phi\beta + \mu\phi + \phi^2) = 0 \quad (\text{A-30})$$

Eqn. A-30 has two roots g_Q^2 and g_M^2 . Solving this equation and substituting back into Eqn. A-22 is possible, but complicated. Instead, consider $\xi=\infty$ which also passes through Q and M. Evaluating Eqn. A-22 for $\xi=\infty$ produces:

$$\frac{|x_1|}{x_{st}} = \frac{1+\phi}{1+\mu} \sqrt{\frac{[2(1+\phi)(1+\mu)g]^2}{[2(1+\phi)^2(1-g^2)g]^2}} = \left| \frac{1}{1-g^2} \right| \quad (\text{A-31})$$

Since Q and M straddle $g=1.0$ and have same $|x_1|/x_{st}$ magnitude, the solution to Eqn. A-31 is:

$$\frac{1}{1-g_M^2} = -\frac{1}{1-g_Q^2} \quad (\text{A-32})$$

Eqn. A-32 leads to the following relationship: $g_Q^2 + g_M^2 = 2$. Since g_Q^2 and g_M^2 are also the roots of Eqn. A-30, taking the summation of two roots of Eqn. A-30 generates:

$$g_Q^2 + g_M^2 = \frac{\mu \frac{(1+\phi)^2}{1+\mu} + (1+\phi)(2\phi+2\beta+\mu+2\mu\beta)}{2\mu \frac{(1+\phi)^2}{1+\mu}} \quad (\text{A-33})$$

And equating Eqn. A-33 to 2 produces:

$$\frac{\mu \frac{(1+\phi)^2}{1+\mu} + (1+\phi)(2\phi+2\beta+\mu+2\mu\beta)}{2\mu \frac{(1+\phi)^2}{1+\mu}} = 2 \quad (\text{A-34})$$

And rearranging and solving for β produces an x_1 target curve equation for balanced fixed points:

$$\beta = \frac{(\mu-\phi)(2-\mu)}{2(1+\mu)^2} \quad (\text{A-35})$$

As evidenced, the target curve produces positive β values for $\phi \leq \mu \leq 2$ (termed Region I) and negative β values for $\mu \geq 2$ (termed Region II). The same approach provide the target curve equation for x_2 :

$$\beta = \frac{(\mu-\phi)(1-2\mu)}{2(1+\mu)^2} \quad (\text{A-36})$$

Eqn. A-36 indicates the target curve of x_2 produces realistic positive β values for $\phi \leq \mu \leq 0.5$ ($\phi < 0.5$) or $0.5 \leq \mu \leq \phi$ ($\phi > 0.5$).

The target curve for \ddot{u}_1 is given in equation Eqn. A-37:

$$\beta = \frac{(\mu-\phi)(\phi+2-\phi\mu)}{2(1+\mu)^2(1+\phi)} \quad (\text{A-37})$$

The target curve for \ddot{u}_2 is given in equation Eqn. A-38:

$$\beta = \frac{(\mu-\phi)(1-\mu-2\phi\mu)}{2(1+\mu)^2(1+\phi)} \quad (\text{A-38})$$

Eqn. A-38 indicates the target curve of \ddot{u}_2 produces realistic positive β values for $\phi \leq \mu \leq 1/(1+2\phi)$ ($\phi < 0.5$) or $1/(1+2\phi) \leq \mu \leq \phi$ ($\phi > 0.5$).

A.2.3 Frequency Values of the Fixed Points

Eqn. A-29 provides the frequency value of the point P by evaluating Eqn. A-28 for a negative sign, which is re-written here:

$$g_P^2 = [\phi(1 + \mu)]/[\mu(1 + \phi)] \quad (\text{A-29})$$

Evaluating Eqn. A-28 for a positive sign, then the equation becomes:

$$2\mu \frac{(1+\phi)^2}{1+\mu} g^4 - \left[\mu \frac{(1+\phi)^2}{1+\mu} + (1 + \phi)(2\phi + 2\beta + 2\mu\beta + \mu) \right] g^2 + (2\phi + 2\beta + 2\phi\beta + 2\mu\beta + 2\mu\phi\beta + \mu\phi + \phi^2) = 0 \quad (\text{A-39})$$

The frequency value of the point Q and M are:

$$g_Q^2 = \frac{2\phi + 2\beta + 2\mu + 4\mu\beta + 3\mu\phi + \mu^2 + 2\beta\mu^2 - \sqrt{-4\beta(\phi - \mu)(\mu - 2)(1 + \mu)^2 + 4\beta^2(1 + \mu)^4 + (\phi - \mu)^2(2 + \mu)^2}}{4\mu(1 + \phi)} \quad (\text{A-40})$$

$$g_M^2 = \frac{2\phi + 2\beta + 2\mu + 4\mu\beta + 3\mu\phi + \mu^2 + 2\beta\mu^2 + \sqrt{-4\beta(\phi - \mu)(\mu - 2)(1 + \mu)^2 + 4\beta^2(1 + \mu)^4 + (\phi - \mu)^2(2 + \mu)^2}}{4\mu(1 + \phi)} \quad (\text{A-41})$$

Note that when $\beta = 0$, Eqn. A-40 turns to be:

$$g_Q^2 = \frac{2\phi + 2\mu + 3\mu\phi + \mu^2 - \sqrt{(\phi - \mu)^2(2 + \mu)^2}}{4\mu(1 + \phi)} = \frac{\phi(1 + \mu)}{\mu(1 + \phi)} \quad (\mu > \phi) \quad (\text{A-42})$$

A.3 Modal Analysis

Fig. A-1 shows the 2DOF modal properties at different β and μ when $\phi = 0.03$. Fig. A-1a and Fig. A-1b show the variation of ω_{h1} , ω_{h2} when β and μ change. A greater value of μ represents more mass attributed to the gravity system, implying a decrease of ω_G and an increase of ω_L .

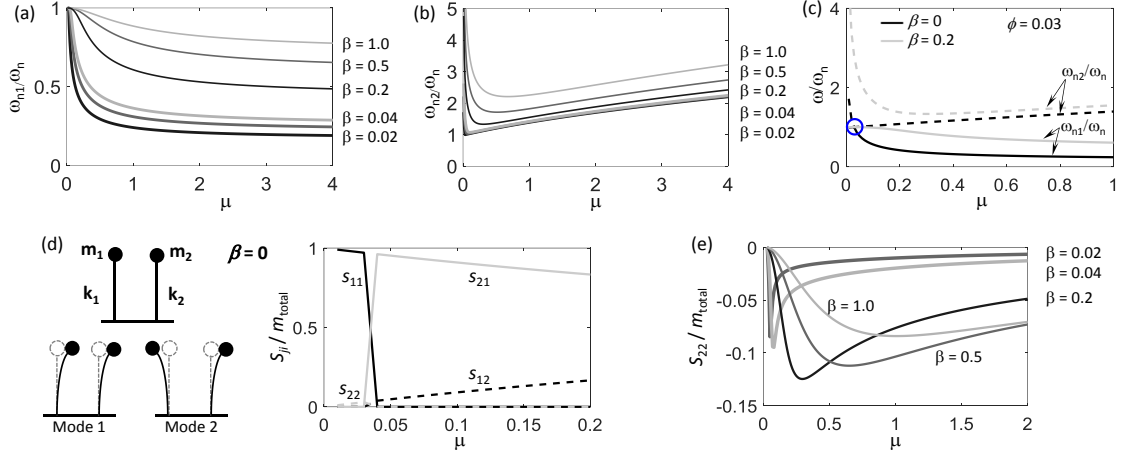


Fig. A-1. Natural Frequencies vs. μ : (a) 1st mode; (b) 2nd mode; (c) switch point; (d) effective modal mass ratio at $\beta = 0$; (e) S_{22} at different β .

Fig. A-1c shows the normalized (by ω_n) frequency of the 2DOF system, with solid and dashed lines representing the 1st and 2nd natural frequencies, respectively. When $\mu = \phi$, $\omega_{h1} = \omega_n$ (See Eqn. 3-3c), implying that since the modal properties of the LFRS and GLRS are the same, the response is independent of β . Also seen in Fig. A-1c: $\omega_{h1} = \omega_L$ when $\mu < \phi$, so ω_{h1} increases with (increasing) μ ; $\omega_{h1} = \omega_G$ when $\mu > \phi$, so ω_{h1} decreases with μ . Therefore, $\mu = \phi$ is indicated as a switch point (See blue circle in Fig. A-1c) where the contribution source to the 1st mode changes. When $\beta = 0$ (indicated by the dark black lines in Fig. A-1c), ω_{h2} decreases with μ when $\mu < \phi$, and increases with μ when $\mu > \phi$.

Fig. A-1d shows the schematic deformed shape of the 2DOF system in two modes and the effective modal mass ratio from each mass of each mode when $\beta = 0$. S_{ji} represents the effective modal mass from m_i in the j^{th} mode, $S_{ji} = \Gamma_j m_i \phi_{ji}$ [116, 118]. m_{total} represents the total mass of the 2DOF system. Black and grey represents the effective modal mass in the 1st and 2nd mode respectively, while solid and dashed lines represent the effective modal mass from m_1 and m_2 respectively. When $\mu < \phi$, the 1st mode is only contributed by m_1 .

Therefore, the effective modal mass component, S_{11} , decreases as μ increases. When $\mu < \phi$, the 2nd mode is only contributed by m_2 . Therefore, S_{22} increases as μ increases. S_{12} and S_{21} are zero because there is no interaction between m_1 and m_2 . When $\mu > \phi$, the 1st mode is contributed by m_2 (S_{12}) and the 2nd mode is contributed by m_1 (S_{21}), a jump is observed at $\mu = 0.04$ because the exchange of the contribution source to each mode. Therefore, the effective modal mass in the 1st mode increases as μ increases, while the effective modal mass in the 2nd mode decreases. S_{11} and S_{22} are zero when $\mu > \phi$ because there is no interaction between m_1 and m_2 .

Eqn. 3-3d shows that $\omega_{h2} > \omega_h$ when $\beta > 0$, implying that the 2nd frequency is larger than one due to the coupling effect between the m_1 and m_2 . The values of ω_{h2}/ω_h at different β is shown in Fig. A-1b and Fig. A-1c ($\beta=0, 0.02$). Fig. A-1c shows that ω_{h2}/ω_h reverses at the switch point when $\beta = 0$, other than that, Fig. A-1b and Fig. A-1c show that ω_{h2}/ω_h continues decreasing when $\mu > \phi$ and the reversal is delayed at a larger μ as β increases. Fig. A-1e shows that the peak of S_{22} shifts to a larger μ as β increases, implying that the maximum contribution to the effective modal mass from m_2 in the 2nd mode occurs at a larger μ . Additionally, ω_G decreases as μ increases. Thus, the reversal delay in ω_{h2}/ω_h is related to the contribution of the mass from m_2 in the 2nd mode, S_{22} .

Fig. A-2 shows the modal property of the 2DOF system versus the IFAS flexibility at different mass ratio. Fig. A-2a –Fig. A-2c show the effective modal mass ratio, $\hat{S}_j = S_j/m_{\text{total}}$ ($S_j = \sum_{i=1}^2 S_{ji}$) vs η at different μ , where $\eta = 1/\beta$. Fig. A-2d - Fig. A-2f show the expansion of the \hat{S}_j in each mass of each mode, S_{ji}/m_{total} vs η , at different μ .

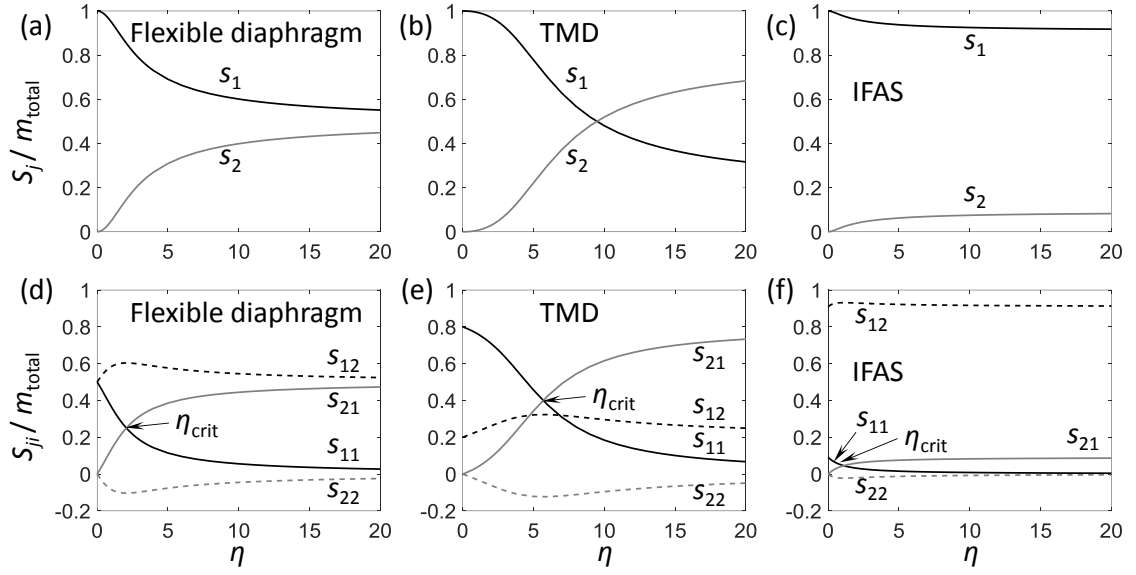


Fig. A-2. Effective modal mass ratio for: (a) $\mu=1$; (b) $\mu=0.25$; (c) $\mu=10$; Modal expansion of effective modal mass ratio for: (d) $\mu=1$; (e) $\mu=0.25$; (f) $\mu=10$.

Fig. A-2a shows the \hat{S}_j variation in two modes when $\mu=1$ as IFAS becomes more flexible. \hat{S}_1 drops from one and \hat{S}_2 increases from zero. This indicates that only one mode exists in the system at rigid IFAS case ($\eta=0$) and the same phenomenon is shown in Fig. A-2b and Fig. A-2c for the 2DOF systems using different μ . The effective modal mass from m_1 (S_{11}/m_{total}) and m_2 (S_{12}/m_{total}) is $1/(1+\mu)$ and $\mu/(1+\mu)$ (See Fig. A-2d - Fig. A-2f).

When $\alpha=\infty$, the 2DOF system turns to two isolated SDOF systems. $\hat{S}_1=\mu/(1+\mu)$ and $\hat{S}_2=1/(1+\mu)$. The effective modal mass from m_2 (S_{12}/m_{total}) and m_1 (S_{21}/m_{total}) is also $\mu/(1+\mu)$ and $1/(1+\mu)$ because S_{11} and S_{22} are zero as mentioned previously.

When η is increased initially from rigid case, both S_{12} and S_{22} are increased and then decreases as η increases. S_{11} keeps decreasing and S_{21} keeps increasing. η_{crit} [118] maximizes participation for the GLRS mass m_2 and also evenly distributed the effective modal mass from m_1 in the two modes, $S_{11}(\eta_{\text{crit}})=S_{12}(\eta_{\text{crit}})$.

A.4 Damping Sweep Method (DSM)

The DSM method is used to obtain the optimized damping (ξ_{opt}) of the 2DOF system that generates the minimized (x_1, \ddot{u}_2) response. Fig. A-3 shows an example of using DSM method to find ξ_{opt} for x_1 . A suite of ξ values ($0.01 \leq \xi \leq 1$, with 0.01 increment) are used to calculate the $|x_1|/x_{\text{st}}$. The minimum of the $|x_1|/x_{\text{st}}$ (1.52) occurs at $\xi=0.14$, therefore $\xi_{\text{opt}}=0.14$.

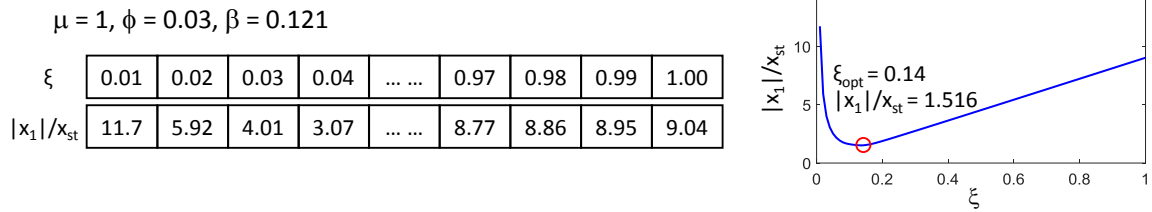


Fig. A-3. DSM method explanation, use x_1 response as an example.

A.5 Numerical Central Differential Method (NCDM)

The NCDM method is used to obtain the optimized damping (ξ_{opt}) of the 2DOF system that generates a minimized (x_1, \ddot{u}_2) response. x_1 is used as an example. x_1 - ξ plot is convex (See Fig. A-4a), two damping values are assumed ($\xi_{\text{left}}=0$ and $\xi_{\text{right}}=100$) as the left and right bound in the response (See Fig. A-4b). Then one current damping value ($\xi_{\text{left}} < \xi_{\text{curr}} < \xi_{\text{right}}$) and two more trial damping values ($\xi_{\text{tri,L}} = (\xi_{\text{left}} + \xi_{\text{curr}})/2$, $\xi_{\text{tri,R}} = (\xi_{\text{right}} + \xi_{\text{curr}})/2$) are assumed. The responses at the three damping values (ξ_{curr} , $\xi_{\text{tri,L}}$, $\xi_{\text{tri,R}}$) are compared and the new damping values (ξ_{left} , ξ_{right} , ξ_{curr} , $\xi_{\text{tri,L}}$, $\xi_{\text{tri,R}}$) will be assigned. This iteration process will stop till the response difference at ξ_{curr} , $\xi_{\text{tri,L}}$, $\xi_{\text{tri,R}}$ is smaller than a predefined tolerance. This iteration process may have two cases:

(1) Case 1 (See Fig. A-4b), when the smaller response at the trial damping ($\xi_{\text{tri,L}}$, $\xi_{\text{tri,R}}$) is lower than the response at the current damping (ξ_{curr}). The $(i+1)$ th iteration will be:

$$\zeta_{\text{left},i+1} = \zeta_{\text{left},i}$$

$$\zeta_{\text{right},i+1} = \zeta_{\text{curr},i}$$

$$\zeta_{\text{curr},i+1} = \zeta_{\text{tri},L,i}$$

$$\zeta_{\text{tri},L,i+1} = (\zeta_{\text{left},i+1} + \zeta_{\text{curr},i+1})/2$$

$$\zeta_{\text{tri},R,i+1} = (\zeta_{\text{right},i+1} + \zeta_{\text{curr},i+1})/2$$

(2) Case 2 (See Fig. A-4c), when the smaller response at the trial damping ($\zeta_{\text{tri},L}$, $\zeta_{\text{tri},R}$) is larger than the response at the current damping (ζ_{curr}). The $(i+1)$ th iteration will be:

$$\zeta_{\text{left},i+1} = \zeta_{\text{tri},L,i}$$

$$\zeta_{\text{right},i+1} = \zeta_{\text{tri},R,i}$$

$$\zeta_{\text{curr},i+1} = \zeta_{\text{curr},i}$$

$$\zeta_{\text{tri},L,i+1} = (\zeta_{\text{left},i+1} + \zeta_{\text{curr},i+1})/2$$

$$\zeta_{\text{tri},R,i+1} = (\zeta_{\text{right},i+1} + \zeta_{\text{curr},i+1})/2$$

The minimized $|x_1|/x_{\text{st}}$ (1.51) occurs at $\zeta_{\text{opt}}=0.137$ (See Fig. A-4a).

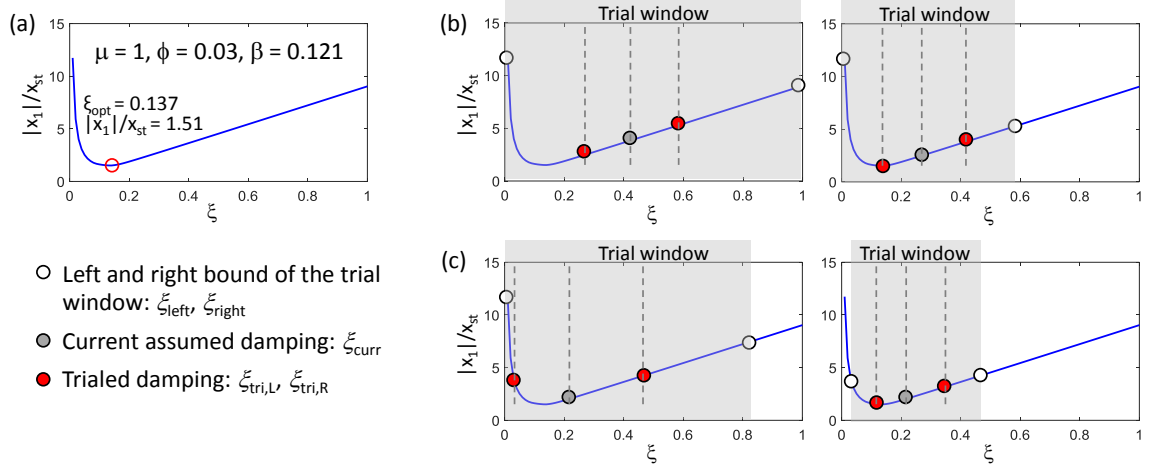


Fig. A-4. NCDM method explanation: (a) x_1 resp. as an example; (b) case 1; (c) case 2.

A.6 Parameter Sweep Method (PSM)

The PSM method is similar to the DSM but with more parameters under investigation. There are four design parameters for the elastic 2DOF system as mentioned previously: $(\mu, \beta, \phi, \zeta)$. The following steps are used for this method:

(1) Calculate the 2DOF system response using Eqn. A-22 – Eqn. A-26. A suite of forcing frequencies ($0 \leq \omega/\omega_n \leq 4$ with 0.001 increment) are used at a given $(\mu, \beta, \phi, \zeta)$, and the maximum response will be used for representing the response (R_1 in Fig. A-5a).

(2) Vary the damping ($0.005 \leq \xi \leq 2$ with 0.005 increment) at a given (μ, β, ϕ) . Then a matrix of the 2DOF system response with varying ω/ω_n and ξ at a given (μ, β, ϕ) is formed (See Fig. A-5a). The maximum response of each ξ case generates a vector R_1 , representing the response of the 2DOF system from the harmonic analysis. Note that a matrix with the 2DOF system response is termed response matrix in this dissertation.

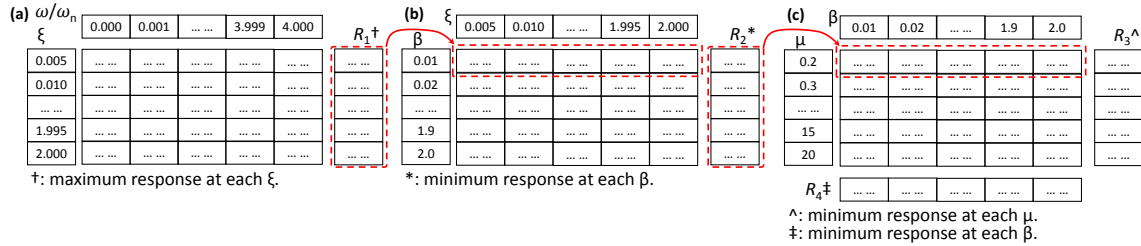


Fig. A-5. 2DOF system response matrix with varying: (a) ξ and ω/ω_n ; (b) β and ξ ; (c) μ and β .

(3) Vary the β ($0.01 \leq \beta \leq 2$) at a given (μ, ϕ) . β represents the IFAS stiffness and doesn't produce minimized response at a large value. Therefore, the candidate β values are not uniformly distributed across the candidate range. The β is discretized finer in lower values and coarser in higher values: $0.01 \leq \beta \leq 0.1$ with 0.01 increment, $0.15 \leq \beta \leq 1$ with 0.05 increment, $1.1 \leq \beta \leq 2$ with 0.1 increment. 38 candidate β values are investigated.

The response R_1 from Step (2) is used to form a new matrix of the 2DOF system response at a given (μ, ϕ) with varying β and ξ (See Fig. A-5b). The lowest response at each β case is treated as the optimized response (R_2 in Fig. A-5b) at a specific (μ, β, ϕ) , and the related damping is treated as the ξ_{opt} .

(4) Vary the μ ($0.2 \leq \mu \leq 20$) at a given ϕ . The response varies large in when the μ is small and less when the μ is large. Therefore, the candidate μ values are not uniformly distributed across the candidate range. The μ is discretized finer in lower values and coarser in higher values: $0.2 \leq \mu \leq 1$ with 0.1 increment, $1.2 \leq \mu \leq 5$ with 0.2 increment, $6 \leq \mu \leq 20$ with 1 increment. 44 candidate μ values are investigated.

The response R_2 from Step (3) is used to form a new matrix of the 2DOF system response at a given ϕ with varying μ (See Fig. A-5c). Then Fig. A-5c shows the optimized response at a given ϕ with different (β, μ) combination. The lowest response at each μ case is treated as the optimized response (R_3 in Fig. A-5c) at a specific (μ, ϕ) . The lowest response at each β case is treated as the optimized response (R_4 in Fig. A-5c) at a specific (β, ϕ) . The lowest response across the matrix in Fig. A-5c is treated as the optimized response at a specific ϕ , and the related (μ, β, ξ) is the optimized design parameter.

(5) Vary ϕ in a predefined set (0.03, 0.05, 0.1, 0.15, 0.19, 0.21, 0.23) and the optimized response of the 2DOF system with different ϕ can be obtained.

A.7 x_1 Target Curve in Region II

The x_1 target curve and related 2DOF system responses will be shown in this section (Fig. A-6). Fig. A-6b shows the square of the frequencies (needed to avoid complex numbers) at P, Q, M as μ increases ($\phi = 0.03$). The figure indicates that, in Region II, the frequency at P is close to zero (static) and Q is negative (complex). The optimization for

this case is shown in Fig. A-6c. Point Q (in the complex range) produces the same x_1 response as at M. The response at P is larger and fairly well minimized at ξ_{opt} . However, a “hump” (rapidly increasing range) is observed to the left of P. Therefore, a larger response than at P can exist in the positive frequency range. Thus, the target curve is not applicable in Region II.

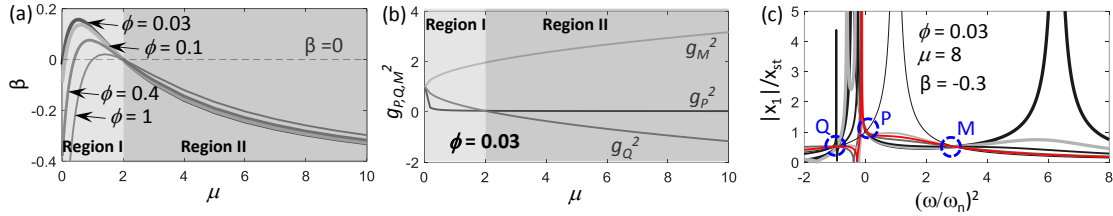


Fig. A-6. Target curve and the 2DOF system frequency response: (a) x_1 target curve; (b) P, Q, M frequency values; (c) example x_1 response in Region II.

A.8 Explanation on PSM when x_1 is Minimized

x_1^* , x_2^* , \ddot{u}_2^* are used to represent the minimized response of x_1 , x_2 , \ddot{u}_2 across the candidate set at each ϕ as mentioned in Sec. 3.4.5. Fig. A-7 shows the contour plot when x_1 is minimized ($\phi = 0.03$).

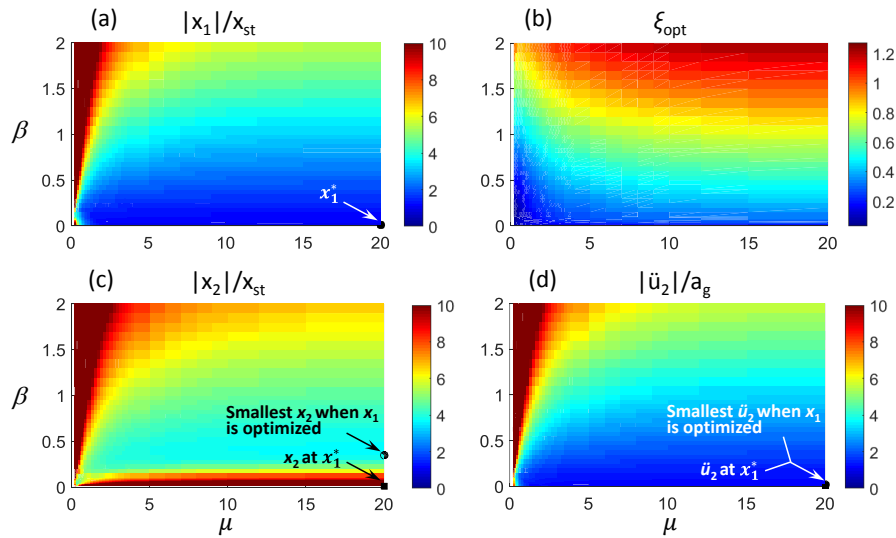


Fig. A-7. Response contour plots of the elastic 2DOF system when optimizing x_1 ($\phi = 0.03$): (a) $|x_1|/x_{\text{st}}$; (b) ξ_{opt} ; (c) $|x_2|/x_{\text{st}}$; (d) $|\ddot{u}_2|/a_g$.

Fig. A-7a shows the optimized x_1 responses at each (μ, β) and indicates that x_1^* occurs at the largest μ and smallest β of a given candidate set. Fig. A-7a shows that the optimized x_1 decreases as μ increases while β decreases. Additionally, the influence from μ becomes negligible when μ is large. Fig. A-7b shows the corresponding ξ_{opt} required for optimizing x_1 at each (μ, β) . The plot indicates that ξ_{opt} is increased as μ and β increase. Fig. A-7c shows the corresponding x_2 at each (μ, β) for x_1 optimization. The figure indicates that x_2 at x_1^* is not the smallest across the whole candidate set. The smallest x_2 in Fig. A-7c occurs at $\beta=0.35$. x_2 decreases as μ increases, however x_2 is more sensitive to β when μ is large. Fig. A-7d shows the corresponding \ddot{u}_2 at each (μ, β) for x_1 optimization. Fig. A-7d shows that the smallest \ddot{u}_2 occurs at the same location as x_1^* , implying a common optimized design for x_1 and \ddot{u}_2 .

A.9 Influence on the Elastic 2DOF System Optimization from ϕ

Consider the 2DOF IFAS response when x_1 is minimized over different ϕ as shown in Fig. A-8. Fig. A-8a shows that x_1^* increases as GLRS stiffness increases relative to LFRS stiffness, implying that lowering the GLRS stiffness can assist in minimizing x_1 . Fig. A-8b, c, d show the associated design parameter values $(\xi_{\text{opt}}, \mu, \beta)$ at x_1^* . The ξ_{opt} is seen to decrease as ϕ increases (See Fig. A-8b). The largest μ (See Fig. A-8c) and smallest β (See Fig. A-8d) from the given candidate set are shown to produce the minimized x_1 for all different ϕ . This (μ, β) combination shows that x_1 can be minimized when more mass is assigned to m_2 and the IFAS is as flexible as possible, indicating that a LFRS with low tributary mass and a near isolated GLRS will produce smaller LFRS demands under excitation. Fig. A-8e shows that $\varepsilon_{\ddot{u}_2}$ increases from 5% to 100% as ϕ increases. Fig. A-8f

shows that ε_{x2} decreases significantly first and then stabilizes as ϕ increases, however ε_{x2} is large when x_1 is minimized ($\sim 700\%$ when $\phi = 0.03$).

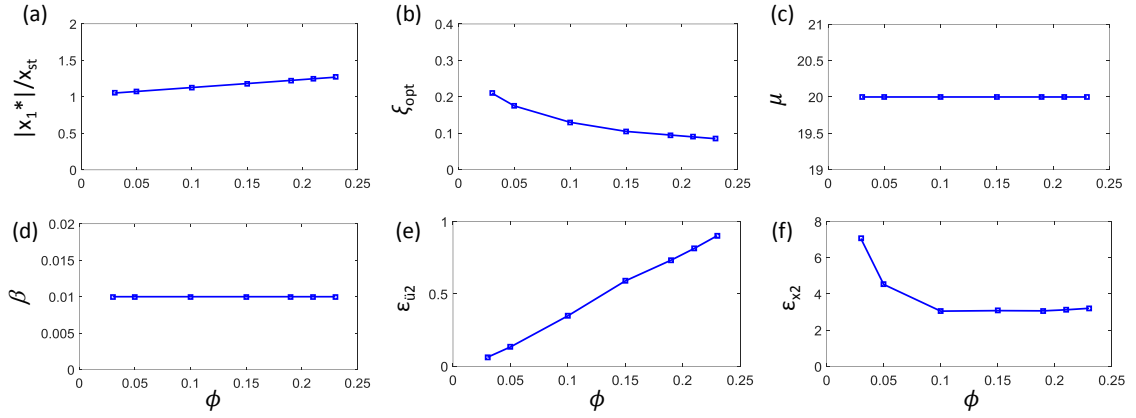


Fig. A-8. Elastic 2DOF response at x_1^* : (a) $|x_1^*|/x_{st}$; (b) ζ_{opt} ; (c) μ ; (d) β ; (e) $\varepsilon_{\ddot{u}2}$; (f) ε_{x2} .

Now consider the 2DOF IFAS response when \ddot{u}_2 is minimized, again for different ϕ , as shown in Fig. A-9. The minimum \ddot{u}_2 increases as GLRS stiffness increases respective to LFRS stiffness (See Fig. A-9a). Thus, a lower GLRS stiffness assists in minimizing \ddot{u}_2 , which is the same as x_1 . Fig. A-9b, c, d show the associated design parameters (ζ_{opt}, μ, β) for minimizing \ddot{u}_2 . The ζ_{opt} decreases as ϕ increases (See Fig. A-9b). The largest μ (See Fig. A-9c) and smallest β (See Fig. A-9d) from the given candidate set are shown to produce the minimized \ddot{u}_2 of the 2DOF systems for all different ϕ . This (μ, β) combination is the same as that for minimizing x_1 .

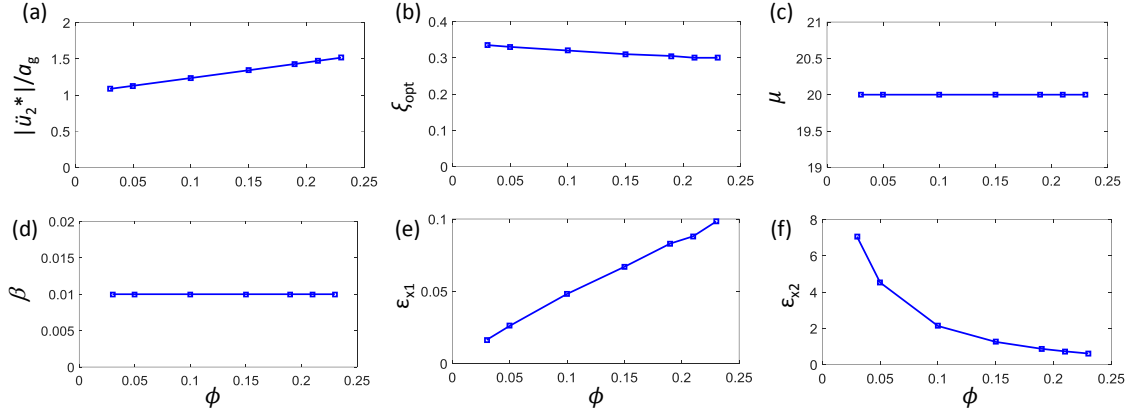


Fig. A-9. Elastic 2DOF response at \ddot{u}_2^* : (a) $|\ddot{u}_2^*|/a_g$; (b) ξ_{opt} ; (c) μ ; (d) β ; (e) ϵ_{x1} ; (f) ϵ_{x2} .

Fig. A-8 – A-9 have indicated that the minimization on x_1 and \ddot{u}_2 follow the same trends: lower ϕ values produce smaller x_1^* , \ddot{u}_2^* . ϵ_{x1} when minimizing \ddot{u}_2 is much smaller than $\epsilon_{\ddot{u}_2}$ when minimizing x_1 . When $\phi > 0.1$, ϵ_{x2} when minimizing \ddot{u}_2 is smaller than that when minimizing x_1 . Therefore, minimizing \ddot{u}_2 produces preferable response than minimizing x_1 . However, both minimization do not produce satisfied x_2 response (about 700% when $\phi = 0.03$).

The minimum x_2 does not vary significantly for different ϕ (See Fig. A-10a). Fig. A-10b, c, d show the associated design parameters (ξ_{opt} , μ , β) for minimized x_2 response. Optimum damping ξ_{opt} has a mostly decreasing trend as ϕ increases (See Fig. A-10b). The mass ratio μ varies within a range of high values at different ϕ (See Fig. A-10c). The IFAS stiffness ratio β generally decreases with increasing ϕ (See Fig. A-10d).

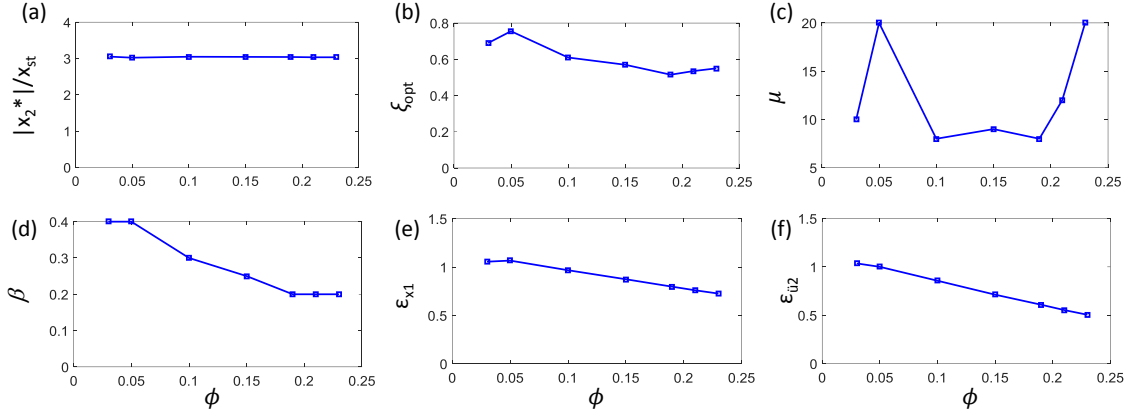


Fig. A-10. Elastic 2DOF response at x_2^* : (a) $|x_2^*|/x_{st}$; (b) ζ_{opt} ; (c) μ ; (d) β ; (e) ϵ_{x1} ; (f) $\epsilon_{\ddot{u}2}$.

Fig. A-8 – A-10 show that minimizing x_1 , \ddot{u}_2 and x_2 are conflicting objectives that can not occur simultaneously. Minimizing any one of these three response will cause an opposite effect on one or both of the other two responses. Therefore, a multi-objective optimization is needed to investigate an optimized design space of the 2DOF IFAS system.

A.10 Global Total Relative Error

The relative error ϵ_{x1} , ϵ_{x2} , and $\epsilon_{\ddot{u}2}$ are not comparable among the 2DOF systems with different ϕ since the minimized values x_1^* , x_2^* , \ddot{u}_2^* are different when ϕ is different. In order to make a comparable relative error across systems with different ϕ , the minimum value of x_1^* (or x_2^* , \ddot{u}_2^*) for all candidate ϕ is denoted as $x_1^{*'} (or $x_2^{*'}, \ddot{u}_2^{*'})$ and termed as *global* minimized response. Global relative error is calculated using:$

$$\epsilon_{x1}' = \frac{(x_1 - x_1^{*'})}{x_1^{*'}} \quad (A-43a)$$

$$\epsilon_{x2}' = \frac{(x_2 - x_2^{*'})}{x_2^{*'}} \quad (A-43b)$$

$$\epsilon_{\ddot{u}2}' = \frac{(\ddot{u}_2 - \ddot{u}_2^{*'})}{\ddot{u}_2^{*'}} \quad (A-43c)$$

The global relative errors defined in Eqn. A-43 when ε_{tot} is minimized are shown in Fig. A-11. Errors ε_{x1}' , $\varepsilon_{\ddot{u}2}'$ and ε_{x2}' doesn't change significantly as ϕ increases. This plot implying that when the ε_{tot} is minimized, the LFRS and GLRS response is not sensitive to the GLRS stiffness.

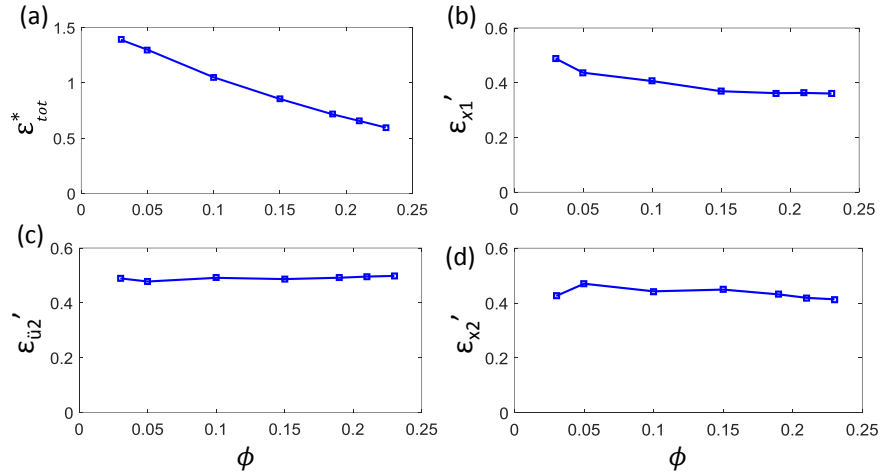


Fig. A-11. Response of the elastic 2DOF system and related design parameters when minimizing ε_{tot} : (a) $\varepsilon_{\text{tot}}^*$; (b) ε_{x1}' ; (c) $\varepsilon_{\ddot{u}2}'$; (d) ε_{x2}' .

A.11 Design Space and Related Relative Errors on x_1, x_2, \ddot{u}_2 for the Elastic 2DOF

The design space and related minimized relative error on x_1, x_2, \ddot{u}_2 of the Elastic 2DOF system using the undamped LFRS (See Fig. 3-1b) with different ϕ is shown in Fig. A-12 – A-18.

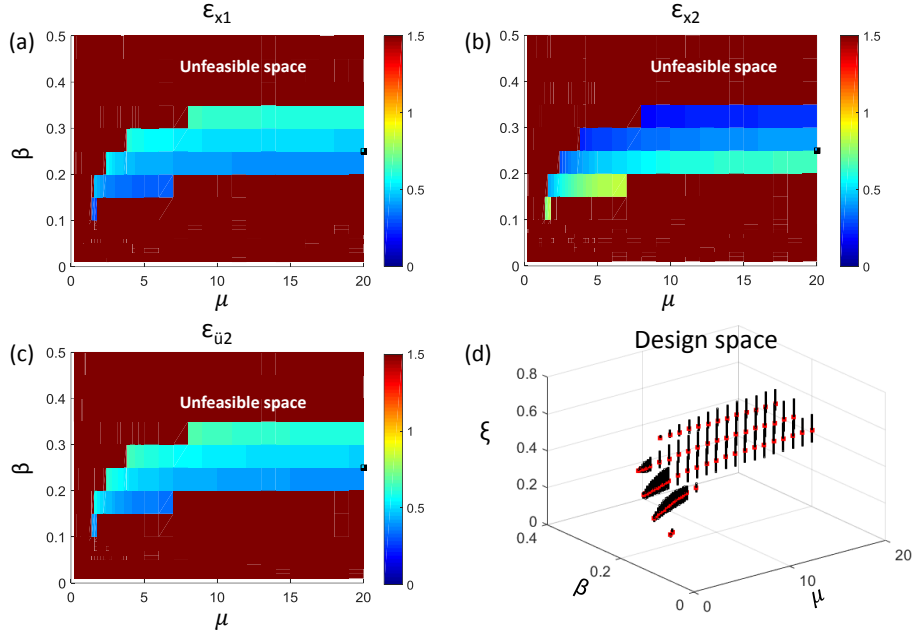


Fig. A-12. Contour plot of minimized x_1 , x_2 , \ddot{u}_2 relative error response at each (μ, β) when $\epsilon_{tot} < 150\%$ ($\phi = 0.03$): (a) ϵ_{x1} ; (b) ϵ_{x2} ; (c) $\epsilon_{\ddot{u}2}$; (d) design space.

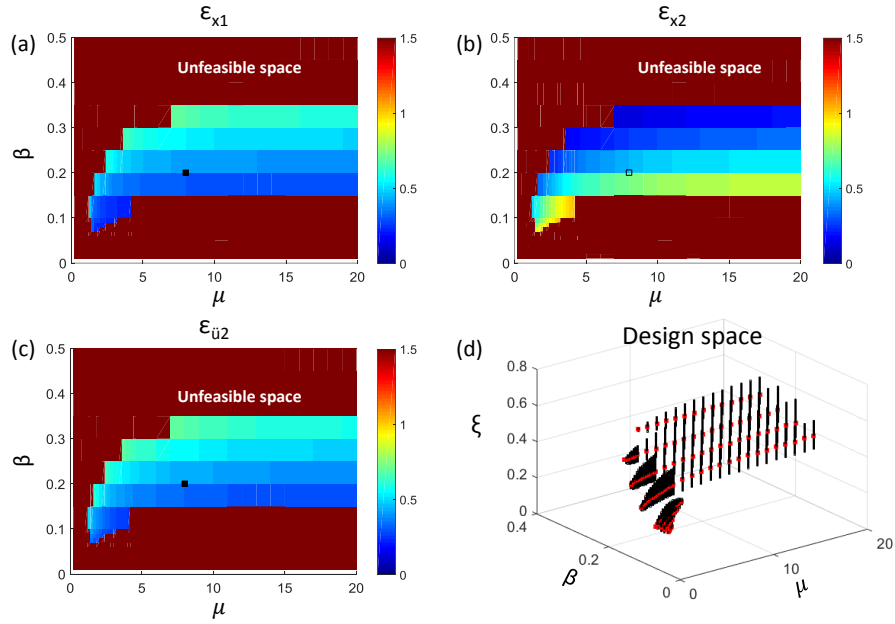


Fig. A-13. Contour plot of minimized x_1 , x_2 , \ddot{u}_2 relative error response at each (μ, β) when $\epsilon_{tot} < 150\%$ ($\phi = 0.05$): (a) ϵ_{x1} ; (b) ϵ_{x2} ; (c) $\epsilon_{\ddot{u}2}$; (d) design space.

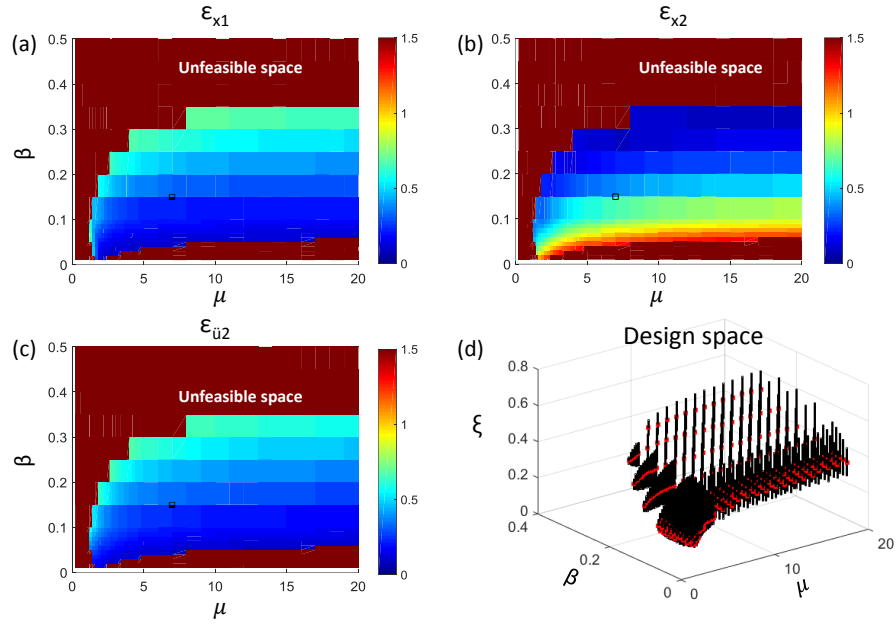


Fig. A-14. Contour plot of minimized x_1 , x_2 , \ddot{u}_2 relative error response at each (μ, β) when $\epsilon_{tot} < 150\%$ ($\phi = 0.1$): (a) ϵ_{x1} ; (b) ϵ_{x2} ; (c) $\epsilon_{\ddot{u}2}$; (d) design space.

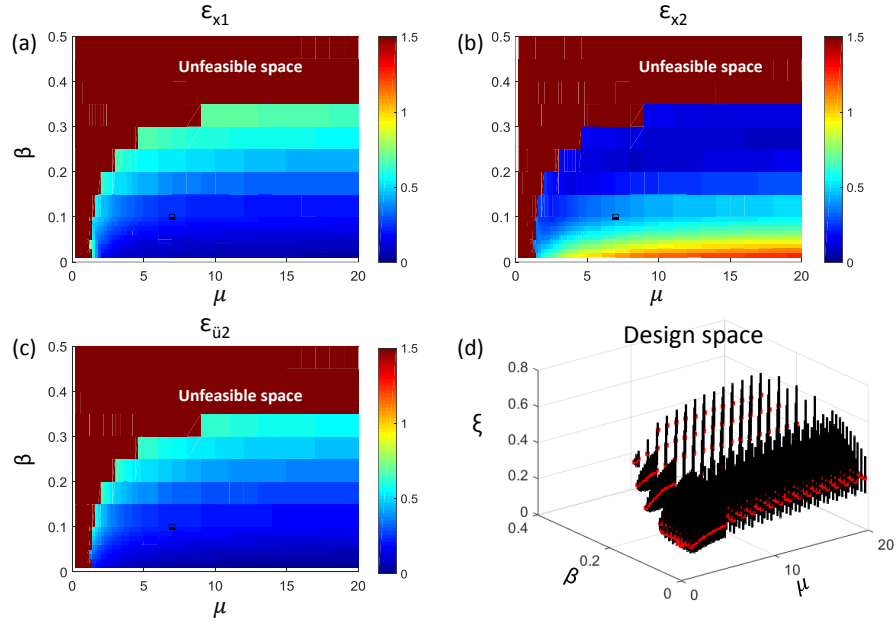


Fig. A-15. Contour plot of minimized x_1 , x_2 , \ddot{u}_2 relative error response at each (μ, β) when $\epsilon_{tot} < 150\%$ ($\phi = 0.15$): (a) ϵ_{x1} ; (b) ϵ_{x2} ; (c) $\epsilon_{\ddot{u}2}$; (d) design space.

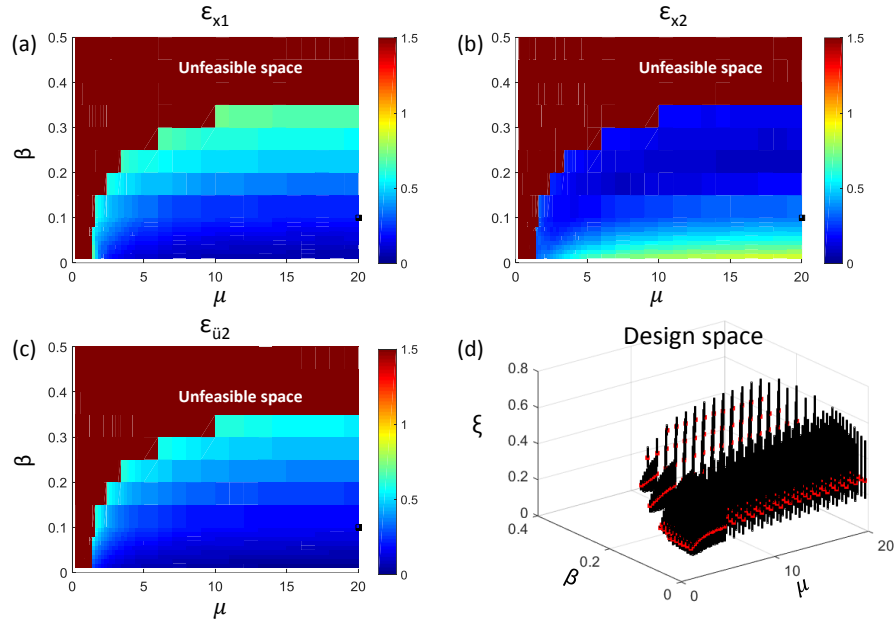


Fig. A-16. Contour plot of minimized x_1 , x_2 , \ddot{u}_2 relative error response at each (μ, β) when $\epsilon_{tot} < 150\%$ ($\phi = 0.19$): (a) ϵ_{x1} ; (b) ϵ_{x2} ; (c) $\epsilon_{\ddot{u}2}$; (d) design space.

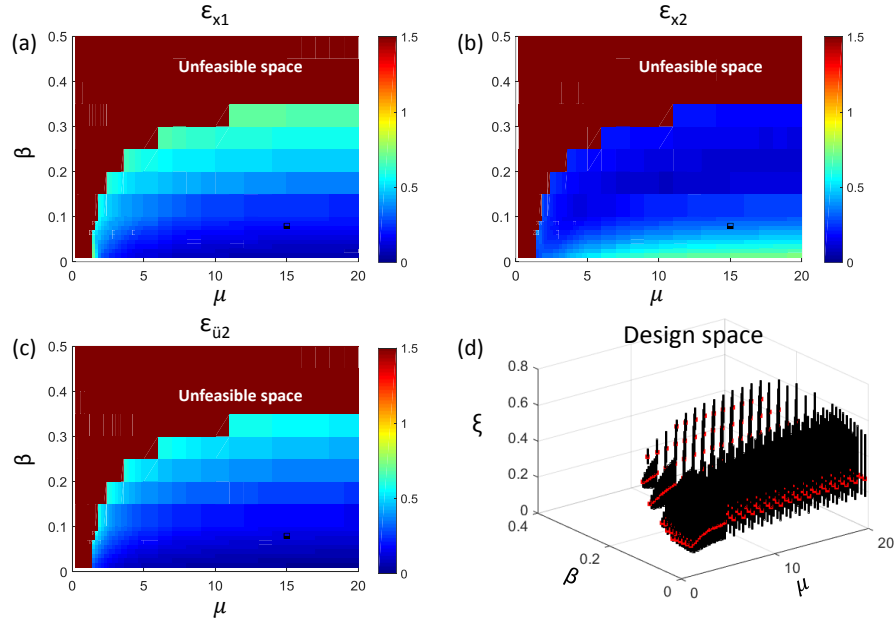


Fig. A-17. Contour plot of minimized x_1 , x_2 , \ddot{u}_2 relative error response at each (μ, β) when $\epsilon_{tot} < 150\%$ ($\phi = 0.21$): (a) ϵ_{x1} ; (b) ϵ_{x2} ; (c) $\epsilon_{\ddot{u}2}$; (d) design space.

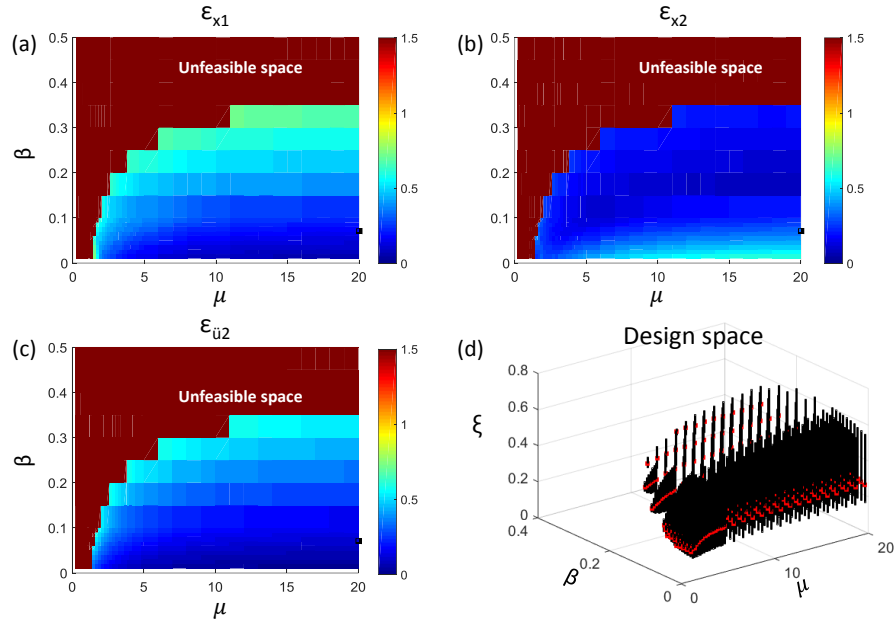


Fig. A-18. Contour plot of minimized x_1 , x_2 , \ddot{u}_2 relative error response at each (μ, β) when $\varepsilon_{tot} < 150\%$ ($\phi = 0.23$): (a) ε_{x1} ; (b) ε_{x2} ; (c) $\varepsilon_{\ddot{u}2}$; (d) design space.

A.12 Sensitivity Study on Design Parameters of the Elastic 2DOF System

A sensitivity study is conducted to check the influences from the design parameters.

Table A-1 shows the 2DOF models that are used in this sensitivity study.

Table A-1. 2DOF systems for comparison ($\phi = 0.03$, $\xi_1 = 0.02$)

Model name	μ	β	ξ	Note
2DOF_R	20	1000	0	Rigid IFAS
2DOF_Opt	20	0.25	0.44	Optimum design
2DOF_μ1	1	0.25	0.44	Changing μ
2DOF_μ5	5	0.25	0.44	
2DOF_μ10	10	0.25	0.44	
2DOF_β1	20	0.02	0.44	Changing β
2DOF_β2	20	0.1	0.44	
2DOF_β3	20	0.5	0.44	
2DOF_ξ1	20	0.25	0.02	Changing ξ
2DOF_ξ2	20	0.25	0.38	
2DOF_ξ3	20	0.25	0.54	
2DOF_ξ4	20	0.25	0.64	

The 2DOF system maximum responses in each earthquake are shown in Fig. A-19 – A-21 for comparing the influence from μ , β and ξ respectively. Black color represents the response of the 2DOF_Tra, red color represents the response of the 2DOF_Opt. Yellow, green, blue and grey (only in Fig. A-21) represent the response of the 2DOF system using other design parameters.

Fig. A-19 – A-21 show significant reduction in acceleration and displacement in the 2DOF_Opt in comparison to that of the 2DOF_Tra for all ten NTHAs. The results proves the effectiveness of the optimization method. Figure a, b show the zoomout and zoomin of the 2DOF system acceleration responses. Figure c, d show the zoomout and zoomin of the 2DOF system displacement responses. In addition, the responses of the 2DOF system using some un-optimized design is smaller than that using the optimized design, this is probably due to the characteristics of the earthquakes.

Fig. A-19 shows that the influence to the response of the 2DOF system from μ is negligible when μ is large, and the influence becomes significant when μ is decreased to a small value. This trend matches the parametric responses in Fig. 3-14a.

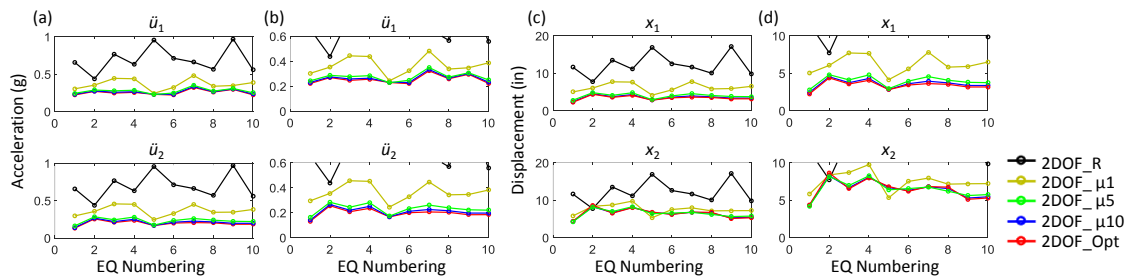


Fig. A-19. Maximum 2DOF system responses in earthquakes at different μ : acceleration: (a) zoom out; (b) zoom in; displacement: (c) zoom out; (d) zoom in.

Fig. A-20 shows that the influence to the responses from β is not that significant, except for x_2 . The response decreases as β decreases, however, the 2DOF system response using the 2DOF_Opt is good enough for obtaining a reduction from the 2DOF_R.

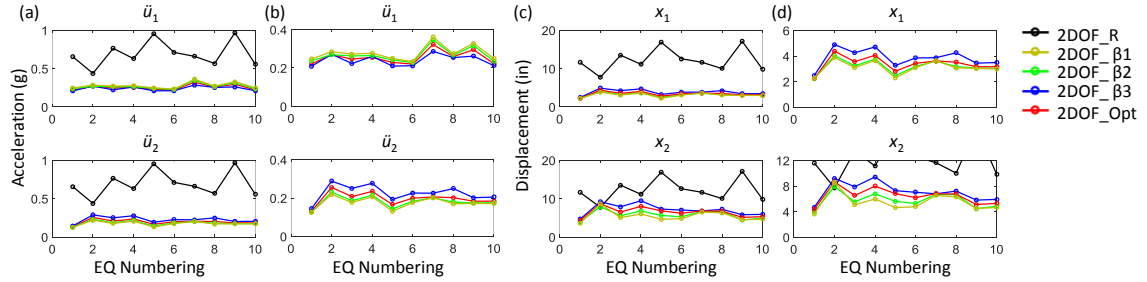


Fig. A-20. Maximum 2DOF system responses in earthquakes at different β : acceleration: (a) zoom out; (b) zoom in; displacement: (c) zoom out; (d) zoom in.

Fig. A-21 shows that the influence from ζ is significant if ζ is too small. However, if ζ is inside the design space, the influence from ζ is negligible.

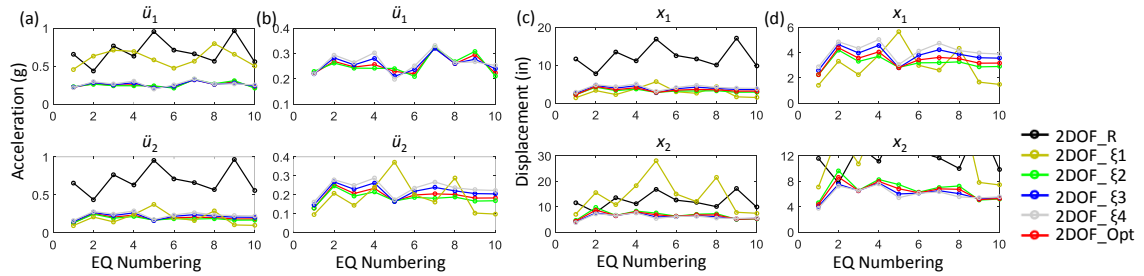


Fig. A-21. Maximum 2DOF system responses in earthquakes at different ζ : acceleration: (a) zoom out; (b) zoom in; displacement: (c) zoom out; (d) zoom in.

A.13 Parameter Sweep Method for Inelastic 2DOF System (PSM_Inelastic)

The PSM_Inelastic method is similar to the PSM. There are four parameters for studying the inelastic 2DOF system as mentioned previously: $(\phi, \mu, \alpha', k', \gamma)$. The following steps are used for this method:

- (1) Vary γ ($0\% \leq \gamma \leq 5\%$) and k' ($0.1 \leq k' \leq 500$) at each (ϕ, μ, α') . Perform NTHAs on the inelastic 2DOF system using 10 ground motion records in A suite of ten spectrum-

compatible earthquakes from FEMA P695 [121] are selected for the parametric studies. The earthquakes are scaled using the factors shown in Table 4-8 to match the 5% damped design spectrum for the generic SDC D site at the DBE level (See Fig. 4-9). The 1st and 2nd period are denoted as black solid and dashed vertical lines respectively for the traditional structures ($\Omega_e=1.3$). The NTHAs are performed at both the DBE and MCE level. The scaled DBE earthquakes are amplified by 1.5 to create MCE motions.

Table 4-8 for each design parameter combination. Mean value of the maximum responses of the 10 NTHAs is used to represent the response of the inelastic 2DOF system and filled in the response matrix in Fig. A-22a. Note that: $0\% \leq \gamma \leq 5\%$ with an interval of 1%. Six candidate γ are investigated. Nine candidate values for k' are: 0.1, 0.5, 1, 5, 10, 50, 100, 200, 500.

(2) The minimum response from Fig. A-22a across γ is used to form a vector R_1 . Vary the IFAS strength ($0.1 \leq \alpha' \leq 3$) at each (ϕ, μ) . R_1 is used to form a response matrix in Fig. A-22b. Note that: $0.1 \leq \alpha' \leq 0.7$ with an interval of 0.1, $0.8 \leq \alpha' \leq 1.2$ with an interval of 0.2, $1.5 \leq \alpha' \leq 3$ with an interval of 0.5. 14 candidate α' values are investigated.

(3) The minimum response from Fig. A-22b across k' is used to form a vector R_2 . Vary the mass ratio μ ($0.5 \leq \mu \leq 20$) at each ϕ . R_2 is used to form a response matrix in Fig. A-22c. Note that: $\mu=0.5$, $1 \leq \mu \leq 9$ with an interval of 1, $10 \leq \mu \leq 20$ with an interval of 2. 16 candidate μ values are investigated.

(4) The minimum response from Fig. A-22c across α' is used to form a vector R_3 . Vary the GLRS stiffness ratio ϕ ($0.03 \leq \phi \leq 0.23$). R_3 is used to form a response matrix in Fig. A-22d. The candidate values of ϕ are: 0.03, 0.05, 0.1, 0.15, 0.19, 0.21, 0.23. Seven candidate ϕ values are investigated.

(5) The minimum response from Fig. A-22d across μ is used to form a vector R_4 .

The value in R_4 is the minimum response of the inelastic 2DOF system at a given ϕ .

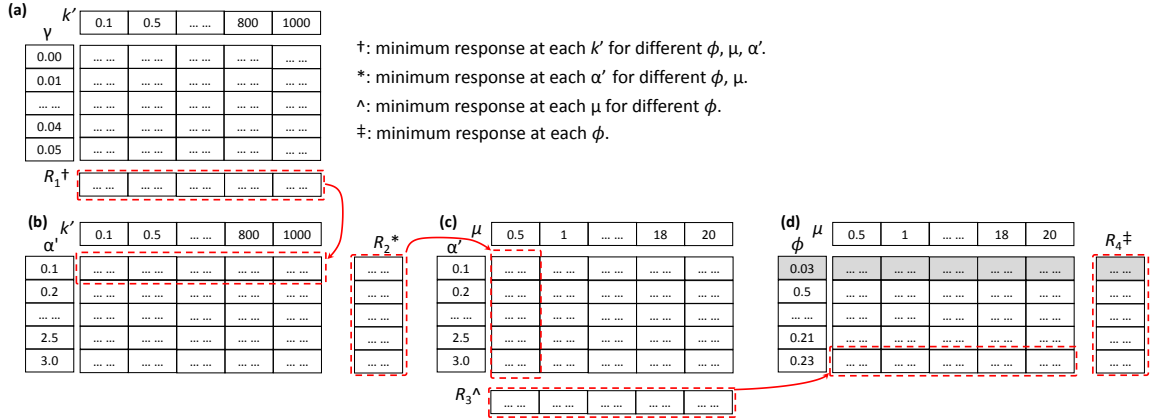


Fig. A-22. PSM_Inelastic method: (a) response matrix for (k', γ) ; (b) response matrix for (k', α') ; (c) response matrix for (μ, α') ; (d) response matrix for (μ, ϕ) .

Note that because higher mode effects is not represented by the 2DOF system, only one GLRS stiffness ratio ($\phi=0.03$) is under investigation in this dissertation. Therefore, only the shaded part (in grey) in Fig. A-22d will be shown in this dissertation.

A.14 NTHA on Traditional Elastic 2DOF and Inelastic 2DOF Systems

Significant reduction in \ddot{u}_2 is observed from the 2DOF_Tra to 2DOF_IFAS of the elastic 2DOF system in Fig. 3-20. This is conflict with what is shown in Fig. 3-22a. The reason for this conflict is the ignorance of the the potential LFRS yielding in the elastic 2DOF system. The LFRS and GLRS shear force and displacement of the 2DOF_R in the elastic and inelastic 2DOF systems are shown in Fig. A-23. The selected earthquake is EQ1 in A suite of ten spectrum-compatible earthquakes from FEMA P695 [121] are selected for the parametric studies. The earthquakes are scaled using the factors shown in Table 4-8 to match the 5% damped design spectrum for the generic SDC D site at the DBE level (See Fig. 4-9). The 1st and 2nd period are denoted as black solid and dashed vertical lines

respectively for the traditional structures ($\Omega_e=1.3$). The NTHAs are performed at both the DBE and MCE level. The scaled DBE earthquakes are amplified by 1.5 to create MCE motions.

Table 4-8. The earthquake is DBE level. Much larger LFRS and GLRS shear force is observed in the elastic 2DOF system than that of the inelastic 2DOF system (See Fig. A-23a, b). Additionally, large difference is observed in x_1 , x_2 . This comparison indicates one drawback of using the elastic 2DOF system.

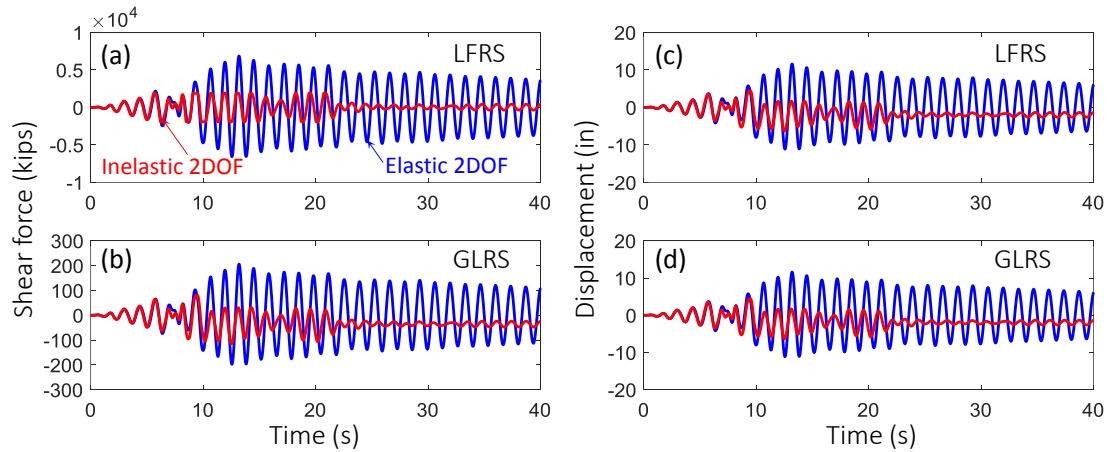


Fig. A-23. Response of the 2DOF_R in the elastic and inelastic 2DOF system: shear force: (a) LFRS; (b) GLRS; displacement: (c) x_1 ; (d) x_2 .

A.15 Single Objective Optimization on the Inelastic 2DOF system

The responses of one parametric study on inelastic 2DOF systems at a given design parameter ($\phi = 0.03$, $\mu = 20$, $\alpha' = 0.8$) is shown in Fig. A-24 as an example. Response of an 2DOF_Tra is shown using black circles. Fig. A-24a shows that the smallest \ddot{u}_2 of the 2DOF_IFAS occurs when $\gamma = 0\%$. The \ddot{u}_2 of the 2DOF_IFAS is even larger than that of the 2DOF_Tra when $\gamma > 0\%$ for the cases using large k_i . A significant reduction in x_1 can be observed in Fig. A-24b. Fig. A-24b shows that the x_1 is increased as k_i increases and nearly

constant when $k_i > 10$. Further, the \ddot{u}_2 and x_1 are increased as γ increases. Fig. A-24 indicates that smaller γ produces preferable 2DOF system responses.

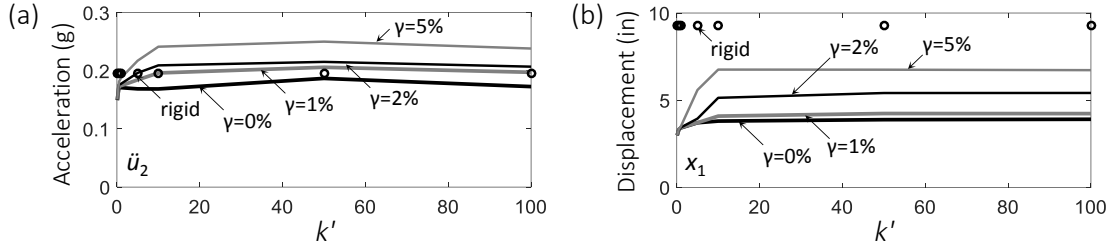


Fig. A-24. Responses of parametric study of inelastic 2DOF systems ($\phi=0.03$, $\mu=20$, $\alpha'=0.8$): (a) acceleration; (b) displacement.

A contour plot of the responses of inelastic 2DOF systems using the same design parameter combination as that of Fig. A-24 is shown in Fig. A-25. Fig. A-25 shows that the 2DOF system responses doesn't change significantly across different k' when $k' > 10$, implying that when k_i is large enough, the 2DOF system responses is independent from k_i . Fig. A-25a, c show that the x_1 and \ddot{u}_2 are reduced significantly as k_i decreases when $k' < 10$. Fig. A-25a, c also show that the x_1 and \ddot{u}_2 are increased as γ increases. Fig. A-25b, d show that the x_2 and $|x_2-x_1|$ are increased significantly as k_i decreases when $k' < 5$. Fig. A-25d shows that the $|x_2-x_1|$ is increased as γ decreases. The effects from k' on x_1 and x_2 are conflict to each other, which is the same as the effect from β of the elastic IFAS to x_1 and x_2 of the elastic 2DOF system.

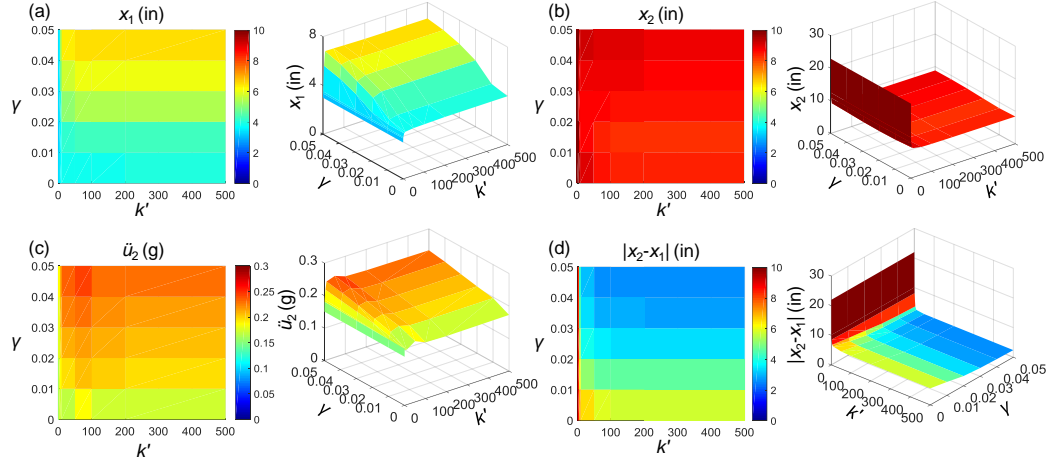


Fig. A-25. Contour plots of parametric study of inelastic 2DOF systems ($\phi=0.03$, $\mu=20$, $\alpha'=0.8$): (a) x_1 ; (b) x_2 ; (c) \ddot{u}_2 ; (d) $|x_2-x_1|$.

The response of the inelastic 2DOF system and related γ when x_1 is minimized at a given ϕ and μ ($\phi=0.03$, $\mu=20$) is shown in Fig. A-26. Fig. A-26a shows that a significant reduction of the x_1 is produced when $\alpha < 1$. The same phenomenon is observed in \ddot{u}_2 (See Fig. A-26c). The x_1 and \ddot{u}_2 are decreased as k' decreases when $k' < 1$. However these two responses have negligible variations as k' increases when $k' > 10$. The x_2 and $|x_2-x_1|$ also have negligible variations when the $k' > 5$ and $\alpha > 1$ (See Fig. A-26b, d). The x_2 and $|x_2-x_1|$ undergo large responses when $k' < 5$ and $\alpha < 1$. The minimized x_1 is obtained when $\gamma = 0\%$ for most of the design cases (See Fig. A-26e). Fig. A-26 shows conflict responses between x_1 & \ddot{u}_2 and x_2 & $|x_2-x_1|$ when $\alpha < 1$.

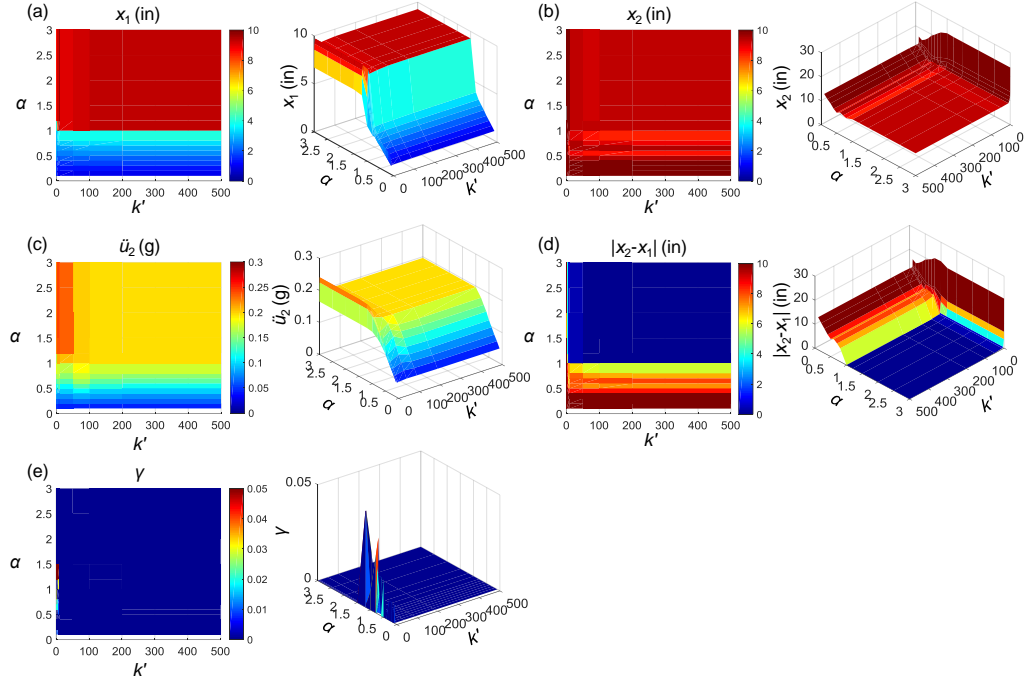


Fig. A-26. Contour plots of parametric study of inelastic 2DOF systems when x_1 is minimized ($\phi = 0.03$, $\mu = 20$): (a) x_1 ; (b) x_2 ; (c) \ddot{u}_2 ; (d) $|x_2 - x_1|$; (e) γ .

The response of the inelastic 2DOF system when x_1 is minimized at $\phi = 0.03$ is shown in Fig. A-27. Fig. A-27a shows two phenomenons: (1) a significant reduction of x_1 is produced when $\alpha < 1$, which is similar to Fig. A-26a; (2) the reduction of x_1 is increased as μ increases. Fig. A-27b shows that x_2 response when x_1 is minimized. Additionally, the minimized x_2 response is also plotted in grey as a reference. Fig. A-27b shows that when x_1 is minimized, the related x_2 response is larger than that of minimized x_2 . A significant difference can be observed when $\alpha > 1$. The difference is decreased when $\alpha < 1$. The changes in μ has small effects on x_2 when $\mu > 2$. x_2 is reduced as α decreases ($0.5 < \alpha < 0.8$) and reversed to increase when $\alpha < 0.5$. Fig. A-27c shows that \ddot{u}_2 undergoes significant reduction as α decreases when $\alpha < 1$. \ddot{u}_2 also undergoes significant reduction as μ increases when $\mu < 5$ and the variation is negligible when $\mu > 5$. Fig. A-27d shows that the relative displacement is decreased significantly as α decreases when $\alpha < 1$ and reversed to increase

when $\alpha < 0.5$. Fig. A-27e, f show that x_1 is minimized mostly when $\gamma = 0\%$ and $k' = 0$. Fig. A-27 shows that $\alpha < 1$ is the interested region for finding the optimized 2DOF system responses.

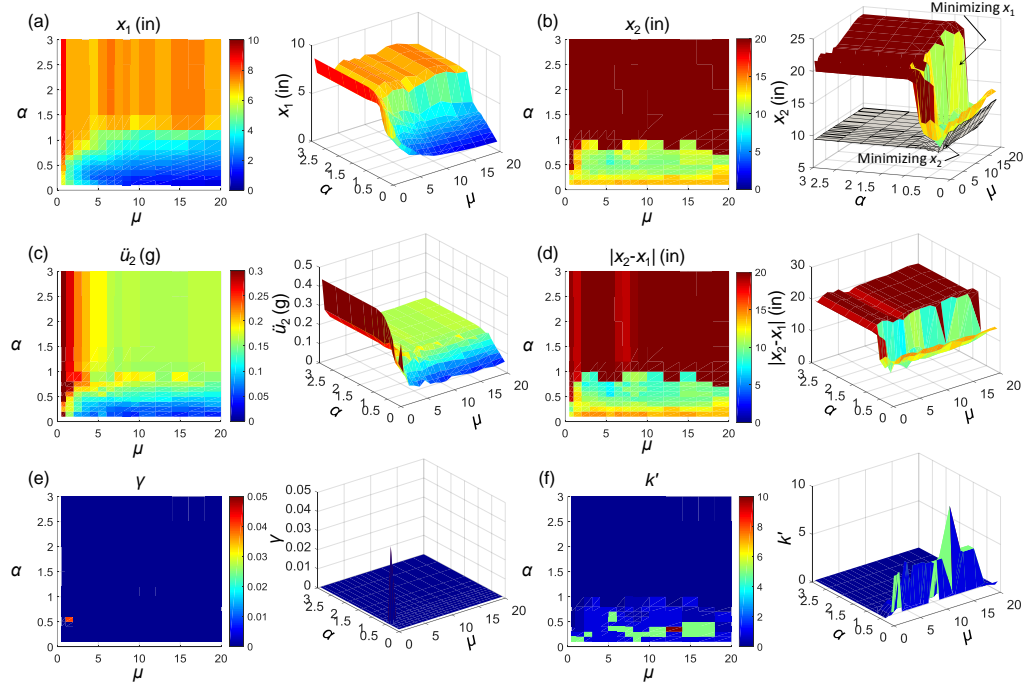


Fig. A-27. Contour plots of parametric study of inelastic 2DOF systems when x_1 is minimized ($\phi = 0.03$): (a) x_1 ; (b) x_2 ; (c) \ddot{u}_2 ; (d) $|x_2 - x_1|$; (e) γ ; (f) k' .

The response of the inelastic 2DOF system when x_2 is minimized at $\phi = 0.03$ is shown in Fig. A-28. Fig. A-28a shows that x_1 is decreased as α decreases when $\alpha < 1$. The x_1 is reversed to increase when $\alpha < 0.4$ and deviates more from the minimized x_1 (in grey) as α decreases. Fig. A-28b shows that x_2 has negligible variation as α decreases when $\alpha > 1$. x_2 is decreased first and then increased significantly as α decreases when $\alpha < 1$. Fig. A-28c shows that \ddot{u}_2 is increased significantly as μ decreases when $\mu < 5$. Fig. A-28d shows that the relative displacement is increased significantly when $\alpha < 1$. Fig. A-28e, f show the γ and k' for obtaining the minimized x_2 .

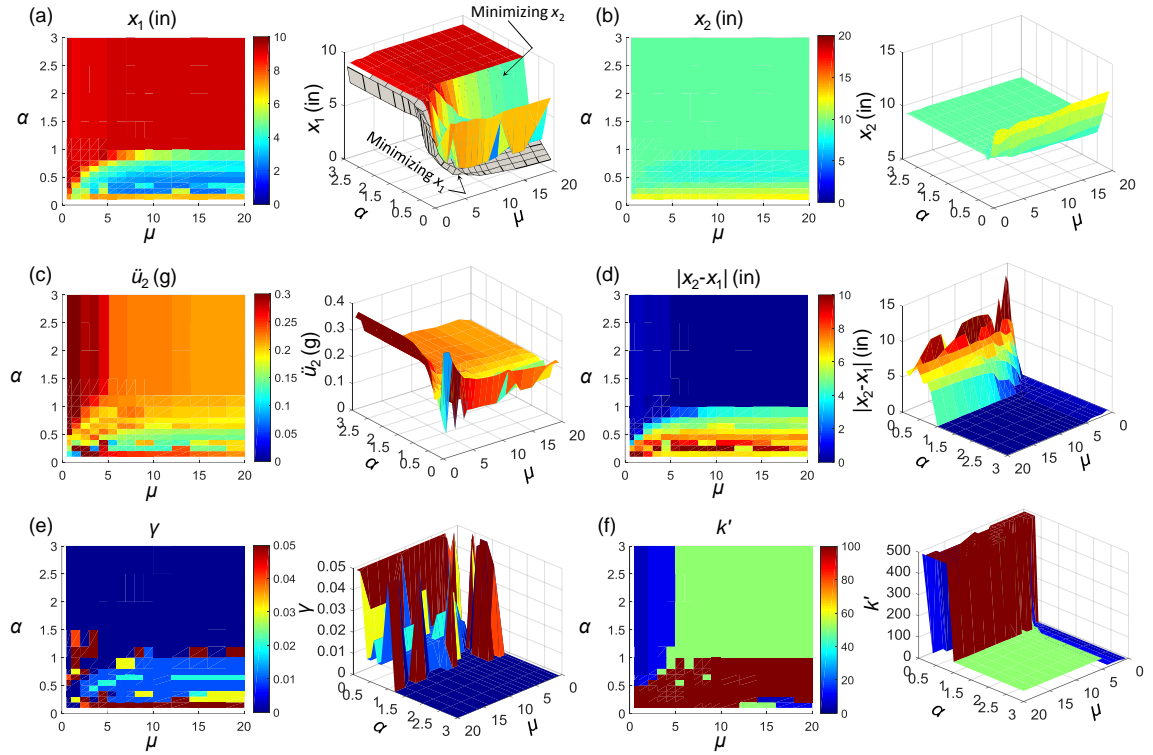


Fig. A-28. Contour plots of parametric study of inelastic 2DOF systems when x_2 is minimized ($\phi=0.03$): (a) x_1 ; (b) x_2 ; (c) \ddot{u}_2 ; (d) $|x_2-x_1|$; (e) γ ; (f) k' .

Fig. A-27 – A-28 show that the responses of the inelastic 2DOF system are not changing in the same trend when minimizing x_1 and x_2 respectively. Additionally, the needed γ and k' for minimizing x_1 and x_2 are not the same. Therefore, multi-objective optimization is needed for finding a design space of the nonlinear 2DOF system.

APPENDIX B – SUPPLEMENTAL INFORMATION FOR CHAPTER 4

B.1 Fundamental Response of the IFAS Structure

The structure responses at the selected time spots in Fig. 4-10 are shown in Fig. B-1. At spot A, the GLRS and wall deforms rightward and the GLRS roof just passed the zero location. The velocity of the wall and GLRS is increased from the bottom to the roof and the GLRS deforms faster than the wall. At spot B, the GLRS and wall continue deforming rightward and the GLRS deforms larger than the wall. The GLRS velocity is still larger than the wall. At spot C, the GLRS and wall reach the maximum positive deformation in the selected cycle and the velocity is close to zero. The maximum relative displacement occurs at the 9th floor. The GLRS and wall then deforms leftward afterwards. At spot D, the GLRS deforms faster than the wall. The velocity at the lower floor levels of the GLRS and wall are still close to zero, implying that the upper floors deforms faster than lower floors. At spot E, the GLRS roof moves back to the zero location, the velocity of the wall is increased from the bottom to the roof, while the velocity of the GLRS is increased from the bottom to the 10th floor and then decreased from the 10th floor to the roof. At spot F, the GLRS and wall reach the maximum negative deformation in the selected cycle and the velocity is close to zero. The relative displacement is increased nearly linear from the bottom to the roof. Afterwards, the GLRS and wall deforms rightward and the GLRS deforms faster than the wall. At spot G, the upper floors of the GLRS deforms with a larger velocity. In this structure deformation cycle, the wall deforms mostly in the 1st mode shape, while the GLRS deforms mostly in a higher mode shape. The GLRS mostly deforms faster than the wall.

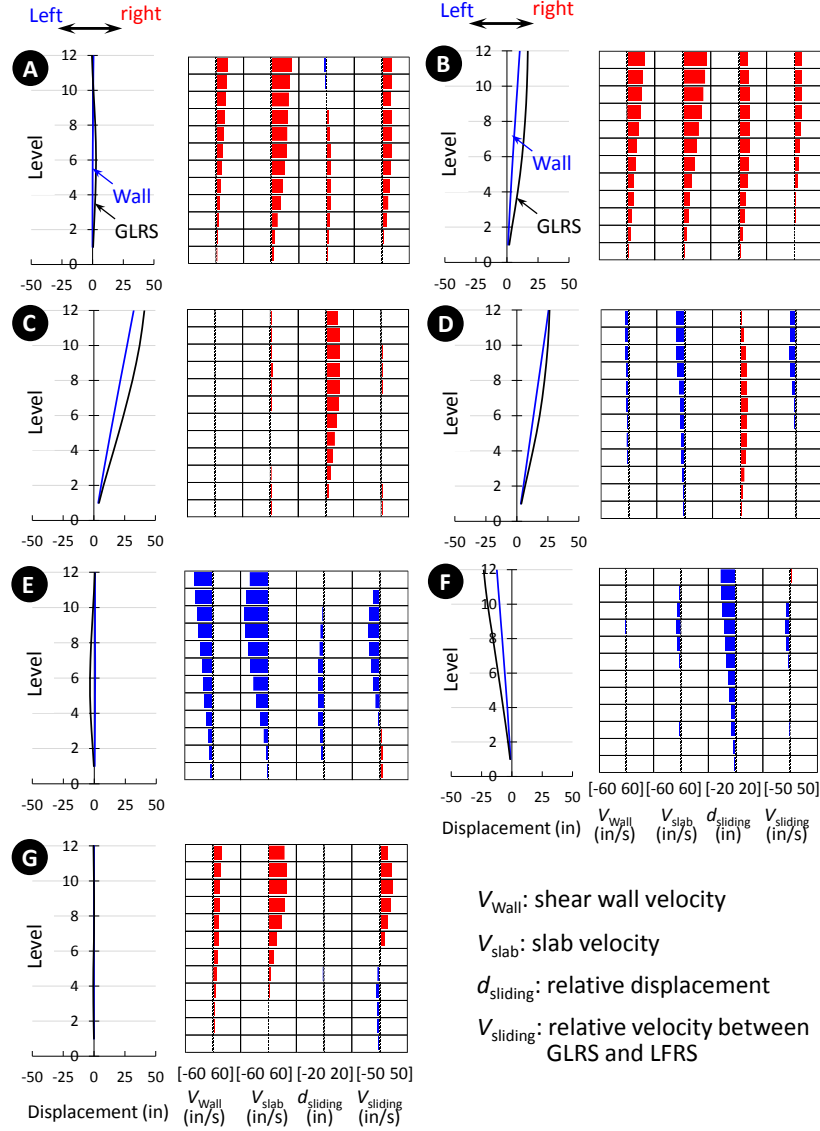


Fig. B-1. Evaluation structure ($\Omega_e=1.0$, $\alpha=0.3$) response at selected time spots in Fig. 4-10.

B.2 Effect of LFRS Overstrength

The influences from Ω_e of 4-, 8-story structures are shown in this section.

Fig. B-2 – B-3 show parametric results (MCE, $\gamma=2\%$) of the 4-story and 8-story evaluation structures with different Ω_e . This set of figures show similar trends that were observed in Fig. 4-15. Fig. B-2f, B-3f show that the energy dissipated in the wall is very

small for a structure with large Ω_e and small α , resulting in nearly a damage free structure system.

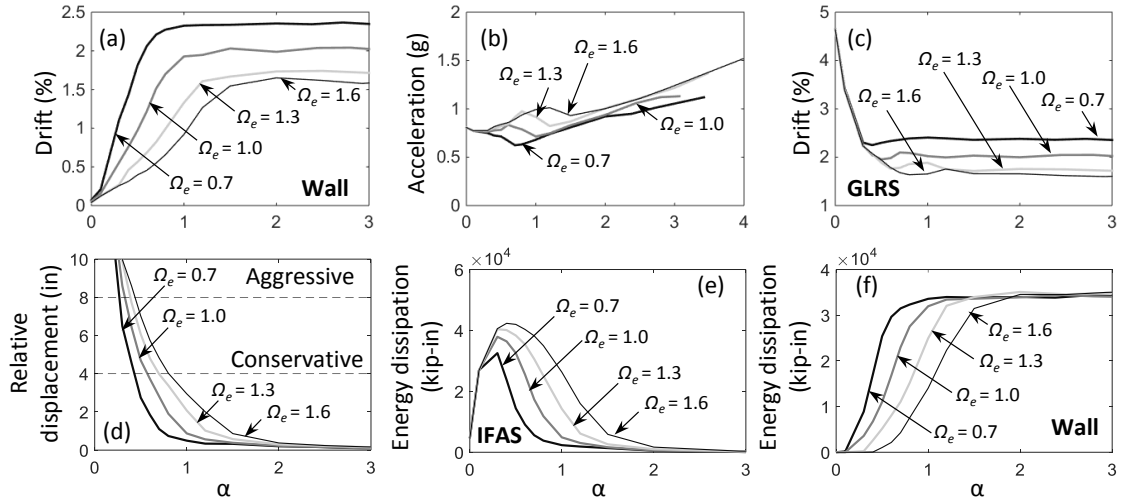


Fig. B-2. 4-story structure response comparison at different Ω_e and α under MCE ($\gamma=2\%$): (a) wall inter-story drift; (b) floor acceleration; (c) GLRS column inter-story drift; (d) relative displacement; (e) IFAS energy dissipation; (f) wall energy dissipation.

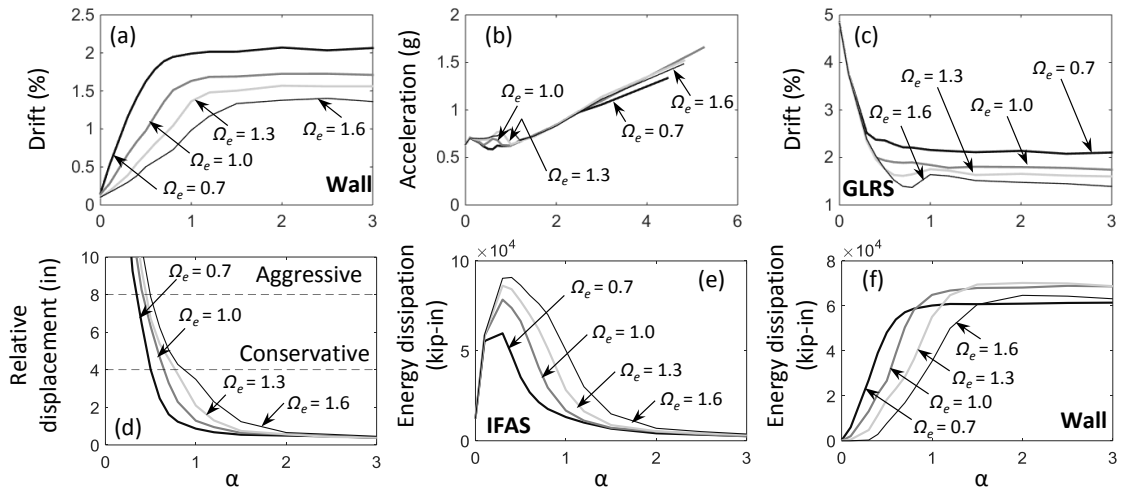


Fig. B-3. 8-story structure response comparison at different Ω_e and α under MCE ($\gamma=2\%$): (a) wall inter-story drift; (b) floor acceleration; (c) GLRS column inter-story drift; (d) relative displacement; (e) IFAS energy dissipation; (f) wall energy dissipation.

B.3 Effect of IFAS Secondary Stiffness

Fig. B-4 shows the response comparison of the 12-story structure using different γ ($\Omega_e=1.0$). The responses of the 12-story structures follow the same trend of the 4-story structures.

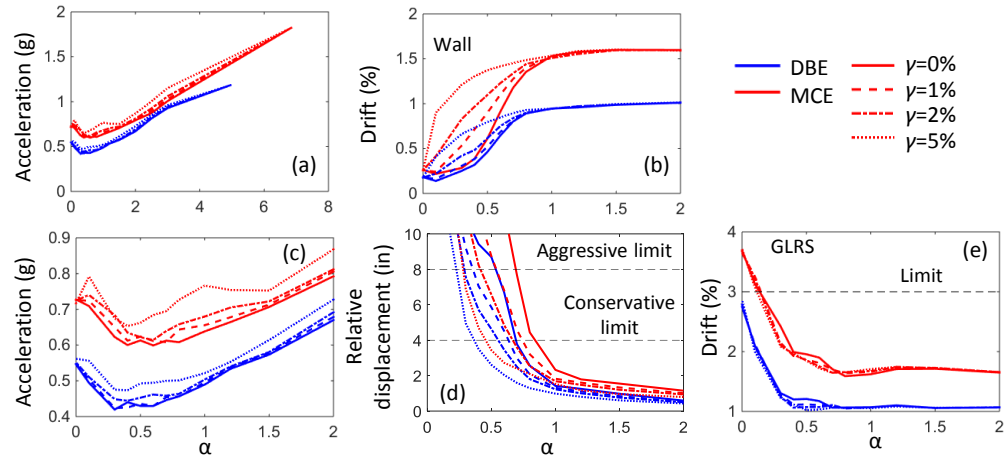


Fig. B-4. 12-story structures using different γ ($\Omega_e=1.0$): (a) floor acceleration ($0 < \alpha < 8$); (b) LFRS drift; (c) floor acceleration ($0 < \alpha < 2$); (d) relative displacement; (e) GLRS drift.

Fig. B-4b shows one interesting phenomenon: when the IFAS strain hardening ratio is small ($\gamma = 0\%, 1\%$), the wall drift is increased as α decreases from 0.1 to 0.01. This phenomenon is conflict to the idea of using the IFAS: the wall drift was supposed to be reduced as the IFAS strength decreases because the external force acting on the wall is reduced. $\alpha < 0.1$ may not be a feasible design space of the IFAS since the relative displacement is larger than the aggressive limit, however, it will be interesting to find out the reason for this phenomenon.

The contribution of the shear wall shear force consists of two parts: IFAS force and shear wall inertial force. The reason for the phenomenon is that the IFAS force is smaller than the wall inertial force when γ and α are small. The structure responses in EQ3 (MCE level) when $\gamma = 1\%$ is shown in Fig. B-5 as an example. Fig. B-5a shows the wall drift

profile when the wall reaches its maximum base moment. The wall drift is larger when $\alpha = 0.01$. Fig. B-5b,c show the wall base moment decomposition. Fig. B-5b shows that the moment is mainly contributed from the inertial force when $\alpha = 0.01$. Fig. B-5c shows that the moment is mainly contributed from the IFAS force when $\alpha = 0.1$. Therefore, the larger wall drift when $\alpha = 0.01$ is due to the contribution from the wall inertial force.

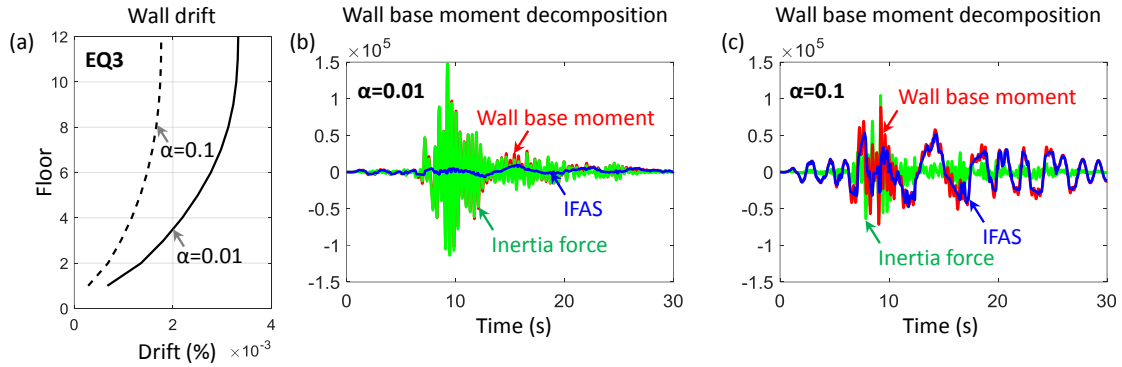


Fig. B-5. 12-story structure responses in EQ3 ($\gamma = 1\%$, MCE): (a) wall drift envelopes; wall base moment decomposition: (b) $\alpha = 0.01$; (c) $\alpha = 0.1$.

The design plots for the different height and γ are shown in Fig. B-6 ($\Omega_e = 1.0, 1.6$). Upper limit α is decreased as γ increases (See Fig. B-6a). The shear wall drift is increased as γ increases when $\gamma > 1\%$ (See Fig. B-6e). However, the shear wall drift is decreased as γ increases when $\gamma < 1\%$. γ has larger influence on the accelerations of shorter structures than taller structures (See Fig. B-6c, f). γ has some influences on the GLRS drift, however, not very significant (See Fig. B-6d).

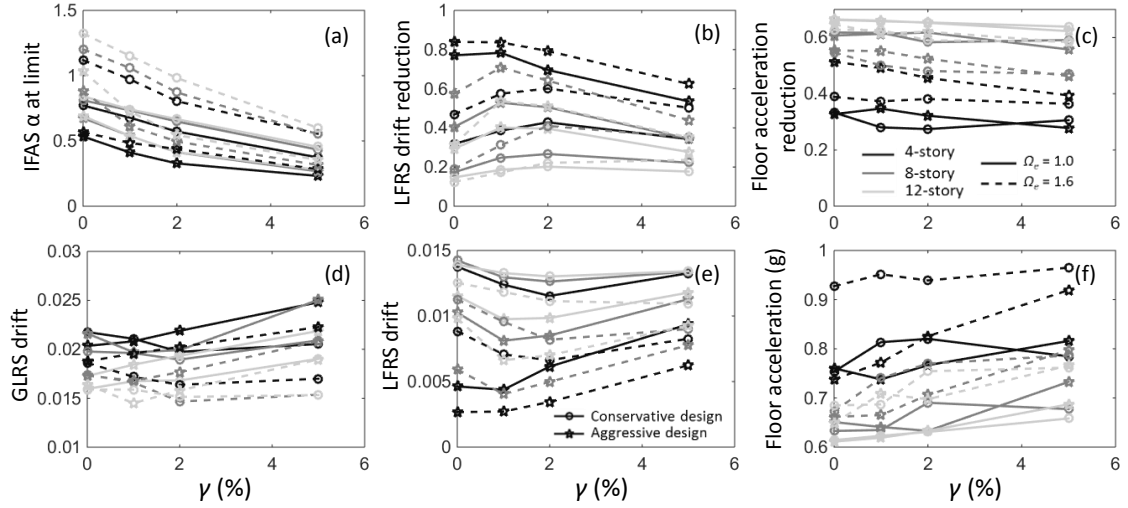


Fig. B-6. Design plot for IFAS secondary stiffness ($\Omega_e=1.0, 1.6$): (a) α ; (b) LFRS drift reduction; (c) floor acceleration reduction; (d) GLRS drift; (e) LFRS drift; (f) floor acceleration.

B.4 Effect of IFAS Initial Stiffness

The effect of changing K_i will be discussed in this section. Fig. B-7 shows the parametric results of the 12-story structure ($\Omega_e=1.0$) using different K_i . The results show that K_i has negligible influence on the LFRS drift, GLRS drift and relative displacement. K_i has some influence on the floor acceleration, but it is not significant. Note that the K_i studied in this section only includes three different values and the variation of the responses is not large. If K_i is too small, the relative displacement and GLRS drift will be increased significantly [16]. The same phenomenon can also be observed in the nonlinear 2DOF system responses under earthquakes (See Fig. A-25b, d).

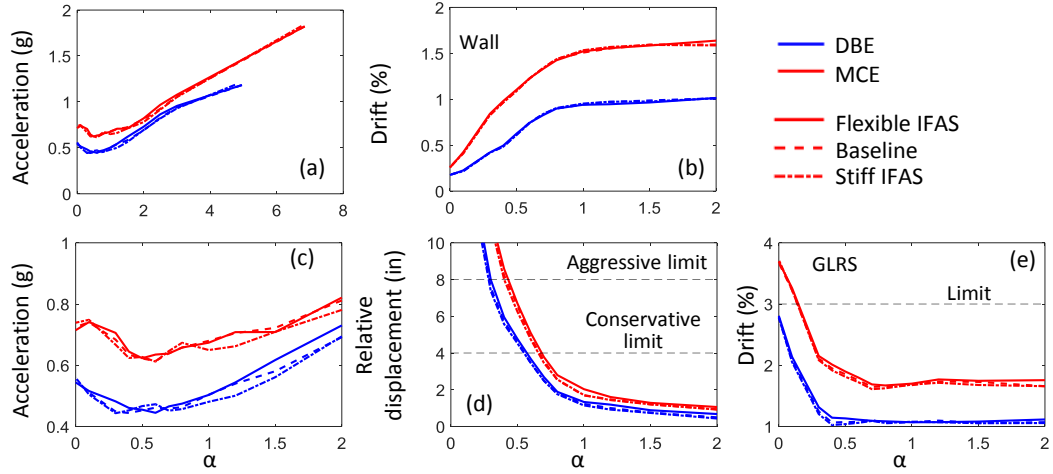


Fig. B-7. 12-story structures using different IFAS K_i : (a) floor acceleration ($0 < \alpha < 8$); (b) LFRS drift; (c) floor acceleration ($0 < \alpha < 2$); (d) relative displacement; (e) GLRS drift.

B.5 Design Plot Considering the LFRS Type Effect

Fig. B-8 shows the design plot for the different structural height and LFRS types ($\Omega_e=1.0$). In most cases, α and LFRS drift reduction at the design limits is decreased as the energy dissipation of the LFRS increases (See Fig. B-8a, b). The LFRS drift at the design limits is reduced as the energy dissipation of the LFRS increases (See Fig. B-8e). Using rocking wall can generate a larger acceleration reduction than the RC wall (See Fig. B-8c), especially for the 4-story structure. However, the floor acceleration of the rocking wall structures at the design limits is larger than the RC wall structure (See Fig. B-8f), implying that the acceleration of a traditional structure using the rocking wall as the LFRS is larger than that using the RC wall. The different energy dissipation capacity of the rocking wall has negligible effect on the floor acceleration in most cases. The GLRS drift at the conservative design limits is decreased as the LFRS energy dissipation increases (except for 4-story RC wall), while the GLRS drift at the aggressive design limits doesn't have much variations (See Fig. B-8d).

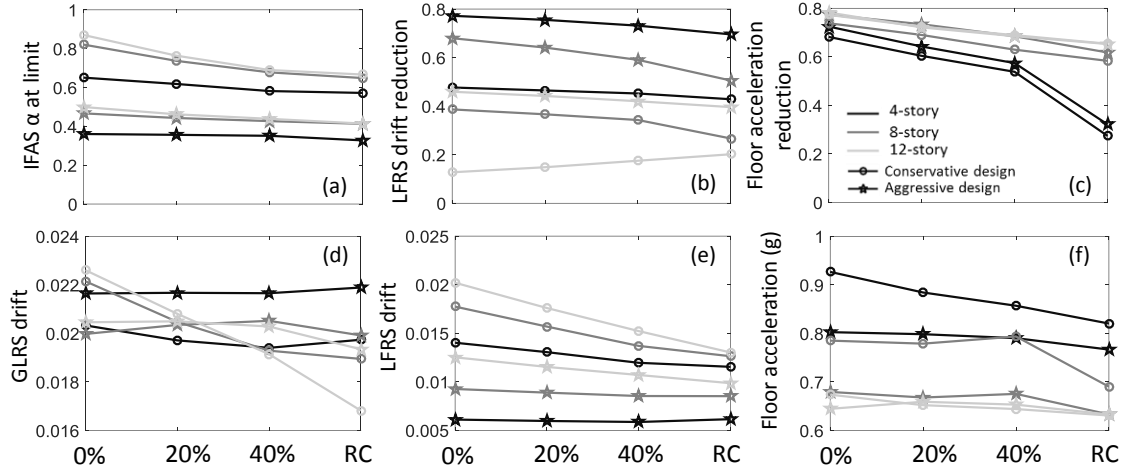


Fig. B-8. Design plot for different LFRS types ($\Omega_e=1.0$): (a) α ; (b) LFRS drift reduction; (c) floor acceleration reduction; (d) GLRS drift; (e) LFRS drift; (f) floor acceleration.

B.6 Effect of GLRS Column Properties

Fig. B-9 shows the parametric results of a 12-story structure (RC wall, $\Omega_e=1.0$) using different GLRS column stiffness. Fig. B-9a, c, d show that larger GLRS column stiffness generates larger floor acceleration and relative displacement. Fig. B-9b shows that the different column stiffness has negligible effect on the shear wall drift.

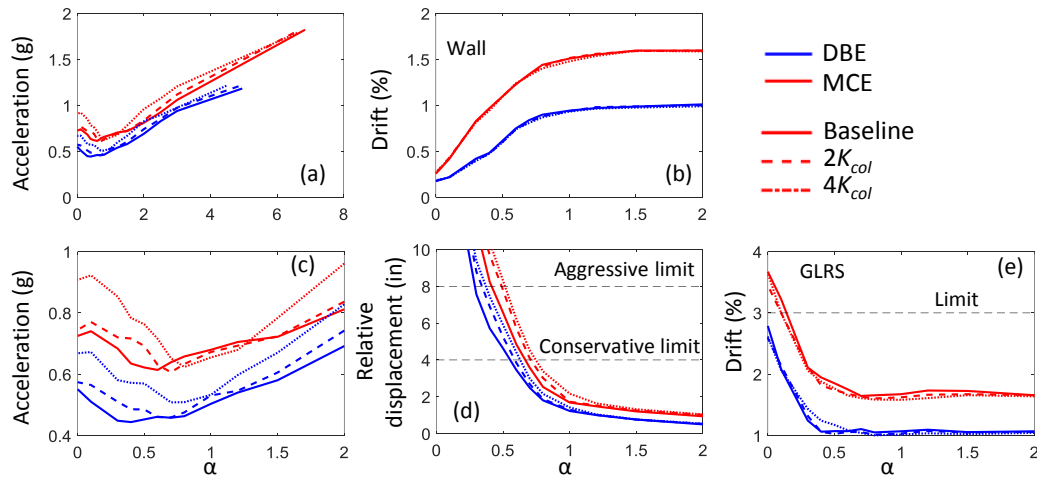


Fig. B-9. 12-story RC wall structures using different column stiffness: (a) floor acceleration ($0 < \alpha < 8$); (b) LFRS drift; (c) floor acceleration; (d) relative displacement; (e) GLRS drift.

Fig. B-10 shows the parametric results of the 12-story structure (Rocking wall, $\Omega_e=1.0$) using different GLRS column stiffness.

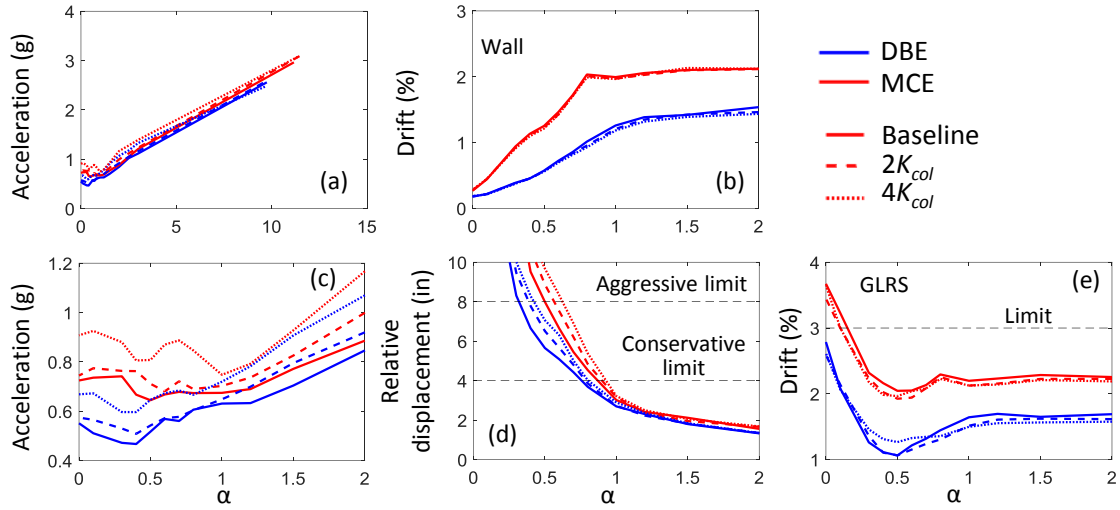


Fig. B-10. 12-story rocking wall structures using different column stiffness: (a) floor acceleration ($0 < \alpha < 15$); (b) LFRS drift; (c) floor acceleration; (d) relative displacement; (e) GLRS drift.

Fig. B-10a, c indicate that larger GLRS column stiffness generates larger floor acceleration. Fig. B-10b shows that variation of the column stiffness has negligible influence on the shear wall drift. Larger column stiffness generates larger relative displacement when $\alpha < 1$ and has negligible influence on the relative displacement when $\alpha > 1$ (See Fig. B-10d). A valley is shown in the GLRS drift when $0.3 < \alpha < 0.8$ for MCE and $0.3 < \alpha < 1$ for DBE (See Fig. B-10e).

Fig. B-11 shows parametric results of the 12-story structure (RC wall, $\Omega_e=1.0$) using different GLRS column base plastic hinge strength (See Fig. 4-6). The results show that the different column strength has negligible effect on the shear wall drift and relative displacement. Stronger column produces larger acceleration (See Fig. B-11c). Stronger column produces larger GLRS drift when α is small (See Fig. B-11e).

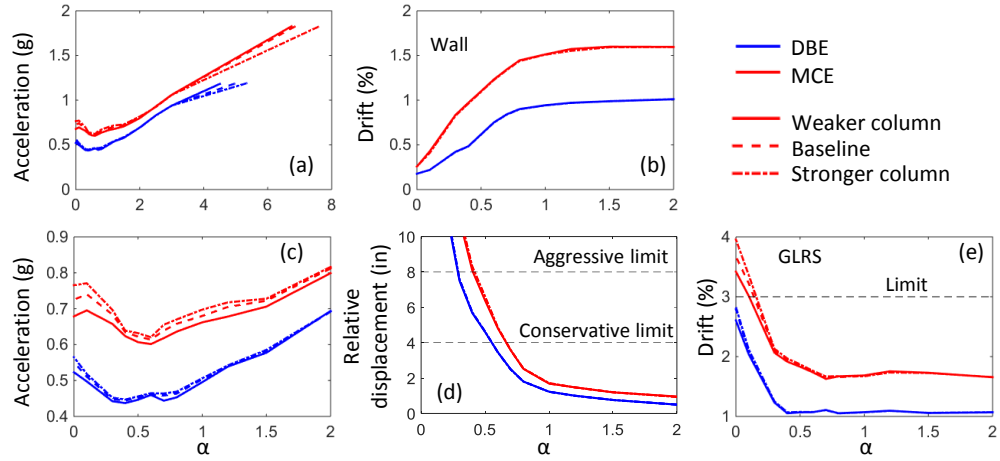


Fig. B-11. 12-story RC wall structures using different column strength: (a) floor acceleration ($0 < \alpha < 8$); (b) LFRS drift; (c) floor acceleration; (d) relative displacement; (e) GLRS drift.

B.7 Effect of IFAS Strength Profiles

Fig. B-12a shows the profiles of the two IFAS strength patterns for the baseline structure and the difference between these two patterns is small. Fig. B-12b, c, d show the shear wall drift, relative displacement, floor acceleration comparison between these two sets of analyses. Results from three IFAS strength ($\alpha=0.1, 0.6, 0.8$) are selected for comparisons. The comparisons show that these two IFAS strength patterns produces very similar structural responses.

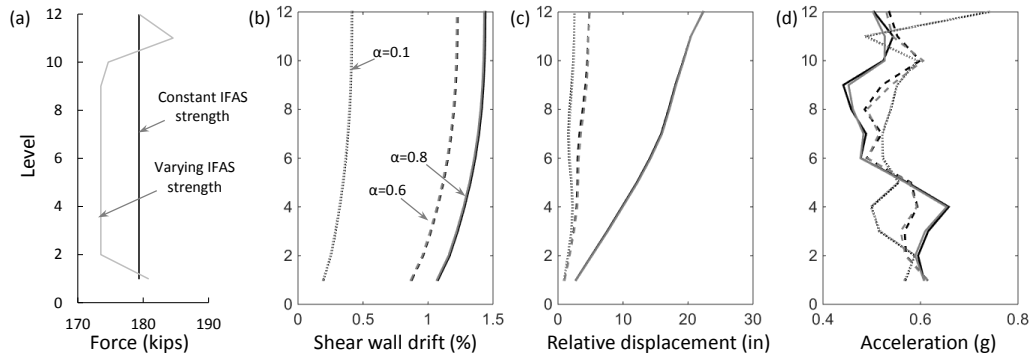


Fig. B-12. 12-story structure response comparison using different IFAS strength pattern: (a) IFAS strength pattern; (b) shear wall drift; (c) relative displacement; (d) floor acceleration.

B.8 Effect of IFAS Configurations

The IFAS has two candidate configurations as mentioned previously: FD + RB and BRB + RB. Section 4.6 – 4.12 describe the structural performance under different design parameters using the FD + RB configuration. This section will discuss the effect to the structural response by using BRB + RB.

The property of the BRB + RB is shown in Table 4-4. The responses of a 12-story evaluation structure (RC wall, $\Omega_e=1.0$) using the BRB + RB are compared with the responses of the same structure using the FD + RB. The strength of the BRB + RB and FD + RB is adjusted to the same value ($\alpha=0.6$) for the purpose of making a fair comparison. In Table 4-4, $\gamma = 5.19\%$ for the BRB + RB and $\gamma = 1.94\%$ for the FD + RB. Therefore, the BRB + RB will produce larger external force on the wall and the wall probably undergoes larger deformation. Thus, a third IFAS configuration, FD + RB with $\gamma = 5.19\%$, is also implemented to the evaluation structure, for the purpose of investigating the difference between the BRB and FD when γ is the same. The responses envelopes are plotted in Fig. B-13. Fig. B-13a shows that the floor acceleration is increased as γ increases. Fig. B-13b shows the wall drift and GLRS drift envelopes. The wall drift is increased as γ increases. The relative displacement is decreased as γ increases (See Fig. B-13c). The BRB + RB and FD+RB when $\gamma = 5.19\%$ produce similar floor acceleration, shear wall drift, GLRS drift and relative displacement. Therefore, using BRB and FD as deformable connections doesn't produce large differences in structure responses when the strength and stiffness of these two devices are close.

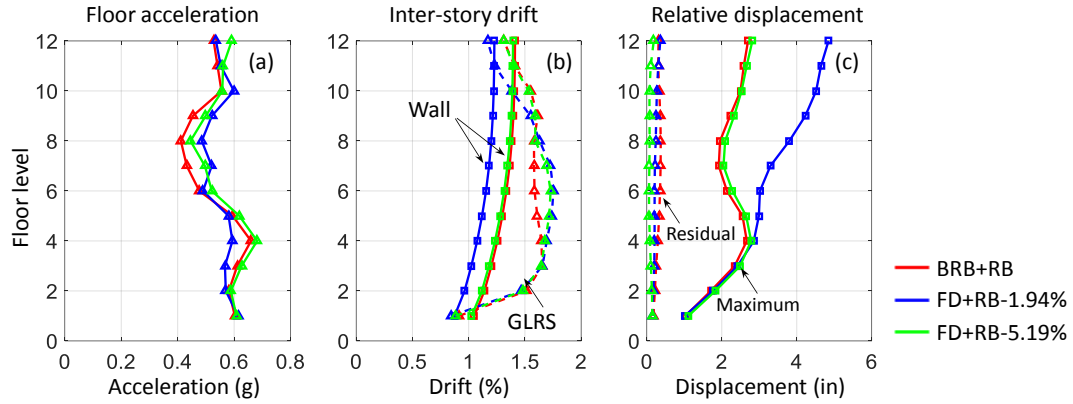


Fig. B-13. Responses envelopes of an evaluation structure with different IFAS configurations: (a) floor acceleration; (b) inter-story drift; (c) relative displacement.

B.9 IFAS Properties

The IFAS properties used for Sec. 4-14 is shown in Table B-1.

Table B-1. IFAS properties for parametric study.

Link device	α	F_y (kips)	Initial stiffness K_i (kip/in)		Secondary stiffness K_{2nd} (kip/in)			
			Idealization	Test	Idealization	Test		
						0.36%	0.36%	1.94% 5.19%
Generic idealization	0.3	81	1802	811	6.55	2.95	42.10	15.70
	0.4	108	2403	1081	8.73	3.93	56.14	20.94
	0.5	135	3003	1351	10.91	4.91	70.17	26.17
	0.6	162	3604	1622	13.09	5.89	84.20	31.41
	0.8	216	4805	2162	17.46	7.85	112.27	41.87
	1	270	6006	2703	21.82	9.82	140.34	52.34
BRB + RB	0.85	229	2080		108(5.19%)			
FD + RB	0.86	231	2427		47(1.94%)			

B.10 Parametric Study of Using Ledges

B.10.1 Description of Design

The IFAS device used in this study are the two IFAS combinations used in Table 4-4. The nonlinear hysteresis property of the IFAS is assigned from Table 4-4. The study matrix is shown in Table B-2.

Table B-2. IFAS eccentricities and concrete coefficient of friction for parametric study.

Study case	IFAS Eccentricity (in)	Coefficient of friction between slab and ledge	IFAS device
Ledge Case	0	0, 0.1, 0.3	FD + RB, BRB + RB
	6	0, 0.1, 0.3	
	12	0, 0.1, 0.3	
	18	0, 0.1, 0.3	
Cantilever Slab Case	0	-	FD + RB, BRB + RB
	6		
	12		
	18		

B.10.2 Description of Model

Each shear wall base fiber includes two fibers: one is steel fiber, the other is concrete fiber. Comparisons between the fiber wall base and the hinge wall base under cyclic load are shown in Fig. B-14. This figure indicates similar strength capacity between these two wall base models, the fiber wall base generates more pinching effect than the hinge wall base.

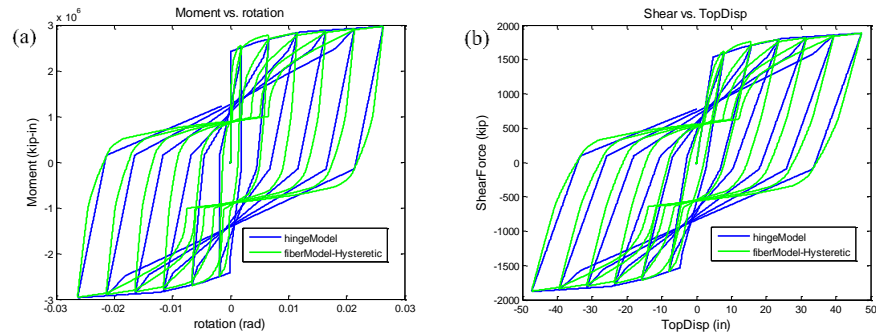


Fig. B-14. Wall base comparison: (a) Moment-rotation; (b) Base shear-top displacement.

B.10.3 Analysis Results on Different IFAS Eccentricity

A schematic plot on deformed IFAS is shown in Fig. B-15. The IFAS deformation comparison is shown in Fig. B-16.

Both sets of figures indicate that higher eccentricity produces larger deformation. Fig. B-16 indicates smaller axial deformation in BRB than FD. BRB produces larger axial force because of higher secondary stiffness, so that a smaller axial deformation is shown in BRB in Fig. B-16c. Fig. B-16b shows larger vertical deformation than the axial deformation which is caused by the rigid rotation of the device. Fig. B-16b also shows larger relative vertical deformation in BRB, this is because BRB (140 in) is longer than FD (44.5 in).

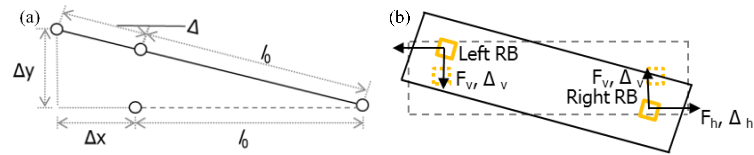


Fig. B-15. Schematic plot on deformed IFAS: (a) energy dissipation device; (b) RB.

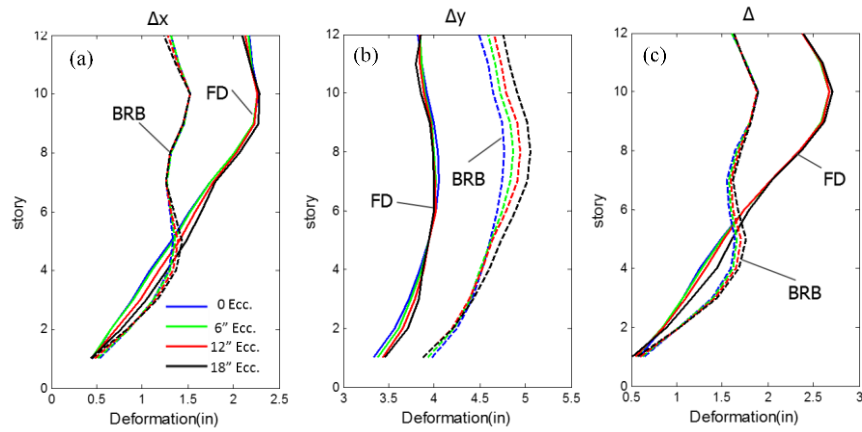


Fig. B-16. Energy dissipation device deformation between two pins: (a) Horizontal direction; (b) Vertical direction; (c) Axial direction.

The IFAS energy dissipation device (FD and BRB in this study) axial force generates local moment on the slab at the anchorage location (See Fig. B-17) because of an eccentricity from the slab center. The Two findings can be observed from Fig. B-17: (1) local moment is increased as increasing the eccentricity; (2) the BRB generates higher local

moment than the FD. The first phenomenon is caused by the increment of the energy dissipation device eccentricity. The second phenomenon is due to the higher secondary stiffness of the BRB, which produces higher force than the FD after yielding.

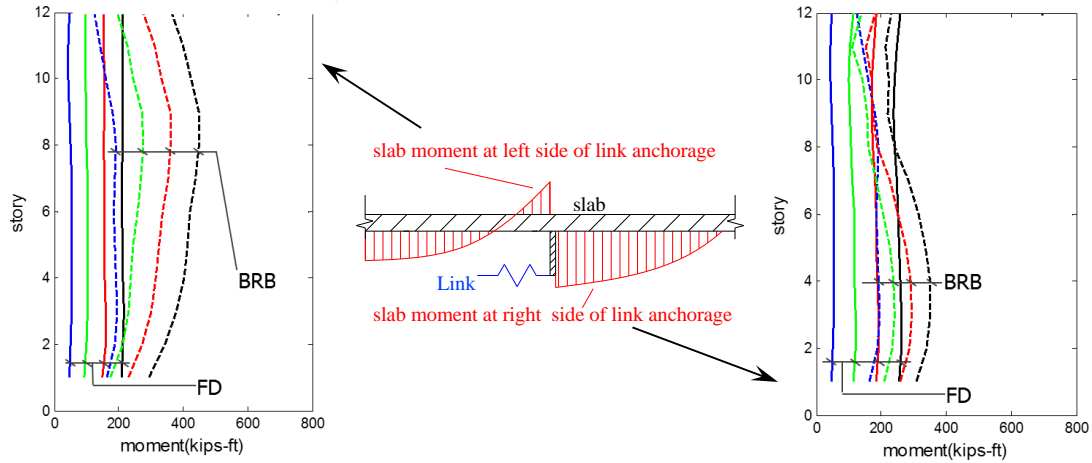


Fig. B-17. Slab local moment: (a) Left side of anchorage; (b) Right side of anchorage.

B.11 Design Space of the FD + RB Combination

B.11.1 Effect of IFAS Secondary Stiffness

This section will described the relationship between different structure responses for different γ . The responses of the 12-story structure (using RC wall as the LFRS, $\Omega_e = 1.0$) with IFAS using different γ in MCE are plotted in Fig. B-18. Fig. B-18a shows that the LFRS drift is decreased as the relative displacement increases. The LFRS drift is decreased from $\gamma=0\%$ to $\gamma=1\%$, and increased from $\gamma=2\%$ to $\gamma=5\%$. The relationship between the LFRS drift and relative displacement is nearly linear. Fig. B-18b shows that the IFAS secondary stiffness doesn't have significant influence on the floor acceleration when the relative displacement is the same. Significant floor acceleration reduction can be obtained when the relative displacement exceeds 1 in for all γ . Fig. B-18c shows that the structure with larger γ obtains larger GLRS drift as the relative displacement increases. The

variations in the GLRS drift are negligible when the relative displacement is smaller than 2 in. Fig. B-18d shows the relationship between α and the relative displacement. Fig. B-18e, f show the relationship between the energy dissipation in the LFRS and IFAS with the relative displacement.

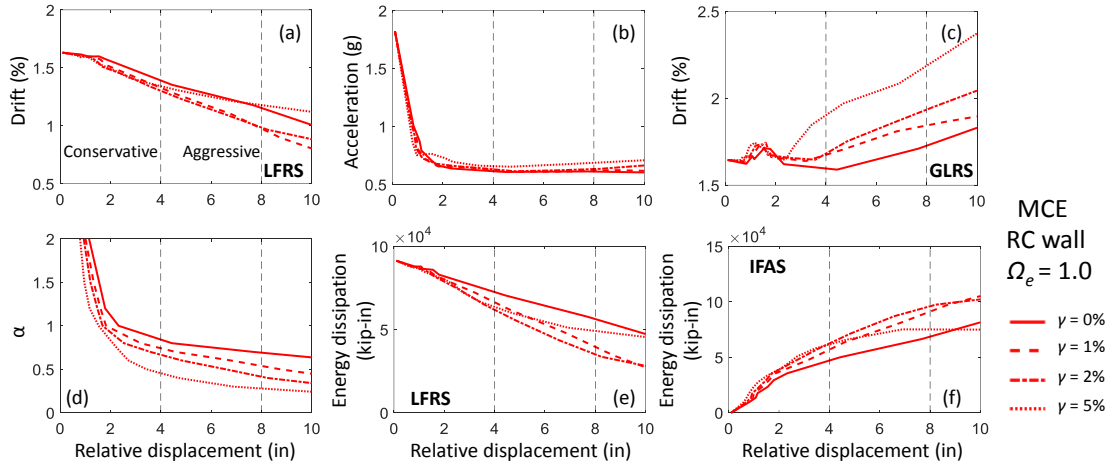


Fig. B-18. 12-story RC wall structures using IFAS with different γ in MCE: (a) LFRS drift; (b) floor acceleration; (c) GLRS drift; (d) α ; energy dissipation: (e) LFRS; (f) IFAS.

B.11.2 Effect of LFRS Type

This section will described the relationship between different structure responses for different types of LFRSs. The responses of the 12-story structure using different types of LFRS ($\Omega_e = 1.0$, $\gamma = 2\%$) in MCE are plotted in Fig. B-19. It can be seen that the LFRS drift, LFRS energy dissipation, IFAS energy dissipation and the GLRS drift are influenced a lot by using different types of the LFRSs. The floor acceleration are influenced a lot when the relative displacement is smaller than 2 in, however this influence is negligible when the relative displacement exceeds 2 in. The relationship between the wall drift and relative displacement is nearly linear (See Fig. B-19a).

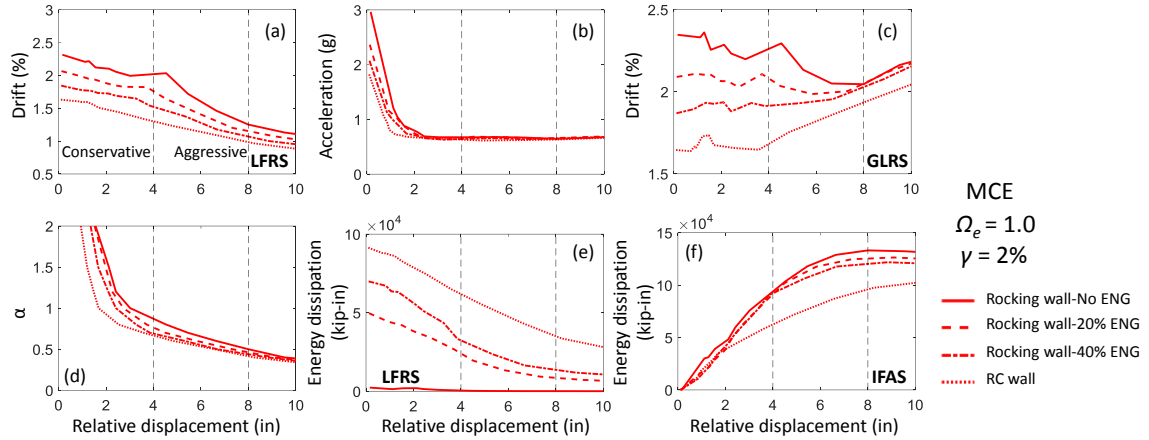


Fig. B-19. 12-story structures using different LFRS: (a) LFRS drift; (b) floor acceleration; (c) GLRS drift; (d) α ; energy dissipation: (e) LFRS; (f) IFAS.

B.11.3 Effect of GLRS Stiffness

This section will described the relationship between different structure responses for different GLRS stiffness. The responses of the 12-story structure ($\Omega_e = 1.0$, $\gamma = 2\%$) using the GLRS with different stiffness in MCE are plotted in Fig. B-20. Two types of LFRS are used in the analysis: (1) RC wall; (2) Rocking wall without energy dissipation capacity. It can be observed that when the structure uses the same type of the LFRS, the LFRS drift, floor acceleration, LFRS energy dissipation don't have significant difference for the different GLRS stiffness when the relative displacement is smaller than the conservative design limit. The LFRS drift, relative displacement, LFRS energy dissipation are increased as the clomn stiffness increases when the relative displacement exceeds the conservative design limit.

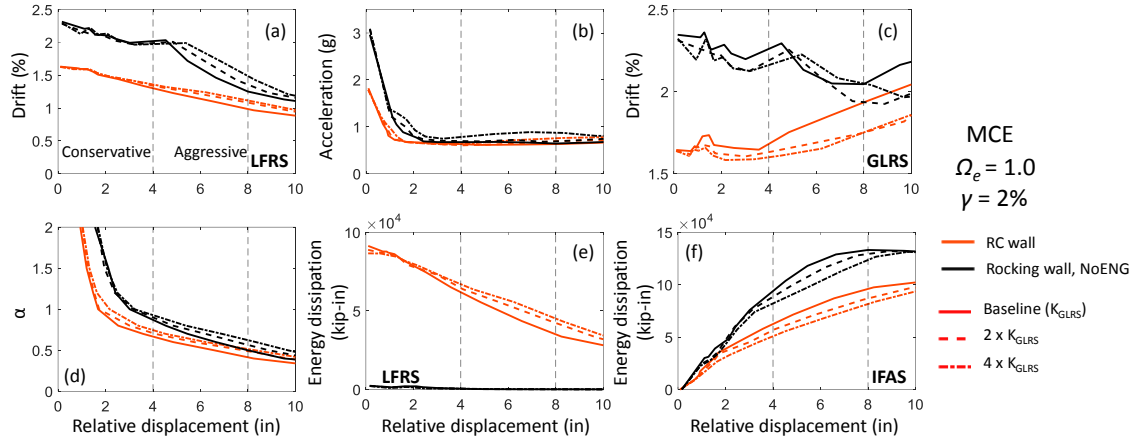


Fig. B-20. 12-story structures using different GLRS stiffness: (a) LFRS drift; (b) floor acceleration; (c) GLRS drift; (d) α ; energy dissipation: (e) LFRS; (f) IFAS.

B.11.4 Effect of Building Height

This section will described the relationship between different structure responses for different building heights. The responses of the structure (using RC wall as the LFRS, $\Omega_e = 1.0$, $\gamma = 2\%$) with different building height (4, 8, 12 story) are plotted in Fig. B-21. It can be observed that the LFRS drift, floor acceleration, GLRS drift, α , LFRS and IFAS energy dissipation are different for the structure with different height. The LFRS drift and relative displacement are nearly in linear relationship (See Fig. B-21a). Additionally, the floor acceleration in 8, 12-story structure can be significantly reduced when the relative displacement exceeds 1 in (See Fig. B-21b). The floor acceleration reduction in the 4-story structure exists, however not as significant as the taller structures (See Fig. B-21b).

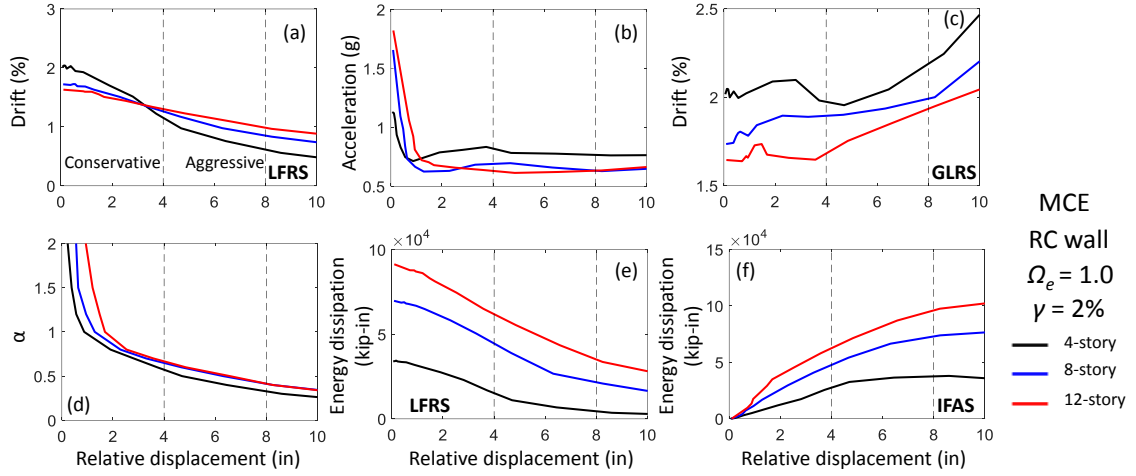


Fig. B-21. Evaluation structures with different building height: (a) LFRS drift; (b) floor acceleration; (c) GLRS drift; (d) α ; energy dissipation: (e) LFRS; (f) IFAS.

B.12 Design Space Equation Development

B.12.1 4-story RC Wall Structure

The 4-story RC wall structure design space equations are shown in the following:

$$\Delta_{\text{LFRS}} = 3.140 - 1.067\Omega_e + (-0.168 - 1.677\gamma - 0.035\Omega_e + 32.202\gamma^2 + 0.008\Omega_e^2 - 0.690\gamma\Omega_e)\delta_r \quad (0.7 \leq \Omega_e < 1.3) \quad (\text{B-1a})$$

$$\Delta_{\text{LFRS}} = 2.241 - 0.376\Omega_e + (-0.168 - 1.677\gamma - 0.035\Omega_e + 32.202\gamma^2 + 0.008\Omega_e^2 - 0.690\gamma\Omega_e)\delta_r \quad (1.3 \leq \Omega_e < 1.6) \quad (\text{B-1b})$$

$$\alpha = (0.534 - 6.885\gamma + 0.619\Omega_e)\delta_r^{-0.807 - 3.339\gamma + 0.682\Omega_e - 0.255\Omega_e^2} \quad (\text{B-2})$$

The coefficients of determination for b_0 , b_1 , c_0 , c_1 are 99.1%, 68.4%, 98.7%, 96.8% respectively. The comparison between the predicted and calculated b_0 , b_1 , c_0 , c_1 are shown in Fig. B-22, Fig. B-23. The predicted and calculated variables are shown in different grey and red scale.

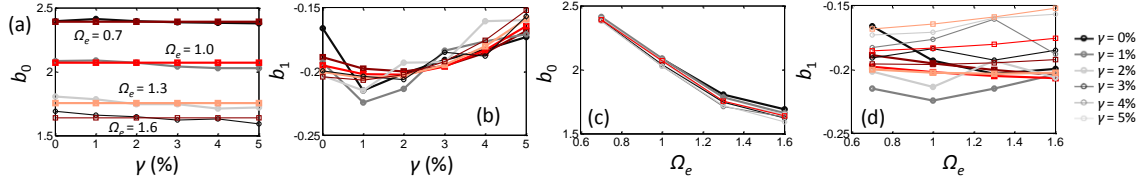


Fig. B-22. Prediction equation of b_0 , b_1 vs. γ : (a) b_0 ; (b) b_1 ; vs. Ω_e : (c) b_0 ; (d) b_1 .

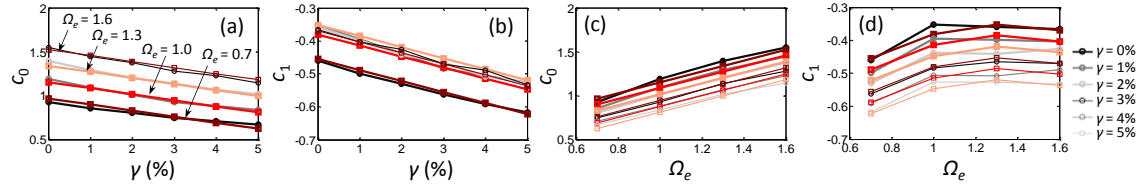


Fig. B-23. Prediction equation of c_0 , c_1 vs. γ : (a) c_0 ; (b) c_1 ; vs. Ω_e : (c) c_0 ; (d) c_1 .

B.12.2 8-story RC Wall Structure

The 8-story RC wall structure design space equations are shown in the following:

$$\Delta_{\text{LFRS}} = 2.660 - 0.820\Omega_e + (-0.081 - 1.964\gamma - 0.019\Omega_e + 48.223\gamma^2 + 0.003\Omega_e^2 - 0.361\gamma\Omega_e)\delta_r \quad (0.7 \leq \Omega_e < 1.3) \quad (\text{B-3a})$$

$$\Delta_{\text{LFRS}} = 2.301 - 0.545\Omega_e + (-0.081 - 1.964\gamma - 0.019\Omega_e + 48.223\gamma^2 + 0.003\Omega_e^2 - 0.361\gamma\Omega_e)\delta_r \quad (1.3 \leq \Omega_e < 1.6) \quad (\text{B-3b})$$

$$\alpha = (0.925 - 9.746\gamma + 0.604\Omega_e)\delta_r^{-0.690 - 4.042\gamma + 0.232\Omega_e - 0.034\Omega_e^2} \quad (\text{B-4})$$

The coefficients of determination for b_0 , b_1 , c_0 , c_1 are 96.6%, 60.0%, 96.2%, 97.4% respectively. The comparison between the predicted and calculated b_0 , b_1 , c_0 , c_1 are shown in Fig. B-24, Fig. B-25. The predicted and calculated variables are shown in different grey and red scale.

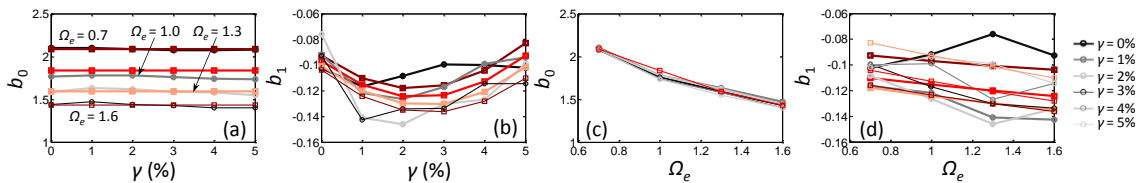


Fig. B-24. Prediction equation of b_0 , b_1 vs. γ : (a) b_0 ; (b) b_1 ; vs. Ω_e : (c) b_0 ; (d) b_1 .

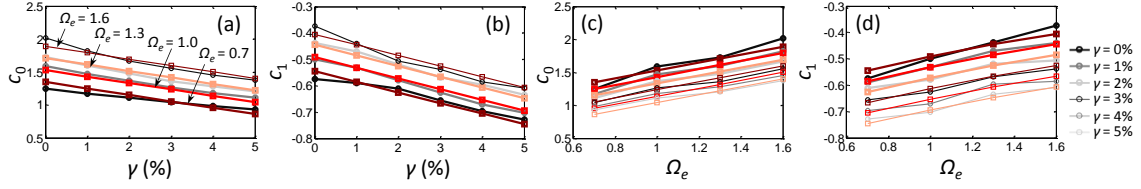


Fig. B-25. Prediction equation of c_0 , c_1 vs. γ : (a) c_0 ; (b) c_1 ; vs. Ω_e : (c) c_0 ; (d) c_1 .

B.12.3 4-story Rocking Wall Structure

The 4-story rocking wall structure design space equations are shown in the following:

$$\Delta_{\text{LFRS}} = 4.644 - 1.761\Omega_e + (-0.255 - 7.430\gamma - 0.046\Omega_e + 53.516\gamma^2 + 0.056\Omega_e^2 - 4.207\gamma\Omega_e)\delta_r \quad (0.7 \leq \Omega_e < 1.3) \quad (\text{B-5a})$$

$$\Delta_{\text{LFRS}} = 2.964 - 0.469\Omega_e + (-0.255 - 7.430\gamma - 0.046\Omega_e + 53.516\gamma^2 + 0.056\Omega_e^2 - 4.207\gamma\Omega_e)\delta_r \quad (1.3 \leq \Omega_e < 1.6) \quad (\text{B-5b})$$

$$\alpha = (0.424 - 12.999\gamma + 1.340\Omega_e)\delta_r^{-0.737 - 3.747\gamma + 0.300\Omega_e - 0.159\Omega_e^2} \quad (\text{B-6})$$

The coefficients of determination for b_0 , b_1 , c_0 , c_1 are 96.4%, 55.7%, 97.6%, 97.9% respectively. The comparison between the predicted and calculated b_0 , b_1 , c_0 , c_1 are shown in Fig. B-26, Fig. B-27. The predicted and calculated variables are shown in different grey and red scale.

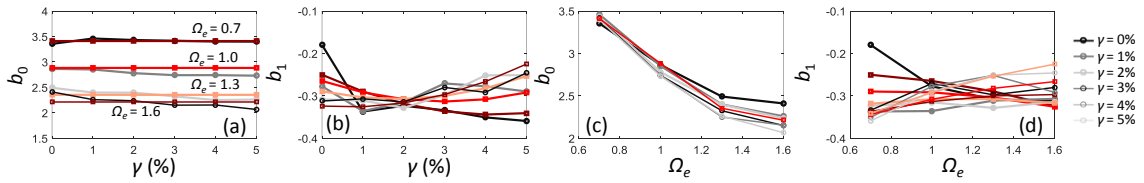


Fig. B-26. Prediction equation of b_0 , b_1 vs. γ : (a) b_0 ; (b) b_1 ; vs. Ω_e : (c) b_0 ; (d) b_1 .

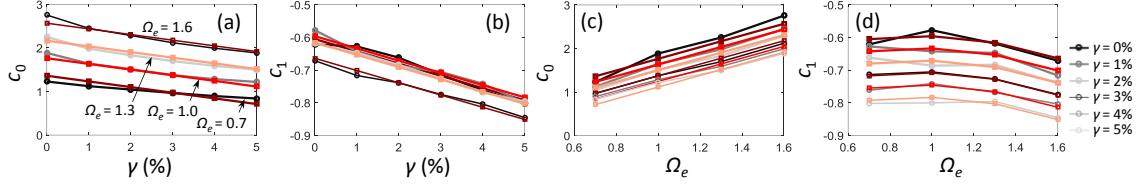


Fig. B-27. Prediction equation of c_0 , c_1 vs. γ : (a) c_0 ; (b) c_1 ; vs. Ω_e : (c) c_0 ; (d) c_1 .

B.12.4 12-story Rocking Wall Structure

The 12-story rocking wall structure design space equations are shown in the following:

$$\Delta_{\text{LFRS}} = (2.537 + 9.756\gamma - 0.314\Omega_e - 99.335\gamma^2 + 0.164\Omega_e^2 - 6.082\gamma\Omega_e) + (-0.064 - 5.740\gamma + 0.074\Omega_e + 82.573\gamma^2 - 0.086\Omega_e^2 + 1.217\gamma\Omega_e)\delta_r \quad (\text{B-7})$$

$$\alpha = (1.031 - 25.026\gamma + 2.416\Omega_e)\delta_r^{-1.126 - 6.679\gamma + 0.756\Omega_e - 0.306\Omega_e^2} \quad (\text{B-8})$$

Note that, for the 12-story rocking wall structure, the design equations for Δ_{LFRS} and δ_r is different from those were used for RC wall structures and 4-story rocking wall structure. The coefficients of determination for b_0 , b_1 , c_0 , c_1 are 57.9%, 55.7%, 96.5%, 96.4% respectively. The comparison between the predicted and calculated b_0 , b_1 , c_0 , c_1 are shown in Fig. B-28, Fig. B-29. The predicted and calculated variables are shown in different grey and red scale.

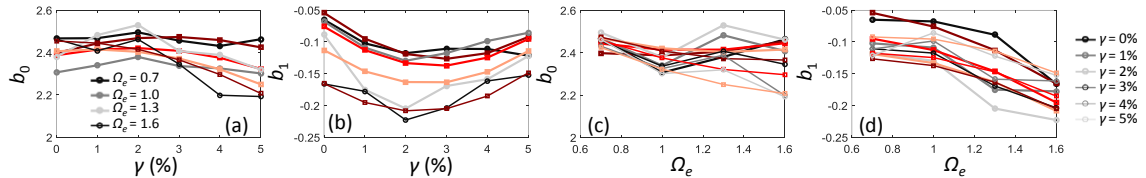


Fig. B-28. Prediction equation of b_0 , b_1 vs. γ : (a) b_0 ; (b) b_1 ; vs. Ω_e : (c) b_0 ; (d) b_1 .

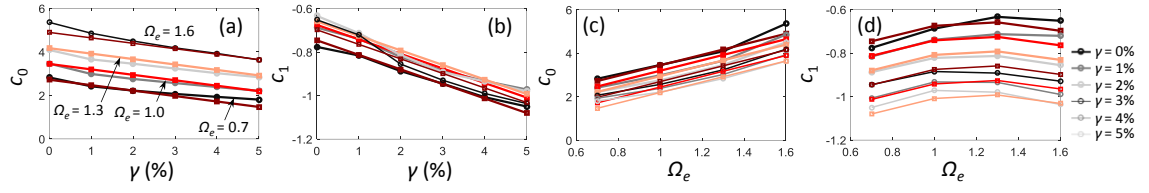


Fig. B-29. Prediction equation of c_0 , c_1 vs. γ : (a) c_0 ; (b) c_1 ; vs. Ω_e : (c) c_0 ; (d) c_1 .

APPENDIX C – SUPPLEMENTAL INFORMATION FOR CHAPTER 5

C.1 Shake Table Test Introduction

C.1.1 Description of the Shake Table Test Specimen

The shake table test specimen was in half-scale with two exceptions: (1) floor to floor height used 2/3 scale in order to allow people to do inspections on the specimen; (2) slab thickness was not scaled in order to provide the right distributed mass, obtain the proper tributary diaphragm force without scaling the ground motion magnitude and maintain the real P-Delta effect on columns.

PT walls were used as the LFRS for both saving on-site construction time and structural repeatability purposes. The PT walls included energy dissipaters (EDs) at base for energy dissipation purpose [100] and unbonded PT bars for self-centering purpose. The PT walls will not suffer as much damage as traditional shear walls. The damage potentially occurs at the PT walls toe area where high local compression exists.

Precast columns were used for both saving on-site construction time and structural repeatability purpose. In addition, cast in place reinforced concrete slab was 9” thick. This unscaled slab thickness created a condition where it was difficult to enforce a strong column-weak beam (slab) design condition to prevent a story mechanism. For this reason, the precast concrete columns were designed with a special joint for suffering less damage under large drift.

C.1.2 Instrumentation Plan

The sensors used in the shake table test are summarized in Table C-1. The instrumentation layout is shown in the plan and elevation schematics of Fig. C-1. String pots were deployed: (1) in X-shape configurations in the northwest and southeast perimeter

bays at each story for measuring inter-story drift of the GLRS; (2) at two locations along the floor east perimeter at each floor level and connected on the other end to a fixed steel frame adjacent to the shake table platen to measure absolute floor displacement in EW (table motion) direction and floor twist in plan; (3) between the slab and the North wall at each level to measure floor relative displacement, attached at sufficient distance from the wall to minimize kinematic error due to wall uplift; and, (4) at the wall bases to measure wall uplift for base rotation calculations and estimate the wall neutral axis for base moment calculations. Linear pots were installed: (1) between the wall and the slab at each level to measure the uplift and horizontal relative displacement; (2) at selected first-story column top and bottom regions to measure column end rotations; (3) at the BRB and FD to measure device deformation; (4) in spring-loaded fashion to measure the roof bumper compressive deformation; and, (5) across the wall side joint to capture lateral deformation of the PSA. Accelerometers were installed: (1) on top of foundations to measure the foundation acceleration; (2) on each floor to measure the EW acceleration at A, B, C on line 1 and NS acceleration at 1 and 3 on line C (EW and NS accelerations were measured at each corner on the roof); (3) on the south surface of the North wall to measure impact effect (from Test 11). The PT force was measured using a pressure transducer; the FD force was measured using a spherical bearing load cell; and, the ED and BRB force was calculated using strain gage readings on components connected in series to these elements that remained elastic during the test. Strain gages were also attached to the high strength reinforcement within the North wall and selected precast columns (not shown in Fig. C-1). Two High-Definition

video camera recorders⁷, 13 GoPros⁸ and 11 closed circuit cameras were deployed to provide overall and close-up video of the specimen. A payload project provided rooftop GPS measurements. The data acquisition system sampling rate was 240 Hz.

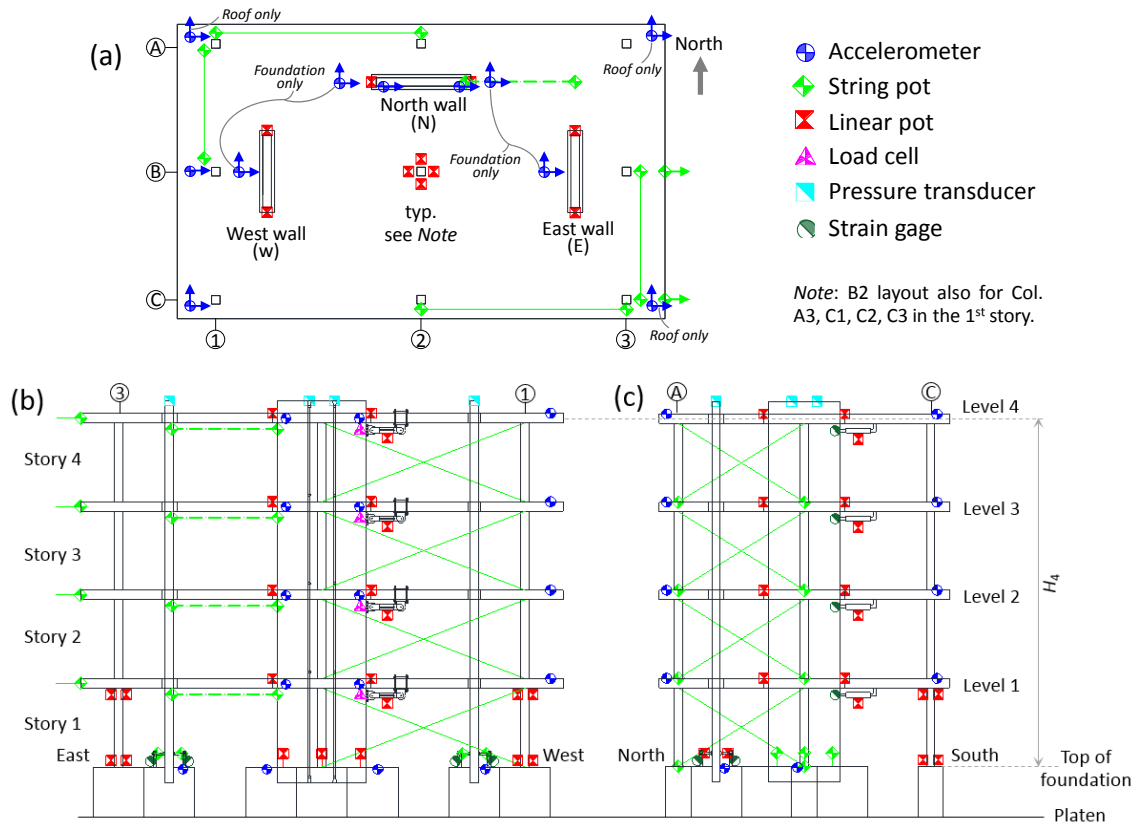


Fig. C-1. Typical instrumentation view: (a) Plan; Elevations: (b) North; (c) West.

Table C-1. Sensor list.

Sensor type	Number	Sensor type	Number	Sensor type	Number
String pots	32	Spring loaded linear pots	12	Load cells	4
Linear pots	58	Accelerometers	63	GPS	6
Pressure Transducers	6	Strain gages	83	Total sensors	264

⁷ Sony, HDR-CX560.

⁸ HD HERO 2.

C.1.3 IFAS Design

The IFAS nominal design strength was selected corresponding to the three strength levels indicated in Fig. C-2. The responses shown in Fig. C-2 is from a 4-story rocking wall IFAS structure ($\Omega_e=1.3$). No energy dissipation is considered in the rocking wall. $\alpha = 0.75$, $\alpha = 0.57$ and $\alpha = 0.43$ are selected as conservative, intermediate and aggressive ratio between the IFAS F_y and F_{px} .

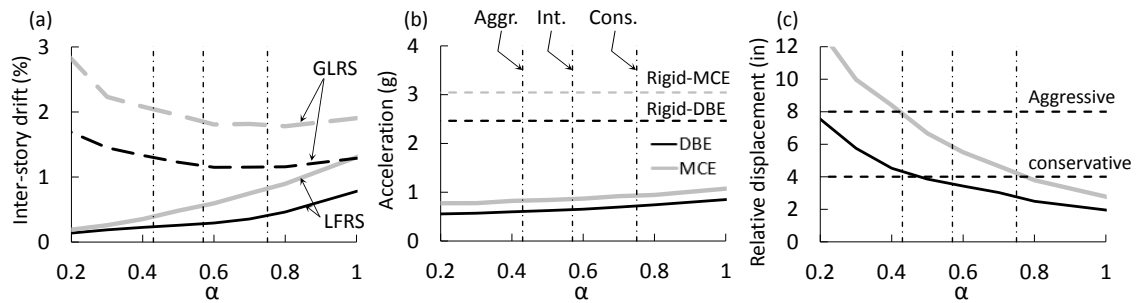


Fig. C-2. IFAS Design Space: (a) Inter-story drift; Floor (b) relative displacement; (c) acceleration.

C.2 Analytical Prediction Results

C.2.1 Prediction Results in SE

Fig. C-3 shows the structure response comparison between Phase I and Phase II in SE DBE and SE MCE. The comparison shows that using IFAS is able to reduce the north wall deformation and floor acceleration in SE. Shear wall PT ratio is 0.6 in this analysis set.

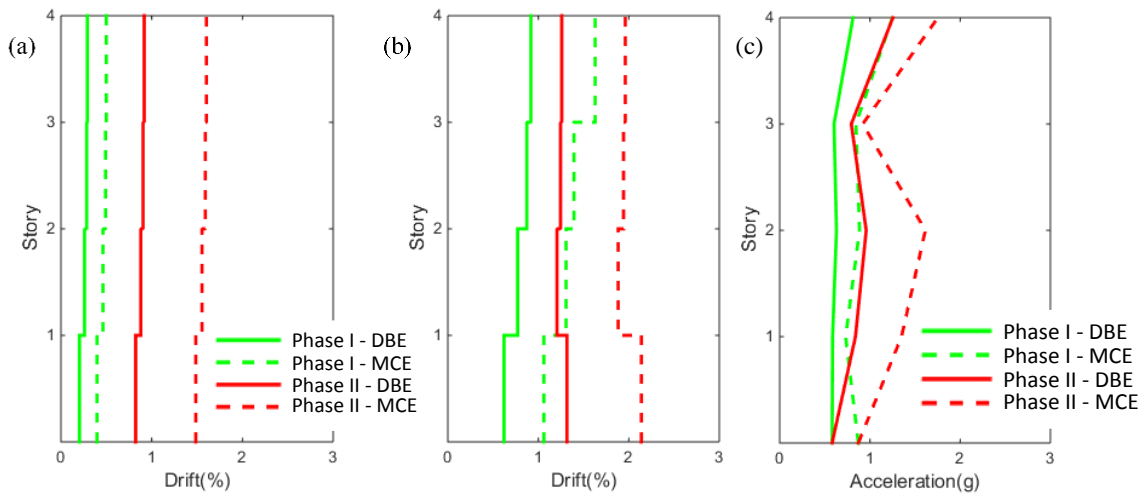


Fig. C-3. Maximum response: inter-story drift: (a) LFRS; (b) GLRS; (c) floor acceleration.

C.2.2 Prediction Results in BE

Fig. C-4 - Fig. C-6 show the structure response comparison between Phase I and Phase II in BE DBE and BE MCE. The comparison indicates that using IFAS is able to reduce the shear wall deformation and floor acceleration in BE. Fig. C-4 shows that higher FD yield strength causes lower north wall deformation reduction. Uplift of the three wall is shown in Fig. C-6. This uplift prediction is used for designing the embedded slotted insert of the PSA. Shear wall PT ratio is 0.6 in this analysis set.

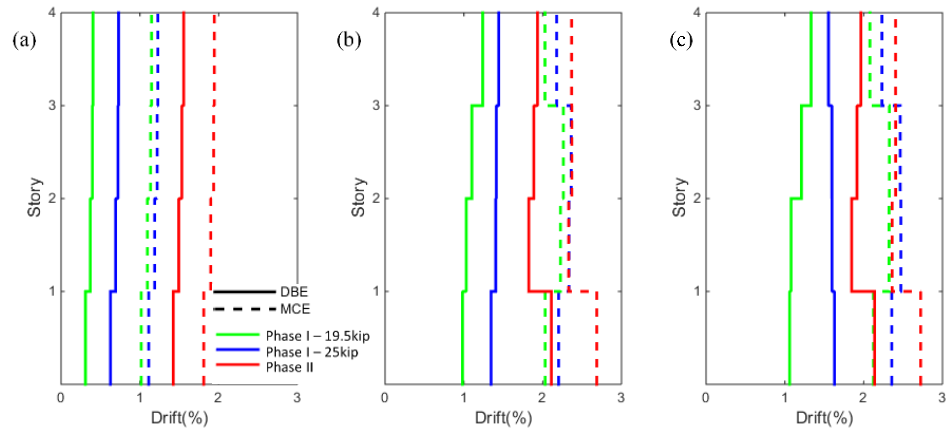


Fig. C-4. Maximum inter-story drift: (a) North wall (EW); (b) GLRS (EW); (c) GLRS (Resultant).

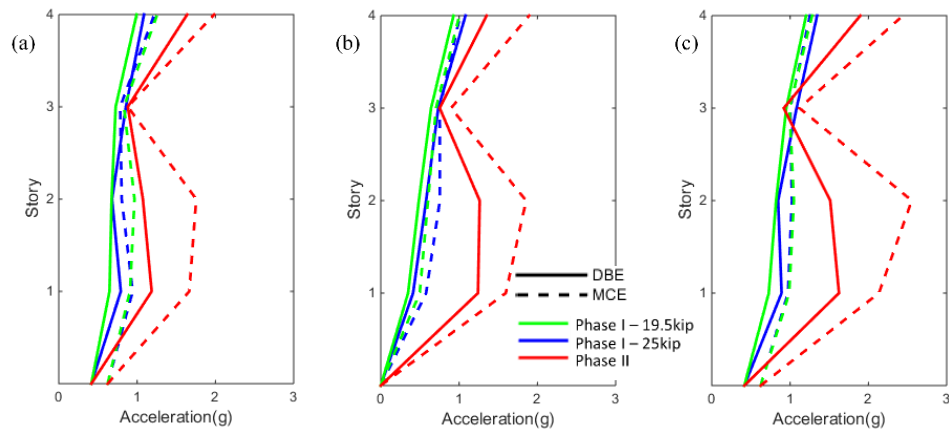


Fig. C-5. Maximum floor acceleration: (a) GLRS (EW); (b) GLRS (NS); (c) GLRS (Resultant).

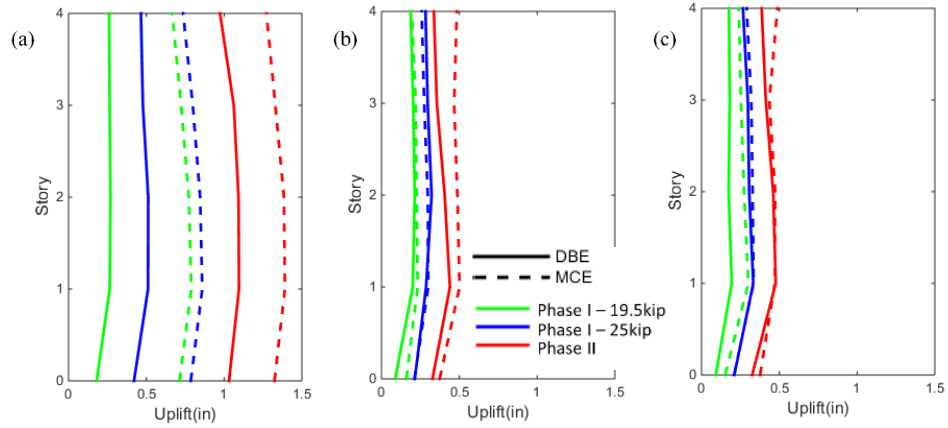


Fig. C-6. Maximum shear wall uplift: (a) North wall; (b) East wall; (c) West wall.

C.3 Structural Response Calculations

Key structural responses presented in this dissertation are calculated using the measured sensor data (indicated in bold in equations below) described in this section. Note that because of the unique nature of the IFAS, distinct inter-story drift and acceleration values exist for both the LFRS and GLRS. Note also that due to the plan eccentricity of the test specimen LFRS, the GLRS responses are reported individually for the EW and NS directions, as well as a total vector sum. The responses in Fig. C-7 are all shown in their positive directions.

C.3.1 Response Calculation

The calculated responses include:

The calculated kinematic responses for the LFRS include: (1) wall base in-plane rotation θ_{wall} (See Fig. C-7a) based on the difference of linear pot measurements δ_1 , δ_3 at each end of the wall base, for all three walls (θ_{wall}^N , θ_{wall}^W , θ_{wall}^E). Linear pots were also deployed on each wall face to capture out-of-plane rotation; (2) LFRS inter-story drift in the table motion (EW) direction at story i , $\Delta_{LS,i}^{EW}$, back-calculated from the absolute GLRS

displacement in line with the North wall u_i^N (extrapolated from measured displacements u_i^B, u_i^C using rigid body floor kinematics, Fig. C-7c) and the floor relative displacement between the North wall and slab, $\delta_{r,i}^N$:

$$\theta_{\text{wall}} = (\delta_1 - \delta_3)/d_{13} \quad (\text{C-1})$$

$$\Delta_{\text{LS},i}^{\text{EW}} = ((u_i^N - \delta_{r,i}^N) - (u_{i-1}^N - \delta_{r,i-1}^N))/h_i \quad (\text{C-2})$$

where h_i is floor-to-floor height of the i^{th} story. In the orthogonal direction, $\Delta_{\text{LS},i}^{\text{NS}}$, can be similarly calculated with floor relative displacement $\delta_{r,i}^W, \delta_{r,i}^E$ measured for the transverse walls.

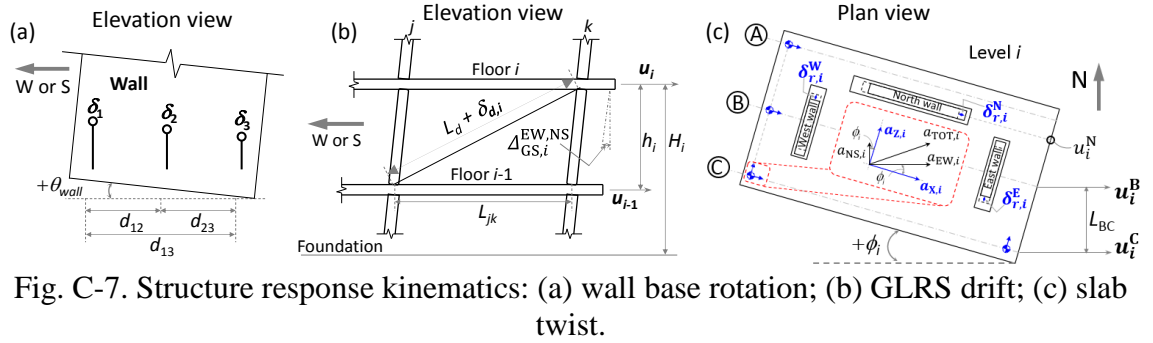


Fig. C-7. Structure response kinematics: (a) wall base rotation; (b) GLRS drift; (c) slab twist.

The calculated kinematic responses for the GLRS include: (3) GLRS inter-story drift at story i , $\Delta_{\text{GS},i}^{(\text{EW or NS})}$ (See Fig. C-7b), defined as the relative horizontal displacement of two adjacent floors in a direction divided by the clear story height. This value is: (a) calculated in each direction (EW or NS) using the diagonal string pots (See Fig. C-7b), where L_{jk} and L_d represent the horizontal and diagonal bay dimensions and $\delta_{d,i}$ represents the measured string pot displacement, and is (b) checked at the location of maximum twisting-amplified drift in the EW direction along column line C using directly measured absolute GLRS displacements u_i^C , which coincides with one of the diagonal string pots

arrays; In addition, the GLRS inter-story drift at story i near the location of the North wall is calculated in Eqn. C-3c; (4) GLRS average EW interstory and roof drift, $\bar{\Delta}_{GS,i}^{EW}$, $\bar{\Delta}_{GS,roof}^{EW}$, the latter defined as the horizontal roof displacement at column line B \mathbf{u}_4^B relative to the top of foundation \mathbf{u}_0^B divided by the roof height, H_4 (refer to Fig. C-1c):

$$\Delta_{GS,i}^{(EW \text{ or } NS)} = \left(\sqrt{(L_d + \delta_{d,i})^2 - h_i^2} - L_{jk} \right) / h_i \quad (C-3a)$$

$$\hat{\Delta}_{GS,i}^{EW} = (\mathbf{u}_i^C - \mathbf{u}_{i-1}^C) / h_i \quad (C-3b)$$

$$\Delta_{GS,i}^N = (u_i^N - u_{i-1}^N) / h_i \quad (C-3c)$$

$$\bar{\Delta}_{GS,i}^{EW} = (\mathbf{u}_i^B - \mathbf{u}_{i-1}^B) / h_i, \quad \bar{\Delta}_{GS,roof}^{EW} = (\mathbf{u}_4^B - \mathbf{u}_0^B) / H_4 \quad (C-4a,b)$$

and, (5) the resultant maximum GLRS inter-story drift (at column C3), $\hat{\Delta}_{GS,i}^{TOT}$, is calculated as:

$$\hat{\Delta}_{GS,i}^{TOT} = \sqrt{\hat{\Delta}_{GS,i}^{EW}{}^2 + \hat{\Delta}_{GS,i}^{NS}{}^2} \quad (C-5)$$

Then, (6) slab twist angle in plan at level i , ϕ_i (See Fig. C-7c) is calculated as:

$$\phi_i = (\mathbf{u}_i^B - \mathbf{u}_i^C) / L_{BC} \quad (C-6)$$

Finally, (7) floor acceleration corrected for twisting (See Fig. C-7c) at level i is given by:

$$a_{EW,i} = \mathbf{a}_{X,i} \cos \phi_i + \mathbf{a}_{Z,i} \sin \phi_i \quad (C-7a)$$

$$a_{NS,i} = \mathbf{a}_{X,i} \cos \phi_i - \mathbf{a}_{Z,i} \sin \phi_i \quad (C-7b)$$

$$\hat{a}_{TOT,i} = \sqrt{\hat{a}_{EW,i}{}^2 + \hat{a}_{NS,i}{}^2} \quad (C-7c)$$

$$\bar{a}_{EW,i} = (a_{EW,i}^A + a_{EW,i}^B + a_{EW,i}^C) / 3 \quad (C-7d)$$

where $\mathbf{a}_{(X \text{ or } Z),i}$, $a_{(EW \text{ or } NS),i}$ and $\hat{a}_{TOT,i}$ are the measured, corrected and maximum (in plan) total accelerations, respectively. $\bar{a}_{EW,i}$ is the floor average acceleration based on the

(corrected) accelerations at column line A,B,C. A 33Hz low-pass filter was applied to the accelerations.

Fig. C-8 shows schematics describing the manner in which structural total and story forces are calculated *for the table motion direction*, including shear and overturning moment.

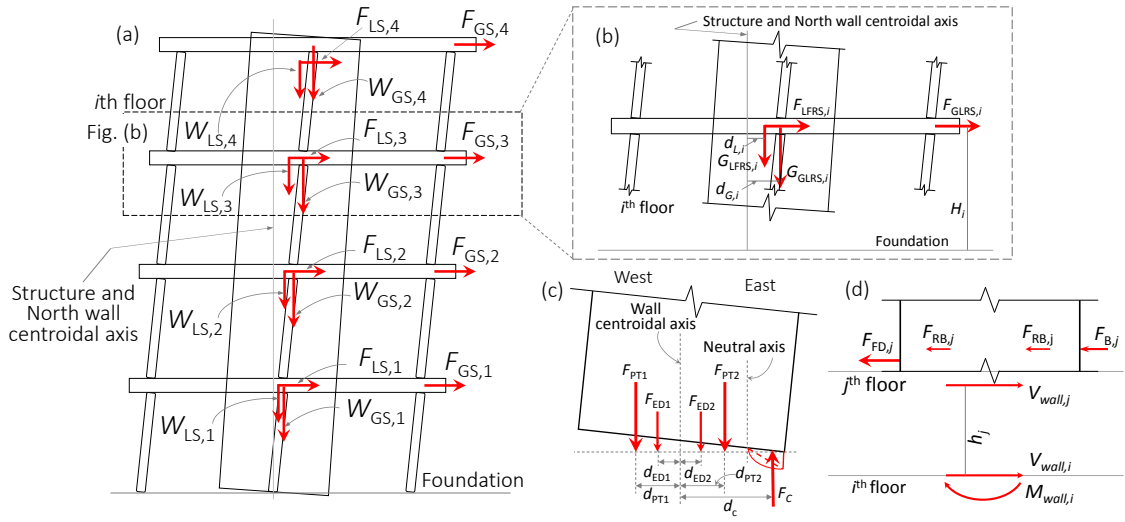


Fig. C-8. Force calculation diagrams: overturning: (a) structure; (b) at i^{th} floor; (c) wall base moment; (d) wall shear force and moment at i^{th} floor.

The structure overturning moment, M_o^{EW} , in the table motion (EW) direction is calculated as:

$$M_o^{\text{EW}} = \sum_{i=1}^4 (F_{\text{GS},i} H_i + F_{\text{LS},i} H_i + W_{\text{GS},i} d_{\text{GS},i} + W_{\text{LS},i} d_{\text{LS},i}) \quad (\text{C-8})$$

where $F_{(\text{GS or LS}),i}$, $W_{(\text{GS or LS}),i}$ are the inertial force and gravity load of the GLRS and North wall, respectively, at level i ; $d_{\text{GS},i}$, $d_{\text{LS},i}$ represent the (P-Delta) displacement of the gravity system and North wall at level i relative to the structure centroidal axis, and H_i is the height of the i^{th} floor above the foundation. $F_{\text{GS},i}$, $F_{\text{LS},i}$ are calculated based on direct acceleration measurements:

$$F_{GS,i} = (W_{flr,i} + W_{col,i} + W_{TW,i})\bar{a}_{EW,i} \quad (C-9)$$

$$F_{LS,i} = W_{wall,i}^N a_{LS,i} \quad (C-10)$$

where $W_{flr,i}$, $W_{col,i}$, $W_{TW,i}$, $W_{wall,i}^N$ are the floor, column, transverse and North wall weight tributary to the i^{th} floor; $a_{LS,i}$ is North wall EW acceleration in the direction at level i , calculated through double differentiation of the wall displacement, as verified by limited direct accelerometer data on the wall. The wall displacement is determined through Eqn. C-2. Seismic mass W is estimated using weight measurements taken under the shake table platen as each floor was added during the specimen construction phase. The EW story shear force at the i^{th} story, V_i^{EW} , is calculated as:

$$V_i^{EW} = \sum_i F_{GS,i} \quad (C-11)$$

The wall base moment, $M_{base}^{N,E,W}$, is calculated based on the free-body in Fig. C-8c:

$$M_{base}^{N,E,W} = \sum_k F_{PTk} d_{PTk} + \sum_j F_{EDj} d_{EDj} + F_C d_C \quad (C-12)$$

where F_{PTk} , d_{PTk} ; F_{EDj} , d_{EDj} represent the force and moment arm distance of the k^{th} PT bar and the j^{th} ED device, respectively. F_C , d_C represent the concrete compression force resultant based on an assumed triangular distribution at low loads and a parabolic distribution at higher loads, with the wall neutral axis estimated by linearly interpolating the zero uplift point using the linear pots at the wall base, and the moment arm measured from the wall centroidal axis. The wall shear force at i^{th} floor, $V_{LS,i}^{EW}$ is calculated with the following equation:

$$V_{LS,i}^{EW} = \sum_{j=i}^4 (F_{FD,j} + F_{RB,j} + F_{B,j} + F_{PSA,j} + F_{roller,j}) \quad (C-13)$$

where $F_{FD,j}$, $F_{RB,j}$, $F_{B,j}$, $F_{PSA,j}$, $F_{roller,j}$ represent the FD, RB, bumper (B), PSA and roller bearing forces acting at the j^{th} floor. The RB, B and PSA forces are estimated by

multiplying the relative displacements directly measured for each device by their design shear stiffness, in the case of the PSA from product test data (Refer to Fig. 5-4b). Some terms in Eqn. C-13 are excluded based on the test phase (e.g. no PSA and roller bearing in Phase I; no roller bearing in Tests 15-17; no FD or bumper in Tests 18+). Certain responses are determined indirectly, for instance, the GLRS shear force at i^{th} story is taken as the difference between total and LFRS shear:

$$V_{GS,i}^{EW} = V_i^{EW} - V_{LS,i}^{EW} \quad (\text{C-14})$$

The roller bearing force is estimated in similar fashion by using the GLRS lateral stiffness for the test prior to the roller bearing installation. Note that $V_{GS,i}^{EW}$ contains a small out-of-plane shear contribution from the transverse walls.

The North wall and gravity system moment at the i^{th} floor is calculated as (See Fig. C-8d):

$$M_{\text{wall},i} = \sum_{j=i}^4 V_{\text{wall},j} h_j, \quad M_{GS,i} = V_{GS,i} h_i / 2 \quad (\text{C-15a,b})$$

where h_j accounts for the offset FD elevation and Eqn. C-15b assumes plastic hinging columns. Eqn. C-1, C-13 to C-15 were validated by using numerical analysis results.

C.3.2 Response Verification

The story shear in the structure, North wall, GLRS and transverse walls in the EW direction from Eqn. C-11, C-13, C-14 are verified using the shear force from the analyses in both Phase I and Phase II in Fig. C-9. Red solid lines represent the shear force obtained from the numerical analysis. Blue dashed lines represent the shear force obtained from the Eqn. C-11, C-13, C-14 respectively. Note that only the 1st story shear force is compared in

the figure. Fig. C-9 shows that the C-11, C-13, C-14 can accurately predict the story shear in the structure, North wall, GLRS and transverse walls.

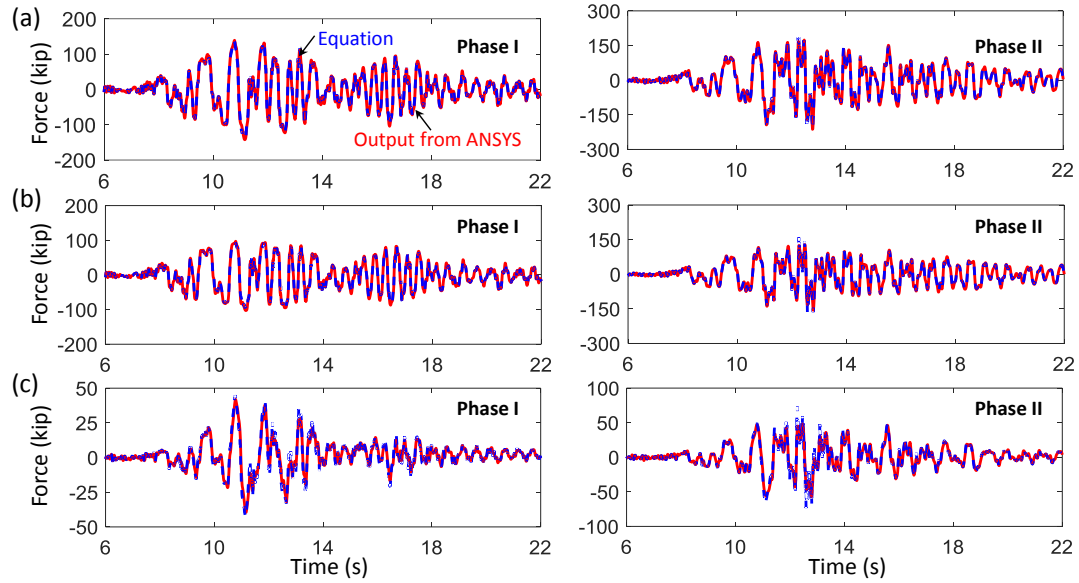


Fig. C-9. Shear force in the EW direction at the 1st floor of: (a) structure; (b) North wall; (c) GLRS and transverse walls.

Fig. C-10 shows the comparison on the EW direction shear force of the GLRS and GLRS & transverse walls from the Phase I analysis in Fig. C-9. Red solid line represents the shear force in the GLRS and transverse walls. Black solid line represents the shear force in the GLRS. The comparison shows that the difference in the shear force is small, implying that the shear force in the transverse walls is not large in comparison to the shear force in the GLRS. Therefore, Eqn. C-14 can be used for the prediction of the GLRS shear force in the shake table test.

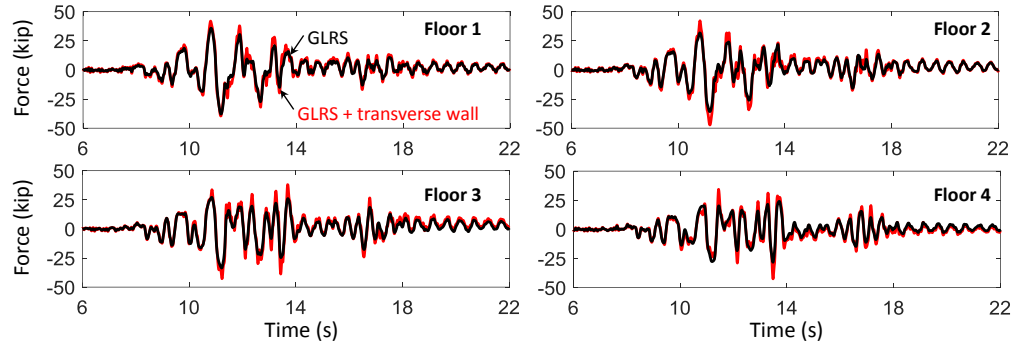


Fig. C-10. Comparison on shear force of GLRS and GLRS & transverse walls from one analysis in Phase I.

Fig. C-11 shows the verification of Eqn. C-12, C-15 using the same Phase I analysis as that of Fig. C-9. Red solid lines represent the moment obtained from the numerical analysis. Black dotted line in Fig. C-11a represents the moment obtained from Eqn. C-12. Blue solid lines represent the moment obtained from Eqn. C-15. Note that the shear force used in Eqn. C-15 is obtained from the analysis output.

Fig. C-11a shows that Eqn. C-15a can accurately predict the moment at the shear wall base, implying Eqn. C-15a can be used to calculate the shear wall moment at any floor. Fig. C-11a shows that the moment from Eqn. C-12 is a little larger than the accurate moment from the analysis, however it is also acceptable to use Eqn. C-12 for calculating the wall base moment. Fig. C-11b shows the end moment about the NS direction of column B2 (See Fig. C-1a). Some difference can be observed at the moment peaks, this is probably caused by the ignorance of the P-Delta effect on the column in Eqn. C-15b. The comparison shows that Eqn. C-12b can be used for predicting the moment in the column.

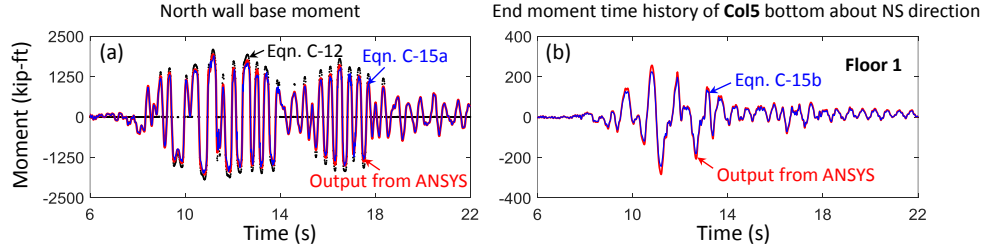


Fig. C-11. Verification of Eqn. C-12, C-15 from one analysis in Phase I: (a) north wall base; (b) Column B2.

This section validates the equations for obtaining the structure or component internal forces from indirect measurements (like acceleration, displacement). Therefore, these equations are applicable for obtaining the structure and component internal forces in the shake table test.

C.4 Accumulated Wall Base Rotation and Structure Drift Envelope in MCE

To estimate overall demands in the BE MCE for the coupled translational/torsional system, consider the response of all three walls, shown in Fig. C-12a for cumulative base rotation, both individually and totaled for the three walls. This approximate index of overall demands indicates a significant response reduction for the IFAS structure, clarifying the conflicting results of Fig. 5-19d and Fig. 5-20d. Note also the asymmetry of response in the traditional structure (Phase II East vs. West wall) in comparison to the IFAS structure.

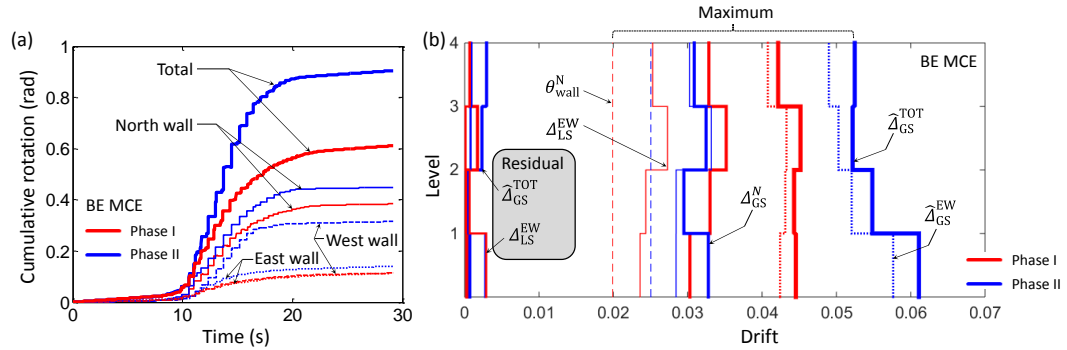


Fig. C-12. BE MCE Phase I & II comparison: (a) cumulative base rotation: (b) inter-story drift.

Fig. C-12b compares different drift response envelopes along the structure height for the BE MCE. The results can be used to illustrate the relationship between the LFRS and GLRS inter-story drifts in an IFAS structure. As a reference, the North wall base in plane rotation (for Phases I, II), θ_{wall}^N , is indicated in the figure as vertical dashed trend lines. The first set of solid lines to the right of the trend lines indicate the resulting inter-story drift of the North wall, $\Delta_{\text{LS}}^{\text{EW}}$. The larger variation in the LFRS inter-story drift for Phase II may be due to larger higher mode effects for the traditional structure. The adjacent thicker solid lines represent the GLRS drift in line with the North wall, Δ_{GS}^N . Note the significant difference in the LFRS and GLRS drift for the IFAS structure due to the partial uncoupling of these elements. Also note that the “traditional” structure specimen approaches but does not exactly realize a rigid diaphragm condition. Given the structural eccentricity in plan, the maximum EW drift (dotted line) occurs at the south perimeter (column line C, See Fig. C-1), $\hat{\Delta}_{\text{GS}}^{\text{EW}}$. $\hat{\Delta}_{\text{GS}}^{\text{EW}}$ is significantly larger than Δ_{GS}^N , as shown in the next set of lines. Finally, the resultant drift, $\hat{\Delta}_{\text{GS}}^{\text{TOT}}$, is somewhat larger, in particular for the traditional structure, which exhibited larger twist in-plan. As seen, even with the deformation in the IFAS, the total drifts are significantly larger for the traditional structure. The residual inter-story drifts are also shown, and are seen to be small, with the LFRS and GLRS residual drift slightly larger for the “traditional” structure.

C.5 Shear and Moment Envelopes

The shear force and moment envelopes of Phase I and Phase II is shown in this section. Fig. C-13 shows the story force comparison (North wall, GLRS and total) for Phases I, II at different earthquake levels: (a) story shear envelopes (Eqns. C-11, C-13, C-

14); and, (b) overturning moment envelopes (Eqns. C-8, C-15a,b). The North wall base moment estimated by Eqn. C-12 is indicated in Fig. C-13b by vertical trend lines for the purpose of verifying Eqn. C-15a. The results indicate smaller North wall and total story shear forces and overturning moment in the IFAS structure for most floors and earthquake levels, indicating the potential for lower seismic force demands with the IFAS. The close correlation of the vertical trend lines with the base of the envelopes in Fig. C-13b indicates the accuracy of the overturning calculation Eqn. C-15a, and also implies accuracy for Eqn. C-13. Note that Test 17 is used as the Phase II test for the comparison at BE DBE. This is because the external force acted on the North wall is easier to be estimated in Test 17 than that in Test 18.

The structure shear force in the IFAS structure is larger than or close to that of traditional structure in SE DBE and BE MCE tests. The reason for a larger structure shear force in the IFAS structure under SE DBE maybe because the structure stiffness in the IFAS structure is larger than that of the traditional structure due to the cumulative damage occurred in the test (See Fig. 5-29a). The reason for a larger total shear force in the IFAS structure under BE MCE is probably due to the following reasons: (1) the engagement of the bumper in Phase I (See Fig. 5-31); (2) excitation of the twisting mode in Phase II structure.

The floor acceleration is increased as the force transferring between the floor and North wall increases due to the engagement of the bumper. Thereby, the floor inertial force is increased.

The structure acceleration was not as high as expected due to the structural damage in the continuous shake table test (See Fig. 6-9). Additionally, the structure twisted more

in Phase II in comparison that in Phase I (See Fig. 5-20, Fig. 5-24). Therefore, the acceleration in the EW direction was not as large as expected.

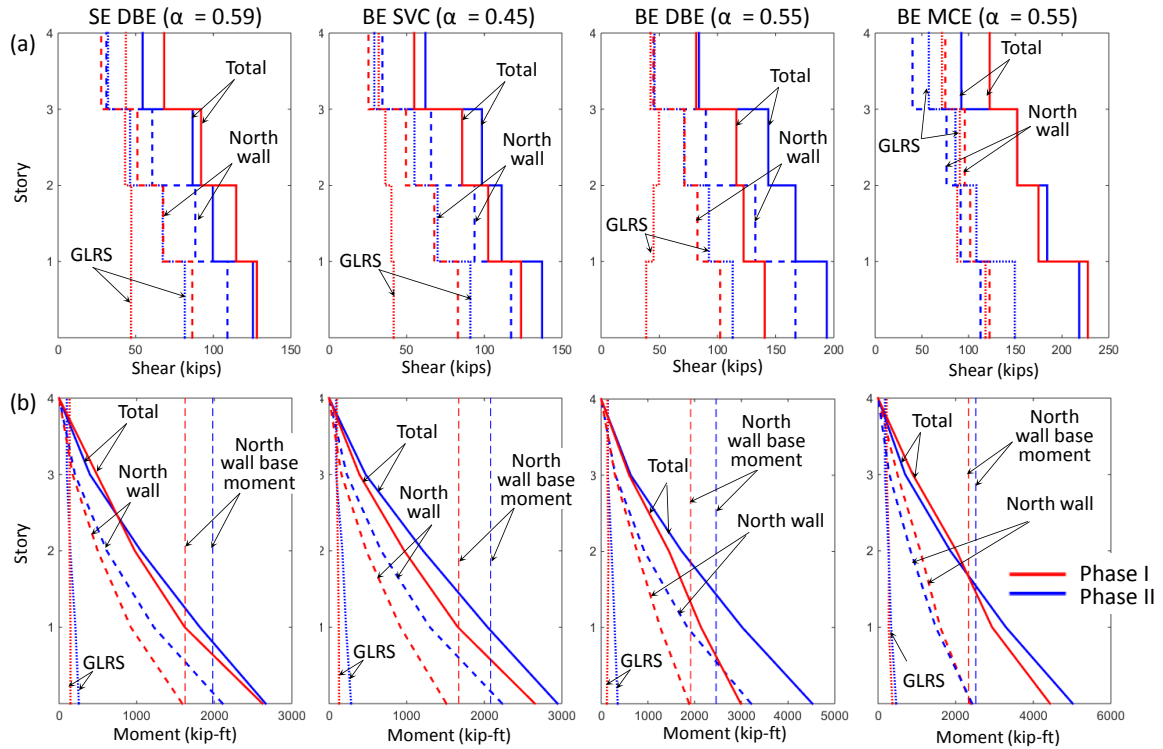


Fig. C-13. Force envelope comparison: (a) story shear (b) overturning moment.

C.6 Floor Acceleration Response in the Shake Table Test

The location of the occurrence of \hat{a}_{TOT} in Fig. 5-23c is shown in Fig. C-14. The maximum resultant acceleration mostly occurs at the south side of the slab in Phase I and Phase II, while the maximum resultant acceleration occurs at the north side of the slab in phase III.

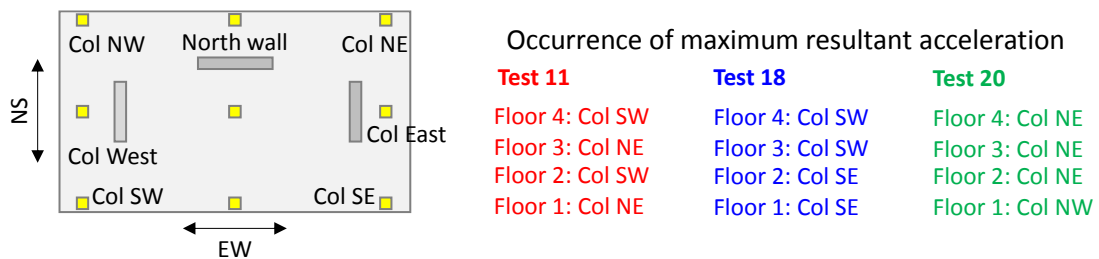


Fig. C-14. Location of maximum resultant acceleration: Test 11; Test 18; Test 20.

Fig. C-15a, b show the Fourier Transform of the floor acceleration in the EW and NS direction at the 2nd and 4th floor level in Fig. C-14 respectively. Since \hat{a}_{TOT} occurs at the south side of the slab in the 2nd and 4th floor in Test 11 and Test 18, the Fourier Transform of the acceleration at Col SW in Test 20 is also plotted in Fig. C-15a, b in grey. Fig. C-15c shows the test specimen fundamental period's variation with the estimated location of the structural periods in Test 11, 18 and Test 20. Fig. C-15a shows that the fundamental mode contributed significantly to the EW acceleration in Test 11 and Test 18. The higher mode contributed significantly to the EW acceleration at Col NE in Test 20. The contribution from the higher modes is decreased significantly at Col SW in comparison to that at Col NE in Test 20. Therefore, higher modes effect to the acceleration is decreased as the measurement location moves farther from the LFRS. Fig. C-15b shows that higher modes contribution to the NS acceleration is increased in Test 11 and Test 18 in comparison to that of EW acceleration.

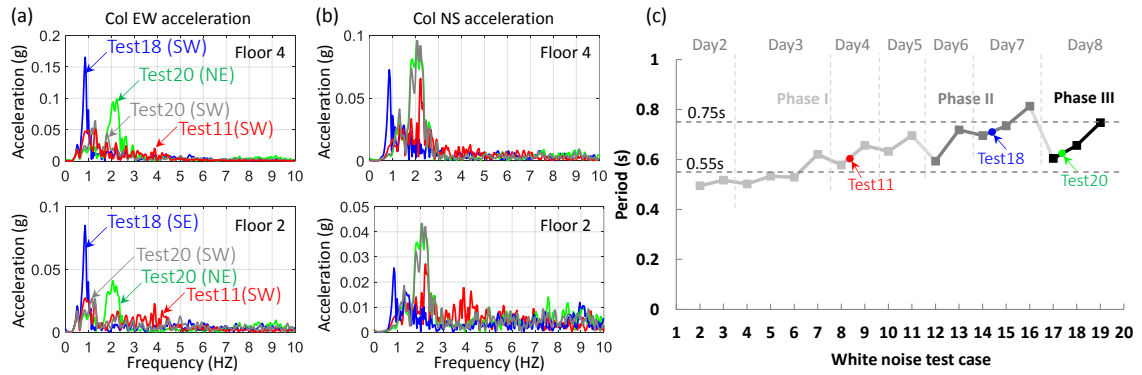


Fig. C-15. Fourier Transform of the floor acceleration at the indicated location in Fig. C-14: (a) EW; (b) NS; (c) structural period variation.

Fig. C-16a, b show the time history of the floor acceleration in the EW and NS direction at the 2nd and 4th floor level in Fig. C-14 respectively. The plot “phase” represents the level of the coincidence of large acceleration in the EW and NS direction.

The acceleration time history in the EW and NS direction is first normalized to a record with unit maximum value. Then, the multiplication of the normalized acceleration in the EW and NS direction is plotted as the “phase” at the bottom of Fig. C-16. If the phase value equals one, it represents that the maximum acceleration in the EW and NS direction occurs simultaneously. Fig. C-16 first shows that the accelerations in the EW and NS direction in Test 20 is much larger than that in Test 11 and Test 18. Also, several large peaks can be observed in the phase plot in Test 20 and the largest peak equals or is close to unit value, implying that the acceleration in the EW and NS direction in Test 20 mostly increase simultaneously. Fig. C-16 shows that the maximum acceleration in the EW direction in Test 11 and Test 18 are similar. Fewer large peaks can be observed in the phase plot in Test 11 than Test 18, implying that the time when the accelerations in the EW and NS direction in phase in an IFAS structure is not as often as that of a traditional structure.

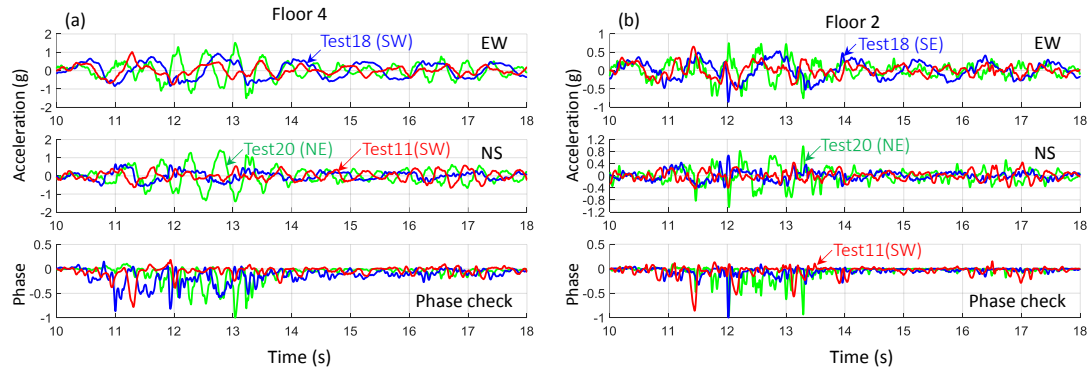


Fig. C-16. Time history of the floor acceleration at the indicated location in Fig. C-14: (a) floor 4; (b) floor 2.

C.7 Selected FD and BRB Force-Deformation Response

Fig. C-17a, b show selected force-deformation response of the IFAS deformable connections for different Phase I tests, including: (a) the North Wall FD on the 2nd and 4th floor; (b) the West transverse wall BRB on the 2nd and 3rd floor (where the BRB

deformation is similar in both comparison tests). The FD provides stable and full hysteretic response (Fig. C-17a), exhibiting excellent energy dissipation characteristics. The tests compared in Fig. C-17a are BE DBE tests with different IFAS design strengths: Test 7 (intermediate, $\alpha=0.61$); Test 8 (aggressive, $\alpha=0.41$), as indicated by horizontal trend lines. As expected, a larger relative displacement is seen for a lower IFAS strength. The BRBs also exhibited excellent energy dissipation characteristics (Fig. C-17b), and in contrast to the FD, work harden under increasing cyclic deformation (Test 11 vs. 6). The response of the deformable connections on other floors also show stable and full hysteretic response, as well as a strength close to the designed strength.

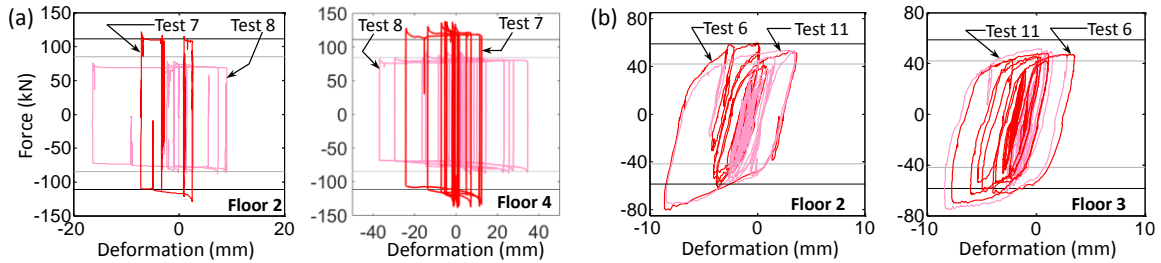


Fig. C-17. Force-deformation response: (a) FD; (b). BRB.

The maximum force under tension and compression of the BRBs at the 2nd, 3rd and 4th floor are normalized by the F_{px} , α_{BRB} , and shown in Fig. C-18. The figure shows that the BRB strength varied around the BRB design strength. The BRB maximum force depends on the maximum deformation the BRB can reach, as well as the isotropic strain hardening effect. However, the effect from the maximum deformation is more dominant.

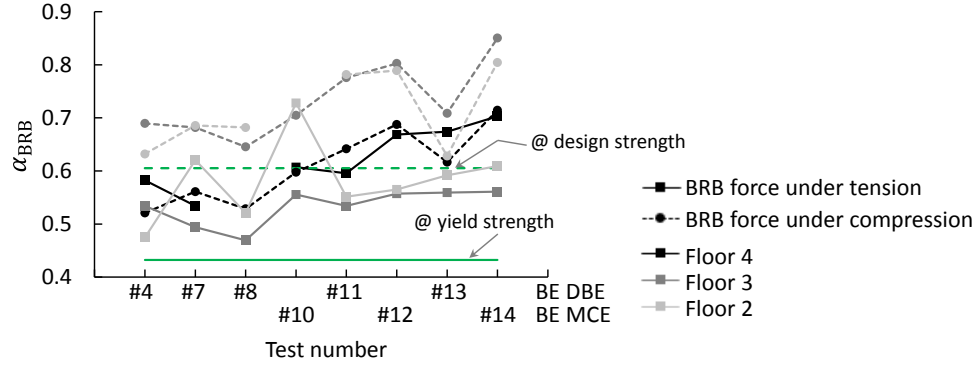


Fig. C-18. Maximum BRB force under tension and compression at each BE DBE and MCE test.

C.8 Model Verification using Sequential Analysis

Test 7 is the second analysis in the sequential analysis of the numerical model. Fig. C-19 shows the time history responses of the floor displacement at column line B, floor acceleration near column B1, slab twisting and North wall base rotation. Note that all the responses are from the roof level except the wall base rotation. Fig. C-19a shows that the UM underestimates the GLRS roof displacement a little bit, however the UM matches the test.

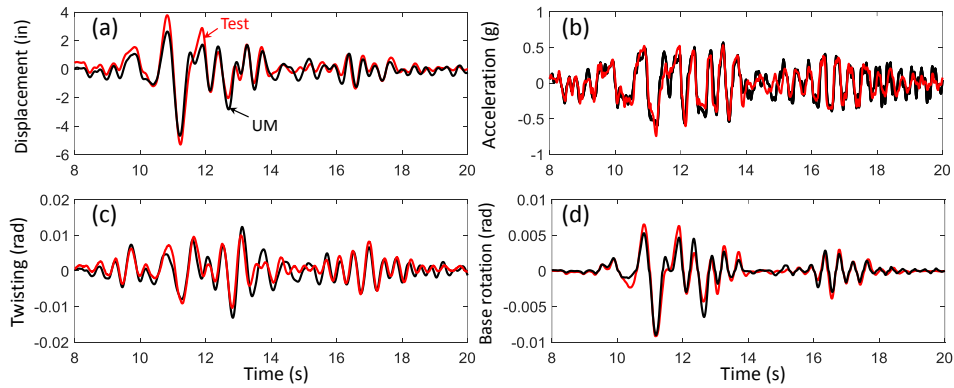


Fig. C-19. Time history responses (Test 7): (a) floor displacement at column line B; (b) floor acceleration near column B1; (c) slab twisting; (d) north wall base rotation.

Fig. C-20 shows the structure overturning moment-roof drift at column line B, north wall base moment-rotation, roof FD and BRB force-deformation responses for Test 7. The comparison shows that the analysis matches the test structure responses.

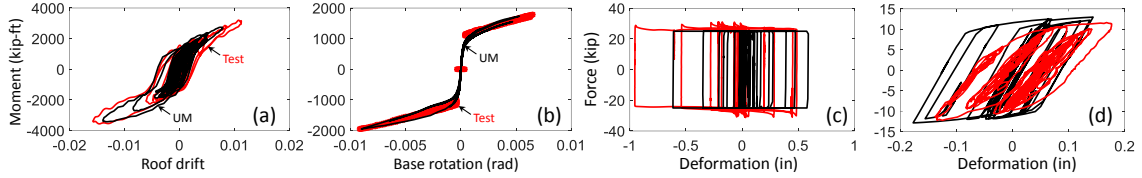


Fig. C-20. Moment-rotation responses (Test 7): (a) structure overturning; (b) North wall base; (c) roof FD force-deformation; (d) roof BRB force-deformation.

Test 11 is the 6th analysis in the sequential analysis of the numerical model and is the first test after the BE MCE level earthquake. Fig. C-21 shows the time history responses of the floor displacement at column line B, floor acceleration near column B1, slab twisting and North wall base rotation. Note that all the responses are from the roof level except the wall base rotation.

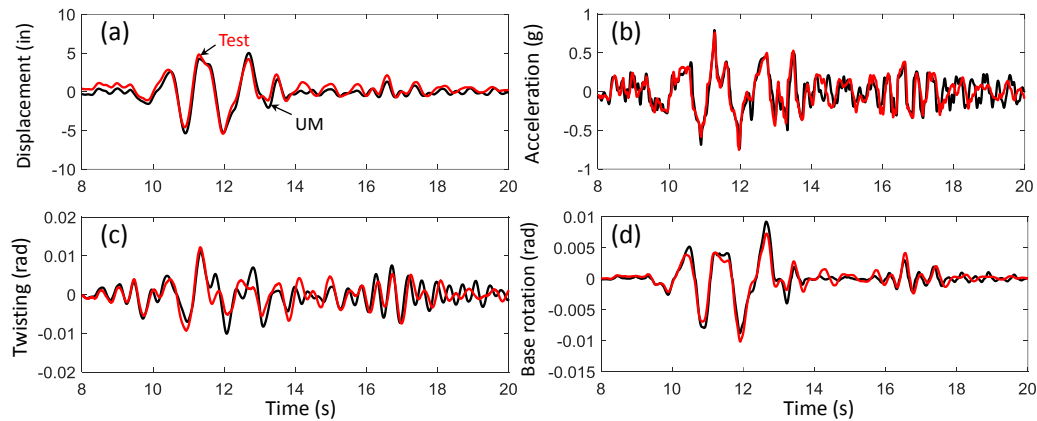


Fig. C-21. Time history responses (Test 11): (a) floor displacement at column line B; (b) floor acceleration near column B1; (c) slab twisting; (d) north wall base rotation.

Fig. C-22 shows the structure overturning moment-roof drift at column line B, north wall base moment-rotation, the roof FD and BRB force-deformation responses. The figure shows that the structure overturning-roof drift, North wall moment-rotation and roof FD

force-deformation from the numerical analysis matches the test responses. However, a large difference can be observed in the roof BRB force-deformation behavior.

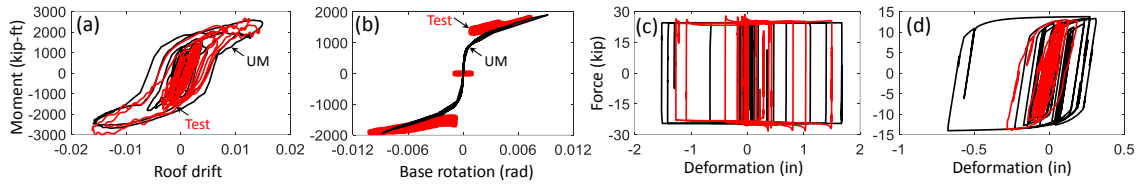


Fig. C-22. Moment-rotation responses (Test 11): (a) structure overturning; (b) North wall base; (c) roof FD force-deformation; (d) roof BRB force-deformation.

APPENDIX D – SUPPLEMENTAL INFORMATION FOR CHAPTER 6

D.1 Energy Dissipation in Different Components

The energy dissipated in different components is plotted and compared in Fig. D-1. The figure shows that much more energy is dissipated in the *PI-0.6* rather than that in *PII-wo/FD-0.6*. The energy dissipated in the PT walls in the Phase II models is much larger than that in the Phase I model, implying the capacity of reducing the damage in the LFRS by using the IFAS.

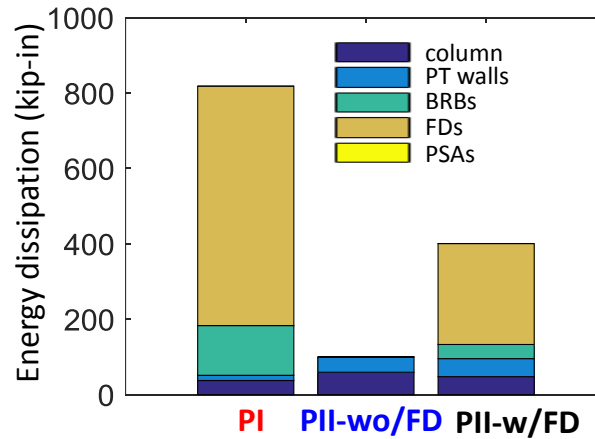


Fig. D-1. Energy dissipation among different components (Eccentric case).

D.2 PSA and FD Force in Phase II

It will be interesting to see how the PSA and FD at the North wall works in the *PII-w/FD*. The deformation time history of the PSAs and FDs from level 2 to level 4 are shown in Fig. D-2a, b. The North wall base rotation is shown in Fig. D-2c. The positive direction is defined when the slab moves westward relative to the North wall, therefore, the positive direction of the force acting on the North wall is also westward. The figure shows that when the structure deforms eastward, the slab moves eastward relative to the North wall (negative direction) and the North wall deforms eastward. Then, the FD undergoes

compression (See Fig. D-2b). When the structure deforms westward, the slab moves westward relative to the North wall (positive direction) and the FD undergoes tension.

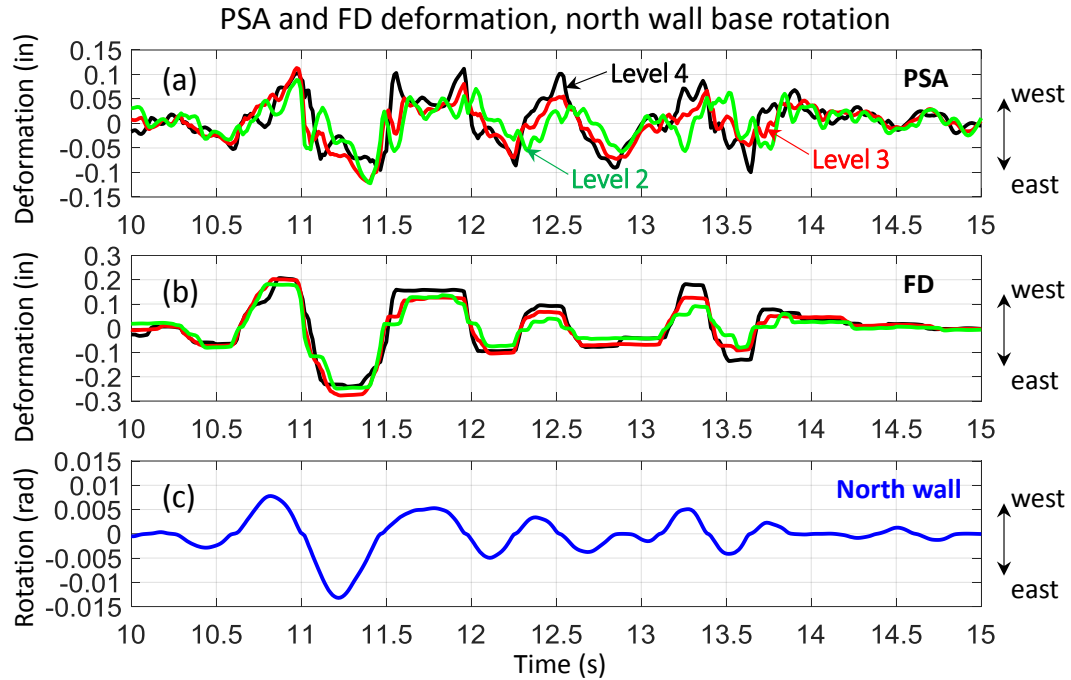


Fig. D-2. Deformation time history: (a) PSA; (b) FD; (c) North wall base rotation.

The force, deformation time history of the PSAs, FD and summation at level 4 is shown with black, red and green respectively in Fig. D-3a, b. Note that the summation force includes the RB force. However because the RB force is much smaller than the force in the PSA and FD, it is not shown separately in Fig. D-3a. The GLRS displacement at column line A and B is shown with pink and blue in Fig. D-3c. The North wall base rotation and slab twisting is shown with blue and black in Fig. D-3d. Fig. D-3a shows that the PSA force is canceled by the FD force sometimes and amplified by the FD force in the rest of the time. A response sequence (time spots A to H) will be used for the purpose of understanding the behavior of the PSA and FD.

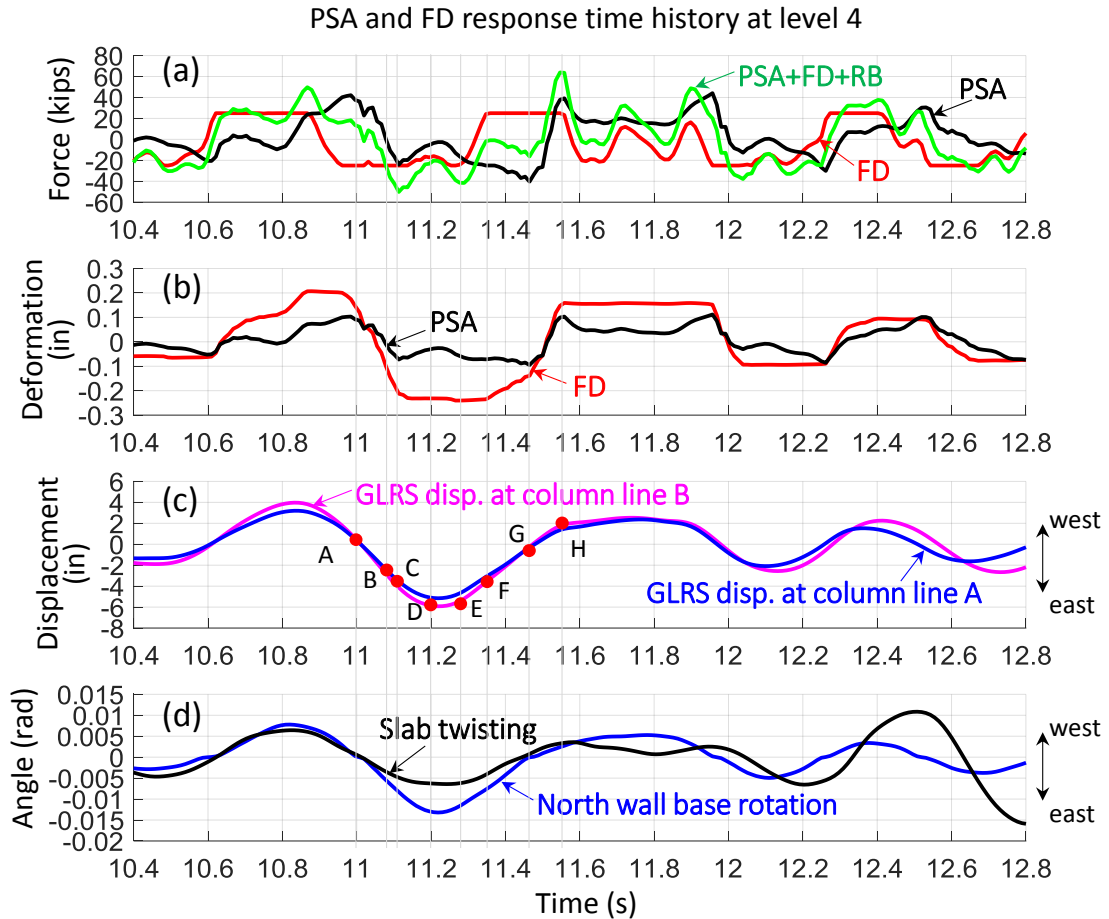


Fig. D-3. Response time history PSA and FD at level 4: (a) force; (b) deformation of FD and PSA; (c) GLRS displacement; (d) North wall base rotation and slab twisting.

At time A, the GLRS and wall deforms eastward (See Fig. D-3c, d), the FD undergoes shortening and the PSA deforms from westward to eastward (See Fig. D-3b). Therefore, the FD force is negative and the PSA force is positive since the PSA deformation is still positive (See Fig. D-3a). Thus, the summation of the floor anchorage force (summation force) is smaller than the PSA force (black to green in Fig. D-3a). At time B, the GLRS and North wall deforms eastward (See Fig. D-3c, d) and the FD undergoes shortening (See Fig. D-3b). The PSA deformation changes from positive to negative (See Fig. D-3b). Therefore, the PSA force is negative and the summation force is larger than the

PSA force (See Fig. D-3a). At time C, the PSA deformation reaches its local maximum, the PSA deformation is decreased afterwards, while the FD still undergoes shortening (See Fig. D-3b). Therefore, the FD force is negative and in the same sign with PSA force. At time D, the GLRS and North wall deforms to the maximum negative displacement in this cycle and will deform westward afterwards. At time E, the GLRS and North wall deform westward (See Fig. D-3c, d). The negative deformation of the PSA is increased due to the wall deforms faster than the GLRS (See Fig. D-3b) and therefore, the PSA force is still negative and increased (See Fig. D-3a). The FD begins undergo elongation and the FD force changes from negative to positive (See Fig. D-3a). At time F, the GLRS and North wall deforms eastward (See Fig. D-3c, d) while the FD reaches the design strength (See Fig. D-3a) and provides constant tensile force on the wall. The PSA force is negative because the PSA deformation is still negative (See Fig. D-3a, b). The summation force is smaller than the PSA force. At time G, the GLRS and North wall continues deforming westward. The North wall base gap is closed (See Fig. D-3d). The PSA reaches its maximum negative deformation in this cycle (See Fig. D-3b). The FD still undergoes elongation (See Fig. D-3b) and the FD force is positive (See Fig. D-3a). The summation force is still smaller than the PSA force. At time H, the PSA reaches its local peak deformation. The FD and PSA force is in the same sign and the summation force is larger than the PSA force (See Fig. D-3a).

The summation force acting on the North wall between *PII-w/FD-0.6* and *PII-wo/FD-0.6* is compared in Fig. D-4. The figure shows that the force acts on the North wall from the case using the FD is smaller than the case without the FD.

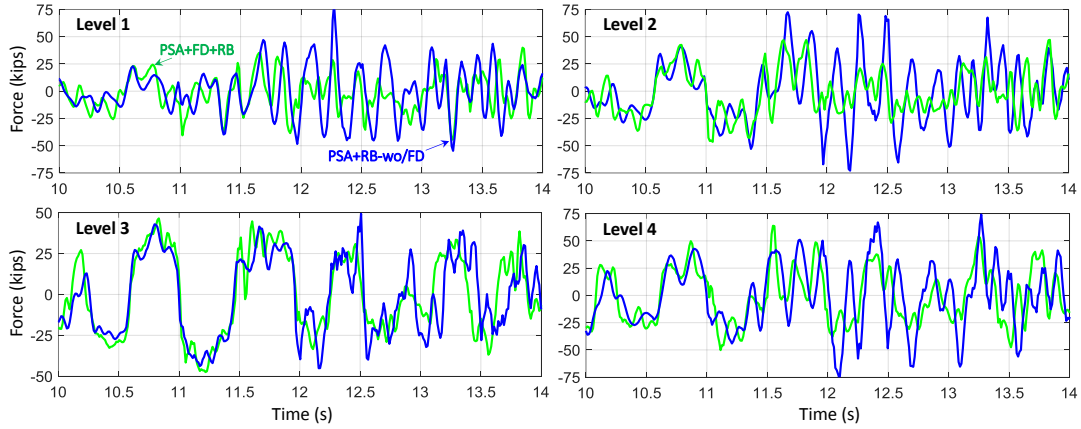


Fig. D-4. Summation force time history between PII-w/FD-0.6 and PII-wo/FD-0.6: (a) level 1; (b) level 2; (c) level 3; (d) level 4.

D.3 Influence from Different Transverse Wall Strength

In this section, the effectiveness of the IFAS is studied for a structure using transverse walls with different yield strength. This different yield strength is obtained by applying different post-tensioned force to the PT bars in transverse walls and the transverse wall moment-rotation behavior is shown in Fig. D-5. The figure shows that the yield strength of the wall is increased as the applied post-tensioned force increases. The strain hardening ratio of the wall is decreased as the applied post-tensioned force increases.

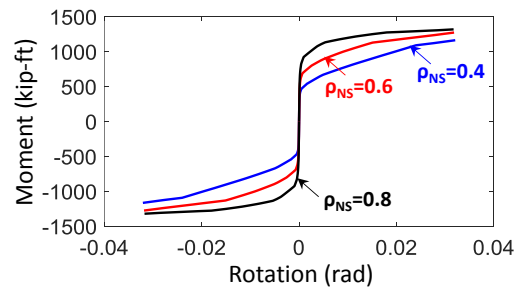


Fig. D-5. Transverse wall moment-rotation behavior using different post-tensioned force.

A list of models used in this section is shown in Table D-1. The earthquake used for the analysis is BE DBE.

Table D-1. Description of models with different transverse wall strength.

Model	PT ratio at North wall (ρ_{EW})	PT ratio at transverse walls (ρ_{NS})	Eccentric or Concentric North wall	Note
PI-0.4	0.6	0.4	Eccentric	IFAS structure, $\alpha=0.57$
PII-wo/FD-0.4	0.6	0.4	Eccentric	Traditional structure wo/FD
PI-0.8	0.6	0.8	Eccentric	IFAS structure, $\alpha=0.57$
PII-wo/FD-0.8	0.6	0.8	Eccentric	Traditional structure wo/FD

The responses of the IFAS structure and traditional structure when $\rho_{NS}=0.4$ and $\rho_{NS}=0.8$ are shown in Fig. D-6 respectively. A significant reduction in the floor acceleration and a good reduction in the North wall drift can be observed (See Fig. D-6a, b). The reduction in the East wall drift is not as significant as that of the North wall (See Fig. D-6c). A good reduction in the slab twisting is observed in Fig. D-6e. The North wall drift of the structure when $\rho_{NS}=0.8$ is larger than that when $\rho_{NS}=0.4$. The East wall drift and slab twisting of the structure when $\rho_{NS}=0.8$ is smaller than that when $\rho_{NS}=0.4$. The stronger transverse wall produces a smaller structure twisting response and larger North wall deformation demand.

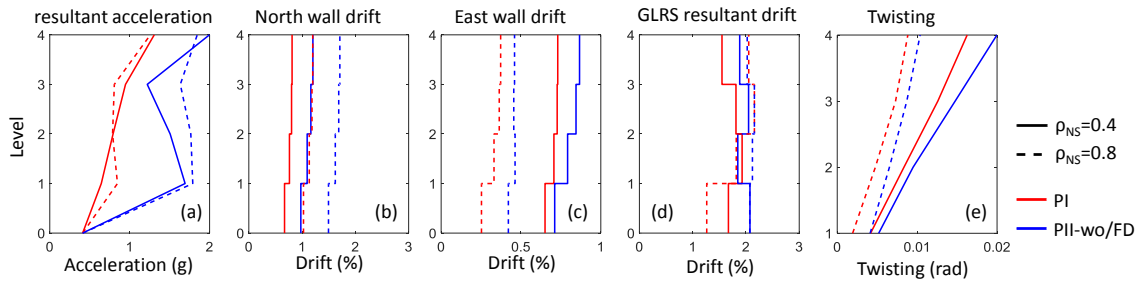


Fig. D-6. Structure response envelopes ($\rho_{NS}=0.4$ and $\rho_{NS}=0.8$ for transverse walls): (a) floor acceleration; (b) North wall drift; (c) East wall drift; (d) GLRS drift; (e) slab twisting.

APPENDIX E – SUPPLEMENTAL INFORMATION FOR CHAPTER 7

E.1 Advantages and Disadvantages of Each Test Protocol

The advantages and limitations of single pulse protocol and cyclic deformation protocol are shown in Table E-1.

Table E-1. Advantages and limitations of different test protocol

	Single pulse protocol	Cyclic deformation protocol using constant loading velocity (equals V_0)	Mimicking bumper deformation from the shake table test
Advantages	Create impact effect	Test repeatability of the bumper	Test repeatability of the bumper
	Reflect the deformation that the bumper underwent in the shake table test	Test combinations of different V_0 and δ_{\max}	Reflect what the bumper underwent in the shake table test
	Test combinations of different test parameters		
Limitations	Doesn't test the bumper repeatability	Doesn't reflect what the bumper underwent in the shake table test	

E.2 Relationships between Different Test Parameters

Fig. E-1 shows the scatter plots on the relationship between δ_{\max} & V_0 , V_r & V_0 , δT & δ_{\max} for different V_0 . Linear regression analyses are used to obtain the relationship between the two test parameters in each scatter plot (solid line). The standard deviation is shown using dashed lines.

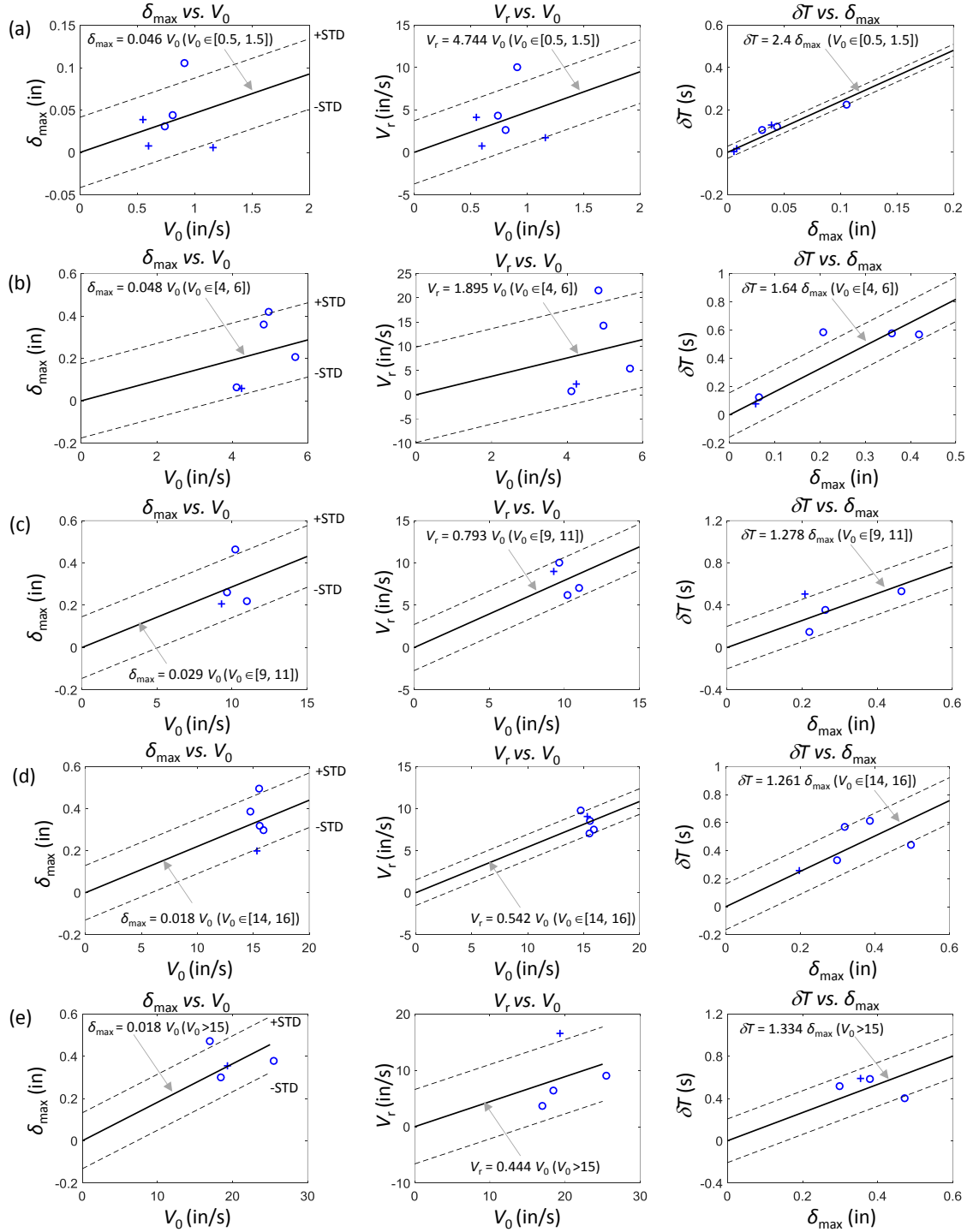


Fig. E-1. Scatter plots: (a) $V_0=1$ in/s; (b) $V_0=5$ in/s; (c) $V_0=10$ in/s; (d) $V_0=15$ in/s; (e) $V_0=20$ in/s.

9. REFERENCES

1. Mar D. and Tipping S. (2000). "Smart frame story isolation system: a new high-performance seismic technology." Internal report of Tipping Mar associates, Berkeley, CA.
2. Crane S. (2004). "Influence of energy dissipation connections between floors and the lateral force resisting system." Master Thesis, University of California at San Diego.
3. Minutes from NEESR Project Meeting #3, Rutherford & Chekene Offices, San Francisco, DATE 2012.
4. ASCE 7-05. (2005). "Minimum design loads for buildings and other structures." American Society of Civil Engineers.
5. ASCE 7-10. (2010). "Minimum design loads for buildings and other structures." American Society of Civil Engineers.
6. <http://neesr-ceem.webhost.uits.arizona.edu/introduction>.
7. Zhang D., Fleischman R., Restrepo J., Sause R., Maffei J., Mar D., Monti G. (2014). "Development of a floor inertia force limiting anchorage system under earthquake loading." Proceedings of the tenth US National Conference on Earthquake Engineering, Earthquake Engineering Research Institute, Anchorage, AK, July, 2014.
8. Fleischman R., Restrepo J., Nema A., Zhang D., Shakya U., Zhang Z., Sause R., Tsampras G., and Monti G. (2015). "Inertial Force-Limiting Anchorage System for Seismic Resistant Building Structures." Structures Congress 2015: pp. 1302-1313.
9. FEMA P-749 (2010). "Earthquake-resistant design concepts. An introduction to the NEHRP recommended seismic provisions for new buildings and other structures." National Institute of Building Sciences Building Seismic Safety Council.
10. Hall J. F. (1994). "Northridge Earthquake January 17, 1994, Preliminary reconnaissance report." Earthquake Engineering Research Institute, 94-01.
11. Tsai K-C, Chen H-W, Hong C-P, Su Y-F (1993). "Design of steel triangular plate energy absorbers for seismic-resistant construction." Earthquake Spectra, Vol. 9, No. 3, 505–528.
12. Lee D. and Taylor D.P. (2001). "Viscous damper development and future trends." Earthquake Engineering and Structural Dynamics, Vol. 10, Issue 5, 311–320.
13. Tsampras G. and Sause R. (2015). "Development and experimental validation of deformable connection for earthquake-resistant building systems with reduced floor accelerations." Report, NEEShub, Lehigh University.

14. Newell J., Uang C., Benzoni G. (2006). "Subassemblage testing of corebrace buckling-restrained braces (G series)." Report No. TR-06/01, Department of Structural Engineering, University of California, San Diego, La Jolla, California.
15. Sabelli R., Mahin S., Chang C. (2003). "Seismic demands on steel braced frame buildings with buckling-restrained braces." *Engineering Structures*, Vol.25, Issue 5, 655-666.
16. Tsampras G., Sause R., Zhang D., Fleischman R. B., Restrepo J. I., Mar D., Maffei J. (2016). "Development of deformable connection for earthquake-resistant buildings to reduce floor accelerations and force responses." *Earthquake Engineering and Structural Dynamics*, DOI: 10.1002/eqe.2718.
17. The United Nations Office for Disaster Risk Reduction. (2015). "Global assessment report on disaster risk reduction." GAR Report, United Nations.
18. PEER/EERI/GEER/Tsunami Field Investigation Team. (2011). "Tohoku Pacific Ocean Earthquake and Tsunami - Quick observations."
19. Scawthorn C., Takada S., Javanbarg M. (2011). "Lifeline aspects." PEER-EERI Preliminary Briefing on 11 March 2011 Tohoku Earthquake and Tsunami, Pacific Earthquake Engineering Research Center, April, 28, 2011. University of California at Berkeley.
20. Deierlein G. (2011). "Eastern japan Earthquake disaster – Performance of structures." PEER-EERI Preliminary Briefing on 11 March 2011 Tohoku Earthquake and Tsunami, Pacific Earthquake Engineering Research Center, April, 28, 2011. University of California at Berkeley.
21. Cabrera C. (2011). "Industrial facilities and business interruption." PEER-EERI Preliminary Briefing on 11 March 2011 Tohoku Earthquake and Tsunami, Pacific Earthquake Engineering Research Center, April, 28, 2011. University of California at Berkeley.
22. Holmes W. T. (2010). "Nonstructural damage." Briefing on the Canterbury, New Zealand, Earthquake of September 3, 2010, EERI, PEER and GEER, October 18, 2010. University of California at Berkeley.
23. Turner F. (2010). "Unreinforced masonry and selected modern buildings and port facilities." Briefing on the Canterbury, New Zealand, Earthquake of September 3, 2010, EERI, PEER and GEER, October 18, 2010. University of California at Berkeley.
24. Ye L., Qu Z., Lu X., Feng P. (2008). "Structural anti-collapse capacity in earthquakes – Lesson from Wenchuan Earthquake building reconnaissance." Workshop on analyzing Wenchuan Earthquake building damage and reconstruction, June 28- June 29, Beijing, China. (In Chinese).

25. Xiao S., Li H., Lu M. (2008). "Preliminary briefing on Sichuan Wenchuan Earthquake." Workshop on analyzing Wenchuan Earthquake building damage and reconstruction, June 28- June 29, Beijing, China. (In Chinese).
26. Lee T. and Mosalam K.M. (2006). "Probabilistic seismic evaluation of reinforced concrete structural components and systems." PEER Report 2006/04, Pacific Earthquake Engineering Research Center, University of California Berkeley.
27. Yang T. Y., Atkinson J. C., and Tobber L. (2015) "Detailed Seismic Performance Assessment of High-Value-Contents Laboratory Facility." *Earthquake Spectra*, Vol. 31, No. 4, 2117-2135.
28. Maruyama Y., Yamazaki F., Matsuzaki S., Miura H. and Estrada M. (2012). "Evaluation of building damage and tsunami inundation based on satellite images and GIS data following the 2010 Chile earthquake." *Earthquake Spectra*, Vol. 28, No. S1, S165–S178.
29. Wilkinson S., Grant D., Williams E., Paganoni S., Fraser S., Boon D., Mason A. and Free M. (2013). "Observations and implications of damage from the magnitude Mw 6.3 Christchurch, New Zealand earthquake of 22 February 2011." *Bulletin of Earthquake Engineering*, Vol. 1, Issue 1, 107–140.
30. Goda K., Pomonis A., Chian S. C., Offord M., Saito K., Sammonds P., Fraser S., Raby A. and Macabuag J. (2013). "Ground motion characteristics and shaking damage of the 11th March 2011 Mw 9.0 Great East Japan earthquake." *Bulletin of Earthquake Engineering*, Vol. 11, Issue 1, 141–170.
31. Hutchinson T. C., Nastase D., Kuester F., and Doerr K. (2010) "Vibration Studies of Nonstructural Components and Systems Within a Full-Scale Building." *Earthquake Spectra*, Vol. 26, No. 2, 327-347.
32. Wang X., Astroza R., Hutchinson T.C., Conte J.P. and Restrepo J.I. (2015) "Dynamic characteristics and seismic behavior of prefabricated steel stairs in a full-scale five-story building shake table test program." *Earthquake Engineering and Structural Dynamics*, Vol. 44, Issue 14, 2507-2527.
33. Chen M., Pantoli E., Wang X, Astroza R., Ebrahimian H., Hutchinson T., Conte J., Restrepo J., Marin C., Walsh K., Bachman R., Hophler M., Englekirk R. and Faghihi M. (2016). "Full-scale structural and nonstructural building system performance during earthquakes: Part I – specimen description, test protocol, and structural response." *Earthquake Spectra*, Vol. 32, No. 2, 737-770.
34. Kao A., Soong T.T. and Vender A. (1999). "Nonstructural damage database." Technical Report MCEER-99-0014, University at Buffalo, State university of New York, Department of Civil, Structural and Environmental Engineering, Buffalo, New York.

35. Taghavi S. and Miranda E. (2003). "Response assessment of nonstructural building elements." PEER Report 2003/05, Pacific Earthquake Engineering Research Center, University of California Berkeley.
36. Comerio M.C. and Blecher H.E. (2010) "Estimating downtime from data on residential buildings after the Northridge and Loma Prieta Earthquakes." *Earthquake Spectra*, Vol. 26, No. 4, 951-965.
37. Werner S.D., Tarylor C.E., Moore III J.E., Walton J.S. and Cho S. (2000). "A risk-based methodology for assessing the seismic performance of highway systems." MCEER-00-0014, Multidisciplinary Center for Earthquake Engineering Research, University at Buffalo, State university of New York, Buffalo, New York.
38. FEMA (2003). "Multi-hazard loss estimation methodology, Earthquake model, Technical Manual." HAZUS MH MR4, Developed by: Department of Homeland Security, Emergency Preparedness and response Directorate, FEMA, Mitigation Division. Washington, D. C.
39. Luna R., Hoffman D. and Lawrence W. (2008). "Estimation of earthquake loss due to bridge damage in the St. Louis Metropolitan Area. I: direct losses." *Natural Hazards Review*, Vol. 9, Issue 1, 1-11.
40. Enke D., Tirasirichai D. and Hoffman D. and Luna R. (2008). "Estimation of earthquake loss due to bridge damage in the St. Louis Metropolitan Area. II: indirect losses." *Natural Hazards Review*, Vol. 9, Issue 1, 12-19.
41. National Research Council (1999). "The impacts of natural disasters: a framework for loss estimation." Committee on Assessing the Costs of Natural Disasters, Board on Natural Disaster, Commission on Geosciences, Environment, and Resources, National Research Council. National Academy Press, Washington, D.C.
42. Tierney K. J. (1997). "Business impacts of the Northridge Earthquake." *Journal of Contingencies and Crisis Management*, Vol. 5, NO. 2, 87-97.
43. Toyoda T. (1997). "Economic impacts of recovery: the case of Hanshin-Awaji Earthquake." Presentation to the Fifth U.S. – Japan Workshop on Urban Earthquake Hazard Reduction, Pasadena, California.
44. Toyoda T. (2008). "Economic impacts of Kobe Earthquake: a quantitative evaluation after 13 years." *Proceedings of the 5th International ISCRAM Conference – Washington, D.C., USA.*
45. Wu J., Li N., Xie W., Zhou Y., Ji Z. and Shi P. (2014) "Post-disaster recovery and economic impact of catastrophes in China." *Earthquake Spectra*, Vol. 30, No. 4, 1825-1846.
46. Cutfield M., Ryan K. and Ma Q. (2016) "Comparative life cycle analysis of conventional and base-iaolated buildings." *Earthquake Spectra*, Vol. 32, No. 1, 323-343.

47. Nakaki S., Stanton J., Sritharan S. (1999). "An overview of the PRESSS five-story precast test building." *PCI Journal*, Vol. 44, Issue 2, 26-39.
48. Kurama Y., Pessiki S., Sause R., Lu L. (1999). "Seismic behavior and design of unbonded post-tensioned precast concrete walls." *PCI Journal*, Vol. 44, Issue 3, 72-89.
49. Priestley M.J.N., Sritharan S., Conley J.R. and Pampinin S. (1999). "Preliminary results and conclusions from the PRESSS five-story precast concrete test building." *PCI Journal*, Vol. 46, Issue 6, 42-67.
50. Holden T., Restrepo J., Mander J.B. (2003). "Seismic performance of precast reinforced and prestressed concrete walls." *Journal of Structural Engineering*, Vol. 129, Issue 3, 286-296.
51. Restrepo J. and Rahman A. (2007). "Seismic Performance of Self-Centering Structural Walls Incorporating Energy Dissipators." *Journal of Structural Engineering*, Vol. 133, special issue: Precast-Prestressed Concrete Structures under Natural and Human-Made Hazards, 1560–1570.
52. ACI ITG (2007). "Acceptance Criteria for Special Unbonded Post-Tensioned Precast Structural Walls Based on Validation Testing." ACI ITG-5.1-07, American Concrete Institute.
53. ACI ITG (2009). "Requirements for Design of a Special Unbonded Post-Tensioned Precast Shear Wall Satisfying ACI ITG-5.1 and Commentary." ACI ITG-5.2-09, American Concrete Institute.
54. Sause R., Ricles J.M., Roke D.A., Chancellor N.B., and Gonner N. (2010). "Seismic performance of a self-centering rocking concentrically-braced frame." *Proceedings, 9th US National and 10th Canadian Conference on Earthquake Engineering*, Toronto, July 25-29, 2010.
55. Roke D., Sause R., Ricles J., and Gonner N. (2009). "Design Concepts for Damage-Free Seismic-Resistant Self-Centering Steel Concentrically Braced Frames." *Structures Congress 2009*: pp. 1-10.
56. Wolski M., Ricles J. M. and Sause R. (2009). "Experimental study of a self-centering beam–column connection with bottom flange friction device." *Journal of Structural Engineering*, Vol. 135, No. 5, 479-488.
57. Eatherton M., Ma X., Krawinkler H., Deierlein G., and Hajjar J. (2014). "Quasi-Static Cyclic Behavior of Controlled Rocking Steel Frames." *Journal of Structural Engineering*, Vol. 140, Issue 11, 04014083.
58. Eatherton M. and Hajjar F. (2014). "Hybrid simulation testing of a self-centering rocking steel braced frame system." *Earthquake Engineering and Structural Dynamics*, Vol. 43, Issue 11, 1725-1742.

59. Garlock M., Sause R. and Ricles R. (2005). "Behavior and design of post-tensioned steel frame system." *Journal of Structural Engineering*, Vol. 133, Issue 3: 389-399.
60. Barbachyn S., Kurama Y., McGinnis M., and Sause R. (2015). "Measured behavior of a reinforced concrete coupled wall with fully post-tensioned coupling beams." *Structures Congress 2015*: pp. 1361-1369.
61. Blakeley R.W.G., Cooney R.C. and Megget L.M. (1975). "Seismic shear loading at flexural capacity in cantilever wall structures." *Bulletin of the New Zealand National Society for Earthquake Engineering* 8:278-290.
62. Chandra R., Masand M., Nandi S.K., Tripathi C.P., Pall R. and Pall A. (2008). "Friction-dampers for seismic control of La Gardenia towers south city, Gurgaon, India." *12WCEE*, New Zealand.
63. De Matteis G., Landolfo R. and Mazzolani F.M. (2003). "Seismic response of MR steel frames with low-yield shear panels." *Engineering Structures*, Vol. 25, Issue 2: 155-168.
64. Nakashima M., Saburi K., Tsuji B. (1996). "Energy input and dissipation behaviour of structures with hysteretic dampers." *Earthquake Engineering and Structural Dynamics*, Vol. 25, Issue 5:483-496.
65. Watanabe A, Hitomi Y, Saeki E, Wada A and Fujimoto M. (1988). "Properties of brace encased in buckling-restraining concrete and steel tube". *Proceedings of Ninth World Conference on Earthquake Engineering*, August 2-9, 1988, Tokyo-Kyoto, Japan. Vol. IV: 719-724.
66. Grigorian C.E., Yang T.S., and Popov E.P. (1993). "Slotted bolted connection energy dissipators". *Earthquake Spectra*, Vol. 9, Issue 3, 491-504.
67. Fahnestock L. A., Sause R. and Ricles J. M. (2007). "Seismic response and performance of buckling-restrained braced frames." *Journal of Structural Engineering*, Vol. 133, No. 9, 195-1204.
68. Speicher M., Hodgson D.E, DesRoches R. and Leon R.T. (2009). "Shape memory alloy tension/compression device for seismic retrofit of buildings." *Journal of Materials Engineering and Performance*, Vol. 18, Issue 5: 746-753.
69. Lin, Y., Sause, R., and Ricles, J. (2013). "Seismic Performance of a Large-Scale Steel Self-Centering Moment-Resisting Frame: MCE Hybrid Simulations and Quasi-Static Pushover Tests." *Journal of Structural Engineering*, Vol. 139, No. 7, 1227-1236.
70. Buckle I.G., and Mayes R.L. (1990). "Seismic isolation: History, application, and performance - A world view." *Earthquake Spectra*, Vol. 6, Issue 2, 161-201.
71. Higashino M. and Okamoto S. (2006). "Response control and seismic isolation of buildings." Taylor & Francis Group.

72. Soong T.T., Masri S.F. and Housner G.W. (1991). "An overview of active structural control under seismic loads." *Earthquake Spectra*, Vol. 7, Issue 3, 483-505.
73. Yang G. (2001). "Large-scale magnetorheological fluid damper for vibration mitigation: modeling, testing and control." Ph.D. Dissertation, University of Notre Dame, Indiana.
74. Symans M. and Constantinou M. (1999). "Semi-active control systems for seismic protection of structures: a state-of-the-art review." *Engineering Structures*, Vol. 21, Issue 6, 469-487.
75. Spencer B.Jr. and Nagarajaiah S. (2003). "State of the art of structural control." *Journal of Structural Engineering*, Vol. 129, Issue 7, 845-856.
76. Sarlis A., Pasala D., Constantinou M., Reinhorn A., Nagarajaiah S., and Taylor D. (2013). "Negative Stiffness Device for Seismic Protection of Structures." *Journal of Structural Engineering*, Vol. 139, Issue 7, 1124-1133.
77. Pasala D., Sarlis A., Nagarajaiah S., Reinhorn A., Constantinou M., and Taylor D. (2013). "Adaptive Negative Stiffness: New Structural Modification Approach for Seismic Protection." *Journal of Structural Engineering*, Vol. 139, Issue 7, 1112-1123.
78. Pasala D., Sarlis A., Reinhorn A., Nagarajaiah S., Constantinou M., and Taylor D. (2014). "Apparent Weakening in SDOF Yielding Structures Using a Negative Stiffness Device: Experimental and Analytical Study." *Journal of Structural Engineering*, 10.1061/(ASCE)ST.1943-541X.0001455, 04016005.
79. Sarlis A., Pasala D., Constantinou M., Reinhorn A., Nagarajaiah S., and Taylor D. (2016). "Negative Stiffness Device for Seismic Protection of Structures: Shake Table Testing of a Seismically Isolated Structure." *Journal of Structural Engineering*, 10.1061/(ASCE)ST.1943-541X.0001455 , 04016005.
80. Nagarajaiah S. and Sun X. (2000). "Response of base-isolated USC hospital building in Northridge Earthquake." *Journal of Structural Engineering*, Vol. 126, Issue 10, 1177-1186.
81. Lambrou V., Constantinou M. C. (1994). "Study of seismic isolation systems for computer floors." Rep. No. NCEER-94-0020, State University of New York at Buffalo, Buffalo, New York.
82. Kelly J.M. (1991). Base isolation: Origins and development EERC NEWs.
83. Clark P., Higashino M., Kelly J. (1994). "Performance of Seismically Isolated Structures in the January 17, 1994 Northridge Earthquake." *Proceedings of Sixth U.S.-Japan Workshop on the Improvement of Building Structural Design and Construction*. Victoria, B.C., Canada: Applied Technology Council and Japan Structural Consultants Association. ATC-15-5.

84. Liu S., Warn G. (2012). "Seismic performance and sensitivity of floor isolation systems in steel plate shear wall structure", *Engineering Structures*, Vol. 42, 115-126.
85. FEMA P-751 (2012). "2009 NEHRP recommended seismic provisions: Design examples." National Institute of Building Sciences.
86. Trevor K. (2001). "Base isolation of structures - Design guidelines." Holmes Consulting Group Ltd.
87. Villaverde R. and Mosqueda G (1999). "Aseismic roof isolation system: analytic and shake table studies." *Earthquake Engineering and Structural Dynamics*, Vol. 28, Issue 3: 217-234.
88. Villaverde R., Aguirre M. and Hamilton C. (2005). "Aseismic roof isolation system built with steel oval elements: exploratory study." *Earthquake Spectra*, Vol. 21, No. 1: 225-241.
89. Villaverde R. (1985). "Reduction in seismic response with heavily-damped absorbers." *Earthquake Engineering and Structural Dynamics*, Vol. 13, Issue 1: 33-42.
90. Tsuneki Y., Torii S., Murakami K. and Sueoka T. (2008). "Middle-story isolated structural system of high-rise building." *Proceedings of the 14th World Conference on Earthquake Engineering*, Beijing, China.
91. Ryan K.L. and Earl C.L. (2010). "Analysis and design of inter-story isolation systems with nonlinear devices." *Journal of Earthquake Engineering*, Vol. 14, Issue 7: 1044-1062.
92. Pan T.C., Ling S.F. and Cui W. (1995). "Seismic response of segmental buildings." *Earthquake Engineering and Structural Dynamics*, Vol. 24, Issue 7: 1039-1048.
93. Zayas V., Low S., Mahin S. (1987). "The FPS earthquake resisting system." Technical report: EERC-87-01, Earthquake Engineering Research Center, University of California at Berkeley.
94. Mokha A., Constantinou M.C., Reinhorn A.M. and Zayas V.A. (1991). "Experimental Study of Friction - Pendulum Isolation System." *Journal of Structural Engineering*, Vol. 117, Issue 4, 1201-1217.
95. Fenz D.M. and Constantinou M.C. (2006). "Behaviour of the double concave friction pendulum bearing." *Earthquake Engineering and Structural Dynamics*, Vol. 35, 1403-1424.
96. Demetriades G.F., Constantinou M.C., Reinhorn A.M. (1993). "Study of wire rope systems for seismic protection of equipment in buildings." *Engineering Structures*, Vol. 15, Issue 5, 321-334.

97. Makris N. and Constantinou M.C. (1992). "Spring-viscous damper systems for combined seismic and vibration isolation" *Earthquake Engineering and Structural Dynamics*, Vol. 21, Issue 8, 649-664.
98. Shi Y., Becker T., Kurata M., Nakashima M. (2013). H^∞ control in the frequency domain for a semi-active floor isolation system." *Frontiers of Structural and Civil Engineering*, Vol. 7, Issue. 3, 264-275.
99. Marin-Artieda C. and Han X. (2015). "Experimental Investigation on the Seismic Performance of a Service Vibration Isolation Platform for Protection of Equipment." *Structures Congress 2015*: pp. 1774-1785.
100. Zhang D. (2010). "Examination of precast concrete diaphragm seismic response by three-dimensional nonlinear transient dynamic analyses." Ph.D. Dissertation, the University of Arizona, Tucson, U.S.
101. Fleischman R.B., Farrow K.T., Eastman K. (2002). "Seismic Performance of Perimeter Lateral-System Structures with Highly Flexible Diaphragms." *Earthquake Spectra*, Vol. 18, No. 2, 251-286.
102. Zhang D., Fleischman R.B. (2016). "Establishment of performance-based seismic design factors for precast concrete floor diaphragms." *Earthquake Engineering and Structural Dynamics*, Vol. 45, Issue 5, 675-698.
103. Rodriguez M., Restrepo J. I., Carr A. J. (2002). "Earthquake-induced floor horizontal accelerations in buildings." *Earthquake Engineering and Structural Dynamics*, Vol. 31, Issue 3, 693-718.
104. ASCE 7-05. (2016). "Minimum design loads for buildings and other structures." American Society of Civil Engineers.
105. Priestley M.J.N., Grant D.N. (2005). "Viscous damping in seismic design and analysis." *Journal of Earthquake Engineering*, Vol. 9, Supplement 2, 229-255.
106. Zhang D., Fleischman R.B., Restrepo J.I., Sause R. "Fundamental behavior of building structures with an inertial force-limiting floor anchorage system." Under preparation.
107. Symans M.D., Charney F.A., Whittaker A.S., Constantinou M.C., Kircher C.A., Johnson M.W., McNamara R.J. (2008). "Energy dissipation systems for seismic applications: current practice and recent developments." *Journal of Structural Engineering*, Vol. 134, No. 1, 3-21.
108. Haldar A. and Mahadevan S. (2000). "Probability, Reliability, and Statistical Methods in Engineering Design." John Wiley & Sons.

109. Toranzo-Dianderas L. A. (2002). "The use of rocking walls in confined masonry structures: a performance-based approach." Ph.D. Dissertation, the University of Canterbury, Christchurch, New Zealand.
110. Scott B. D., Park R. and Priestley M. J. N. (1982). "Stress-Strain Behavior of Concrete Confined by Overlapping Hoops at Low and High Strain Rates." ACI Journal Proceedings, Vol. 79, Issue 1, 13-27.
111. Guerrini, G., Restrepo, J., Massari, M., and Vervelidis, A. (2015). "Seismic Behavior of Posttensioned Self-Centering Precast Concrete Dual-Shell Steel Columns." Journal of Structural Engineering, Vol. 141, Issue. 4: 04014115.
112. Villaverde R. and Koyama L. (1993). "Damped resonant appendages to increase inherent damping in buildings." Earthquake Engineering and Structural Dynamics, Vol. 22, Issue 6, 491–507.
113. Den Hartog J.P. (1956). "Mechanical Vibrations (Edition 4)". New York: McGraw-Hill Book Company.
114. Miyama T. (1992). "Seismic response of multi-storey frames equipped with energy absorbing storey on its top." Tenth World Conference on Earthquake Engineering, Balkema, Rotterdam. ISBN 9054100605.
115. Sadek F., Mohraz B., Taylor A. and Chung R. (1997). "A method of estimating the parameters of tuned mass dampers for seismic applications." Earthquake Engineering & Structural Dynamics, 26(6), 617-635.
116. Anil K.C. (2011). "Dynamics of structures (Edition 4)." New Jersey: Prentice Hall. ISBN-13: 978-0132858038.
117. Fleischman R. (2013). "CE438/538 Behavior and design of structural systems." Department of Civil Engineering and Engineering Mechanics, University of Arizona.
118. Fleischman R. and Farrow K. (2001). "Dynamic behavior of perimeter lateral-system structures with flexible diaphragms." Earthquake Engineering & Structural Dynamics, 30(5), 745-763.
119. Andersson J. (2000). "A survey of multiobjective optimization in Engineering design." Technical Report, LiTH-IKP-R-1097, Department of Mechanical Engineering, Linköping University.
120. Tsai H. and Lin G. (1993). "Optimum tuned-mass dampers for minimizing steady-state response of support-excited and damped systems." Earthquake Engineering & Structural Dynamics, 22(11), 957-973.
121. Applied Technology Council. (2009). "Quantification of building seismic performance factors." FEMA P695.

122. ACI Committee 318 (2008). "Building code requirements for structural concrete (ACI 318-08) and commentary."
123. OpenSees. (2014). "User manual".
http://opensees.berkeley.edu/wiki/index.php/OpenSees_User.
124. Zhao J. and Sritharan S. (2007). "Modeling of strain penetration effects in fiber-based analysis of reinforced concrete structures." ACI Structural journal, Vol. 104, Issue 2, 133-141.
125. Shaikh, A. F. and Gehlhoff, J. (2007). "Load tests on new JVI PSA slotted inserts anchored in concrete slabs." Report on test results, Department of Civil Engineering and Mechanics, College of Engineering and Applied Science, University of Wisconsin-Milwaukee.
126. Mander J. B., Priestley M. J. N. and Park R. (1988). "Theoretical stress-strain model for confined concrete." Journal of Structural Engineering, Vol. 114, No. 8, 1804-1826.
127. Horan S. M. (2002). "Materials Modeling for Unbonded Post-Tensioned Precast Concrete Walls," M.S. Thesis, Department of Civil and Environmental Engineering, Lehigh University, Bethlehem, PA.
128. Scodeggio A., Quaranta G., Marano G., Monti G., Fleischman R. (2016). Optimization of force-limiting seismic devices connecting structural subsystems. Computers and Structures, Vol. 162, 16-27.